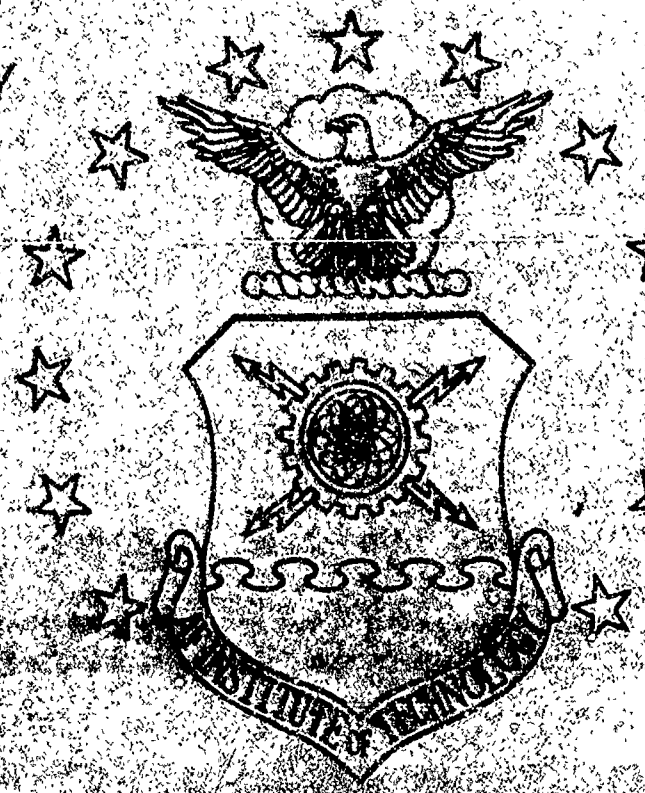

AUTOMATIC FLIGHT CONTROL SYSTEM DESIGN FOR AN UNMANNED RESEARCH VEHICLE USING DISCRETE QUANTITATIVE FEEDBACK THEORY

THESIS

David G. Wheaton
Captain, USAF

AFIT/GE/ENG/90D-66

DEPARTMENT OF THE AIR FORCE
AIR UNIVERSITY
AIR FORCE INSTITUTE OF TECHNOLOGY
Wright-Patterson Air Force Base, Ohio

AFIT/GE/ENG/90D-66

AUTOMATIC FLIGHT CONTROL SYSTEM DESIGN FOR AN UNMANNED RESEARCH VEHICLE USING DISCRETE QUANTITATIVE FEEDBACK THEORY

THESIS

David G. Wheaton
Captain, USAF

AFIT/GE/ENG/90D-66

Approved for public release; distribution unlimited

AFIT/GE/ENG/90D-66

AUTOMATIC FLIGHT CONTROL SYSTEM DESIGN FOR AN UNMANNED RESEARCH VEHICLE USING DISCRETE QUANTITATIVE FEEDBACK THEORY

THESIS

Presented to the Faculty of the School of Engineering

of the Air Force Institute of Technology

Air University

In Partial Fulfillment of the

Requirements for the Degree of

Master of Science in Electrical Engineering

David G. Wheaton, B.S.E.E.

Captain, USAF

Dec, 1990

Acknowledgments

I would like to thank Dr. Constantine Houpis and Dr. Isaac Horowitz for their guidance in this thesis. Without their constant support, the successful completion of this thesis would have been in serious jeopardy. I feel quite fortunate indeed to have had the opportunity to work closely with them for the last year and a half and to have gained valuable insight into the finer elements of control theory and design under their direction. I look forward to a continued association with you both.

Reliable computing resources were vital to this work. Nearly all of the work was done on the Noah SUN systems here at AFIT. Many thanks to Capt Ron Eddy and Tony Schoole for their no less than superior efforts in providing me with the computer support I needed. They were instantly attentive to my needs and the needs of all other users and quickly resolved all problems encountered to my great satisfaction.

To my fellow QFT'ers and classmates Capt Ken Crosby and Lt Russ Miller, I hope I've been as much help to you both as you both have been to me. It's been a long haul and I only wish it could have been a little easier for all of us. I sincerely wish the best of luck to you both and I hope we can see each other again some day.

Last and most importantly, a special thanks to my wife, Linda, and my kids, Brooke, Sandra, and Joseph. I greatly appreciate your patience and endurance during this work. I love you all very much.

David G. Wheaton

Table of Contents

List of Figures

List of Tables

Abstract

This thesis presents the application of non-minimum phase (NMP) w'-plane discrete MIMO (multiple-input-multiple-output) Quantitative Feedback Theory (QFT) to the design of a three-axis rate-commanded automatic flight control system for an unmanned research vehicle (URV). The URV model used has seven inputs and three outputs derived from the small-angle perturbation equations of motion. Plant parameter uncertainty consists of six flight conditions derived from variations in the aircraft center of gravity, airspeed, and gross weight. A weighting matrix $\mathbf{\Delta}$ is used to post-multiply the plants for blending the seven effector inputs into three *effective* rate-command inputs and resulting in an *effective* plant $\mathbf{P}_e = \mathbf{P}\mathbf{\Delta}$. Second order effector models and first order feedback sensor models are included in the plant. A time-scaled recursive algorithm is used to transform the continuous plant models to the w'-plane thereby avoiding the numeric problems associated with an intermediate z-plane representation. All the URV plant elements are minimum phase (MP). The transformation produces, however, a *sampling* NMP zero and one other NMP zero due to the three pole excess actuator/sensor model elements. These NMP elements limit the available loop bandwidth ($l_i(jv)$). Standard QFT design is used, with plant templates $\mathcal{P} = \{\mathbf{P}(jv)\}$ which quantitatively express the plant uncertainty. Due to the loop bandwidth limitations, only stability bounds are derived. The loop transmissions ($l_i(jv)$) are then shaped to achieve the maximum levels subject to the stability bounds. This is followed in the usual QFT manner with design of the prefilters. The design performance verification results include both linear (no limiting) and hybrid (amplitude limiting) simulations up to and including limiting of all surfaces. Some flight conditions are open-loop unstable so, in these cases, limiting induces instability. In this design, instability results only when all surfaces are at or very close to limiting. Hard limiting and nominal performance is shown.

AUTOMATIC FLIGHT CONTROL SYSTEM DESIGN FOR AN UNMANNED RESEARCH VEHICLE USING DISCRETE QUANTITATIVE FEEDBACK THEORY

I. Introduction

Unmanned research vehicles (URV 's) give flight control system engineers unique flight testing capabilities. This class of a flight test vehicle provides a much needed testbed environment for the efficient evaluation of components and algorithms, and is used for testing everything from complete flight control systems and new flight control concepts to individual components such as actuators and gyros. The Flight Dynamics Laboratory (WRDC/FIGL) at Wright-Patterson Air Force Base, Ohio, has developed a URV it calls Lambda to provide the Air Force with an affordable, flexible, and adaptable airborne testbed.

Lambda was designed specifically as a testbed and, in keeping with that design philosophy, an automatic flight control system will be implemented. Presently, Lambda is flown by radio-link from the ground. The incoming signals from the pilot are used to directly manipulate the seven effectors. The automatic flight control system will be inserted between the incoming signals from the pilot on the ground and the effector actuators of the aircraft to implement the control laws for Lambda's response to pilot three-axis rate commands. On past URV's, the flight control system implementation has been hardware intensive and thus not inherently flexible to modification and upgrade. Lambda's overall design strategy places the automatic flight control system implementation in software and thus does indeed make future upgrade and modification much easier. In fact, planned upgrades to Lambda's basic flight control system, to further enhance its testbed utility, include three-axis rate stabilization and pilot command augmentation. Future plans call for the ad-

dition of autopilot functions including wings leveling, altitude hold, heading hold, and out-of-sight maneuvering.

1.1 Background

The equations of motion (EOM) for any aircraft are in general highly coupled, nonlinear, and time-varying. The coefficients of these EOM can exhibit large variations throughout the aircraft flight envelope. Figure 1.1 shows a typical flight envelope for a high performance aircraft.

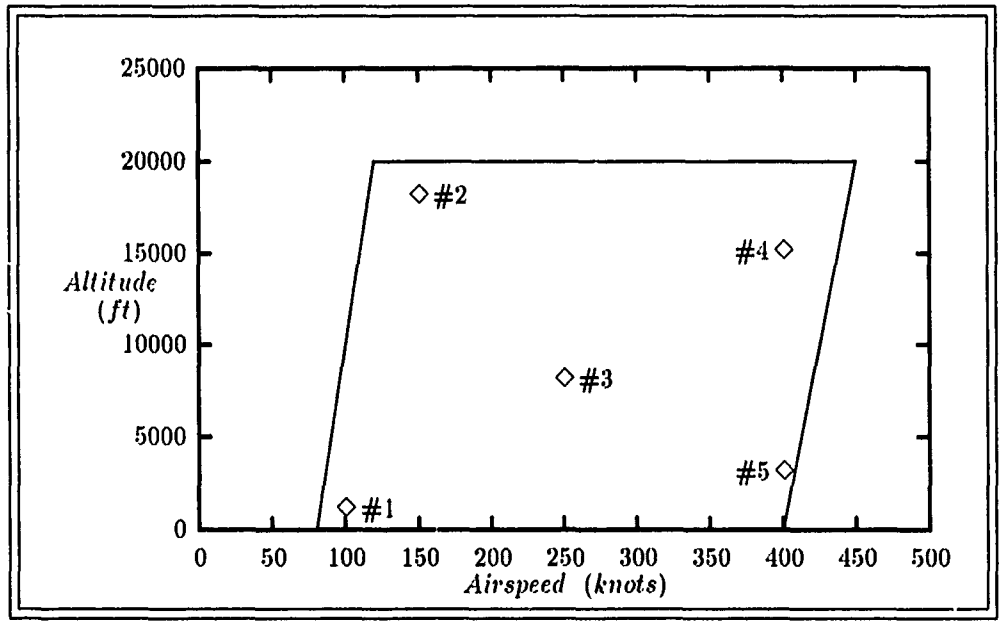

Figure 1.1. Typical High Performance Aircraft Fight Envelope

In general, a different set of equations exists describing the motion of the aircraft at every point within the flight envelope. Design of a control system at a given operating point within the flight envelope, such as any of those depicted in Figure 1.1 above, is a relatively straight-forward task. Practical flight control design, however, requires specified performance throughout all or part of the flight envelope or, in other words, at an infinite number of operating points. This significantly complicates the design problem since the designer will have or, for obvious practical reasons, may only want to use the EOM for a few operating points, maybe as few as five, as shown in Figure

1.1 above. The design method used then must be able to manage the variation from one operating point to the next and the uncertainty associated with all operating points in between. It must provide valid specified robust compensation over the entire range of plant parameter variation.

Since an aircraft in flight represents a highly uncertain, nonlinear MIMO (multiple-input-multiple-output) system plant, it becomes quite beneficial for the designer to simplify the problem to make the design synthesis as easy as possible. In this thesis, the small-angle perturbation EOM set is used for each flight condition considered. The plant is linear and time-invariant in this form, and the EOM set, to an acceptable approximation, describes the plant dynamics and is valid for small-angle perturbations about a nominal or *trim* flight condition.

A large class of problems exists where the parameters of the plant are uncertain and where the variation in these parameters are known and can be bounded. Many flight control problems, including the Lambda URV, fall into this class. Quantitative Feedback Theory (QFT), developed by Dr. Isaac Horowitz, is a feedback design technique capable of guaranteeing *a priori* specified performance in a large problem class where the plant parameter variation is uncertain but bounded. This technique is used in this thesis to synthesize compensation to provide a three-axis rate-commanded flight control system for the Lambda URV.

1.2 QFT History

QFT has been shown to provide guaranteed control system performance for a large class of systems with highly uncertain plants [6:686–687] [8, 31, 12]. The designer can specify the allowable range of system response and, with knowledge only of the range of variation in the plant, synthesize the compensator required to guarantee the *a priori* specified system performance. This is different than other point design techniques in that every operating point falling within the designed-for range of plant variation, an infinite number to be sure, will have the desired response characteristics instead of only the finite number designed for in the point design techniques.

In flight control system design, the designer usually has more control inputs than outputs to be controlled. Lambda has seven possible control inputs (effectors) and three controlled outputs of q, p, and r and is referred to as a MIMO system. In 1963, Dr. Horowitz presented, for the first time, a technique capable of synthesizing a design around uncertain MIMO system plants [10:Chap 10]. This was the first and beginning formulation of quantitative feedback design techniques. Considerable work in multivariable control system design preceded and followed this book but dealt with design synthesis in cases where the system plant was known. In 1979, Dr. Horowitz presented a simpler multivariable design technique, based on his earlier work, for designing feedback around highly uncertain plants [12, 13]. It is now well-known as Quantitative Feedback Theory or QFT. The features of the QFT method are [14:677]:

- It is quantitative in nature
- The MIMO solution is reducible to a set of MISO (multiple-input-single-output) equivalent problems
- The design is tuned to the extent of the uncertainty and performance tolerances established *a priori*
- It is a frequency domain technique

QFT is particularly attractive in the MIMO case since the design problem can be decomposed into the more tractable MISO cases where the design execution is performed on the single-loop equivalent systems with no coupling between the loops and no iteration required [12]. A quick look at the complexity of even a 3-dimensional MIMO problem shows vividly the significance of this capability.

QFT was, in spite of its demonstrated merit, almost immediately criticized for its inherent nonoptimality and overdesign. Dr. Horowitz admitted from the start that the method made no optimality claim [12, 14]. He was quick to point out though that "the technique guarantees a

satisfactory design. ..y a comparatively straightforward systematic procedure" and no other design technique could make that claim [14:699].

In later work in 1982, Dr. Horowitz improved his formulation of QFT and proposed a method to reduce the inherent overdesign by making use of the fact that there is some correlation in the uncertainties between the elements of the system plant [14:697] [13]. Knowledge of this correlation would allow the designer to further reduce the loop design bandwidth and thus the overdesign of the final design solution.

This improved formulation of QFT is presently being used extensively for flight control system design problems at the Air Force Institute of Technology (AFIT). It has been applied quite successfully to a number of very different design problems and aircraft. The following partial list enumerates some of the AFIT thesis efforts in QFT flight control research.

- J. M. Adams — *Digital QFT Design for the AFTI/F- 16* [1]
- P. B. Arnold — *FCS Reconfiguration Using QFT* [2]
- B. T. Clough — *Reconfiguration for a STOL Aircraft Using QFT* [4]
- J. S. Coucoules — *Effects of Discretizing QFT Designs* [5]
- S. W. Hamilton — *Digital QFT Design for an Unmanned Research Vehicle* [8]
- B. S. Migyanko — *Integrated Flight/Propulsion Control for a STOL Aircraft Using QFT* [25]
- K. N. Neumann — *Digital QFT Design for the Control Reconfigurable Combat Aircraft* [28]
- P. T. Ott — *URV Reconfiguration using Digital QFT* [29]
- H. H. Russell — *Analog QFT Design for the KC-135* [30]
- D. L. Schneider — *AFTI/F-16 FCS Design Using Digital QFT* [31]

QFT has been highly developed for the design of analog control systems. For the past few years, flight control research has and is being directed toward the design of digital flight control

systems. Thus, great interest exists now in discrete control design technique development and application. Discrete plane control system design for digital application is generally superior to earlier methods of implementing discretized analog designed controllers [18, 17, 24, 32].

Control system designs meant for digital implementation are executed by two basic methods. In what's referred to as the *emulation approach* by Tischler [32], the design is executed in continuous-time and the synthesized compensator is then discretized for implementation. It has been shown that this method does not produce as good a design when compared to executing a discrete design process of the same system [24, 32]. In general terms, an equivalent discrete-time design of a given system meant for discrete-time implementation will produce a lower-order design and at a slower sampling rate [32:71]. This method is sometimes preferred as a first cut and for trade-off studies since designing in the discrete-time domain is somewhat more difficult. In general, the *emulation method* will yield flyable more conservative (higher sample rate) digital compensators. Most importantly, the *emulation approach* provides no information on the interaction of digital system elements with the analog plant. The most important of these issues and interactions are [32:70]:

- Zero Order Hold (ZOH) dynamics
- Frequency aliasing
- Intersample Response
- Hidden Oscillations
- Tustin transformation
- Computational delays
- Sensitivity to parameter variations
- Computer quantization and roundoff errors

In the second and preferred *direct* digital design method, these issues can be addressed because information about their effects is available in the design process. In the direct approach, the plant is discretized by transformation to either the z-plane or the w′-plane and the design is executed [18, 20, 16]. Here, as mentioned above, the design process is more difficult. Pole-zero loop shaping, required in a z-plane design, is a much poorer method of coping with plant parameter uncertainty [17]. Since QFT is formulated to take advantage of Bode frequency response shaping techniques, transformation to the w′-plane, because of the similarity between the w′-plane and the s-plane, is the preferred digital QFT approach. This is in fact exactly what is done in applying QFT to flight control design problems.

The Lambda plants, for this study, are digitized and the design executed in the w′-plane. Capt Ott, in his design effort, digitized the plant first in the z-plane and then transformed it, by use of the bilinear transformation, to the w′-plane [29:3.1–3.11]. He had some numerical difficulty with this that unfortunately plagued the rest of the design effort. Lt Hamilton, however, was able to employ the Hofmann routine [9] to transform the continuous-time plant to the w′-plane and was able to avoid the problems Capt Ott had in forming the w′-plane transfer functions [8].

QFT is applied to square ($n = m$) system plants with n inputs and m outputs. Whenever $n > m$ inputs are available to control m outputs, a decision is made as to how to use the extra inputs. This is always the case no matter what design technique is employed [17]. For most flight control problems, it is desirable to use all available inputs. For the QFT flight control design problem, all plant inputs are used by designing an mxn weighting matrix $\mathbf{\Delta}$ to blend these n inputs into m effective inputs. It is apparent that forming the equivalent QFT plant ($\mathbf{P\Delta}$) produces a variation of the original system plant and thus selection of the weighting matrix is critical to maintaining the integrity of the original plant. A further consideration on the weighting matrix selection is that the determinant of the resulting mxm effective plant is *preferably* minimum phase or, in other words, the determinant must have no zeros located in the right half s-plane for a continuous-time design

or in the right half w'-plane for a discrete design [6:699]. *Preferably* minimum phase implies that certain non-minimum phase characteristics can be dealt with.

In one of the first digital QFT flight control system designs, Maj Arnold used a $\mathbf{\Delta}$ matrix of plus ones, zeros, and minus ones whose elements were assigned based solely on physical insight and on the particular aircraft-specific control knowledge [2]. Later, Capt Clough adjusted the magnitudes of the elements to other than ones and zeros in his $\mathbf{\Delta}$ matrix using basically a trial and error procedure with favorable results [4]. Other later efforts tried to improve the trial and error procedure. Lt Hamilton made good progress at identifying some possible analytic approaches to improving the $\mathbf{\Delta}$ matrix trial and error selection process [8]. The weighting matrix selection for QFT compatibility is probably the single most important part of the overall design effort [18].

1.3 Problem

The purpose of this thesis is to design a three-axis rate-commanded flight control system for the Lambda URV. A rate-commanded flight control system is one where the pilot commands pitch-rate (q), roll-rate (p), and/or yaw-rate (r). Two factors motivate this study. First, Lambda uses no compensation between the pilot and the effectors. As a result, the pilot must provide the compensation required to attain noninteracting three-axis responses. In the lateral mode, this requires simultaneous actuation of the ailerons and the rudder to produce either a pure roll or yaw. To produce a pure roll, for example, the pilot must actuate the ailerons, interpret the aircraft motion, and apply the appropriate rudder command to counter the adverse yaw induced by the ailerons. Properly designed feedback control laws do this automatically. Second, without a basic core flight control system, the planned autopilot function enhancements would be much more difficult to design and implement.

Discrete QFT is used to design the compensators and pre-filters needed to implement the control laws for Lambda's response to pilot three-axis rate commands. Six flight conditions are

used in the design to provide the bounds of plant parameter uncertainty. They are derived from variations in airspeed, total aircraft weight, and center-of-gravity (CG) location.

1.4 Scope

The focus of this thesis is the application of discrete QFT to the task of designing a non-interacting rate-commanded flight control system for the Lambda URV. Special emphasis will be on investigating directly the problems associated with meeting the design criteria for a w'-plane discrete design with effector and sensor dynamics included in the system plant. Prior theses have documented problems in this area [8, 29]. Issues associated with implementation of the controller and prefilter designs such as finite word length limitations, rounding errors, etc. will not be addressed. Implementation issues directly impacted by the design, such as compensation order and difference equation accuracy requirements, will be coordinated with WRDC/FIGL since this design will be coded on the flight control computer aboard Lambda and flight tested.

1.5 Assumptions

This thesis uses a time-invariant linear state space model for the Lambda URV provided by WRDC/FIGL. A number of assumptions are generally made to simplify the system model for this type of design problem. Below is a list of all the assumptions that apply for this study.

- The EOM are time-invariant and linearized about a nominal or *trim* flight condition so that small-angle perturbation models are valid
- Effectors (control surface actuators) are not driven to saturation by command inputs thus invalidating the assumed linear model used for the design process
- Aircraft mass is constant during command input
- The aircraft is a rigid body
- The earth is an inertial reference frame

- The atmosphere is fixed in relation to the earth
- Aircraft thrust is constant

Additional assumptions pertinent to the control system design are:

- The commanded inputs and the commanded outputs are measurable
- Three-axis rate signals (q, p and r) and bank angle (ϕ) are available on the Lambda URV
- The effectors can be individually operated
- All signals and system elements are Laplace transformable
- A sampling rate of 60 Hz is implementable on Lambda

1.6 Approach

Discrete-time QFT is used to design a diagonal three-channel cascade compensator and prefilter. The basic continuous-time QFT block diagram for a three channel MIMO system like Lambda is shown in Figure 1.2.

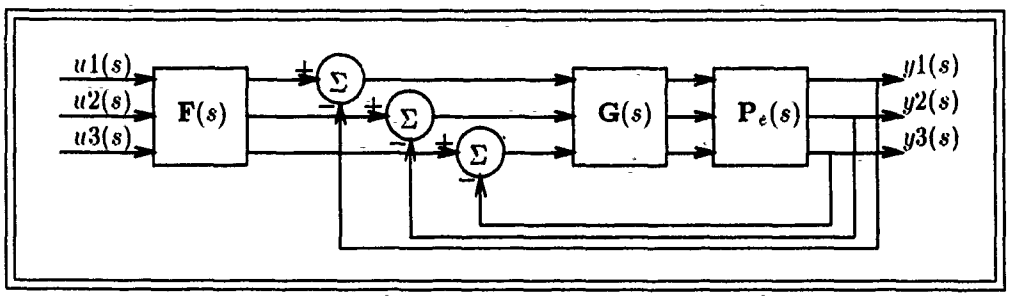

Figure 1.2. Continuous-Time QFT Block Diagram

QFT is used to synthesize the $\mathbf{F}(s)$ and $\mathbf{G}(s)$ in Figure 1.2. In the most general case, $\mathbf{F}(s)$ and $\mathbf{G}(s)$ are nxn dimensional matrices of prefilter and compensator transfer functions where n is the dimension of the plant $\mathbf{P}_e(s)$. $\mathbf{P}_e(s)$ denotes the *effective* system plant and it must be square. This requirement is addressed later. The $\mathbf{P}_e(s)$ notation implies a variation from the original system

plant; more precisely, it is the squared down $n \times n$ version of the system. For the majority of system designs, and normally as a first cut, the off diagonal elements of $\mathbf{F}(s)$ and $\mathbf{G}(s)$ are not needed and therefore diagonal $\mathbf{F}(s)$ and $\mathbf{G}(s)$ are synthesized. n is three for this study.

The basic steps to completing this QFT design are:

1. Form the s-plane plant transfer function matrix for each flight condition
2. Apply effector weights to blend the effectors such that a new effective plant matrix is formed having the desired rate command inputs of q, p, and r
3. Add the effector and rate sensor models to the effective plant matrix and transform this system to the w′-plane
4. Determine if $|\mathbf{P}_e(s)|$ is MP and, if not MP, adjust the elements of the weighting matrix $\mathbf{\Delta}(s)$ until $|\mathbf{P}_e(s)|$ is MP or *almost* MP
5. Invert the w′-plane system plant and apply continuous QFT methods to design the first loop compensator and prefilter
6. Apply the modified QFT design technique to the second and third loops in succession
7. Simulate the w′-plane design for verification
8. Transform the w′-plane compensators and prefilters to the z-plane and simulate the hybrid system (discrete prefilters and compensators and a continuous plant)

1.7 Presentation

This thesis contains seven chapters. Chapter II presents the Lambda URV aircraft. The models used and the effector deflection sign convention are given. The pre-QFT design weighting matrix synthesis and the resulting effective QFT design plants are fully developed. Chapter III presents the discrete QFT theory applicable to this study and Chapter IV describes the actual QFT cascade compensator and pre-filter designs. Chapter V presents the design simulation results. The completed designs are simulated on a SUN III workstation running SUN OS version 4.1 with the CAD/CAE program Matrix_x [23] SUN workstation version 2.03. Chapter VI presents a wing

leveler autopilot design and simulation based on the implementation of the rate-commanded system designed in this thesis. Finally, Chapter VII presents a summary of the highlights of the study, the conclusions drawn and recommendations for future progress.

1.8 Notation

Some of the standard notation used in this study is given below. This list is not all inclusive. Notation used for the QFT design process is generally standard QFT notation as it appears in the literture and its meaning will be specified as it appears in this writing.

- Scalar variables and scalar components of vectors and matrices are denoted by upper or lower case italic type
- Vectors are denoted by lower and upper case boldface letters
- Upper case vectors have s-plane, z-plane or w′-plane transformed elements
- Lower case vectors have time-domain element variables or are frequency plane elements of a matrix or vector
- Matrices are denoted by upper case boldface letters
- Matrices will contain either time-domain or frequency-domain elements. $\mathbf{A}(t)$, $\mathbf{A}(s)$, $\mathbf{A}(z)$, and $\mathbf{A}(w')$ denote a matrix with time-domain and s-plane, z-plane, and w′-plane frequency-domain elements respectively
- When the independent variable is not given the time-domain is usually assumed unless the frequency domain is indicated by the context
- $\mathbf{adj[A]}$ denotes the adjoint matrix of $\mathbf{A}$ and $\mathbf{adj}_{ij}\mathbf{[A]}$ denotes the ij element of $\mathbf{adj[A]}$
- $\mathbf{A}^{-1}$ denotes the inverse matrix of $\mathbf{A}$
- $\mathbf{A}^{T}$ denotes the transpose of a matrix or vector

II. The Aircraft

This chapter presents the aircraft models used and the development of these models to a form compatible with the application of discrete QFT. The basic aircraft model is given in state space and all system parameters identified. QFT is a frequency domain technique and thus the plant transfer function matrix $\mathbf{P}(s)$ is developed. For QFT application, the plant transfer function matrix $\mathbf{P}(s)$ must be square. This is not generally the case in most flight control applications so the plant must be made square by post-multiplying $\mathbf{P}(s)$ by a weighting matrix $\mathbf{\Delta}(s)$ to form a square effective plant matrix $\mathbf{P}_e(s)$. The $\mathbf{\Delta}(s)$ matrix selection used in this thesis is presented. Finally, the effector deflection sign convention, the effector actuator models and the rate feedback sensor models are given.

2.1 Aircraft Model

The aircraft used in this thesis is the Lambda URV owned by the Flight Dynamics Laboratory (WRDC/FIGL) at Wright-Patterson AFB, Ohio. It is a small (14 ft wing span) unmanned pusher propeller driven radio-controlled flight research vehicle. Appendix A lists some of Lambda's known performance specifications.

The aircraft model used is provided in the state space form of:

$$\dot{\mathbf{x}}(t) = \mathbf{A}\,\mathbf{x}(t) + \mathbf{B}\,\mathbf{u}(t) \tag{2.1}$$

$$\mathbf{y}(t) = \mathbf{C}\,\mathbf{x}(t) + \mathbf{D}\,\mathbf{u}(t) \tag{2.2}$$

where

- $\mathbf{x}(t)$ is the state vector (8x1)
- $\mathbf{u}(t)$ is the input or forcing function vector (7x1)
- $\mathbf{y}(t)$ is the output vector (3x1)

- **A** is the plant dynamics matrix of constant coefficients (8x8)
- **B** is the input or forcing function matrix of constant coefficients (8x7)
- **C** is the output matrix of constant coefficients (3x8)
- **D** is the input or forcing function feedforward matrix of constant coefficients (3x7)

The aircraft model has no input feedforward elements and thus $\mathbf{D} = \mathbf{0}$ so that the state space model for the URV becomes:

$$\dot{\mathbf{x}}(t) = \mathbf{A}\,\mathbf{x}(t) + \mathbf{B}\,\mathbf{u}(t) \tag{2.3}$$

$$\mathbf{y}(t) = \mathbf{C}\,\mathbf{x}(t) \tag{2.4}$$

The aircraft state space model is derived from the aerodynamic stability and control derivative data generated by the Digital DATCOM CAD package used to design Lambda. This model represents the linearized time-invariant small-angle perturbation equations of motion. Numerous textbooks and other sources exist that fully present the derivation of a generic perturbed EOM set and its representation in state space form. References [3, 7] are used in this thesis.

The aircraft system perturbation states and the engineering units for each perturbation state variable of this model are shown in Equation 2.5. By definition, a perturbed EOM set has zero initial conditions so that:

$$\mathbf{x}_0 = \begin{bmatrix} 0 & 0 & 0 & 0 & 0 & 0 & 0 & 0 \end{bmatrix}^T$$

The perturbation states ($\mathbf{x}_{pert}$) therefore represent changes in the aircraft motion from the trim condition about which the perturbed EOM set is derived. The *true* system states are a combination

of the *trim* condition states and the perturbed states and are represented as:

$$\mathbf{x}_{true} = \mathbf{x}_{trim} + \mathbf{x}_{pert}$$

$$\mathbf{x}(t) = \begin{bmatrix} \theta(t) \\ u(t) \\ \alpha(t) \\ q(t) \\ \phi(t) \\ \beta(t) \\ p(t) \\ r(t) \end{bmatrix} \quad \begin{matrix} pitch\ angle\ (rad) \\ forward\ velocity\ (\frac{ft}{sec}) \\ angle-of-attack\ (rad) \\ pitch\ rate\ (\frac{rad}{sec}) \\ bank\ angle\ (rad) \\ sideslip\ angle\ (rad) \\ roll\ rate\ (\frac{rad}{sec}) \\ yaw\ rate\ (\frac{rad}{sec}) \end{matrix} \tag{2.5}$$

Lambda has seven effectors (control surfaces) and each one is used as an input to this aircraft model. These effector inputs are:

$$\mathbf{u}(t) = \begin{bmatrix} \delta_{e_L}(t) \\ \delta_{e_R}(t) \\ \delta_{f_L}(t) \\ \delta_{f_R}(t) \\ \delta_{a_L}(t) \\ \delta_{a_R}(t) \\ \delta_r(t) \end{bmatrix} \quad \begin{matrix} left\ elevator\ (rad) \\ right\ elevator\ (rad) \\ left\ flap\ (rad) \\ right\ flap\ (rad) \\ left\ aileron\ (rad) \\ right\ aileron\ (rad) \\ rudder\ (rad) \end{matrix} \tag{2.6}$$

The outputs controlled in a rate-commanded flight control system are:

$$\mathbf{y}(t) = \begin{bmatrix} q(t) \\ p(t) \\ r(t) \end{bmatrix} \quad \begin{matrix} pitch\ rate\ (\frac{rad}{sec}) \\ roll\ rate\ (\frac{rad}{sec}) \\ yaw\ rate\ (\frac{rad}{sec}) \end{matrix} \tag{2.7}$$

The plant matrix $\mathbf{P}(s)$ of system transfer functions, assuming zero initial conditions, is derived from Equations 2.3 and 2.4. In Laplace transform notation, these equations become:

$$s\mathbf{X}(s) = \mathbf{A}\,\mathbf{X}(s) + \mathbf{B}\,\mathbf{U}(s) \tag{2.8}$$

$$(s\mathbf{I} - \mathbf{A})\mathbf{X}(s) = \mathbf{B}\,\mathbf{U}(s) \tag{2.9}$$

$$\mathbf{X}(s) = (s\mathbf{I} - \mathbf{A})^{-1}\mathbf{B}\,\mathbf{U}(s) \tag{2.10}$$

$$\mathbf{Y}(s) = \mathbf{C}(s\mathbf{I} - \mathbf{A})^{-1}\mathbf{B}\,\mathbf{U}(s) \tag{2.11}$$

$$\mathbf{Y}(s) = \mathbf{P}(s)\mathbf{U}(s) \tag{2.12}$$

and therefore the plant matrix is written as:

$$\mathbf{P}(s) = \mathbf{C}(s\mathbf{I} - \mathbf{A})^{-1}\mathbf{B} \tag{2.13}$$

Dimensionally $\mathbf{P}$, for the Lambda URV, is:

$$\mathbf{P}_{3x7}(s) = \mathbf{C}_{3x8}[(s\mathbf{I} - \mathbf{A})^{-1}]_{8x8}\mathbf{B}_{8x7} \tag{2.14}$$

The individual elements of **P** are all functions of the Laplace variable s and relate each system output to each system input. $\mathbf{P}(s)$ is thus represented as:

$$\mathbf{P}(s) = \begin{bmatrix} \frac{q(s)}{\delta_{e_L}(s)} & \frac{p(s)}{\delta_{e_L}(s)} & \frac{r(s)}{\delta_{e_L}(s)} \\ \frac{q(s)}{\delta_{e_R}(s)} & \frac{p(s)}{\delta_{e_R}(s)} & \frac{r(s)}{\delta_{e_R}(s)} \\ \frac{q(s)}{\delta_{f_L}(s)} & \frac{p(s)}{\delta_{f_L}(s)} & \frac{r(s)}{\delta_{f_L}(s)} \\ \frac{q(s)}{\delta_{f_R}(s)} & \frac{p(s)}{\delta_{f_R}(s)} & \frac{r(s)}{\delta_{f_R}(s)} \\ \frac{q(s)}{\delta_{a_L}(s)} & \frac{p(s)}{\delta_{a_L}(s)} & \frac{r(s)}{\delta_{a_L}(s)} \\ \frac{q(s)}{\delta_{a_R}(s)} & \frac{p(s)}{\delta_{a_R}(s)} & \frac{r(s)}{\delta_{a_R}(s)} \\ \frac{q(s)}{\delta_r(s)} & \frac{p(s)}{\delta_r(s)} & \frac{r(s)}{\delta_r(s)} \end{bmatrix}^T \tag{2.15}$$

2.2 *Effector Actuation Sign Convention and Angle Limits*

The effector actuation sign convention used in the Lambda aircraft model is shown in Figure 2.1. The effectors on Lambda have the following deflection angle limits.

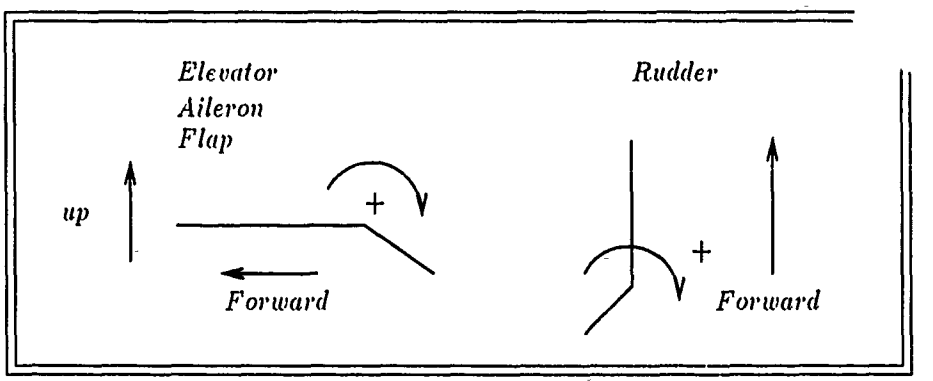

Figure 2.1. Effector Actuation Sign Convention

Elevators – $\pm$ 15° ($\pm$ 0.26 *rad*)

Flaps – +0° $\Rightarrow$ −20° (+0 *rad* $\Rightarrow$ −0.35 *rad*)

Ailerons – +15° $\Rightarrow$ −10° (+0.26 *rad* $\Rightarrow$ −0.17 *rad*)

Rudder – $\pm$ 25° ($\pm$ 0.44 *rad*)

Actuator rate limits are not required due to the small physical size of Lambda and are not used in this study.

2.3 Effector Actuator and Sensor Models

This study accounts for the effects of effector actuator and rate sensor dynamics. A second order actuator model identical for all seven effectors is used. The model is:

$$\frac{\delta_{actuator}(s)}{\delta_{cmd}(s)} = \frac{324}{s^2 + 25.4s + 324} \tag{2.16}$$

Gyros provide the three-axis rate signals for feedback to the URV flight control system. The gyro dynamics are modeled as:

$$\frac{RATE_{gyro}(s)}{RATE_{cmd}(s)} = \frac{50}{s + 50} \tag{2.17}$$

With seven effector actuators and three sensors, the basic (uncompensated) Lambda URV model in block diagram form is shown in Figure 2.2 on page 2-7. In matrix notation, the actuators and sensors are represented as:

$$\mathbf{ACT}(s) = \begin{bmatrix} 1 & 0 & 0 & 0 & 0 & 0 & 0 \\ 0 & 1 & 0 & 0 & 0 & 0 & 0 \\ 0 & 0 & 1 & 0 & 0 & 0 & 0 \\ 0 & 0 & 0 & 1 & 0 & 0 & 0 \\ 0 & 0 & 0 & 0 & 1 & 0 & 0 \\ 0 & 0 & 0 & 0 & 0 & 1 & 0 \\ 0 & 0 & 0 & 0 & 0 & 0 & 1 \end{bmatrix} \frac{324}{s^2 + 25.4s + 324} \tag{2.18}$$

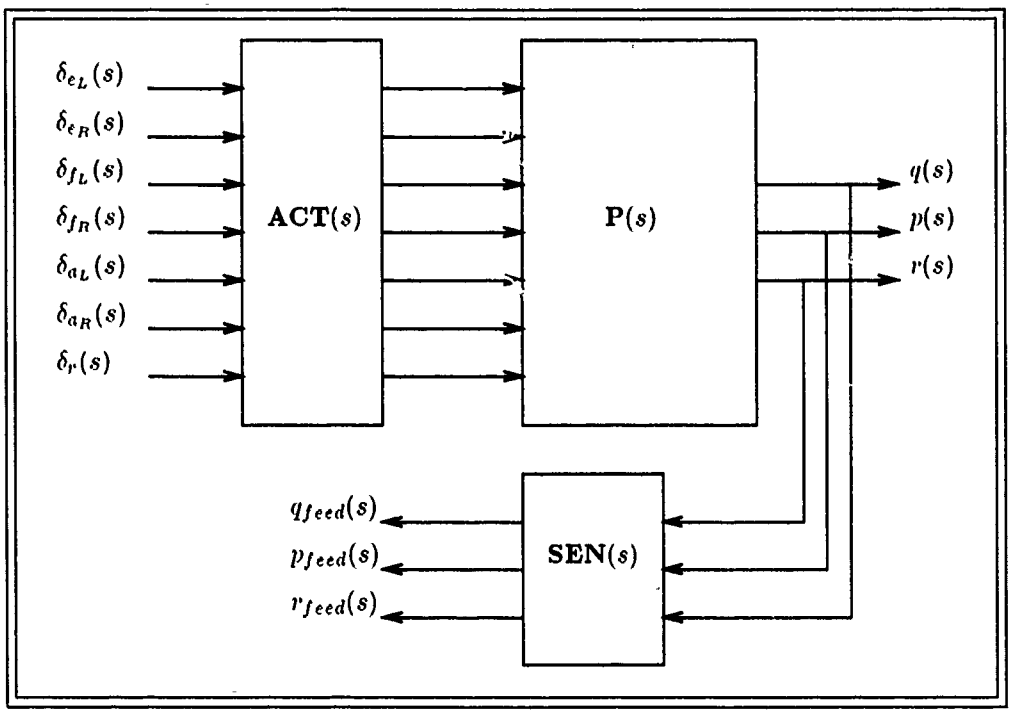

Figure 2.2. Basic URV Model With Actuators and Sensors

$$\mathbf{SEN}(s) = \begin{bmatrix} 1 & 0 & 0 \\ 0 & 1 & 0 \\ 0 & 0 & 1 \end{bmatrix} \frac{50}{s+50} \tag{2.19}$$

2.4 Flight Conditions

Successful application of QFT relies on having knowledge of the bounds of the variation in the plant parameters. This study uses six flight conditions to quantify the plant parameter uncertainty. These six flight conditions are selected as the very extremes of the flight envelope. Since the URV is flown close to the ground, altitude is not a significant variable in its flight envelope. Instead, airspeed, CG location and gross weight are the variables that most affect the plant variation and thus the particular flight condition. Table 2.1 shows the maximum, minimum and nominal values for these parameters. In that table, MAC refers to the mean aerodynamic chord. Refer to Appendix

A for these and other Lambda aircraft data of interest. Table 2.2 gives the flight conditions used to generate the six Lambda plants used for this study.

Table 2.1. Maximum, Minimum and Nominal Lambda Parameters

	Minimum	Maximum	Nominal
Weight (lbs)	150	200	168
CG empty fuel (%) †	26	41	N/A
CG full fuel (%) †	32	47	32
Speed (knots)	45	100	N/A
† % of MAC aft of leading edge			

Table 2.2. The Aircraft Flight Conditions

Plant #	Speed (kts)	CG (% MAC)	Weight (lbs)	α	C'_L	$C'_{L_{\dot{\alpha}}}$	C'_m	$C'_{m_{\dot{\alpha}}}$
1	40	50	150	10.4°	1.289	1.091	0.0653	−4.528
2	100	50	150	−1.64°	0.210	1.806	0.0615	−5.266
3	100	25	200	−0.96°	0.280	1.94	−0.0072	−6.133
4	70	50	200	1.9°	0.564	1.554	0.0682	−4.527
5	70	25	150	0.556°	0.427	1.769	−0.0448	−5.595
6 ‡	70	25	150	0.556°	0.427	1.769	−0.0448	−5.595

‡Note that plant #5 and #6 appear to be the same. Their flight parameters shown in Table 2.2 are identical however changes were made to the stability derivatives such that plant #6 represents the very worst case combination of the derivatives C'_{m_q} , C'_{m_α} , C'_{n_β} , C'_{n_r} and C'_{l_p} .

2.5 *Effective Plant* $\mathbf{P}_e(s)$

QFT application requires a square *nxn* plant. It must be square because the QFT design equations require the inversion of $\mathbf{P}(s)$, the system plant. For systems like Lambda where the plant is not square, and where the number of inputs exceeds the number of outputs, an *effective* system plant is formed by means of a weighting matrix preceding the plant. Lambda's basic system with dimensions is represented as:

$$\mathbf{Y}_{3x1}(s) = \mathbf{P}_{3x7}(s)\ \mathbf{U}_{7x1}(s) \tag{2.20}$$

The effective system plant is formed by blending the seven control inputs into three effective control inputs with a weighting matrix $\mathbf{\Delta}(s)$.

$$\mathbf{U}_{7x1}(s) = \mathbf{\Delta}_{7x3}(s)\ \mathbf{V}_{3x1}(s) \tag{2.21}$$

Substitute Equation 2.21 into Equation 2.20 such that:

$$\mathbf{Y}_{3x1}(s) = \mathbf{P}_{3x7}(s)\ \mathbf{\Delta}_{7x3}(s)\ \mathbf{V}_{3x1}(s) \tag{2.22}$$

and rewrite Equation 2.22 so that:

$$\mathbf{Y}_{3x1}(s) = \mathbf{P}_{e_{3x3}}(s)\ \mathbf{V}_{3x1}(s) \tag{2.23}$$

where

$$\mathbf{P}_{e_{3x3}}(s) = \mathbf{P}_{3x7}(s)\ \mathbf{\Delta}_{7x3}(s) \tag{2.24}$$

$\mathbf{P}_e(s)$ now becomes the squared down effective plant compatible with QFT design application. The outputs of $\mathbf{P}_e(s)$ are the desired three-axis rates q, p, and r and the inputs $\mathbf{V}(s)$ to the effective system now are three-axis rate commands. Figure 2.3 shows the effective Lambda model after blending the seven effectors.

The last step in the development of $\mathbf{P}_e(s)$ is to incorporate the effector actuator and rate sensor signal models. Figures 2.2 and 2.3 show that the rate sensors are physically located in the feedback loop of the URV model. This is not a problem since QFT compensation synthesis relies on shaping the open loop $\mathbf{HP}_e\mathbf{G}$ and therefore, specific placement of the loop elements in the forward branch before $\mathbf{\Delta}$ or in the feedback branch after $\mathbf{H}$ does not matter. Figure 2.3 and Equations 2.18

and 2.19 are used to develop $\mathbf{P}_e(s)$ with actuators and rate sensors included.

$$\mathbf{P}_e(s) = \mathbf{I}_{3x3}\left[\frac{50}{s+50}\right]\mathbf{P}_{3x7}(s)\,\mathbf{I}_{7x7}\left[\frac{324}{s^2+25.4s+324}\right]\mathbf{\Delta}_{7x3}(s) \tag{2.25}$$

$$\mathbf{P}_e(s) = \mathbf{P}_{3x7}(s)\,\mathbf{\Delta}_{7x3}(s)\left[\frac{(324)(50)}{(s^2+25.4s+324)(s+50)}\right] \tag{2.26}$$

One actuator/sensor model is cascaded with each element of $(\mathbf{P\Delta})_{3x3}(s)$. From this point on, the *effective* plant $\mathbf{P}_e(s)$ is assumed to have the effector actuator and sensor model included.

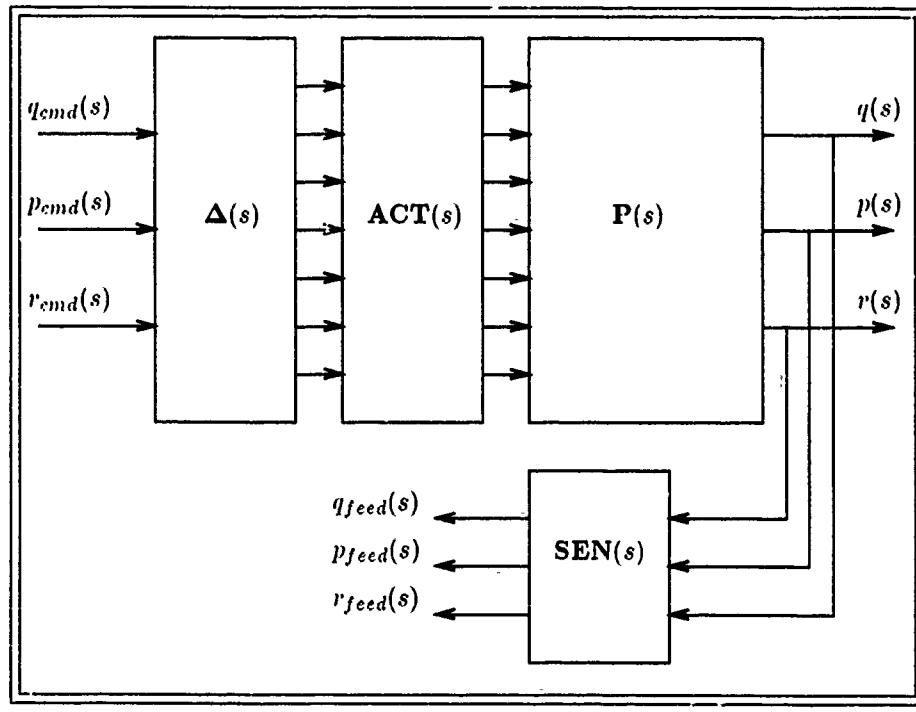

Figure 2.3. Effective QFT Plant Model With Actuators and Sensors

2.6 The Weighting Matrix $\mathbf{\Delta}(s)$

Component selection for the weighting matrix $\mathbf{\Delta}(s)$ developed in the previous section is very critical to the success of the overall design. $\mathbf{\Delta}(s)$ is normally used to achieve the most efficient use of the available control system effectors compatible with a minimum-phase (MP) or almost MP plant. A MP element is one that has no *right half plane* (RHP) zeros.

The critical requirement in selecting $\mathbf{\Delta}(s)$ is that the resulting $|\mathbf{P}_e(s)|$ be preferably minimum phase (MP) or have only far-off RHP zeros (almost MP). The benefits of feedback are severely reduced or nonexistent in a non-minimum phase (NMP) system depending on the location of the NMP zeros. The requirement for a MP $|\mathbf{P}_e(s)|$ comes directly from the derivation of the MISO (multiple-input-single-output) equivalent design equations for the MIMO QFT system. This requirement is fundamental and applies to ALL linear time-invariant compensation techniques, not just QFT. In fact, QFT has the ability to extract the maximum attainable feedback in a NMP system [17].

In the QFT MISO loop transmission synthesis, the design equations use the $\mathbf{Q}(s)$ matrix. $\mathbf{Q}(s)$ is related to $\mathbf{P}_e(s)$ in the following way.

$$\mathbf{P}_e^{-1}(s) = \begin{bmatrix} p^*_{1,1}(s) & p^*_{1,2}(s) & \cdots & p^*_{1,j}(s) \\ p^*_{2,1}(s) & p^*_{2,2}(s) & \cdots & p^*_{2,j}(s) \\ \vdots & \vdots & & \vdots \\ p^*_{i,1}(s) & p^*_{i,2}(s) & \cdots & p^*_{i,j}(s) \end{bmatrix} = \frac{\mathbf{adj}[\mathbf{P}_e(s)]}{|\mathbf{P}_e(s)|} \tag{2.27}$$

$$\mathbf{Q}(s) = \begin{bmatrix} q_{1,1}(s) & q_{1,2}(s) & \cdots & q_{1,j}(s) \\ q_{2,1}(s) & q_{2,2}(s) & \cdots & q_{2,j}(s) \\ \vdots & \vdots & & \vdots \\ q_{i,1}(s) & q_{i,2}(s) & \cdots & q_{i,j}(s) \end{bmatrix} = \begin{bmatrix} \frac{1}{p^*_{1,1}(s)} & \frac{1}{p^*_{1,2}(s)} & \cdots & \frac{1}{p^*_{1,j}(s)} \\ \frac{1}{p^*_{2,1}(s)} & \frac{1}{p^*_{2,2}(s)} & \cdots & \frac{1}{p^*_{2,j}(s)} \\ \vdots & \vdots & & \vdots \\ \frac{1}{p^*_{i,1}(s)} & \frac{1}{p^*_{i,2}(s)} & \cdots & \frac{1}{p^*_{i,j}(s)} \end{bmatrix} \tag{2.28}$$

The MISO equivalent plant transfer functions are the elements $q_{ij}(s)$ of $\mathbf{Q}(s)$ such that:

$$q_{ij}(s) = \frac{1}{p^*_{ij}(s)} = \frac{|\mathbf{P}_e(s)|}{\mathbf{adj}_{ij}[\mathbf{P}_e(s)]} \tag{2.29}$$

Equation 2.29 demonstrates that the NMP characteristics for the QFT design elements are contained in $|\mathbf{P}_e|$. Rewriting Equation 2.29 in terms of $\mathbf{\Delta}$ and $\mathbf{P}$ gives:

$$q_{ij}(s) = \frac{1}{p^*_{ij}(s)} = \frac{|\mathbf{P}(s)\mathbf{\Delta}(s)|}{\mathbf{adj}_{ij}[(\mathbf{P}\mathbf{\Delta})(s)]} \quad (2.30)$$

Equation 2.30 shows that the selection of $\mathbf{\Delta}(s)$ will affect the NMP characteristics of the design element $q_{ij}(s)$ and thus $\mathbf{\Delta}(s)$ must be selected to yield a MP or *almost* MP (far-off RHP zeros) $|\mathbf{P}_e(s)|$.

The Binet-Cauchy theorem [22] is applied to the problem to initially test for the existence of a weighting matrix that will produce a MP $|\mathbf{P}_e|$. The theorem states that if the determinant of one of the $n \times n$ submatrices of $\mathbf{P}$ (the basic system plant) is MP then a weighting matrix does exist that will produce a MP $|\mathbf{P}_e|$. Even if the plant fails this test, it may still be possible to achieve a MP $|\mathbf{P}_e|$. The theorem thus is a sufficient but not necessary condition for the existence of a satisfactory weighting matrix. It verifies the existence of a satisfactory weighting matrix but yields no insight into the selection of its elements. All plant cases for this study showed that a satisfactory weighting matrix exists.

The NMP requirement on the selection of $\mathbf{\Delta}(s)$ can be relaxed somewhat given knowledge of the exact location of the NMP root(s). If, for instance, the NMP zero(s) are located far enough from the origin so that their phase contribution is negligible in the passband of the system, then those NMP characteristics can be dealt with [17]. If the NMP zero(s) are close to the origin, then the $\mathbf{\Delta}$ matrix selection may be unsatisfactory. NMP zeros VERY close to the origin can, in most flight control applications, be acceptable [16].

As noted in Chapter I, the weighting matrix selection has received some attention in past studies of QFT flight control design. Results from those studies show that a successful weighting matrix selection may be achieved by analysis of the particular problem and a familiarity with the flight vehicle. Analytical techniques exist to aid in this process [8:21–42], however, some cut and

try is presently still required.

The focus for the weighting matrix selection in this study is to select as simple a $\mathbf{\Delta}$ as possible that results in a MP $|\mathbf{P}_e|$. Optimality is not considered. The selection criteria are as follows:

- Do not consider frequency sensitive elements
- Use elevators as the primary surface for pitch-rate (q)
- Use ailerons as the primary surface for roll-rate (p)
- Use the rudder as the primary surface for yaw-rate (r)
- Weight the primary surfaces with + or − 1
- Weight secondary surfaces a magnitude lower than the primary
- Use flaps only as a secondary surface to aid in generating roll-rate (p)
- Select weights that make the surfaces work together

The rows and columns of the 7x3 constant coefficient weighting matrix, developed in Equation 2.24, associate each output with each effector as shown in Equation 2.31. For example, element $d_{1,1}$ weights the amount of left elevator used for generating pitch-rate. Element $d_{6,3}$ weights the amount of right aileron used to generate yaw-rate and so forth. With the above criteria, some elements of the weighting matrix are selected and shown in Equation 2.32. Plots of the basic system $\mathbf{P}$ for each flight condition are studied to aid in this selection and the formulation of the above criteria. Note the independent variable (s) is dropped since frequency sensitive elements are not used.

$$\Delta(s) = \begin{matrix} \\ \Downarrow \\ \end{matrix} \begin{matrix} q \\ \Downarrow \\ \end{matrix} \begin{matrix} p \\ \Downarrow \\ \end{matrix} \begin{matrix} r \\ \Downarrow \\ \end{matrix} \begin{bmatrix} d_{1,1}(s) & d_{1,2}(s) & d_{1,3}(s) \\ d_{2,1}(s) & d_{2,2}(s) & d_{2,3}(s) \\ d_{3,1}(s) & d_{3,2}(s) & d_{3,3}(s) \\ d_{4,1}(s) & d_{4,2}(s) & d_{4,3}(s) \\ d_{5,1}(s) & d_{5,2}(s) & d_{5,3}(s) \\ d_{6,1}(s) & d_{6,2}(s) & d_{6,3}(s) \\ d_{7,1}(s) & d_{7,2}(s) & d_{7,3}(s) \end{bmatrix} \begin{matrix} \Leftarrow \delta_{e_L} \\ \Leftarrow \delta_{e_R} \\ \Leftarrow \delta_{f_L} \\ \Leftarrow \delta_{f_R} \\ \Leftarrow \delta_{a_L} \\ \Leftarrow \delta_{a_R} \\ \Leftarrow \delta_r \end{matrix} \tag{2.31}$$

$$\Delta = \begin{bmatrix} -1 & 0 & 0 \\ -1 & 0 & 0 \\ 0 & 0.1 & 0 \\ 0 & -0.1 & 0 \\ -0.1 & 1 & d_{5,3} \\ -0.1 & -1 & d_{6,3} \\ 0 & -1 & d_{7,3} \end{bmatrix} \tag{2.32}$$

Elevators are used only to generate pitch. They are otherwise ineffective in producing roll or yaw even when independently controlled and are not used for that purpose. Flaps are used to aid in producing roll only as a secondary effector. They deflect down only and induce the largest drag of all the effectors. The X'_δ derivatives in Table B.3 in Appendix B show the relative drag penalties associated with actuation of each effector. Ailerons are the only effector weighted for each output. The ailerons effectively produce both roll and yaw. They have a much smaller drag penalty and are

thus used to aid in generating pitch. Studies of the basic plants revealed that producing a yaw rate with the rudder comparable in magnitude to the roll produced by the ailerons, required a weighting magnitude of 5. This weighting is justified by the fact that the rudder deflection limits are greater than that of the other effectors. Weights of 0.5 are used for generating yaw with ailerons to keep that secondary surface weighted at one magnitude less than the rudder.

Weighting matrix element signs are selected based on bode plots of the basic plants. The elements $d_{7,2}$, $d_{5,3}$ and $d_{6,3}$ violate the last selection criteria slightly. The -1 weight on $d_{7,2}$ works to correct the *adverse yaw* induced by actuation of the ailerons. The signs on the elements $d_{5,3}$ and $d_{6,3}$ work to correct the roll resulting from a commanded yaw. The weighting matrix used for the remainder of this study is:

$$\mathbf{\Delta} = \begin{bmatrix} -1 & 0 & 0 \\ -1 & 0 & 0 \\ 0 & 0.1 & 0 \\ 0 & -0.1 & 0 \\ -0.1 & 1 & -0.5 \\ -0.1 & -1 & 0.5 \\ 0 & -1 & -5 \end{bmatrix} \tag{2.33}$$

The longitudinal and lateral modes of the Lambda model used in this thesis are completely decoupled. Refer to Equations B.3 and B.4 in Appendix B. A block diagonal $\mathbf{P}_e$ results when the above weighting matrix is applied to the system. The *effective* plants for this study have the form:

$$\mathbf{P}_e(s) = \begin{bmatrix} p_{1,1}(s) & 0 & 0 \\ 0 & p_{2,2}(s) & p_{2,3}(s) \\ 0 & p_{3,2}(s) & p_{3,3}(s) \end{bmatrix} \tag{2.34}$$

The zero elements of column one in Equation 2.34 are always zero except for plant #2. Nonsymmetric coefficients for the ailerons in the **B** matrix of plant #2 produced $-60\ dB$ responses where it should have been identically zero in the first column of the plant matrix (see the boxed coefficients in the **B** matrix for plant #2 on page B-7). This was a minor error in the original data provided by WRDC/FIGL that was not discovered until after the design work was done. Further investigation into the significance of this error showed that it would not affect the design at all and th[illegible] the error was not corrected. These plant elements are approximated as zero for the design synthesis.

The zero elements in row one of Equation 2.34 are actually nonzero for all plant cases. The responses for these elements are very small ($-300\ dB$) and are thus approximated as zero.

Refer to Appendix C for listings of $\mathbf{P}_e(s)$.

III. Discrete-Time Theory

This chapter presents the theory directly related to this study. It's assumed the reader is familiar with the basic continuous system MISO (multiple-input-single-output) and MIMO QFT design methods. If not, then Chapter 21 of the D'Azzo and Houpis text [6] is a good place to start. A more detailed treatment of the QFT MISO and MIMO design methods in addition to the issues with its discrete-time application are found in a Flight Dynamics Laboratory technical report [19]. Numerous references exist for discrete-time sampled-data control system analysis and design. For this thesis, references [6, 21, 20] are used. A complete treatment of the QFT design process and discrete QFT design methods is found in references [10, 16, 12, 13].

3.1 Sampled-Data Theory

3.1.1 Sampled-Data Signals. Consider the sampled signal in Figure 3.1. Assume the

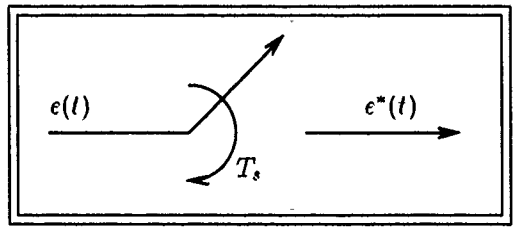

Figure 3.1. Sampled-Data Signal

sampling pulse is much smaller in width than the pulse period so it is well approximated as an ideal sampler. The continuous band-limited $e(t)$ contains a frequency spectrum or *fundamental* spectrum. A band-limited signal has no frequency components above ω_c rad/sec. Ideal sampling of this signal produces both a fundamental spectrum and replica complimentary spectra at multiples of the sampling frequency $\pm n\omega_s$. If ω_s is not high enough,the complimentary spectra will corrupt the fundamental and *aliasing* occurs in $e^*(t)$. In a digital flight control system, this high frequency *aliasing* can result in the shifting of high frequency plant and actuator dynamics into the low

frequency control system band and thus interfere with its proper operation [32:68]. If ω_s is large enough, the complimentary spectra do not corrupt the fundamental and a low-pass filtered $e^*(t)$ will have the same frequency content as the original $e(t)$ [20:82–87].

Shannon's sampling theorem guarantees that $e(t)$ can be reconstructed after sampling if the signal is sampled at greater than two times the band-limited frequency [20:87–88].

$$\omega_s > 2\omega_c \tag{3.1}$$

3.1.2 Zero-Order Hold. The zero-order hold (ZOH) device converts the impulse train $e^*(t)$ into a pseudo-continuous time signal approximating the original $e(t)$. Very simply, the ZOH holds the value of the last impulse until the next impulse is received. As the name implies, a zero-order hold will pass, without distortion, a constant or zero-order polynomial.

The fundamental spectrum of the sampled-data compensator output signal $e^*(t)$ is what the control system designer has synthesized for input to the plant. The higher frequency complimentary components resulting from the sampling process are thus not desirable elements of the compensator output but are never-the-less still present. Low-pass filtering $e^*(t)$ so that only the fundamental spectrum is passed will acceptably reduce its high frequency complimentary spectra elements. It is true that control system plants are inherently low-pass, however, these low-pass characteristics are usually not sufficient to completely minimize the effects the complimentary spectra can have on the system. The plant must see a filtered $e^*(t)$. A ZOH device is inherently a low-pass device and provides low-pass filtering to an input sampled-data signal. With a ZOH device between the discrete compensator and the system plant, the control sampled-data signal is properly low-pass filtered.

The transfer function for the ZOH device is:

$$G_{ZOH}(s) = \frac{1 - e^{-Ts}}{s} \tag{3.2}$$

For physical reasons, it is not desirable to apply narrow pulses to a continuous plant [17]. A ZOH converts the discrete signal pulse train to the pseudo-continuous time signal required for driving a continuous system and is normally always used for this reason. Its low-pass filtering nature is a desirable secondary characteristic and acceptably filters the effects of the high-frequency compliments spectra of a sampled-data control signal. On Lambda, the controller will be implemented in software so that the control signals to the plant will be discrete. A ZOH device is assumed to exist between the onboard computer and the control surface actuators.

3.1.3 Discrete Planes. The final compensator designs for this study will be implemented as difference equations derived from their z-plane representation. The relationship between the z-plane and the s-plane is:

$$z \equiv e^{Ts} \tag{3.3}$$

where T is the sample period. This transformation maps the entire left-half (stable) s-plane into the z-plane unit circle and the right-half (unstable) s-plane to all the area outside the unit circle. The location of the poles and zeros in the z-plane are affected by the sample time T such that as the sample time decreases, the poles and zeros migrate toward the $+1 \pm j0$ point in the z-plane and more significant figures are required to properly maintain the z to s plane mapping. For this reason, z-plane design can be tedious and error prone.

A bilinear transformation from the z-plane will map z-plane poles and zeros into the discrete w′-plane. This transformation is:

$$w' = \frac{2}{T}\frac{z-1}{z+1} \tag{3.4}$$

$$z = \frac{2+w'T}{2-w'T} \tag{3.5}$$

w′-plane similarity with the s-plane is the most dominant feature of this transformation. As sample time T decreases and approaches zero, the w′-plane approaches equivalence with the s-plane. Equation 3.6 is given to show the relationship between frequency in the s-plane, frequency in the w′-plane and sample time.

$$\omega_{w'p} = \frac{2\ \tan\frac{\omega_{sp}T}{2}}{T} \tag{3.6}$$

When the w′-plane and s-plane are compared like this, the entire w′-plane imaginary axis maps onto the imaginary axis of the primary strip of the s-plane. The primary strip is $\pm\, j\omega_s/2$.

QFT was formulated for application in the s-plane. In certain cases, the w'-plane and the s-plane are acceptably equivalent so that continuous QFT methods can be employed for a discrete design. The similarity between the w′-plane and the s-plane for a given problem, is dependent on the sampling rate and the frequency content of the system plant. If the poles and zeros of the system plant lie in the primary strip of the s-plane, then a w′-plane transformation will be acceptably equivalent to the s-plane provided the sample rate is low enough. Since the s-plane complimentary strips also map onto the entire w′-plane imaginary axis, its obvious that the w′-plane transformation of a plant with poles or zeros in the complimentary strip of the s-plane may not be acceptably equivalent to the s-plane. If the design method requires $w' \approx s$ then a sample rate that places all the system poles and zeros in the primary strip must be used. There is a trade-off here. As sample rate increases, equivalence with the s-plane decreases and significant warping

occurs. So, system plants with high frequency components may not be acceptably transformable to the w'-plane for design synthesis. A sample rate of 60 Hz is used for this design. With that sample rate, all the poles and zeros of each of the Lambda plants lie in the primary strip and $w' \approx s$.

Transformation to the z-plane and then to the w'-plane can still be plagued with numerical problems for the reasons mentioned above. The Hofmann algorithm, introduced next, is a way of transforming a system from $s \Rightarrow z \Rightarrow w'$ without the numeric problems of an intermediate z-plane plant representation.

3.1.4 Hofmann Algorithm [9]. With the zero initial condition Laplace transformed state space system:

$$s\mathbf{X}(s) = \mathbf{A}\,\mathbf{X}(s) + \mathbf{B}\,\mathbf{U}(s) \tag{3.7}$$

$$\mathbf{Y}(s) = \mathbf{C}\,\mathbf{X}(s) + \mathbf{D}\,\mathbf{U}(s) \tag{3.8}$$

and the transformations in Equations 3.3, 3.4 and:

$$w' = \frac{2}{T}\tanh\left(\frac{sT}{2}\right) \tag{3.9}$$

the w' transformed state space system can be derived.

$$w'\mathbf{X}(w') = \frac{2}{T}\tanh\left(\frac{\mathbf{A}T}{2}\right)\mathbf{X}(w') + \left[1 - \frac{w'T}{2}\right]\left[\frac{\mathbf{A}T}{2}\right]^{-1}\tanh\left(\frac{\mathbf{A}T}{2}\right)\mathbf{B}\mathbf{U}(w') \tag{3.10}$$

$$\mathbf{Y}(w') = \mathbf{C}\mathbf{X}(w') + \mathbf{D}\mathbf{U}(w') \tag{3.11}$$

These equations are rewritten in terms of the key system matrices of $\mathbf{A}^*$ and $\mathbf{B}^*$ where $\mathbf{A}^*$ and $\mathbf{B}^*$ are functions of the hyperbolic tangent and the $\mathbf{A}$ matrix so that:

$$w'\mathbf{X}(w') = \mathbf{A}^*\mathbf{X}(w') + \left[1 - \frac{w'T}{2}\right]\mathbf{B}^*\mathbf{U}(w') \tag{3.12}$$

$$\mathbf{Y}(w') = \mathbf{CX}(w') + \mathbf{DU}(w') \tag{3.13}$$

and

$$\mathbf{A}^* = \mathbf{A}\left[\frac{\mathbf{A}T}{2}\right]^{-1}\tanh\left(\frac{\mathbf{A}T}{2}\right) = \mathbf{A}\,\mathbf{A}_e \tag{3.14}$$

$$\mathbf{B}^* = \left[\frac{\mathbf{A}T}{2}\right]^{-1}\tanh\left(\frac{\mathbf{A}T}{2}\right)\mathbf{B} = \mathbf{A}_e\,\mathbf{B} \tag{3.15}$$

Computation of the w′ system with an intermediate transformation to the z-plane and a bilinear transformation to the w′-plane is not numerically robust. Hofmann's paper presents a robust time-scaled recursive algorithm for computing $\mathbf{A}_e$ shown above. In this thesis, a six term Taylor series approximation for $\mathbf{A}_e$ is used.

$$\mathbf{A}_e \approx \mathbf{I} - \frac{1}{3}\left[\frac{\mathbf{A}T}{2}\right]^2 + \frac{2}{15}\left[\frac{\mathbf{A}T}{2}\right]^4 - \frac{17}{315}\left[\frac{\mathbf{A}T}{2}\right]^6 + \frac{62}{2835}\left[\frac{\mathbf{A}T}{2}\right]^8 - \frac{1382}{155925}\left[\frac{\mathbf{A}T}{2}\right]^{10} \tag{3.16}$$

The six term Taylor series is used since it is so easy to implement in Matrix$_x$. Experimentation with fewer terms shows that the first two terms of this series provide an acceptable transformation.

Equations 3.12 and 3.13 are represented in the standard form of:

$$\mathbf{Y}(w') = \mathbf{P}(w')\,\mathbf{U}(w') \tag{3.17}$$

where

$$\mathbf{P}(w') = \mathbf{C}_{w'}\,[w'\mathbf{I} - \mathbf{A}_{w'}]^{-1}\,\mathbf{B}_{w'} + \mathbf{D}_{w'} \tag{3.18}$$

$$\mathbf{A}_{w'} = \mathbf{A}^* = \mathbf{A}\mathbf{A}_e \tag{3.19}$$

$$\mathbf{B}_{w'} = \mathbf{B}^* - \frac{T}{2}\mathbf{A}^*\mathbf{B}^* = \mathbf{A}_e\mathbf{B} - \frac{T}{2}\mathbf{A}\mathbf{A}_e\mathbf{A}_e\mathbf{B} \tag{3.20}$$

$$\mathbf{C}_{w'} = \mathbf{C} \tag{3.21}$$

$$\mathbf{D}_{w'} \;=\; \mathbf{B} - \frac{T}{2}\mathbf{C}\mathbf{B}^* \;=\; \mathbf{B} - \frac{T}{2}\mathbf{C}\mathbf{A}_\epsilon\mathbf{B} \tag{3.22}$$

Hofmann's algorithm transforms the system with the assumption that the input is piecewise constant between samples as is usually customary. This assumption incorporates data-hold or ZOH with the system plant.

$$\mathbf{P}_\epsilon(s) \;\Rightarrow\; \boxed{\text{Hofmann Algorithm}} \;\Rightarrow\; [\mathbf{G}_{ZOH}\mathbf{P}_\epsilon](w') \tag{3.23}$$

In the paper Hofmann states "all effects of sampling and data-hold operations are embodied in the $(\mathbf{A}T/2)^{-1}\tanh(\mathbf{A}T/2)$ factor and the zeros, $[1 - w'/(2/T)]$, of the w' domain input-output system representation". Thus the Hofmann algorithm robustly transforms a continuous system to the discrete w'-plane and includes a ZOH in the discrete result. This algorithm is easily implemented on Matrix_x. A small Matrix_x program, based on the equations presented above, transforms the Lambda plants to the w'-plane and is shown below:

```
// Hofmann Algorithm for Matrixx
t=1/60;
[a,b,c,d]=split(s,ns);
ae=[eye-1/3*(a*t/2)**2+2/15*(a*t/2)**4...
                    -17/315*(a*t/2)**6...
                  +62/2835*(a*t/2)**8...
              -1382/155925*(a*t/2)**10];
aw=ae*a;
be=ae*b;
bw=be-t/2*aw*be;
cw=c;
dw=d-t/2*c*be;
sw=[aw,bw;cw,dw];
```

Refer to Appendix C for listings of the w'-plane transformed effective plants $\mathbf{P}_\epsilon(w')$.

3.2 QFT Theory

3.2.1 Sampled-Data QFT Compensation. Figure 3.2 shows the MIMO sampled-data QFT system block diagram. The starred system variables denote impulse sampled signals. Note the

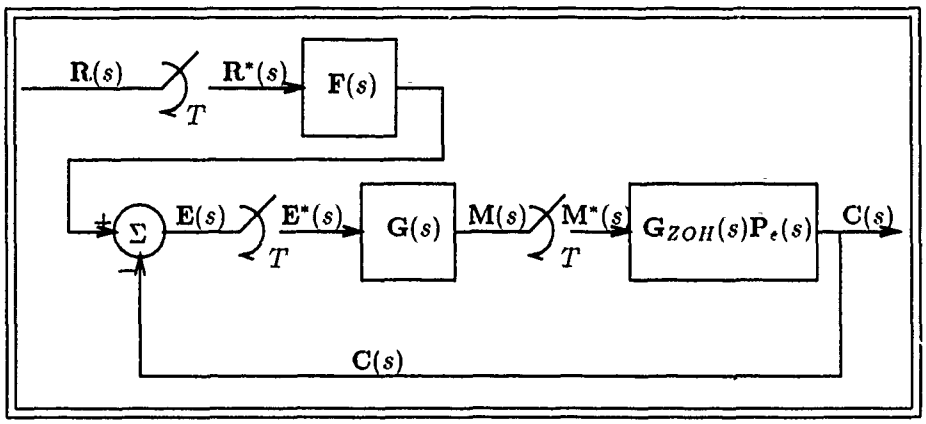

Figure 3.2. MIMO Sampled-Data QFT System

position of the samplers and the differences between this discrete system and the continuous QFT system depicted in Figure 1.2 on page 1-10. The controllers and prefilters designed in this study will be implemented in software on Lambda. The pilot input and the rate feedback signals are sampled on the aircraft and the controller output is through a digital-to-analog (DAC) converter.

The control ratio is derived from the block diagram by first writing all the intermediate system equations. Note that Figure 3.2 represents a MIMO system.

$$\mathbf{E}(s) = \mathbf{F}(s)\,\mathbf{R}^*(s) - \mathbf{C}(s) \tag{3.24}$$

$$\mathbf{C}(s) = \mathbf{G}_{ZOH}(s)\,\mathbf{P}_e(s)\,\mathbf{M}^*(s) \tag{3.25}$$

$$\mathbf{M}(s) = \mathbf{G}(s)\,\mathbf{E}^*(s) \tag{3.26}$$

These equations are rearranged to provide the relationship $\mathbf{T}$ between $\mathbf{C}$ and $\mathbf{R}$. The actual procedure is not given. Similar systems analysis for the MISO case is found in reference [20] and is easily extended to the MIMO case.

$$\mathbf{C}^*(s) = \left[\mathbf{I} + [\mathbf{G}_{ZOH}\mathbf{P}_e]^*(s)\,\mathbf{G}^*(s)\right]^{-1} [\mathbf{G}_{ZOH}\,\mathbf{P}_e]^*(s)\,\mathbf{G}^*(s)\,\mathbf{F}^*(s)\,\mathbf{R}^*(s) \tag{3.27}$$

$$\mathbf{T}^*(s) = \left[\mathbf{I} + [\mathbf{G}_{ZOH}\mathbf{P}_e]^*(s)\,\mathbf{G}^*(s)\right]^{-1} [\mathbf{G}_{ZOH}\,\mathbf{P}_e]^*(s)\,\mathbf{G}^*(s)\,\mathbf{F}^*(s) \tag{3.28}$$

Reference [20:108] shows that an impulse sampled signal is equivalent to the $\mathcal{Z}$-transform of the signal and further transformable to the w'-plane so that Equation 3.28 is now expressed in the w'-plane.

$$\mathbf{T}(w') = [\mathbf{I} + [\mathbf{G}_{ZOH}\,\mathbf{P}_e](w')\mathbf{G}(w')]^{-1}\,[\mathbf{G}_{ZOH}\,\mathbf{P}_e](w')\,\mathbf{G}(w')\,\mathbf{F}(w') \tag{3.29}$$

$$\mathbf{T}(w') = [\mathbf{I} + \mathbf{L}(w')]^{-1}\,\mathbf{L}(w')\,\mathbf{F}(w') \tag{3.30}$$

The principal result of this derivation is that the zero-order hold must be cascaded with the plant before discretizing to the w'-plane. The Hofmann algorithm makes this transformation with data-hold assumptions. All other elements of the control ratio can be synthesized and transformed separately.

MIMO design synthesis is not applied directly to the MIMO system in the form of Equation 3.30. Instead, the problem is decomposed into a set of n^2 equivalent MISO system problems to which QFT is then applied. The derivation of the MISO equivalent systems is presented in the design equations section.

3.2.2 Sample Rate. If the sample rate is not necessarily fixed for a particular design and instead a variable, then determination of a minimum sampling rate acceptable to produce a successful design becomes the first principle QFT design step. The sample time implementable on Lambda is fixed at 0.01667 sec so determination of $\omega_{s_{min}}$ is not required. The sample rate for this design is:

$$\omega_s = \frac{2\pi}{T} \tag{3.31}$$

$$\omega_s = 2(60)\pi = 377\ (rad/sec) \tag{3.32}$$

Before a w′-plane design can proceed, accuracy of the approximation

$$w' \approx s \tag{3.33}$$

is determined. The following equations, provided by Dr. Houpis, are given as the yardstick to measure this w′ to s plane approximation. These equations result from the experience gained in successful w′ design application and good engineering judgement both with QFT and other techniques. If

$$\left[\frac{\sigma_{sp}\,T}{2}\right]^2 \ll 2 \tag{3.34}$$

$$\frac{\omega_{sp}\,T}{2} \leq 0.297 \tag{3.35}$$

where

$$s = \sigma_{sp} \pm j\omega_{sp} = \sigma \pm j\omega \tag{3.36}$$

$$w' = \sigma_{w'p} \pm j\omega_{w'p} = u \pm jv \tag{3.37}$$

are satisfied, then the w′-plane is a *good enough* approximation to the s-plane. σ_{sp} and ω_{sp} in these equations should represent the components of the fastest pole or zero of the effective plant. σ_{sp} for this design results from the rate sensor pole at $\sigma = 50$ (rad/sec). ω_{sp} for this design results from the imaginary part of the control surface actuator model at $\omega = 12.8$ (rad/sec). For the approximation then, Equations 3.34 and 3.35 become:

$$\left[\frac{\sigma_{sp}\,T}{2}\right]^2 = 0.174 \ll 2 \tag{3.38}$$

$$\frac{\omega_{sp}\,T}{2} = 0.107 \leq 0.297 \tag{3.39}$$

The conditions of Equations 3.34 and 3.35 are satisfied for this design and the w'-plane is an excellent approximation to the s-plane. This also verifies that the fixed sample rate of 0.01667 sec is sufficient for the Lambda URV.

3.2.3 Response Models. QFT design synthesis begins by specifying the time-domain control system tracking response bounds. An upper and lower (fast and slow) response bound for each system output is synthesized. For the MIMO case, the **T** matrix of system control ratios given in Equation 3.28 is:

$$\mathbf{T}(w') = \begin{bmatrix} t_{1,1}(w') & t_{1,2}(w') & \cdots & t_{1,n}(w') \\ t_{2,1}(w') & t_{2,2}(w') & \cdots & t_{2,n}(w') \\ \vdots & \vdots & & \vdots \\ t_{n,1}(w') & t_{n,2}(w') & \cdots & t_{n,n}(w') \end{bmatrix} \tag{3.40}$$

A principle purpose of this design is to synthesize a basically non-interacting closed-loop (BNIC) multivariable system. Thus, the off-diagonal control ratios of Equation 3.40 are assumed to be acceptably close to zero so that the QFT compensated system of control ratios for the three output Lambda URV is:

$$\mathbf{T}(w') \approx \begin{bmatrix} t_{1,1}(w') & 0 & 0 \\ 0 & t_{2,2}(w') & 0 \\ 0 & 0 & t_{3,3}(w') \end{bmatrix} = \begin{bmatrix} \frac{q(w')}{q_{cmd}(w')} & 0 & 0 \\ 0 & \frac{p(w')}{p_{cmd}(w')} & 0 \\ 0 & 0 & \frac{r(w')}{r_{cmd}(w')} \end{bmatrix} \tag{3.41}$$

An upper bound tracking model (T_{R_u}) and a lower bound tracking model (T_{R_l}) for each element of Equation 3.41 are synthesized first in the s-plane to satisfy the required gain K and the specified step input figures-of-merit and then transformed to the w'-plane. T_{R_u} must satisfy the peak overshoot (M_p), settling time (t_s) and rise time (t_r) specifications. T_{R_l} must satisfy the settling time (t_s) and the rise time (t_r) specifications. Table 3.1 shows the figures-of-merit for the response models

of this design. The notation in the table is:

Table 3.1. Figures-of-Merit for the QFT Response Models

Model	T_r (sec)	T_s (sec)	M_p $\frac{rad}{sec}$	FV $\frac{rad}{sec}$
$\frac{q_{LB}(s)}{q_{cmd_{LB}}(s)}$	0.84	1.56	1.0	1.0
$\frac{q_{UB}(s)}{q_{cmd_{UB}}(s)}$	0.15	0.34	1.25	1.0
$\frac{p_{LB}(s)}{p_{cmd_{LB}}(s)}$	0.87	1.56	1.0	1.0
$\frac{p_{UB}(s)}{p_{cmd_{UB}}(s)}$	0.44	0.78	1.0	1.0
$\frac{r_{LB}(s)}{r_{cmd_{LB}}(s)}$	3.48	6.22	1.0	1.0
$\frac{r_{UB}(s)}{r_{cmd_{UB}}(s)}$	1.76	3.13	1.0	1.0

- T_r —rise time
- T_s —settling time
- M_p —maximum peak value
- FV —final value

The frequency response for the tracking models define bounds on the individual single-loop equivalent loop transmissions. The term *loop transmission* is used in referring to the frequency transmission of a unity feedback loop. It is a closed-loop frequency specification derived from the response models. The difference between the values of magnitude of the upper and lower tracking response model at a given frequency v_k is denoted by δ_R and provides the loop transmission requirement needed to meet closed-loop tracking specifications.

$$|T_{R_u}(jv_k)| - |T_{R_l}(jv_k)| = |\delta_R(jv_k)| \tag{3.42}$$

It is desired that the compensated closed-loop system be BNIC and therefore off-diagonal relationships in the system plant represent disturbances to the desired BNIC system. Usually a

disturbance rejection requirement is specified for a QFT design to guarantee a certain level disturbance response during loop synthesis. High disturbance rejection requires high loop transmission. Maximum loop transmission can be seriously constrained by the NMP characteristics of the w′ loop transmission and therefore governed almost completely by those NMP elements. For this reason, the maximum allowable loop transmission is synthesized and a disturbance rejection requirement is not needed. The same applies for tracking bounds. The tracking performance achievable is also governed by the NMP elements of the loop transmission. Those NMP elements may make it impossible to meet the desired tracking performance even when maximum loop transmission is synthesized. If this is true, then the tracking models may be too ambitious for the dynamics of the plant or, in the case of a discrete design, the sample rate may be too low. For example, if the NMP elements of $\mathbf{Q}(w')$ result from transformation to the w′-plane, then increasing the sample rate tends to move those elements farther away from the origin and thus may allow enough loop transmission to meet the performance bounds. NMP elements present in $\mathbf{Q}(s)$ before transformation will be minimally affected by sample rate changes. It is stressed that this is not a QFT specific problem. All robust compensation techniques must deal with NMP elements, for those elements may represent the invariant physical characteristics of the plant or characteristics associated with the modeling or plant representation (w′-plane). Since tracking bounds and disturbance bounds are not used in the design synthesis, the achieved disturbance rejection and tracking performance is specified from the completed design simulations.

Appendix D contains all the synthesized response models for this design. Figure D.3 in Appendix D shows the loop transmission specifications for the q, p and r equivalent loops used to synthesize the compensated loop transmissions. The complete loop transmission synthesis is presented in the next chapter.

3.2.4 Design Equations–MISO Equivalent Method. From Equation 3.30, the MIMO system equation is rewritten without reference to a frequency plane and with $\mathbf{L}(w')$ represented as $\mathbf{P}_{zo}\,\mathbf{G}$

so that:

$$\mathbf{T} = [\mathbf{I} + \mathbf{P}_{zo}\mathbf{G}]^{-1}\ \mathbf{P}_{zo}\mathbf{G}\mathbf{F} \tag{3.43}$$

Premultiplying Equation 3.43 by $[\mathbf{I} + \mathbf{P}_{zo}\mathbf{G}]$ and then, for a nonsingular $\mathbf{P}_{zo}$ by $\mathbf{P}_{zo}^{-1}$ yields:

$$[\mathbf{I} + \mathbf{P}_{zo}\mathbf{G}]\ \mathbf{T} = \mathbf{P}_{zo}\mathbf{G}\mathbf{F} \tag{3.44}$$

$$[\mathbf{P}_{zo}^{-1} + \mathbf{G}]\ \mathbf{T} = \mathbf{G}\mathbf{F} \tag{3.45}$$

Diagonal matrices are used, so $\mathbf{P}_{zo}^{-1}$ is partitioned as:

$$\mathbf{P}_{zo}^{-1} = \mathbf{\Lambda} + \mathbf{B}_p \tag{3.46}$$

where

$$\mathbf{\Lambda} = \begin{bmatrix} \frac{1}{q_{1,1}} & 0 & \cdots & 0 \\ 0 & \frac{1}{q_{2,2}} & \cdots & 0 \\ \vdots & \vdots & & \vdots \\ 0 & 0 & \cdots & \frac{1}{q_{i,i}} \end{bmatrix} \tag{3.47}$$

$$\mathbf{B}_p = \begin{bmatrix} 0 & \frac{1}{q_{1,2}} & \cdots & \frac{1}{q_{1,i}} \\ \frac{1}{q_{2,1}} & 0 & \cdots & \frac{1}{q_{2,i}} \\ \vdots & \vdots & & \vdots \\ \frac{1}{q_{i,1}} & \frac{1}{q_{i,2}} & \cdots & 0 \end{bmatrix} \tag{3.48}$$

With a diagonal $\mathbf{G}$ and $\mathbf{F}$ and the components of $\mathbf{P}_{zo}^{-1}$ from Equation 3.46, Equation 3.45 is rearranged to a form similar to Equation 3.43 for the 3x3 case of this study. Note that $q_{i,i}$ and $q_{i,j}$ in Equations 3.47, 3.48 and those following in the remainder of this section denote elements of the

Q matrix and are not the system output of pitch-rate q.

$$\mathbf{T} = [\mathbf{\Lambda} + \mathbf{G}]^{-1} [\mathbf{GF} - \mathbf{B}_p\mathbf{T}] \tag{3.49}$$

$$\mathbf{T} = \begin{bmatrix} \frac{q_{1,1}}{1+g_1 q_{1,1}} & 0 & 0 \\ 0 & \frac{q_{2,2}}{1+g_2 q_{2,2}} & 0 \\ 0 & 0 & \frac{q_{3,3}}{1+g_3 q_{3,3}} \end{bmatrix} \left\{ \begin{bmatrix} g_1 f_1 & 0 & 0 \\ 0 & g_2 f_2 & 0 \\ 0 & 0 & g_3 f_3 \end{bmatrix} - \begin{bmatrix} 0 & \frac{1}{q_{1,2}} & \frac{1}{q_{1,3}} \\ \frac{1}{q_{2,1}} & 0 & \frac{1}{q_{2,3}} \\ \frac{1}{q_{3,1}} & \frac{1}{q_{3,2}} & 0 \end{bmatrix} \begin{bmatrix} t_{1,1} & t_{1,2} & t_{1,3} \\ t_{2,1} & t_{2,2} & t_{2,3} \\ t_{3,1} & t_{3,2} & t_{3,3} \end{bmatrix} \right\} \tag{3.50}$$

Recall from Chapter II page 2-11 that the Q matrix is related to $\mathbf{P}_e^{-1}$ such that:

$$\mathbf{Q}(s) = \begin{bmatrix} q_{1,1}(s) & q_{1,2}(s) & \cdots & q_{1,j}(s) \\ q_{2,1}(s) & q_{2,2}(s) & \cdots & q_{2,j}(s) \\ \vdots & \vdots & & \vdots \\ q_{i,1}(s) & q_{i,2}(s) & \cdots & q_{i,j}(s) \end{bmatrix} = \begin{bmatrix} \frac{1}{p^*_{1,1}(s)} & \frac{1}{p^*_{1,2}(s)} & \cdots & \frac{1}{p^*_{1,j}(s)} \\ \frac{1}{p^*_{2,1}(s)} & \frac{1}{p^*_{2,2}(s)} & \cdots & \frac{1}{p^*_{2,j}(s)} \\ \vdots & \vdots & & \vdots \\ \frac{1}{p^*_{i,1}(s)} & \frac{1}{p^*_{i,2}(s)} & \cdots & \frac{1}{p^*_{i,j}(s)} \end{bmatrix} \tag{3.51}$$

Also recall from Equation 2.34 on page 2-15 that $\mathbf{P}_e$ is block-diagonal for this design. The Q matrix for Lambda now becomes:

$$\mathbf{Q}(s) = \begin{bmatrix} \frac{1}{p^*_{1,1}(s)} & \frac{1}{0} & \frac{1}{0} \\ \frac{1}{0} & \frac{1}{p^*_{2,2}(s)} & \frac{1}{p^*_{2,3}(s)} \\ \frac{1}{0} & \frac{1}{p^*_{3,2}(s)} & \frac{1}{p^*_{3,3}(s)} \end{bmatrix} = \begin{bmatrix} q_{1,1}(s) & \infty & \infty \\ \infty & q_{2,2}(s) & q_{2,3}(s) \\ \infty & q_{3,2}(s) & q_{3,3}(s) \end{bmatrix} \tag{3.52}$$

Equation 3.50 is expanded using the results of Equation 3.52 to show the MISO equivalent control ratio transfer function matrix elements (**T**) for the Lambda URV design.

$$t_{1,1} = \frac{q_{1,1}}{1 + g_1 q_{1,1}} (g_1 f_{1,1}) \tag{3.53}$$

$$t_{1,2} = t_{1,3} = 0 \tag{3.54}$$

$$t_{2,1} = \frac{q_{2,2}}{1 + g_2 q_{2,2}} \left(-\frac{t_{3,1}}{q_{2,3}} \right) \tag{3.55}$$

$$t_{2,2} = \frac{q_{2,2}}{1 + g_2 q_{2,2}} \left[g_2 f_{2,2} - \frac{t_{3,2}}{q_{2,3}} \right] \tag{3.56}$$

$$t_{2,3} = \frac{q_{2,2}}{1 + g_2 q_{2,2}} \left(-\frac{t_{3,3}}{q_{2,3}} \right) \tag{3.57}$$

$$t_{3,1} = \frac{q_{3,3}}{1 + g_3 q_{3,3}} \left(-\frac{t_{2,1}}{q_{3,2}} \right) \tag{3.58}$$

$$t_{3,2} = \frac{q_{3,3}}{1 + g_3 q_{3,3}} \left(-\frac{t_{2,2}}{q_{3,2}} \right) \tag{3.59}$$

$$t_{3,3} = \frac{q_{3,3}}{1 + g_3 q_{3,3}} \left[g_3 f_{3,3} - \frac{t_{2,3}}{q_{3,2}} \right] \tag{3.60}$$

The desired tracking control ratios appear in the elements of **T** as:

$$\frac{q_{i,i}}{1 + g_i q_{i,i}} [g_i f_{i,i}] \tag{3.61}$$

The disturbance control ratios due to MISO loop interaction appear in the elements of **T** in the form of:

$$\frac{q_{i,i}}{1 + g_i q_{i,i}} (d_{i,j}) \tag{3.62}$$

where $d_{i,j}$ represents the coupling disturbance from other elements in **T** as shown above in Equations 3.55, 3.56, 3.57, 3.58, 3.59 and 3.60. The relationship of the MISO equivalent system for the Lambda URV is best shown by signal flow graphs. Figure 3.3 shows the MISO equivalent elements of **T**. Note that coupling disturbances are applied directly at the input of the plant. Also note that no coupling disturbance exists in the first row of **T**. This is the pitch-rate channel and is due to the

decoupled lateral and longitudinal URV model used. Finally, note the tracking inputs are applied to the diagonal elements of **T** only. This is a result of choosing to synthesize a diagonal prefilter **F**.

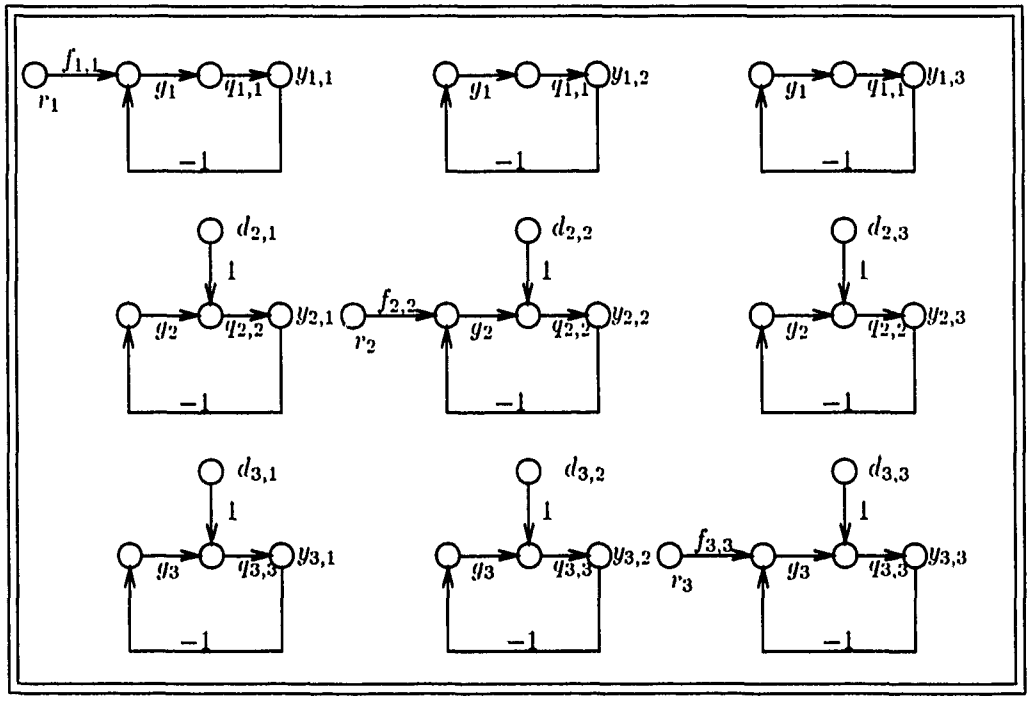

Figure 3.3. MISO Equivalent System Signal Flow Graphs

The above development of **T** and its elements are the MISO equivalent loops of the MIMO system. Dr. Horowitz shows that fixed-point mapping theory proves this equivalent relationship [12]. The design variable g_i appears in each element of row i in **T**. In fact, the factor $q_{i,i}/(1+g_i q_{i,i})$ appears in each element of row i in **T**. Thus, in the MISO equivalent form, the design synthesis involves selecting g_i to attenuate the coupling disturbances and attain the tracking performance for the elements of row i of **T**. Selection of g_i affects tracking and disturbance performance, and selection of $f_{i,i}$ affects only tracking performance. Three separate single-loop equivalent design synthesis problems result from the MISO equivalent URV system instead of nine interrelated design problems represented by the MIMO system **T**.

Two conditions must be met for application of QFT to a MIMO system and its MISO equivalent form. These conditions result directly from the MISO equivalent derivation. First, $\mathbf{P}_e^{-1}$ must exist. This condition is obvious from Equation 3.45 and serves to ensure controllability of $\mathbf{P}_e$. Second, *diagonal dominance* must exist. This condition results from a disturbance response analysis of the MISO equivalent form. For the $2x2$ case, *diagonal dominance* exists if:

$$|p_{1,1}p_{2,2}| \geq |p_{1,2}p_{2,1}| \quad as \ \omega \Rightarrow \infty \tag{3.63}$$

where $p_{i,j}$ are elements of a $2x2$ plant matrix $\mathbf{P}_e$. The same analysis for the $3x3$ case results in:

$$|p_{1,1}p_{2,2}p_{3,3}| \geq |p_{1,1}p_{2,3}p_{3,2}| + |p_{1,2}p_{2,1}p_{3,3}| + |p_{1,2}p_{2,3}p_{3,1}| + |p_{1,3}p_{2,2}p_{3,1}| + |p_{1,3}p_{2,1}p_{3,2}|$$
$$as \ \omega \Rightarrow \infty \tag{3.64}$$

Diagonal dominance is derived in references [12, 19]. If *diagonal dominance* does not exist, it may be possible to achieve by reordering of the input and output vectors. For the Lambda URV, both conditions were checked and found acceptable for all plant cases.

The decoupled URV models led to two separate QFT design problems. The longitudinal channel (q) is $1x1$ and SISO. The lateral channels (p, r) are MIMO $2x2$. The elements of $\mathbf{T}$ in Equations 3.53–3.60 show this decoupling clearly and verify that the MISO equivalent form of the $3x3$ MIMO system decomposes into two separate design problems.

3.2.5 Templates. The development above yields insight into the power of the MISO equivalent method of representing a MIMO system, but the principle synthesis problem remains in handling the plant parameter uncertainty. Frequency templates quantify the uncertainty and provide a way to design compensation for specified system performance in spite of the uncertainty.

The Nichols chart (NC) is the best graphical tool for QFT design synthesis. The rectangular

grid on the Nichols chart displays the magnitude in dB and the phase in degrees of a transfer function parameterized by frequency along the curve. Gain and phase margins of a plotted open-loop system are easily determined [6:302–305]. The constant M and α contours on the Nichols chart are the loci of constant closed-loop magnitude and phase respectively for the plotted open-loop system in the unity-feedback configuration. Use of the M and α contours makes it possible to exactly shape the closed-loop system frequency response.

The plant parameter regions of uncertainty are easily displayed on the NC as templates by plotting all plant transfer functions $q_{i,j}$ representing the plant parameter variations for a given frequency and connecting the points to form an uncertainty region. Figure 3.4 shows the rectangular grid on the NC and a typical template for a frequency v_k ($w' = u + jv$). An excellent discussion of the NC and its M and α contours is contained in reference [6:332–338]. Look on page 335 of reference [6] for an excellent picture of a NC.

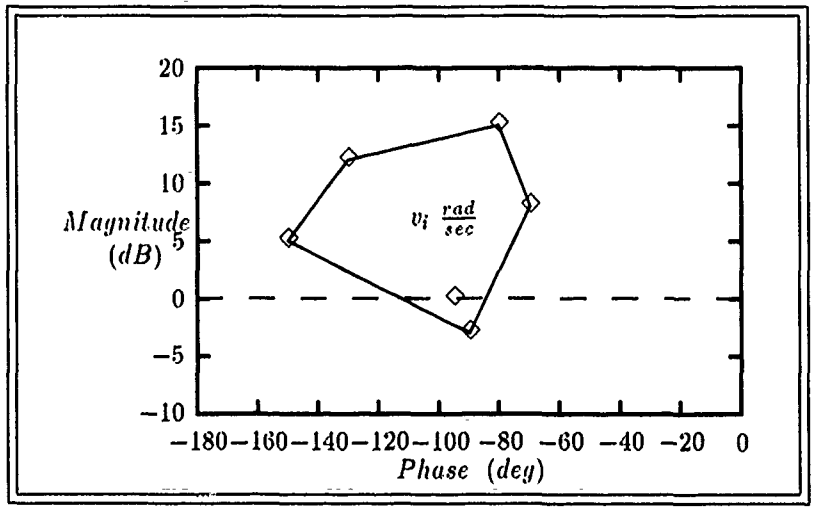

Figure 3.4. Typical Plant Parameter Uncertainty at a Frequency v_k *rad/sec*

To the extent that the enclosed region is the "true" bounded range of plant uncertainty, the area inside represents all possible plant variations. Generation of templates for all frequencies of interest gives a clear picture of the frequency dependent variation in the uncertainty regions.

Two issues are considered in template generation. First, how should the plant points for a given template be connected to produce the most realistic uncertainty region? Notice in Figure 3.4 that the uncertainty region includes one of the plant points. Since this point was close to another point and both points were at the boundary of the uncertainty region, the outermost point was used and the other was included within the region. Experience and familiarity with the physics of the problem guide the designer here. As a general rule, points that lie close to others can be included within the boundary as long as the outermost point is used as the boundary, but "stand-alone" points must lie on the uncertainty boundary. Also, points are joined by straight line segments and in general, with few exceptions, the particular order of connection is adhered to for each frequency of interest. A point may be considered close if it is within 5 dB and 10 to 20 deg of another point but this is not always so.

Generating the appropriate number of templates at the proper frequencies to acceptably describe the plant variation is the second issue. The general rule is to generate a template at least every decade where the plant uncertainty remains nearly constant, and generate templates much more frequently in regions where the plant uncertainty changes rapidly. Bode plots of the plants show this variation in uncertainty and help a great deal in determining at which frequencies to generate templates.

Before determination of system performance bounds, it is necessary to choose one of the plant points as a nominal or reference plant. The nominal plant P_{o_i} is used to synthesize the nominal loop transmission l_{o_i} and thus to synthesize the loop compensator g_i . Performance bounds are constructed with the templates using the nominal plant as the reference. This guarantees that if the nominal loop transmission meets or exceeds all performance bounds so will all plant cases and all other points within the uncertainty regions. Selection of a nominal plant with the fewest number of and preferably no unstable roots (RHP poles) makes the loop transmission phase shaping somewhat easier. The nominal plant must be used throughout the loop transmission synthesis, however, a

different nominal plant can be used for the other loops in the MISO equivalent MIMO design.

3.2.6 Performance Bounds. Tracking performance and disturbance attenuation are the performance specifications of interest in most control system designs. In QFT, tracking and disturbance specifications are met by graphically determining bounds for each on the NC and designing a loop transmission to meet or exceed these bounds. The bounds are constructed by use of the templates. A disturbance and tracking bound is generated for each v_k and a composite boundary consisting of the most constraining of the two is plotted for each v_k for the loop transmission synthesis. Detailed information on constructing these bounds is contained in reference [6:Chap 21].

Specification of a minimum damping ratio ζ on the dominant roots of the closed-loop system is the final point of interest in the performance bounds of the system. The disturbance response is very sensitive to changes in ζ so a further requirement on the loop transmission synthesis is added.

$$\left|\frac{L_o}{1+L_o}\right| \leq M_L \tag{3.65}$$

The above requirement holds for a range of frequencies v_k and over the entire range of plant uncertainty. MIL-STD-1797A [26] provides guidance for military flight control design by specifying a 45° phase margin requirement on military aircraft. This corresponds to the 3 dB contour on the NC. This requirement stipulates only that the phase margin $(180° - \angle l_{o_i}(jv_k))$ be 45° at the 0 dB crossing so that v_ϕ is equal to v_k where $|l_{o_i}(jv_k)|$ is 0 dB. Equation 3.65 extends the MIL Standard phase margin requirement such that $\angle l_{o_i}(jv_k) \approx -135°$ over a range of frequencies v_k and not just at crossover. Templates are used to extend the phase margin requirement in accordance with Equation 3.65 for the range of v_k of interest and over the plant parameter variation. The template for each v_k is moved around the M_L contour without penetrating and a loci of points is constructed by periodically marking the nominal point. This extends the phase margin boundary for each v_k to guarantee a 45° phase margin for the closed loop system as long as the loop transmission does

not penetrate these boundaries.

To provide the required tracking, attenuate the undesirable coupling disturbances and guarantee a minimum phase margin, three sets of bounds are constructed. The specified closed-loop system performance is met if none of these bounds are penetrated by the nominal loop transmission synthesis.

3.2.7 Loop Shaping. Reasonable optimality in LTI systems is achieved by minimizing the high frequency loop gain K [15, 11]. This is also restated by saying that the less bandwidth used to do a particular control job, the more optimal it is. For the QFT problem, this translates to synthesizing l_o, such that it exactly meets every composite boundary and remains just outside the phase margin boundary. The tradeoff here is complexity of compensation. More compensator poles and zeros are required to closely meet the optimum loop transmission.

In many applications, high-order compensation is not desirable. The computational power onboard Lambda mandates low-order controllers for implementation. The object of the loop transmission synthesis for this problem is to produce the lowest-order compensation required to meet the performance specifications. More loop gain is used to meet performance bounds rather than more poles and zeros when possible.

A w′-plane transfer function numerator and denominator are always equal order polynomials in w′. Thus the transformation generates zeros to make up for the excess number of poles to zeros in the s-plane transfer function. The transformation always produces at least one NMP *sampling* zero at ω_s/π *rad/sec* because any practical s-plane transfer function will have an excess of at least one pole. Other transformation zeros are produced when the s-plane transfer function has n zeros and $n+2$ or greater poles. Some of these other zeros may also be NMP too. Dr. Horowitz has studied this transformation in some detail and claims that for a given excess of s-plane poles, the w′-plane zeros produced tend to be roughly symmetric about the origin [17]. In other words, the NMP zeros created in the transformation are roughly located at the same place in the RHP as the

MP zeros in the LHP . He also found that the NMP zeros tended also to be far enough away from the origin so as to be easy enough to deal with in the QFT loop transmission synthesis.

Past digital QFT designs introduced an all-pass filter to handle the *sampling* zero NMP characteristics of the nominal loop transmission.

$$L_{oNMP}(w') = A(w')\, L_{oMP}(w') \tag{3.66}$$

$A(w')$ in Equation 3.66 is the all-pass filter. It separates the NMP characteristics from the problem where the universal high frequency boundary (UHFB) is shifted according to the phase of the all-pass filter at values of frequency w_k [19:Appendix C]. The shifted UHFB is plotted on the NC and a MP L_{oMP} is synthesized. Use of the all-pass filter allows the designer to shape a MP loop transmission subject to the phase shifting UHFB. This loop shaping technique was used in earlier discrete QFT flight control designs and worked well with the first order effector actuator models used in those designs. Ott and Hamilton extended the use of the all-pass filter to cases where more than one NMP zero existed in the nominal loop transmission resulting from the inclusion of higher than first order actuator models with the plant [29, 8]. The higher order effector actuator models coupled with the plant dynamics in those studies resulted in excessive loop phase lag and made successful loop transmissions that met all stability bounds impossible. The all-pass filter is a good way of dealing with the NMP elements in a discrete design especially if the designer prefers shaping MP loop transmissions. A more direct approach is used in this study to deal with the NMP zeros of a w'-plane loop transmission.

Lambda's effector actuator and sensor models combined are zero order over third order, or an excess of three poles. No matter what the order of the design transfer functions for the effective plant, at least two new zeros are created along with the *sampling* zero in the transformation to the w'-plane from just the inclusion of these models in the problem. It turns out that one other NMP zero results in addition to the NMP *sampling* zero. The two NMP zeros for this

design are approximately invariant moving only slightly and not significantly for any plant case. It is logically assumed that the new NMP zero resulted from the invariant effector actuator/sensor model. Another more variable LHP zero is created in the transformation and is assumed to correlate to the variable nature of the different plant cases.

A variety of ways exist for actually synthesizing the loop transmission. In this study, low-order compensation is required, so the loop is shaped by considering and including all elements of the nominal plant. In this way, poles and zeros added during shaping are only those of the compensator and a minimum order compensator is synthesized. The all-pass filter is not used. Dr. Horowitz feels that the NMP zeros of the w' transformed design elements $q_{i,i}$ can be dealt with directly during the loop shaping by including them in the nominal plant and in the template generation. The phase contribution of NMP zeros at all frequencies of interest w_k is included in the frequency shaping this way. Also, RHP (unstable) pole(s) of the nominal plant P_{o_i} must also be included in the nominal loop transmission synthesis to ensure their phase contribution is accounted for. For each MISO loop transmission problem, the nominal loop l_{o_i} is shaped to meet the performance bounds.

$$l_{o_i}(w') \quad = \quad g_i(w') \;\; q_{o_{i,i}}(w') \tag{3.67}$$

$q_{o_{i,i}}$ contains all the NMP properties of all the plant cases and any unstable poles for that plant case as a very minimum. For this study, however, and in the interest of lowest-order synthesis, all elements of $q_{o_{i,i}}$ are included in the loop synthesis.

It is beneficial at this point to present the phase relationships of RHP and LHP poles and zeros. Table 3.2 shows the low and high frequency phase contribution of each of these elements. The angles shown in the table were measured in the positive or counterclockwise sense. Note that angles in the denominator change sign.

Table 3.2. Low and High Frequency Properties of LHP and RHP Poles and Zeros

ω rad/sec	0	∞	$\delta\angle$
$\angle$ LHP zero	0°	+90°	+90°
$\angle$ LHP pole	0°	−90°	−90°
$\angle$ RHP zero	+180°	+90°	−90°
$\angle$ RHP pole	−180°	−90°	+90°

Application of the Nyquist stability criterion during the loop transmission synthesis is required to guarantee stable closed-loop systems. The Nyquist criterion in equation form is:

$$Z_R = P_R - N \tag{3.68}$$

where Z_R is the number of RHP zeros in the characteristic equation of the closed-loop system $(1 + L)$, P_R is the number of RHP poles in the open-loop transfer function (L), and N is the net number of encirclements of the $-1 \pm j0$ point of the open-loop transfer function (L) [6:283-298]. Positive $(+N)$ net encirclements are in the counterclockwise (CCW) sense and negative $(-N)$ net encirclements are in the clockwise (CW) sense. For a stable closed-loop system, $Z_R = 0$ so that:

$$P_R = N \tag{3.69}$$

The number of RHP poles in L must equal the net number of CCW encirclements L makes of the $-1 \pm j0$ point. The Nyquist criterion is applied by determining N from the polar plot of L. If P_R does not equal N as determined from the polar plot, then L must be reshaped.

For the Lambda loop shaping, one RHP pole exists in some plant cases of each loop channel. Two invariant RHP zeros exist in all plant cases for each loop channel. The Nyquist stability criterion was applied during each loop transmission synthesis and showed that the resulting closed-loop systems were stable.

3.2.8 Improved QFT Method. The loop transmission synthesis resulting from the MISO equivalent MIMO system representation is shown to produce a satisfactory closed-loop MIMO system. No iteration between the MISO equivalent loops is required for a successful design [12]. Even though no iteration between the loops is required, correlation does exist between the MISO equivalent loops. This correlation can be used to further optimize the loop transmissions by applying the improved formulation of MIMO QFT loop transmission synthesis.

With standard QFT, the MISO channel loops are shaped separately and in no particular order. The compensation and filtering required in a particular loop design, however, correspond to *knowledge* not available until after loop transmission synthesis has begun and thus not included in the development of the original MISO design equations shown on page 3-16. In these original equations, the *worst case* disturbance inputs due to other loops are utilized. With knowledge of compensation required for a particular loop, the overdesign inherent in the *worst case* assumption can be reduced. This relationship is exploited in the improved MIMO QFT method.

The improved method requires one loop transmission synthesis completed by the old method, however, the loop chosen can sometimes be important. The basic rule is to choose the loop with the least uncertainty. This will be the smallest bandwidth loop. This is in line with the basic bandwidth minimization optimality criterion stated earlier. The $f_{i,i}$ and g_i of this loop are now known and the disturbance contribution of this loop to the other MISO equivalent loops can be modified to reflect this *knowledge* and reduce the uncertainty associated with the disturbance from this loop. Further subsequent loop design *knowledge* is similarly used. Dr. Horowitz presents this improved method in reference [13].

For Lambda, the improved method is only used on the lateral 2x2 MIMO system due to the decoupling of the longitudinal modes from the lateral modes. The 2x2 and 3x3 modified design equations are given below without derivation. The subscripts on the elements of these equations denote the order of loop synthesis. 1 is first loop synthesized, 2 the second, etc. For the 2x2 system,

loop 1 is synthesized first resulting in $f_{1,1}$ and g_1. The effective design equation for the next loop then is formed and used for the second loop transmission synthesis.

$$l_{2_e} = g_2 q_{2,2_e} = \frac{g_2 q_{2,2}(1 + g_1 q_{1,1})}{1 - \gamma_{1,2} + g_1 q_{1,1}} \tag{3.70}$$

where

$$\gamma_{1,2} = \frac{p_{1,2} p_{2,1}}{p_{1,1} p_{2,2}} \tag{3.71}$$

$q_{2,2_e}$ is notation used to denote the effective design transfer function of loop two modified by the known compensator and filter of loop one.

The first two loops of a $3x3$ system are synthesized with the $2x2$ equations above. The effective design transfer function of the last loop of the $3x3$ system is given in Equation 3.72. It is derived assuming knowledge of $f_{1,1}$ and g_1 of loop one and $f_{2,2}$ and g_2 of loop two.

$$l_{3_e} = \frac{g_3 q_{3,3}(1 + l_1)(1 + l_{2_e}) - \gamma_{1,2}}{(1 + l_1)(1 + l_{2_e}) - \gamma_{1,2} - \gamma_{2,3}(1 + l_1) - \gamma_{1,3}(1 + l_{2_e}) + \gamma_{1,2}\mu_2 + \gamma_{1,3}\mu_3} \tag{3.72}$$

where

$$l_1 = g_1 q_{1,1} \tag{3.73}$$

$$l_{2_e} = g_2 q_{2,2_e} \tag{3.74}$$

$$\gamma_{1,2} = \frac{p_{1,2} p_{2,1}}{p_{1,1} p_{2,2}} \tag{3.75}$$

$$\gamma_{2,3} = \frac{p_{2,3} p_{3,2}}{p_{2,2} p_{3,3}} \tag{3.76}$$

$$\gamma_{1,3} = \frac{p_{1,3} p_{3,1}}{p_{1,1} p_{3,3}} \tag{3.77}$$

$$\mu_2 = \frac{p^*_{2,3} p^*_{3,1}}{p^*_{2,1} p^*_{3,3}} = \frac{q_{2,1} q_{3,3}}{q_{2,3} q_{3,1}} \tag{3.78}$$

$$\mu_3 = \frac{p^*_{3,2} p^*_{2,1}}{p^*_{3,1} p^*_{2,2}} = \frac{q_{3,1} q_{2,2}}{q_{3,2} q_{2,1}} \tag{3.79}$$

The starred variables above denote elements of $\mathbf{P}_c^{-1}$ as given in Equation 2.27.

3.2.9 Prefilter Synthesis. Recall $|\delta_R(jv)|$ represents the maximum allowable magnitude variation in the closed-loop tracking response for a specific loop transmission $l_i(w')$. A properly designed $l_{o_i}(w')$ meeting all performance bounds guarantees the closed-loop tracking response at frequency v_k will be less than or equal to the allowable variation of $|\delta_R(jv_k)|$. The magnitude variation is thus guaranteed but not its placement in the frequency plane. The pre-filter positions the closed-loop response in the frequency plane to meet the tracking model loop transmission specifications.

Execution of the prefilter design synthesis is easily done graphically with the NC or with Bode plots. References [6, 19, 12] present the technique thoroughly and use the NC. The Bode plot method was used in this study. The pre-filter design methods are identical, its only the graphical tools used that are different.

Design of the prefilter begins by generating the magnitude frequency response for the loop transmission of all plant cases used to synthesize $l_{o_i}(w')$. These are closed-loop responses of the form in Figure 3.5.

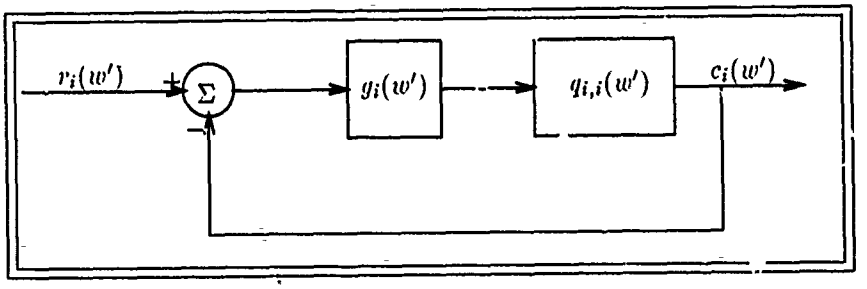

Figure 3.5. Loop Transmission Response Configuration

These loop transmissions are plotted for all plant cases with the tracking response frequency bounds on the same Bode plot. Filter poles and zeros are placed where required to position all loop transmissions within the frequency response bounds. The filter design is verified by generating

filtered loop transmission responses of the form in Figure 3.6.

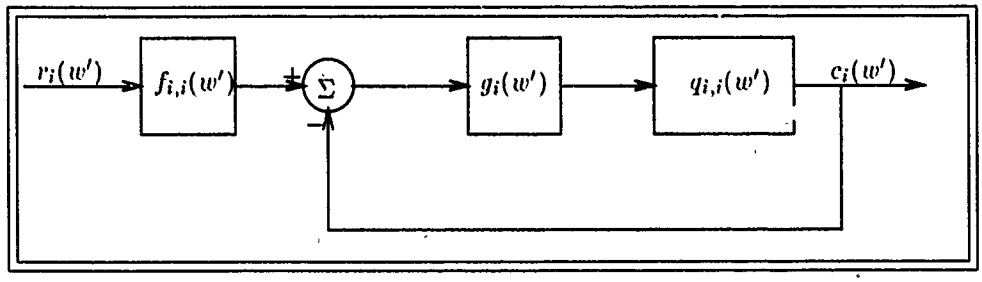

Figure 3.6. Filtered Loop Transmission Response Configuration

The placement of one filter element at a time with subsequent iteration is used and found to be the easiest way to design the prefilter. The pitch-rate loop filter design described in the next chapter fully describes this procedure.

3.2.10 Compensator and Prefilter Discretization. The final step in the discrete QFT design process is transforming the compensator $g_i(w')$ and prefilter $f_{i,i}(w')$ discrete designs to the z-plane for implementation and simulation. Since $g_i(w')$ and $f_{i,i}(w')$ have equal order numerators and denominators, and the w'-plane is approximately equal to the s-plane, the Tustin transformation (Equation 3.4) is used to transform them to the z-plane.

$$g_i(w') \Rightarrow \boxed{\text{Tustin Transform}} \Rightarrow g_i(z) \tag{3.80}$$

$$f_{i,i}(w') \Rightarrow \boxed{\text{Tustin Transform}} \Rightarrow f_{i,i}(z) \tag{3.81}$$

The last step in the transformation is to verify the frequency responses of the w′ and z plane compensators and prefilters. Poles and zeros of the w′-plane compensators and prefilters that are not in the good Tustin region may transform with significant *warping* depending on their particular placement. The frequency responses of the w′ and z plane elements will show the significance of the *warping* present. If there is good correlation between the responses out to approximately

$\omega_s/3$ (rad/sec) then the *warping* was insignificant. This verifies a proper transformation and implementable compensators and prefilters.

3.2.11 QFT Compensator/Plant Pole/Zero Cancellation. The fixed compensators and prefilters synthesized in a QFT design provide compensation so that all points within the plant parameter uncertainty region meet closed-loop performance specifications. The nominal plant P_{o_i} is a reference for shaping this closed-loop response relative to all points within the bounds of the uncertainty regions for all frequencies ω_k. It is not required that the plant ever operate at the nominal condition nor that it operate anywhere on the boundary, including at all the other plant cases used to generate the uncertainty regions. Because of this, specific pole/zero combinations between g_i and $q_{o_{i,j}}$ are not expected or required, and close cancellation of the nominal plant dynamics is not a problem.

It is true, that certain elements are added to the plant cases to model other systems and devices of an over-all system. Control surface actuator models and dynamic sensor models in aircraft subsystems are good examples. It is also true that mostly the models used for these subsystems are considered completely certain, however this is also an approximation. These device dynamics can also be cancelled for the same reasons as mentioned above.

It should be pointed out here that the system sensitivity for tracking to the elements of g_i and $q_{o_{i,j}}$ are exactly the same and therefore also for any cascaded subsystems. Inaccuracies and uncertainty in the cascaded subsystems, like actuator and sensor models, can be accounted for by enlarging the uncertainty regions. Uncertainty in g_i can also be accounted for this way.

The issue could be raised that the uncertainty associated with the subsystem models was not injected into the problem so, effectively, the uncertainty available to the plant dynamics is now less than before. One can compensate for this by slightly increasing the uncertainty region bounds to take this into account. For example, if subsystem models are judged to be 5% uncertain then increase the uncertainty regions or $q_{o_{i,j}}$ templates accordingly. Generally, though, and for this

study, *deterministic* subsystem dynamics models are excellent approximations with insignificant uncertainty in comparison to the higher plant parameter uncertainty.

IV. Discrete Compensator Designs

This chapter presents the QFT compensator designs for g_i and $f_{i,i}$. The decoupling present in the Lambda models allow separation of the longitudinal and lateral aircraft modes. The design equations presented in the last chapter show the longitudinal system to be SISO without disturbance inputs, and the lateral system to be $2x2$ MIMO.

The following sections present the SISO pitch-rate (q) design problem for the longitudinal system and the MIMO lateral system design problem. The yaw-rate (r) MISO equivalent loop is designed first in the MIMO lateral system followed by the roll-rate (p) MISO equivalent loop. The SISO pitch-rate loop design is presented in detail to illustrate the complete design procedure. The lateral design is presented by highlighting only those issues specific to that design and different from the pitch-rate loop.

4.1 Pitch-Rate (q) SISO Design

Plant case #1 is selected as the nominal plant for the pitch-rate loop design since it has no unstable poles, and thus, $\mathbf{P}_o = \mathbf{P}_1$. For this, and the subsequent lateral MISO loop designs, tracking and disturbance bounds are not determined for reasons specified in the discussion on page 3-12. Very simply, the loop transfer function is synthesized so that loop gain is maximized subject to the phase margin bounds, the w'-plane NMP modeling characteristics, and the desire for low order compensation. With Lambda, higher order structural modes not modeled are estimated to be insignificant in the passband of this control system design and a loop transmission 0 dB crossover frequency limit is not used. If it were required, then the nominal loop transmission l_o, synthesis, and the resulting g_i, would be constrained to ensure that all plant case loop transmissions $l_i = g_1 q_{1,1}^i$ crossed 0 dB at or below the crossover frequency limit. The shaping then requires only that the phase margin bounds be drawn on the NC and that the nominal loop transmission be synthesized

such that the bound corresponding to each frequency v_k is not penetrated. The template data and the templates used for this loop transmission shaping are presented in Appendix E.

For this loop then:

$$l_{o_1}(w') = g_1(w')\, q_{o_{1,1}}(w') \tag{4.1}$$

$$q_{o_{1,1}}(w') = \frac{5.4517e{-}5\ (0)(-0.6263\pm j0.1696)(120)(-140.1131)(155.5707)(-947.3232)}{(-0.0198\pm j0.5799)(-1.2908\pm j1.8704)(-12.7956\pm j12.6603)(-47.2948)} \tag{4.2}$$

The negative signs in these formulas denote LHP roots and no sign is positive and denotes RHP roots.

The loop l_{o_1} is shaped as a Type 1 loop to ensure zero steady state error to a step input for the SISO system. Since $q_{o_{1,1}}$ has a zero at the origin and a Type 1 loop transmission is required, $g_1(w')$ must have two poles at the origin. Thus $g_1(w')$ initially becomes:

$$g_1(w') = \frac{1}{w'^2} \tag{4.3}$$

Since $\mathbf{P}_o$ is nearly the lowest left point on the templates at frequencies above 5 rad/sec, the phase margin bounds, for v_k above 5 rad/sec, lie nearly along the $-135°$ line on the NC. This is evident from phase margin bounds for this loop shaping shown on the NC in Figure 4.1. The phase margin bound terminology used here is also known in the literature as the stability bounds. Dr. Horowitz uses the stability bound terminology. For this loop design, the particular shape of the bounds at the higher v_k frequencies and the nominal plant position on the templates requires that the shaped loop transmission follow, as far as possible, the $-135°$ phase line.

The easiest way to loop shape with NMP nominal plant elements is to consider only the loop phase initially with all RHP zeros and unstable poles of $q_{o_{1,1}}$ included. The NMP and unstable characteristics of the other plant case elements are incorporated in the plant templates. Once the loop phase is shaped, loop gain is adjusted to provide the maximum gain attainable subject to the

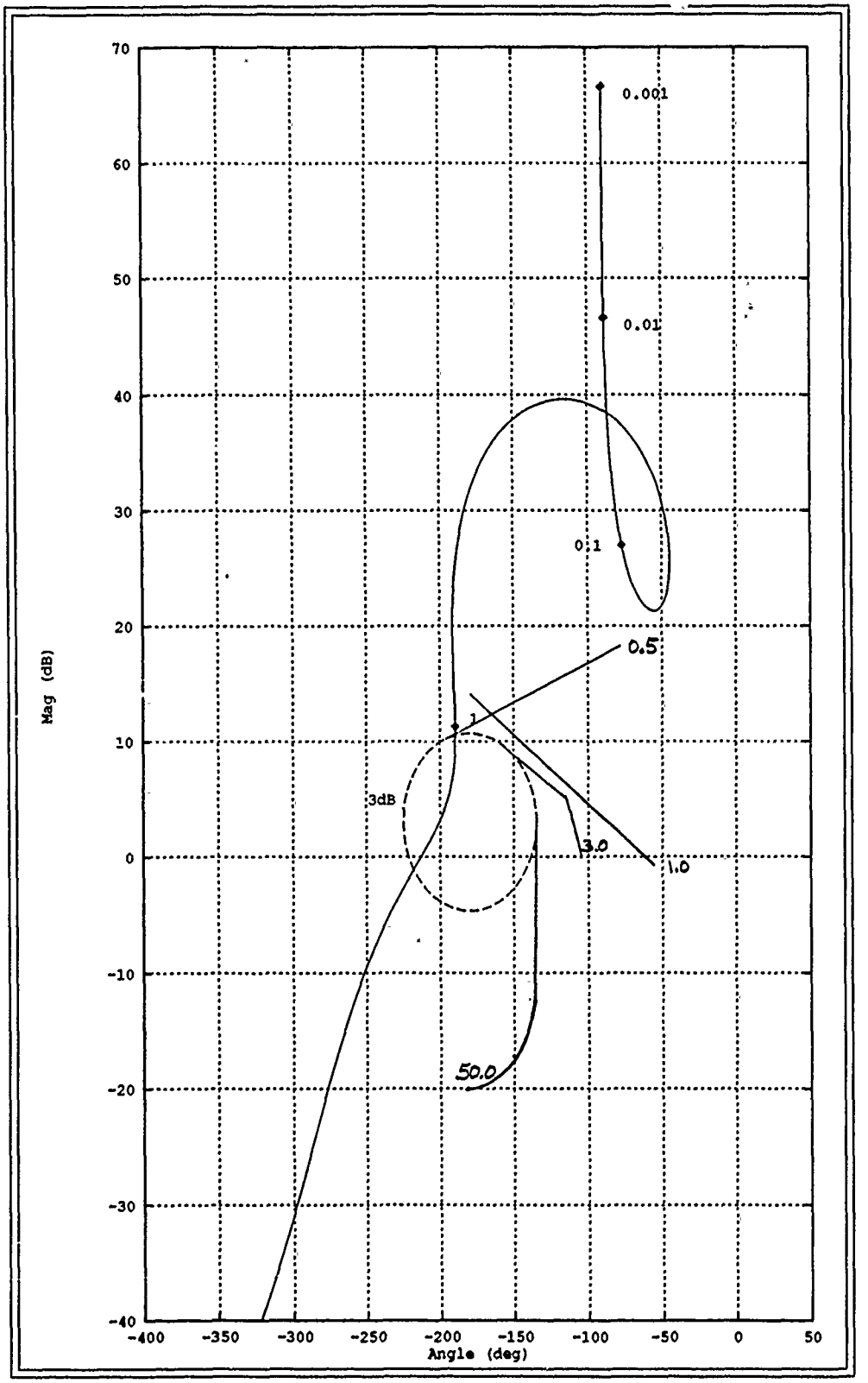

Figure 4.1. Pitch-Rate Loop ($q_{1,1}$) Phase Margin Bounds and Nominal Loop Transmission $l_{o_1}(w')$ For $g_1(w') = 1/w'^2$

given bounds. Note the NMP zeros at +140 and +120. The phase lag from these zeros and the actuator and sensor poles begins to contribute significantly at frequencies above 12 rad/sec and thus dominates the loop transmission above this. The Bode phase plot $\angle l_{o_1}(jv)$ for $g_1(w')$ equal to $1/w'^2$ is shown in Figure 4.2 along with the $-135°$ high frequency phase bound derived from the phase margin bounds for the frequencies v_k shown in Figure 4.1.

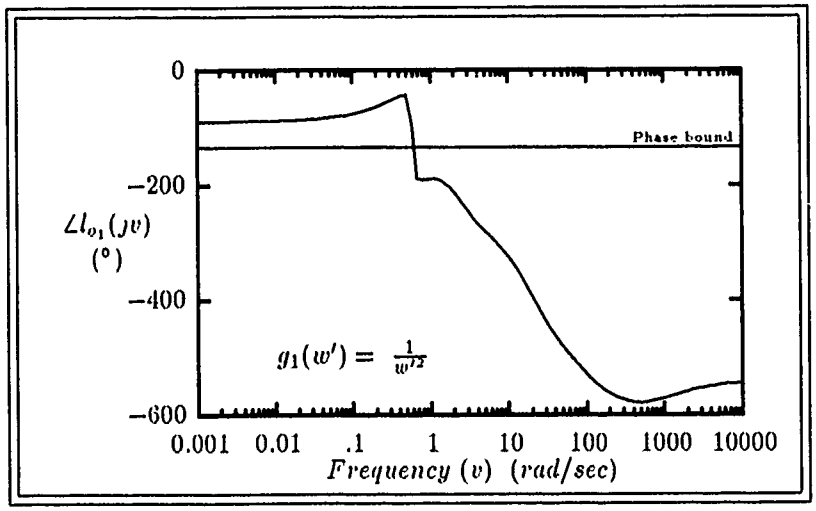

Figure 4.2. Type 1 Pitch-Rate Loop Phase $\angle l_{o_1}(jv)$ For $g_1(w') = 1/w'^2$

It's obvious from Figures 4.1 and 4.2 that compensator zeros are needed to decrease the phase lag to above $-135°$ in the frequency range from 0.5 to 20 rad/sec. A pair of zeros are added at 0.3 and 6 rad/sec to g_1 to bring the loop phase close to $-135°$ since it is desirable, in the interest of optimality, to stay as close to the phase margin bound as possible for as large a range of frequency v as possible. These figures also clearly show that the excess phase lag at the high end of the system passband is due to the actuator/sensor poles and NMP zeros in $q_{o_{1,1}}$ and more lead compensation in the actuator model frequency range is indicated. Thus, a complex zero pair is added to g_1 at the actuator model natural frequency of 18 rad/sec, however, a lower damping ratio ζ is used. The

$g_1(w')$ synthesized to meet the loop shaping bounds is:

$$g_1(w') = \frac{562(w'+0.3)(w'+6)(w'^2+20w'+324)}{w'^2(w'^2+500w'+250000)} \tag{4.4}$$

Figure 4.3 shows the Bode plot magnitude and phase of the compensated loop transmission.

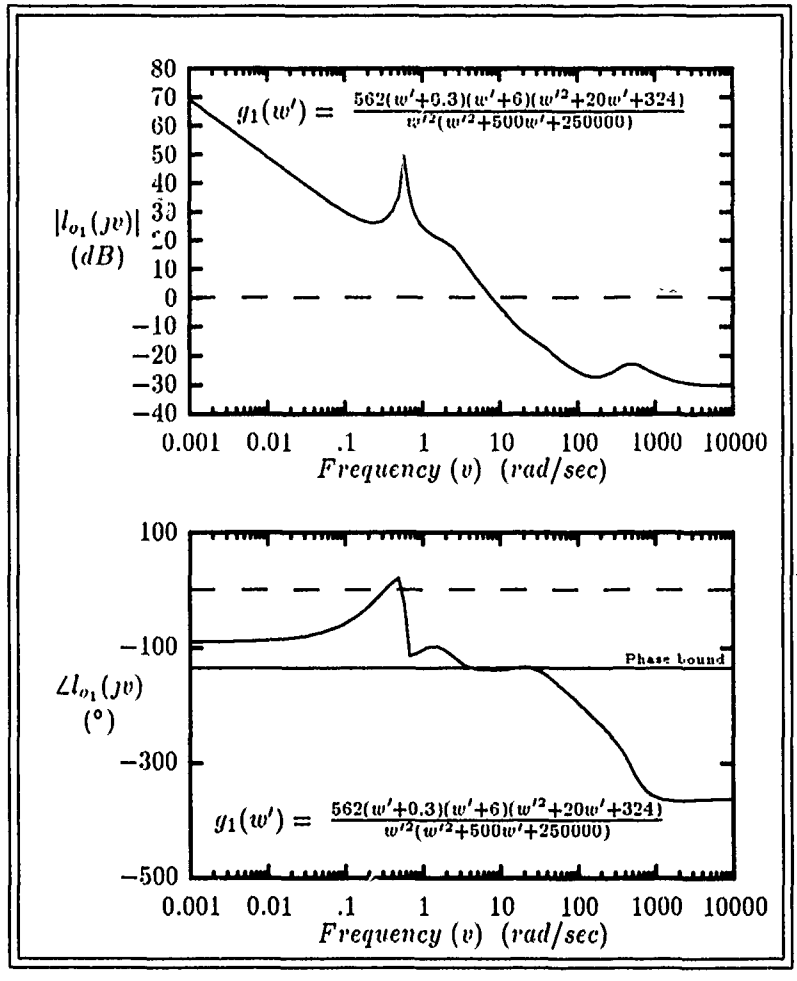

Figure 4.3. Pitch-Rate Loop Transmission $l_{o_1}(w')$ Design #1

It is emphasized that the NC with phase margin bounds and the Bode plots of l_{o_1} are used together during loop shaping and provide a complete and very transparent picture of the options involved in choosing the compensator elements. Note the g_1 selected basically provides for a Type

l loop transmission with the poles at the origin, and provides phase lead in the system passband to compensate for the lagging plant and actuator dynamics. The high frequency 2nd order poles in g_1 make it a proper w'-plane transfer function by ensuring proper phase as v approaches ∞.

The shaped loop transmission with bounds is shown on the NC in Figure 4.4. The bounds shown are only portions of the phase margin bounds required to illustrate the loop transmission bound compliance.

Figures 4.3 and 4.4 show that a severe *droop* exists in the loop transmission between 0.01 and 1 rad/sec. In this range of frequencies, some tracking bounds are not met by the loop transmission $|l_{o_1}(jv)|$ as verified by the construction of a partial tracking bound at 0.3 rad/sec. A second design is initiated to try to improve this situation.

One way to improve this is to extend the high frequency phase roll-off so that the loop phase remains at $-135°$ out to higher frequencies v_k thus, increasing the bandwidth of the loop transmission. The loop gain is then increased appropriately to increase the feedback at all frequencies. Compensation is successfully added to extend the phase roll-off, but the resulting loop magnitude proves to be unacceptable due primarily to the NMP zeros and sensor/actuator poles. Further, this method may not be acceptable in some situations and particularly in aircraft systems since structural modes may be excited by the higher loop bandwidth thus invalidating the dynamics model used.

A second approach is used to provide compensation directly in the frequency range of interest. A lag-lead pole-zero pair is placed and design #2 for $g_1(w')$ now is:

$$g_1(w') = \frac{562(w'+0.3)(w'+6)(w'^2+20w'+324)}{w'^2(w'^2+500w'+250000)} \frac{(w'+0.2)}{(w'+0.02)} \tag{4.5}$$

Bode plots of both design #1 and #2 loop transmissions are shown in Figure 4.5. Note the increase in gain for all the *droop* frequencies. Also note the loop transmission phase at the lower frequencies.

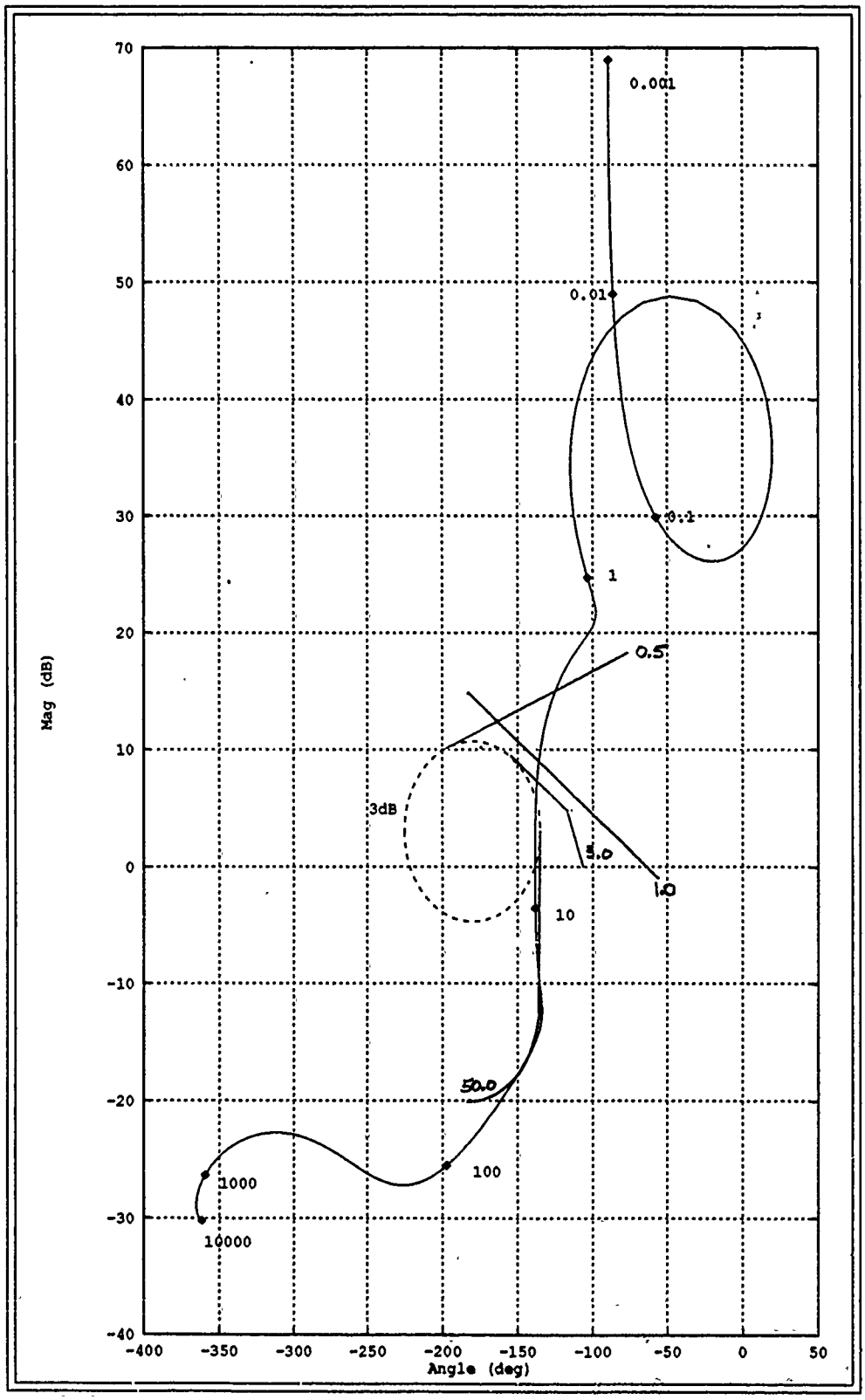

Figure 4.4. Pitch-Rate Loop ($q_{1.1}$) Phase Margin Bounds and Nominal Loop Transmission $l_{o_1}(w')$ For $g_1(w')$ Design #1

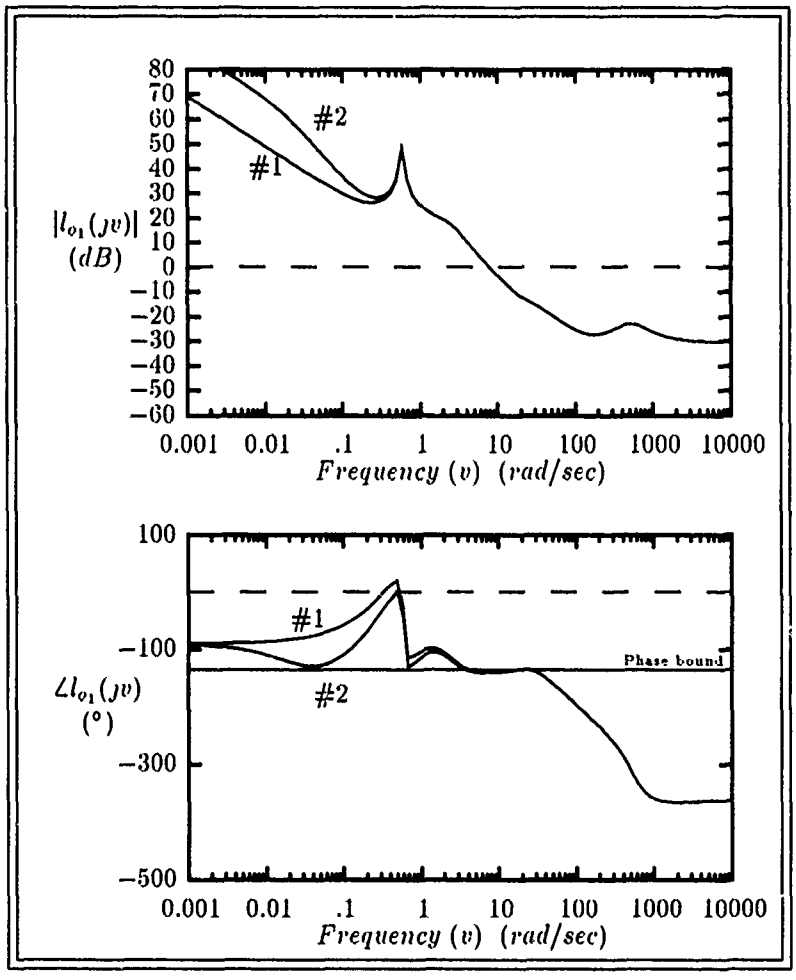

Figure 4.5. Pitch-Rate Loop Transmission $l_{o_e}(w')$ For Design #1 and #2

More low frequency phase lag is present in design #2 and raises concern as to whether design #2 is really better. The NC in Figure 4.6 shows that design #2 is better since, even though the loop size has not changed significantly, the low frequency loop gain is increased significantly over that for design #1.

The pre-filter is synthesized as described in Chapter III by first forming the frequency responses of the closed-loop systems for each plant case with $g_1(w')$. These responses and the pitch-rate channel response bounds of B_l and B_u are plotted in Figure 4.7. Only $g_1(w')$ design #1 is shown in the figure since the prefilter requirements are identical for design #1 and #2.

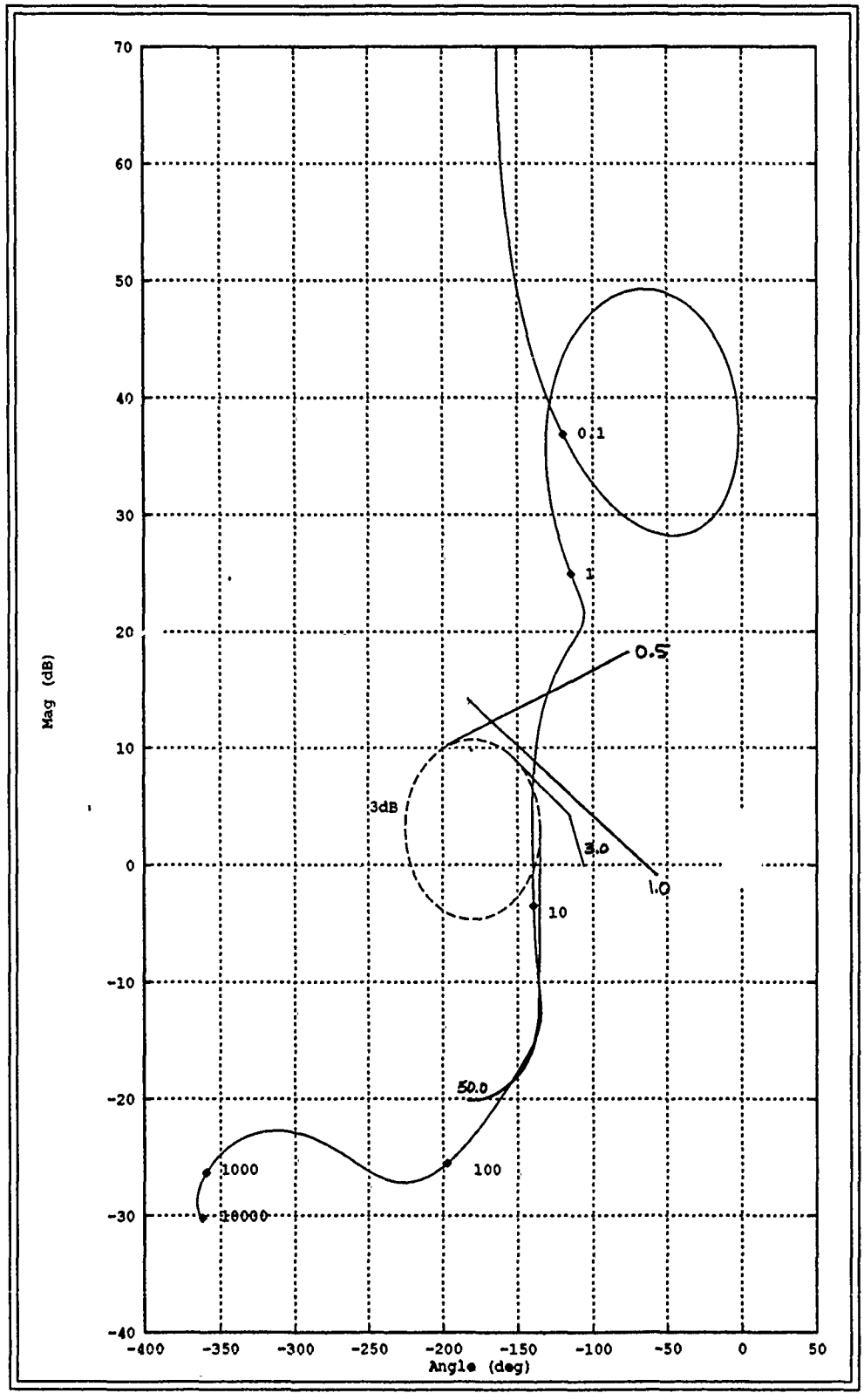

Figure 4.6. Pitch-Rate Loop ($q_{1,1}$) Phase Margin Bounds and Nominal Loop Transmission $l_{o_1}(w')$ For $g_1(w')$ Design #2

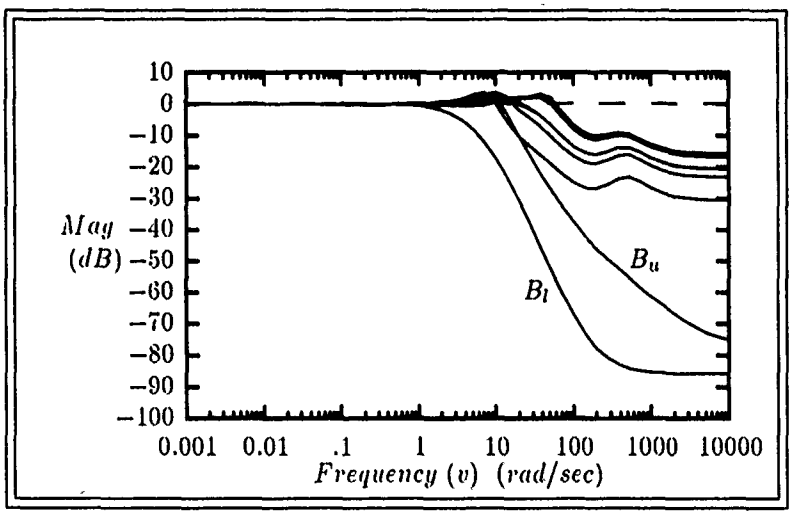

Figure 4.7. $l_i/(1+l_i)$ Design #1 Pitch-Rate Channel Frequency Responses for Plant Cases 1-6

The prefilter poles and zeros are selected to move all plant case responses within the response model bounds shown in Figure 4.7. The $f_{1,1}(w')$ required for this is:

$$f_{1,1}(w') = \frac{0.0012(w'+100)(w'+500)}{(w'+4)(w'+15)} \tag{4.6}$$

The filtered closed-loop frequency response for design #1 is shown in Figure 4.8. Filtered closed-loop responses for design #1 and #2 are shown in Figure 4.9 expanded at the lower frequencies to show the effect of the increased *droop* frequency gain. Design #1 with the lower low frequency gain has the largest *droop*. This *droop* effect is quite evident in the step response loop verification simulations in Appendix G Figure G.1.

Closed-loop attenuation in the *droop* range of frequencies for plant #1 exists for both designs as shown in the plots in Figure 4.9. The *droop* in design #2, however, is reduced. Plant #1 (the nominal plant) still does not meet the tracking bounds in this range of frequencies for either design even though maximum loop transmission, in both cases, is synthesized. Thus, it is clear, the plant actuator/sensors and the NMP elements dictate the maximum achievable loop transmission as claimed earlier. Step responses to the w'-plane pitch-rate channel are shown in Figure G.1 on

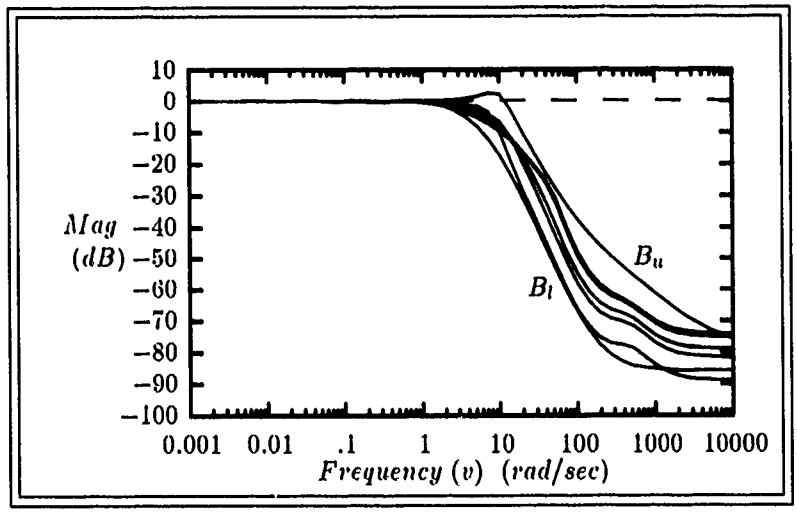

Figure 4.8. $f_{1,1}l_i/(1+l_i)$ Design #1 Pitch-Rate Channel Filtered Frequency Responses for Plant Cases 1-6

page G-1. The effect of this low frequency attenuation is apparent in those plots in the *sagging* time response of plant #1 between 3 and 10 sec.

Design #2 is the better design in terms of more closely meeting the response model specifications, however, design #1 is quite useable. In fact, design #1 may be more desirable since it is lower order than design #2. Further, the order can be reduced even more by designing a Type 0 loop transmission to allow some steady state error to a step input. A small amount of steady state error may not degrade the design and may be imperceptible to the pilot in most cases. This is also done and the resulting w'-plane step response is shown along with design #1 and #2 in Appendix G. It too is, in the interest of lowest order compensation, quite acceptable.

The w'-plane designs for g_1 and $f_{1,1}$ are:

$$Type\ 0 \quad \Rightarrow \quad g_1(w') = \frac{562(w'+6)(w'^2+20w'+324)}{w'(w'^2+500w'+250000)} \tag{4.7}$$

$$Design\ \#1 \quad \Rightarrow \quad g_1(w') = \frac{562(w'+0.3)(w'+6)(w'^2+20w'+324)}{w'^2(w'^2+500w'+250000)} \tag{4.8}$$

$$Design\ \#2 \quad \Rightarrow \quad g_1(w') = \frac{562(w'+0.2)(w'+0.3)(w'+6)(w'^2+20w'+324)}{w'^2(w'+0.02)(w'^2+500w'+250000)} \tag{4.9}$$

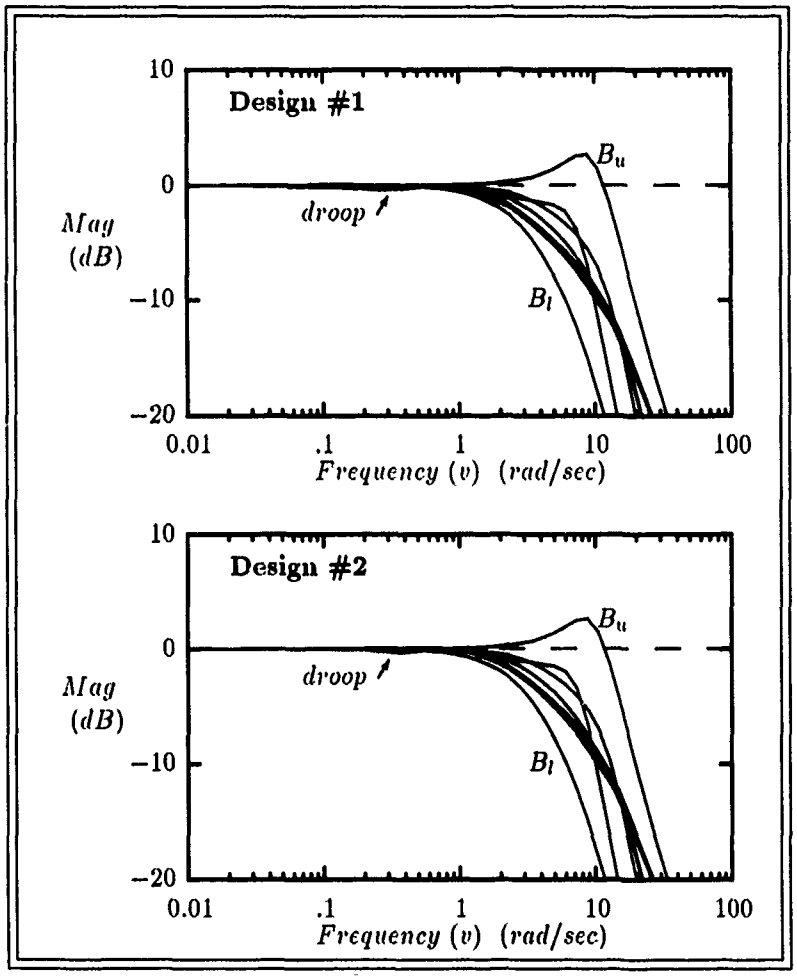

Figure 4.9. $f_{1,1}l_i/(1+l_i)$ Design #1 and #2 Pitch-Rate Channel Filtered Frequency Responses for Plant Cases 1–6

$$\textit{Type } 0 \quad \Rightarrow \quad f_{1,1}(w') = \frac{0.003(w'+1000)}{(w'+3)} \tag{4.10}$$

$$\textit{Design } \#1 \ \& \ 2 \quad \Rightarrow \quad f_{1,1}(w') = \frac{0.0012(w'+100)(w'+500)}{(w'+4)(w'+15)} \tag{4.11}$$

Since, for this design, $w' \approx s$, the bilinear transformation of Equation 3.4 is used to transform g_1 and $f_{1,1}$ to the z-plane. Appendix F contains all the z-plane representations of g_1 and $f_{1,1}$ and their difference equations for implementation.

The Tustin or bilinear transformation of the w′-plane compensators and prefilters to the z-plane is the last step in completing the loop design. Equation 3.4 is used to obtain the z-plane compensators and prefilters. It is important that the frequency responses of both the w′and z-plane elements be essentially equal out to $\omega_s/3$ (rad/sec). For this loop design and the MISO loop designs of the lateral system, this is checked and found to hold for all compensators and prefilters designed in this study. Figure 4.10 shows the z-plane and w′-plane frequency responses for g_1 of design #1 and illustrates this requirement.

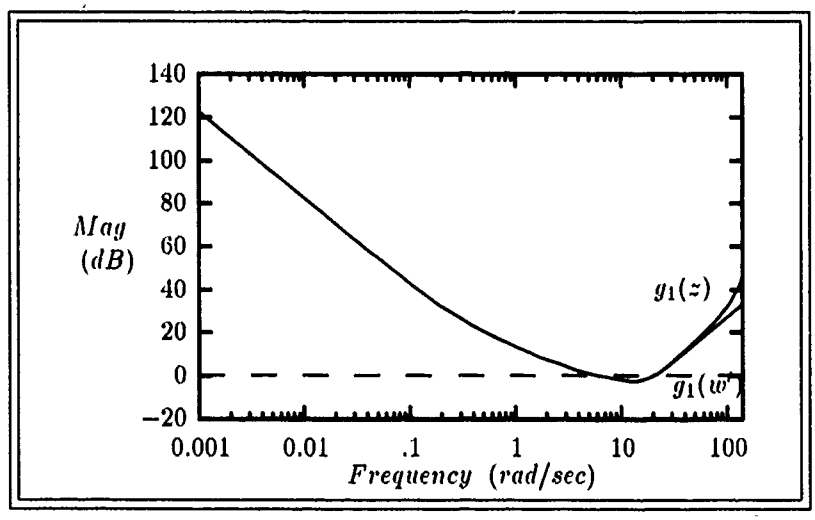

Figure 4.10. g_1 Design #1 z-plane and w′-plane Magnitude Frequency Response

4.2 Yaw-Rate (r) MISO Equivalent Loop Design

The lateral modes of the Lambda model are decoupled from the longitudinal modes, however, the subscripts on variables denoting the original and full 3x3 MIMO system are retained for continuity of the continuing design discussion. Subscripts of 3 and 2 for the yaw-rate and roll-rate loops respectively are used.

The improved QFT MISO design procedure is used for the 2x2 MIMO lateral system. The selection of the first MISO loop to shape is a subjective decision governed by the requirements specified in Chapter III. Very simply, the lowest bandwidth MISO equivalent loop is shaped first. Sometimes it's not altogether obvious which loop this may be. Bode plots of the $\mathbf{Q}(w')$ matrix elements $q_{i,i}(w')$ for all plant cases and the MISO equivalent loop templates are used to help make this decision. The Bode plots of the $q_{i,i}$ elements serve to display the magnitude and phase uncertainty explicitly as a function of frequency v. It is difficult to obtain a quantitatively complete picture of the loop uncertainty and its comparison to another channel loop with only Bode plots. The loop templates, on the other hand, are plots of the magnitude variation vs. the phase variation at a given frequency v_k and thus frequency v is implicit in the template plot. The area enclosed in a template describes the uncertainty of the plant at a frequency v_k. The area enclosed by the plant templates quantifies the uncertainty of a particular MISO channel loop. This area is compared to the other MISO channel loops for resolving bandwidth issues. Appendix E Figures E.3 and E.4 on pages E-12 and E-17 show plots of the roll-rate and yaw-rate MISO loop templates respectively. It is easy to see from those template plots that the yaw-rate channel is the smaller bandwidth loop since the total area enclosed by all its templates is much smaller than the roll-rate MISO loop. This conclusion is also reached using Bode plots since the phase and magnitude uncertainty in yaw is low at high and low frequencies unlike in the roll channel where low frequency uncertainty is substantially higher. Figure 4.11 shows the Bode plots used in the bandwidth determination. The yaw-rate channel is selected as the first loop to design in the lateral MIMO system.

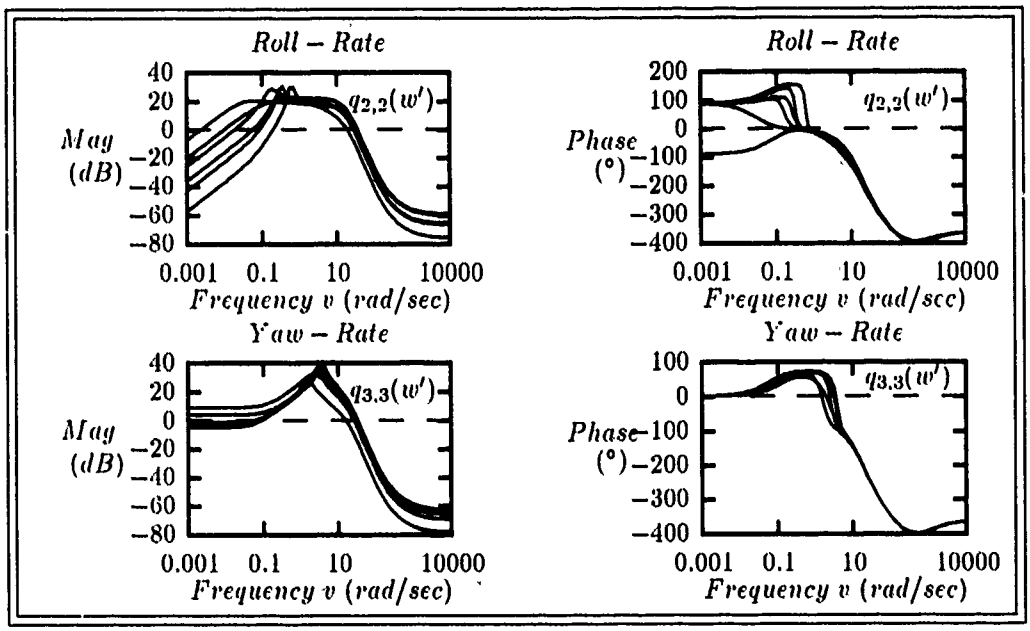

Figure 4.11. Roll-Rate and Yaw-Rate MISO Loop Channel Uncertainty With Bode Plots of $q_{2,2}(w')$ and $q_{3,3}(w')$ For Plant Cases 1-6

Similar to the pitch-rate channel design, plant case #1 is also selected as the nominal plant for this loop so that again $\mathbf{P}_o = \mathbf{P}_1$. Appendix E contains the template data and templates used for this loop shaping. The nominal loop transmission for the yaw-rate channel is:

$$l_{o_3}(w') = g_3(w')\, q_{o_{3,3}}(w') \tag{4.12}$$

$$q_{o_{3,3}}(w') = \frac{1.29993e{-}4\,(-0.066135)(120)(-140.0997)(155.5963)(-935.7121)}{(-0.4265\pm j1.4601)(-12.8472\pm j12.6911)(-47.3705)} \tag{4.13}$$

The Type 1 loop transmission requirement applies to this loop also so that, since $q_{o_{3,3}}$ has no free poles or zeros, g_3 must have one free pole. The initial loop transfer function is:

$$l_{o_3}(w') = \frac{1}{w'}\, q_{o_{3,3}}(w') \tag{4.14}$$

The phase margin bounds and the loop transmission of Equation 4.14 are shown on the NC in Figure 4.12.

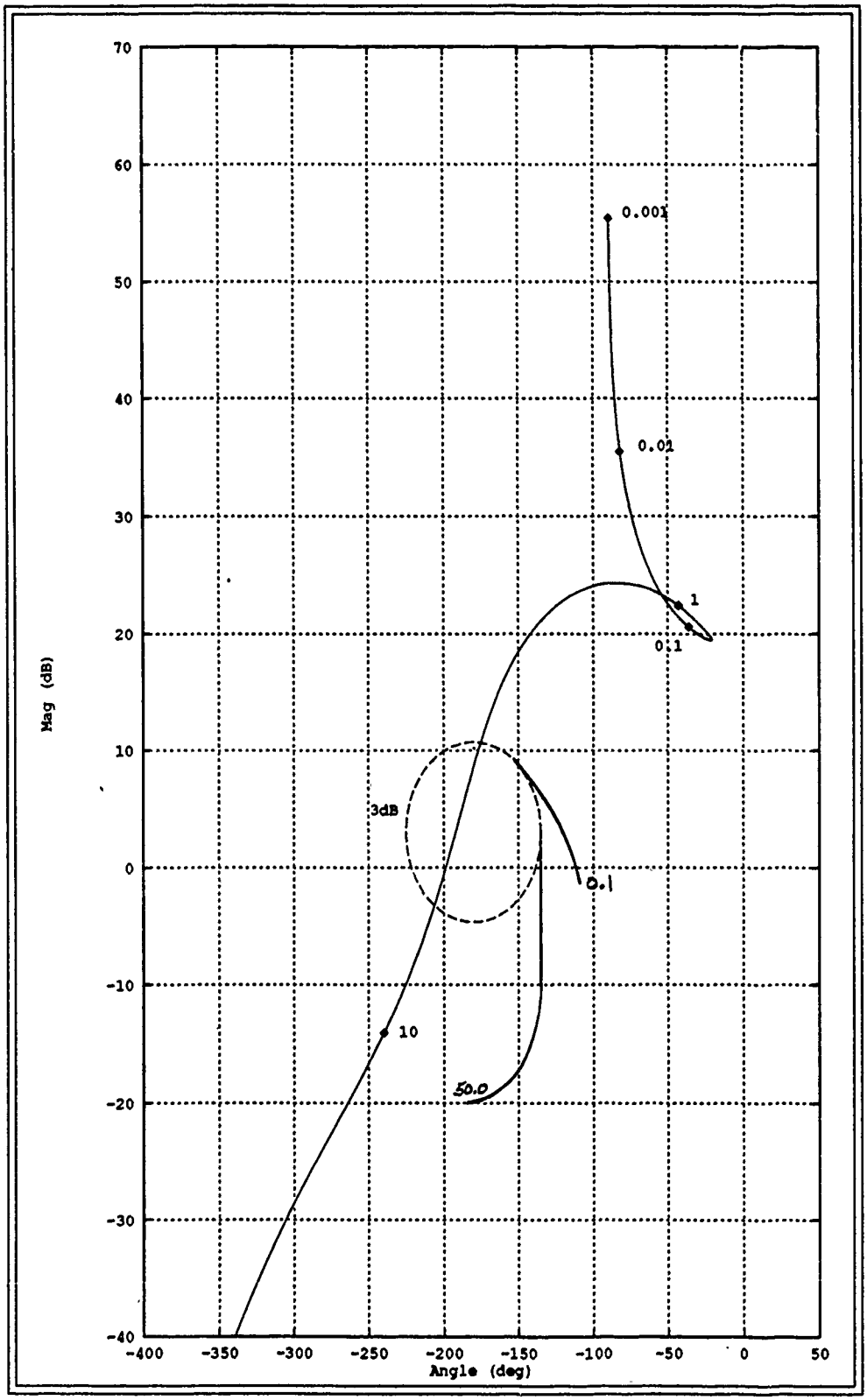

Figure 4.12. Yaw-Rate Loop ($q_{3,3}$) Phase Margin Bounds and Loop Transmission $l_{v_3}(w')$ For $g_3(w') = 1/w'$

The loop transmission synthesis follows similarly as for the previous pitch-rate loop. The Bode plot analysis used in this loop design is not shown but it is again emphasized that the use of Bode plots in conjunction with the NC make the loop transmission synthesis much easier. Here also, low frequency lead compensation is needed and is apparent from the NC in Figure 4.12. The $g_3(w')$ designed for this loop is:

$$g_3(w') = \frac{223(w'+4.5)(w'^2+20w'+324)}{w'(w'^2+500w'+250000)} \tag{4.15}$$

This compensated loop transmission is shown on the NC in Figure 4.13.

Again, as in the previous loop design, a *droop* range of frequencies exists in the loop transmission, however, the *drooping* is not as pronounced as in the pitch-rate channel. Compensation is applied in that range of frequencies to decrease the magnitude *drooping* and design #2 for $g_3(w')$ becomes:

$$g_3(w') = \frac{223(w'+4.5)(w'^2+20w'+324)}{w'(w'^2+500w'+250000)} \frac{(w'+0.3)}{(w'+0.009)} \tag{4.16}$$

The NC in Figure 4.14 shows the design #2 compensated loop transmission.

The filter design procedure is identical to the previous loop and the filter transfer function is the same for design #1 and #2 since the high frequency plant characteristics are not altered by the low frequency *droop* compensation added. The filter required for the yaw-rate channel is:

$$f_{3,3}(w') = \frac{0.004(w'+200)}{w'+0.8} \tag{4.17}$$

With design #1, some *droop* frequency v_k tracking bounds are not met. This is apparent in the step response yaw-rate loop simulation verifications in Appendix G Figure G.3. Design #2, on the other hand, meets all performance bounds and thus, in the verification plots in Appendix G,

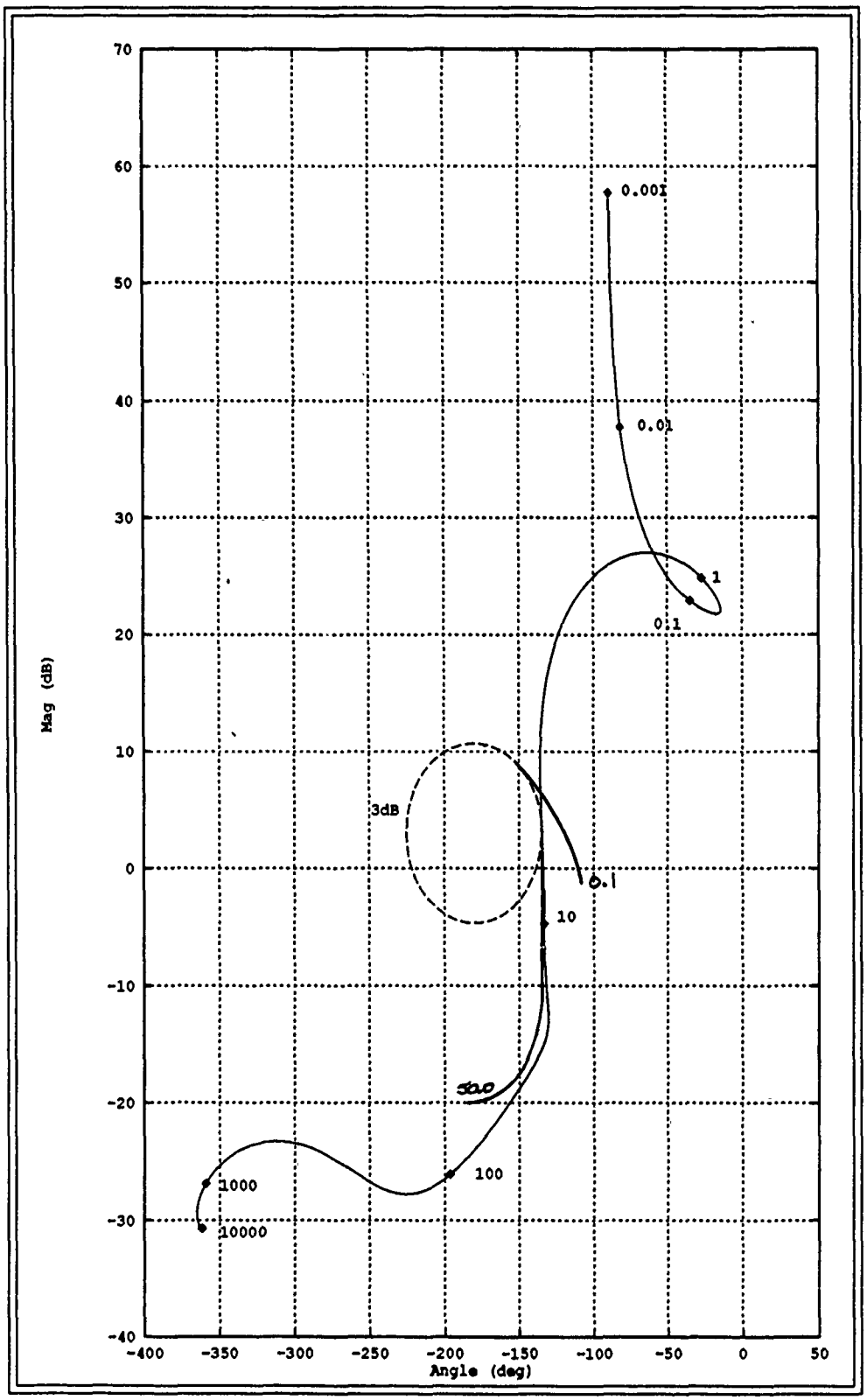

Figure 4.13. Yaw-Rate Loop ($q_{3,3}$) Phase Margin Bounds and Loop Transmission $l_{v_3}(w')$ For $g_3(w')$ Design #1

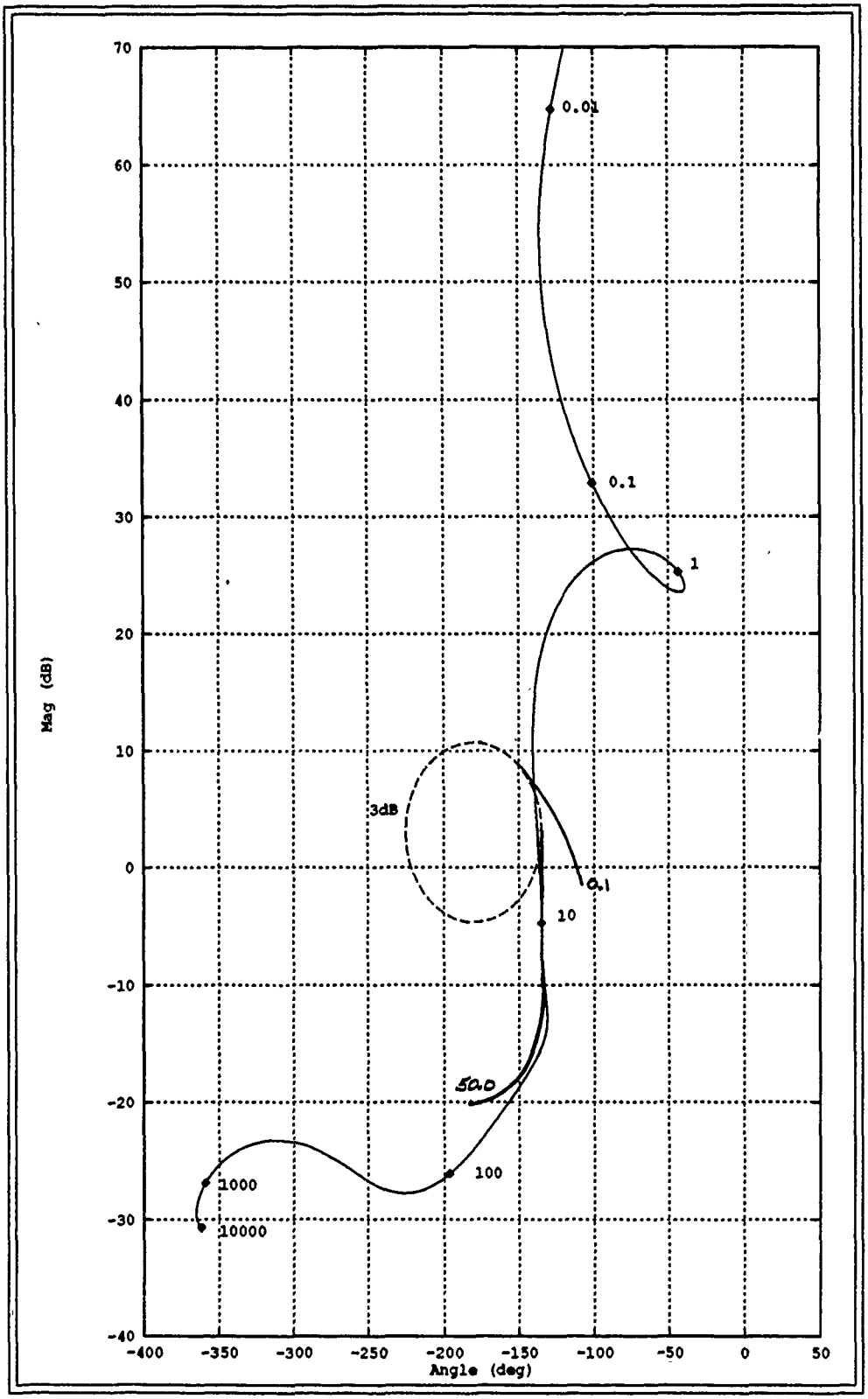

Figure 4.14. Yaw-Rate Loop ($q_{3,3}$) Phase Margin Bounds and Loop Transmission $l_{o_3}(w')$ For $y_3(w')$ Design #2

remains within the specified performance bounds.

The yaw-rate channel w'-plane designs are:

$$\textit{Design \#1} \quad \Rightarrow \quad g_3(w') = \frac{223(w'+4.5)(w'^2+20w'+324)}{w'(w'^2+500w'+250000)} \tag{4.18}$$

$$\textit{Design \#2} \quad \Rightarrow \quad g_3(w') = \frac{223(w'+0.3)(w'+4.5)(w'^2+20w'+324)}{w'(w'+0.009)(w'^2+500w'+250000)} \tag{4.19}$$

$$\textit{Design \#1 \& \#2} \quad \Rightarrow \quad f_{3,3}(w') = \frac{0.004(w'+200)}{w'+0.8} \tag{4.20}$$

The difference equations for implementing these designs are presented in Appendix F.

4.3 Roll-Rate (p) MISO Equivalent Loop Design

The improved QFT loop design procedure is used for the final roll-rate MISO loop transmission shaping. For each plant case i the effective loop transmission, denoted $l^i_{2_e}(w')$ is:

$$l^i_{2_e}(w') = g_2(w')\, q^i_{2,2_e}(w') = g_2(w')\, q^i_{2,2}(w') \frac{1 + g_3 q^i_{3,3}(w')}{1 + g_3 q^i_{3,3}(w') - \gamma^i_{3,2}(w')} \tag{4.21}$$

$$= g_2(w')\, q^i_{2,2}(w') \frac{1 + l^i_3(w')}{1 + l^i_3(w') - \gamma^i_{3,2}(w')} \tag{4.22}$$

where

$$\gamma^i_{3,2}(w') = \frac{p^i_{3,2}(w') p^i_{2,3}(w')}{p^i_{3,3}(w') p^i_{2,2}(w')} \tag{4.23}$$

Plant case #1 is nominal for this loop shaping so that the nominal loop is:

$$l_{o_{2_e}}(w') = g_2(w')\, q^1_{2,2}(w') \frac{1 + l^1_3(w')}{1 + l^1_3(w') - \gamma^1_{3,2}(w')} \tag{4.24}$$

$$= g_2(w')\, q^1_{2,2_e}(w') = g_2(w')\, q_{o_{2,2(e)}}(w') \tag{4.25}$$

The loop transmission is shaped by generating the effective nominal plant element $q_{o_{2,2(e)}}(w')$ with $\gamma_{o_{3,2}}(w')$ and $l_{o_3}(w')$. Bode plots of γ_o and $(1+l_{o_3})/(1+l_{o_3}-\gamma_o)$ in Figures 4.15 and 4.16 illustrate these relations.

Figure 4.17 shows the comparison of the resulting $q_{o_{2,2(e)}}$ with $q_{o_{2,2}}$. Notice there is very little difference between the effective MISO nominal plant element and the original indicating that very little correlation exists between nominal yaw loop design and the nominal roll loop plant element. In fact, generation of the effective roll loop plant elements $q^i_{2,2_e}$ for all plant cases showed similar relations and thus are not shown here.

In spite of the small difference in the effective plant elements, and in the interest of completeness, the $q^i_{2,2_e}$ elements are used in the roll-rate channel design. Appendix E contains the effective

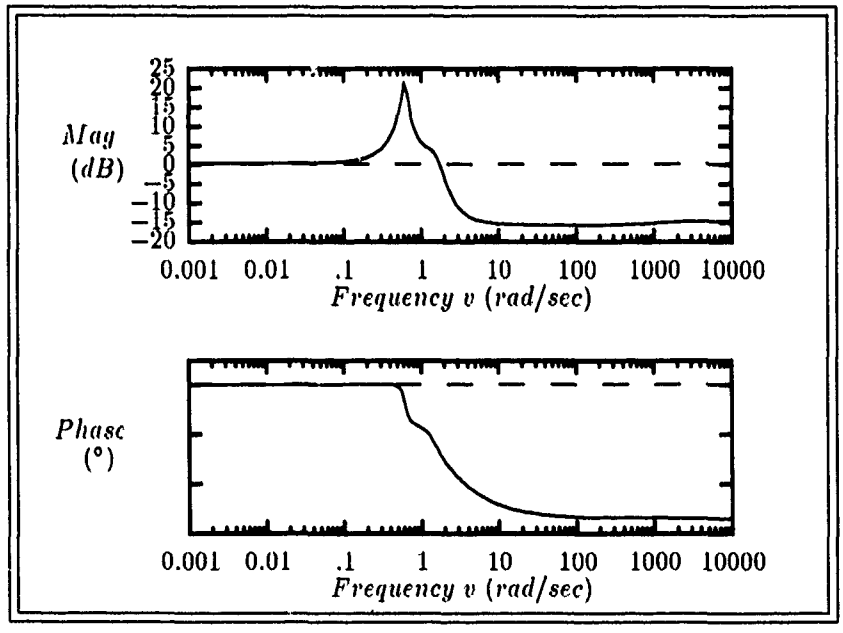

Figure 4.15. Roll-Rate MISO Loop Nominal $\gamma_o(w')$

plant element ($q^i_{2,2_e}$) generated templates used in this loop shaping.

The nominal loop plant element $q_{o_{2,2(e)}}(w')$ is shown in tabular form in Table 4.1.

For a Type 1 loop transmission, g_2 must have 2 poles at the origin so that the initial loop transfer function is:

$$l_{o_{2(e)}}(w') = \frac{1}{w'^2} q_{o_{2,2(e)}}(w') \tag{4.26}$$

The phase margin bounds and loop transmission of Equation 4.26 are shown on the NC in Figure 4.18. This is the starting point of the loop shaping.

The *droop* problem is present in this design also as for the previous two loops and so two designs are synthesized. Prefilter design is accomplished as usual and only one prefilter is needed

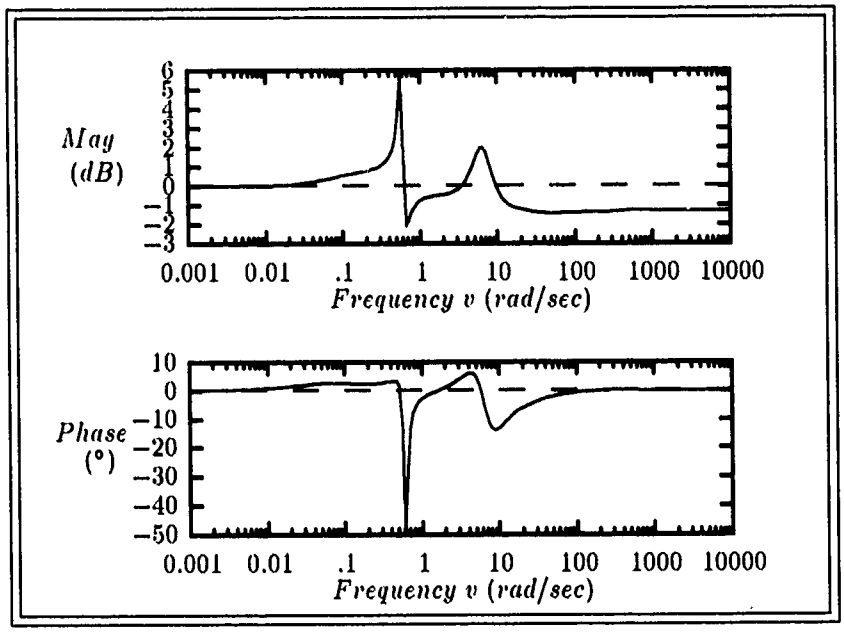

Figure 4.16. Roll-Rate MISO Loop Nominal $(1 + l_{o_3}(w'))/(1 + l_{o_3}(w') - \gamma_o(w'))$

for both designs. The controllers (g_2) and prefilter ($f_{2,2}$) for the two designs are:

$$\textit{Design \#1} \quad \Rightarrow \quad g_2(w') = \frac{3.55(w' + 0.1)(w'^2 + 16w' + 100)}{w'^2(w' + 500)} \tag{4.27}$$

$$\textit{Design \#2} \quad \Rightarrow \quad g_2(w') = \frac{3.55(w' + 0.1)(w' + 0.3)(w'^2 + 16w' + 100)}{w'^2(w' + 0.009)(w' + 500)} \tag{4.28}$$

$$\textit{Design \#1 \& \#2} \quad \Rightarrow \quad f_{2,2}(w') = \frac{0.125(w' + 20)}{w' + 2.5} \tag{4.29}$$

The compensated loop transmissions are shown on the NCs in Figures 4.19 and 4.20. The difference equations for implementing these designs are presented in Appendix F.

4.4 Discussion

4.4.1 NMP Loop Shaping. It was recognized from the start that the phase lag from the NMP w'-plane nominal plant elements $q_{o_{i,j}}$ and the effector actuator and rate sensor model poles would place an upper bound on the maximum achievable loop transmission and thus the maximum loop gain. As previously discussed, the tracking and channel interaction disturbance rejection

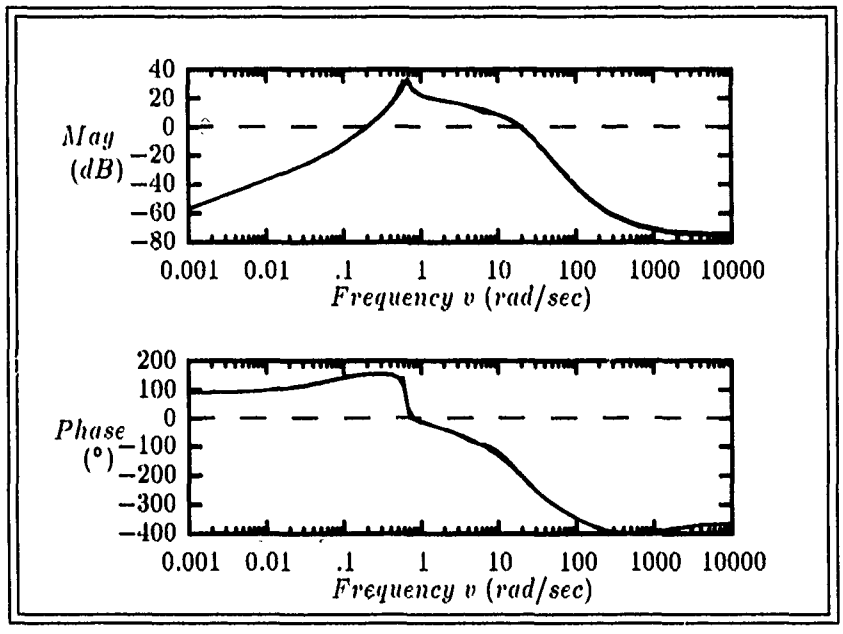

Figure 4.17. Roll-Rate MISO Loop Nominal Plant Element $q_{o_{2,2}}(w')$ vs. $q_{o_{2,2(c)}}(w')$ Comparison

performance achievable is subject to this limitation on loop transmission. The loop transmissions in each of the MISO channels described in this chapter are maximized subject to the phase margin bounds and the limitations imposed by the NMP elements and the effector actuator and sensor model poles. To that extent, the performance achieved with these channel designs is the best that can be expected.

4.4.2 Bandwidth Specifications. In general, a system model is developed with implicit limitations. Many systems may have higher order structural modes that are ignored in the model development under the assumption that the control system will operate at frequencies that do not excite any significant response from these modes. Thus, most systems have inherent bandwidth limitations because of this. It's of interest then to give specifications on the bandwidth of the control system design. The higher order structural modes on Lambda are estimated to be quite high and well above any frequency achieved by the digital NMP loop transmissions. Table 4.2 gives the loop transmission crossover frequencies for each MISO loop channel.

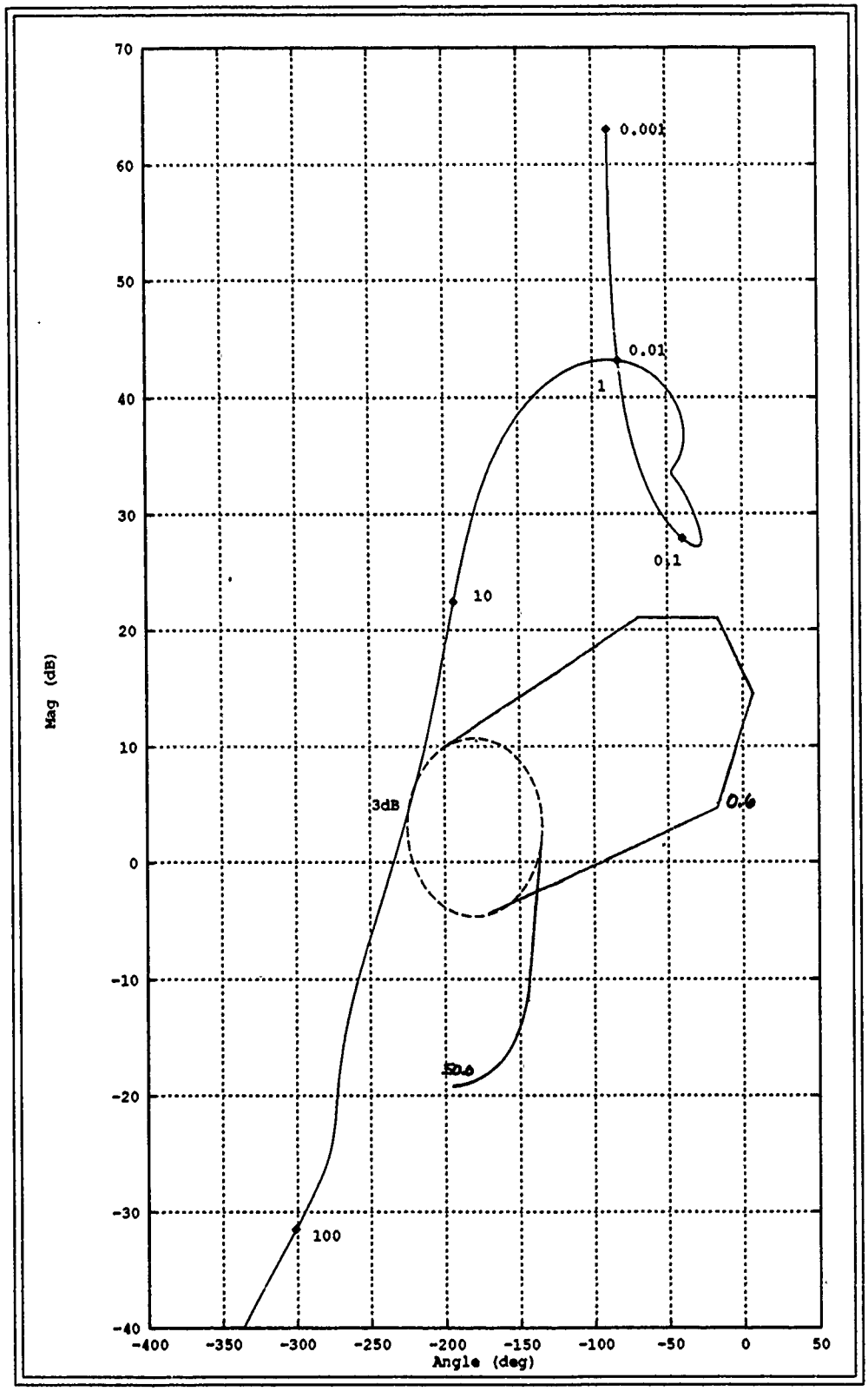

Figure 4.18. Roll-Rate Loop ($q_{2,2_e}$) Phase Margin Bounds and Loop Transmission $l_{o_{2_e}}(w')$ For $g_2(w') = 1/w'^2$

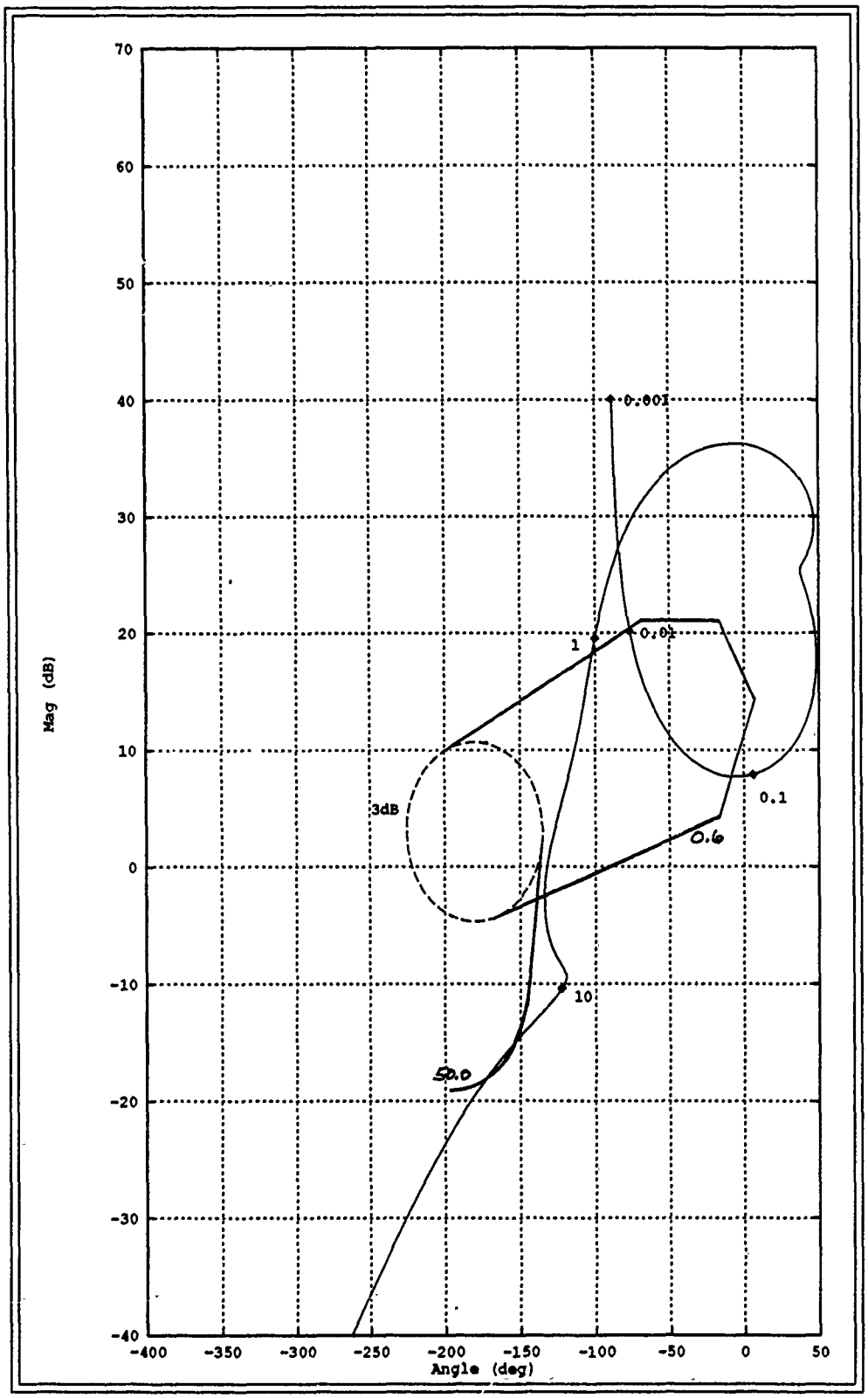

Figure 4.19. Roll-Rate Loop ($q_{2.2_c}$) Phase Margin Bounds and Loop Transmission $l_{v_{2c}}(w')$ For Design #1

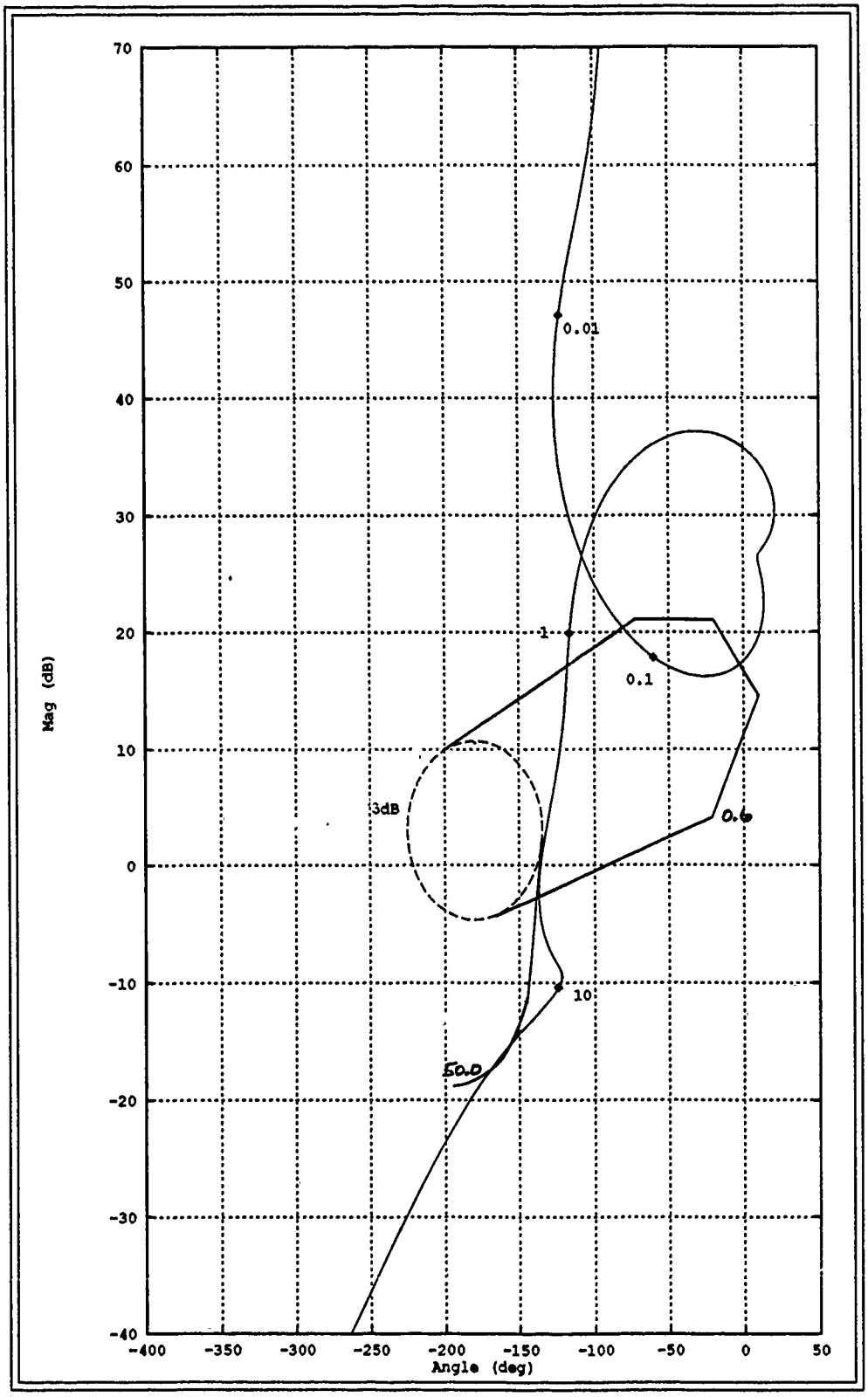

Figure 4.20. Roll-Rate Loop ($q_{2,2_c}$) Phase Margin Bounds and Loop Transmission $l_{v_{2_c}}(w')$ For Design #2

Table 4.1. Roll-Rate Nominal Plant Element Transfer Function Roots Listing $q_{o_{2,2(e)}}(w')$

Numerator Roots	Denominator Roots
0.0	−0.060926
−0.066135	$-0.047368 \pm j0.608091$
−0.066161	$-0.047368 \pm j0.608091$
$-0.029422 \pm j0.576535$	$-3.687902 \pm j0.0$
$-3.010474 + j0.000101$	$-3.404659 \pm j5.410768$
$-2.211016 \pm j5.864527$	$-12.849075 \pm j12.663185$
120.0	−47.123026
−140.099668	
155.596309	
−972.268112	

Table 4.2. Minimum & Maximum Crossover (Phase Margin) Frequencies For the MISO Loop Channels

Channel	v_ϕ Plant #1 (Min) (rad/sec)	v_ϕ Plant #2 & #3 (Max) (rad/sec)
l_1^l (q)	7.8	30
l_2^l (p)	4.0	10
l_3^l (r)	8.0	30

V. Design Simulation

This chapter describes the various simulations used to verify the design of the Lambda three-axis rate-commanded automatic flight control system. All simulations performed in this study are done with the Matrix$_x$ CAD/CAE program on a SUN III workstation. All applicable simulation plots are presented in Appendix G. The block diagrams depicting each method of simulation are presented in the following sections along with a final section summarily presenting the pertinent simulation results and final system specifications.

5.1 An Engineering Philosophy

Engineering design *always* requires approximation. Why? Because, "*mother nature*" is <u>*never*</u> "*truly*" as even the most complex and comprehensive mathematical description would have it. Sometimes the mathematical description of a physical phenomenon is so close to the natural manifestation of the phenomenon that the difference is imperceptible. Many times, though, the *accurate* mathematical descriptions required to match nature are impractical for design synthesis or analysis and so suitable approximations are made. Physical modeling errors judged to be insignificant or compensatable are even admitted to facilitate a tractable engineering solution. In the final analysis, "*mother nature*" rules and the engineering solution must obey her rules. Simulation in flight is the "final analysis" in flight control system engineering.

Two types of simulations are considered, design synthesis technique verification and "truth" model or "mother nature" comparison. The w'-plane simulations described below are design synthesis verifications. They verify proper execution of the design technique. The hybrid simulations are the "truth" model comparisons used in this study. It is good engineering practice to simulate the final engineering solution against the *best* available *truth* model. For this study, the linearized continuous-time EOM are the *truth* model. It is also good practice to recognize the limitations of the results derived from the simulations since it would obviously be better to test the design in

flight. This linearized Lambda model is judged to be very close to "true" since Lambda is basically a statically stable open-loop aircraft with relatively docile flying characteristics as opposed to the very nonlinear and highly dynamic flying characteristics of a modern fighter aircraft.

The nonlinear Lambda EOM are a better *truth* model. These equations, implemented on an analog computer like the SIMSTAR computer, would provide the *best* comparison to the "true" conditions of flight without actually flight testing the design. Lambda's nonlinear EOM are not presently available. They would have to be derived from flight test data of the aerodynamic derivatives which are also not available. Derivation of these equations would, in any event, be beyond the scope of this thesis.

The *best* "true" testbed is the aircraft itself. The validity of the linearized EOM and all the other approximations that resulted in the linearized system representation will be clear as a result of flight testing. Flight testing is a major undertaking and also beyond the scope of this work. It is planned that this flight control system will be implemented and flown at a later date and thus its "true" performance will then be seen.

5.2 w' Loop Transmission Design Verification

Each QFT loop design is simulated to verify the synthesized loop transmission $l_i(w')$. The block diagram implemented in Matrix$_x$ is shown in Figure 5.1.

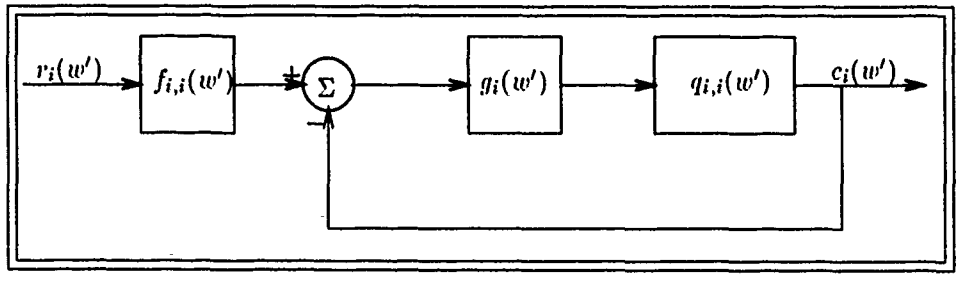

Figure 5.1. Filtered w'-plane Loop Transmission Response Configuration

Step inputs are applied to the system in Figure 5.1 for $i = 1, 2, 3$ and for each i, the system response $q_{i,i}$ for each plant case 1-6 is generated. Thus six system responses are generated for each channel. These verification responses are in Appendix G Figures G.1, G.2 and G.3. Since two designs are completed for each channel, simulations for both are shown. The Type 0 design for the pitch-rate channel is also shown there.

5.3 w' System Simulations

The loop transmission simulations in the previous section are SISO simulations with no disturbances and only verify proper design synthesis. The full MIMO w'-plane systems are simulated to verify both proper tracking performance and disturbance rejection with the MIMO interchannel interaction present. These simulations are conducted in accordance with Figure 5.2.

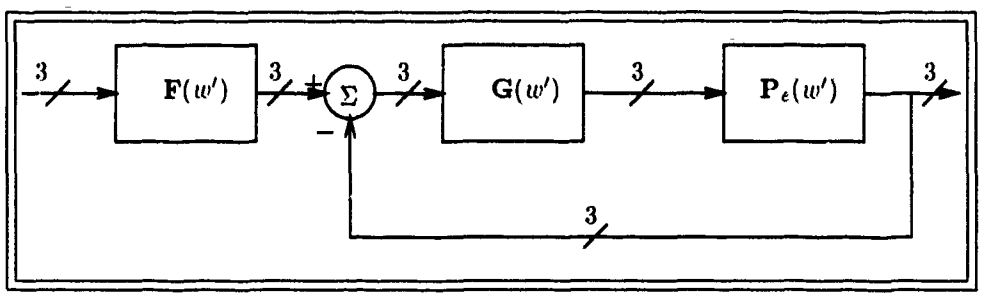

Figure 5.2. w'-plane MIMO System Simulation Configuration

These simulations are performed without amplitude limits on the control surfaces and proved to match nearly exactly, when the surfaces are not limiting, with the hybrid simulations described next. For this reason, these simulation results are not shown since they are equivalent to the hybrid simulations.

5.4 Hybrid System Noninteracting Simulations

Figure 5.3 shows the Matrix_x block diagram implementation for the hybrid single-channel excitation noninteracting simulations.

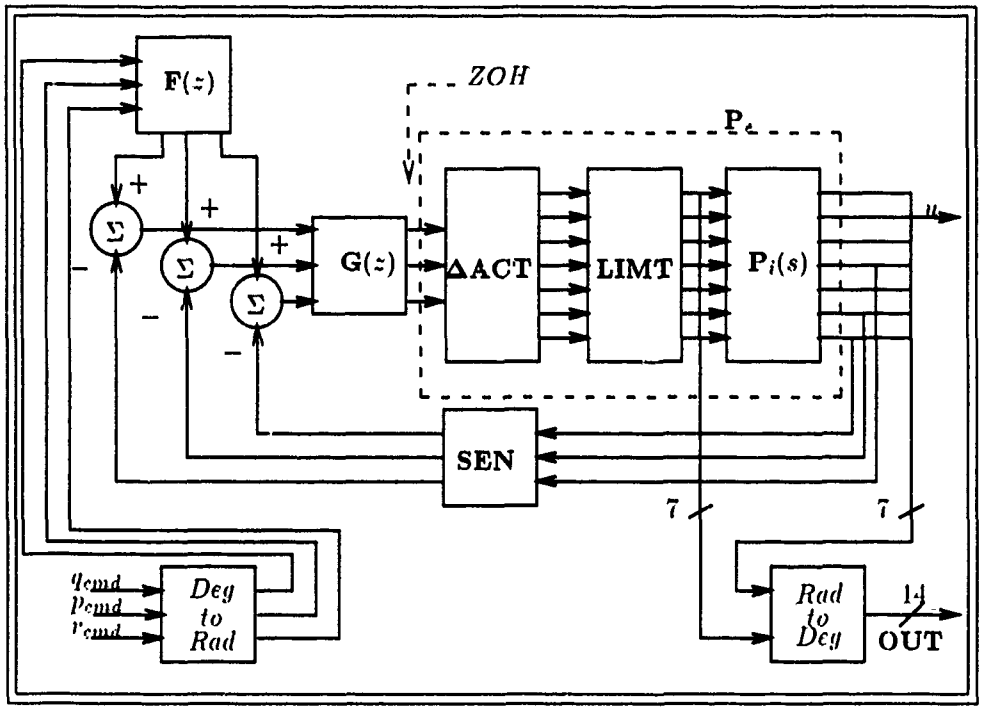

Figure 5.3. Hybrid Nonlinear (Effector Amplitude Limiting) Lambda MIMO System Simulation Configuration With z-plane Controllers and Prefilters and s-plane Aircraft Plant, Actuators and Sensors

The command inputs q_{cmd}, p_{cmd}, and r_{cmd} are applied in units of (deg/sec) and converted to (rad/sec) immediately at the simulation input and back to (deg/sec) just before output. The automatic flight control system requires (rad/sec) internally. The $\mathbf{F}(z)$ and $\mathbf{G}(z)$ blocks in the simulation contain the discretized w'-plane QFT designed prefilters and controllers respectively. The **ΔACT** block contains the weighting matrix elements and the continuous effector actuator models. Amplitude limits specified in Chapter II on page 2-5 are implemented in the **LIMT** block. Amplitude limited effector angles are also outputs of the simulation. The continuous plants $\mathbf{P}_i(s)$ are used and the continuous rate-sensors are contained in the feedback block **SEN**.

Perturbation EOM are derived by linearizing a system about a nominal or *trim* flight condition. By definition, the initial conditions on the system states in a perturbation EOM set are zero, however, in the case of an aircraft system, the effector positions required to reach and maintain the

trim condition are not usually zero and thus, the effective amplitude limits on effector actuation for a given flight condition can be different. For example, plant #1 for flight condition #1 is a trim condition in slow flight at a high angle-of-attack where the elevator is deflected up significantly. Obviously, for this plant, further up elevator deflection is limited and any pitch-up maneuver will be subject to this limitation. Normally, a simulation is designed so that these effector deflection limits with trim deflections accounted for is used. These trim effector positions are not available for Lambda and are not used. For the subsequent simulations, it is assumed that each effector is not deflected (0°). This assumption is significant for plant case #1 only as described above. Trim effector deflections for the other five plant cases are not nearly as significant as for plant case #1. Thus, pitch-up maneuvers for plant case #1 may not be as simulated since the elevators will limit sooner than the simulations show. It should be noted here that this is not desirable since it would be much better to use the correct angle limits based on the trim effector positions in the simulations. However, knowledge of the trim effector positions is not required in the design procedure and thus does not change the design synthesis.

Recall that $\mathbf{P}_e(s)$ is transformed to the w′-plane with the data hold or ZOH assumption. Matrix$_x$ performs hybrid simulations of continuous and discrete system blocks by inserting a ZOH device between the output of a discrete system block driving a continuous system block. Figure 5.3 shows where the ZOH device is inserted by Matrix$_x$. The discussion in Chapter III outlines the reasons why it's not desireable to drive continuous systems with discrete signals.

The basic system plants $\mathbf{P}_i(s)$ for each flight condition are modified to provide, in addition to the desired controlled outputs of q, p, and r, all system state variables. Also, the amplitude limited effector angles are tagged as desired simulation outputs. This is shown in the block diagram as the simulation **OUT** vector such that **OUT** in system variables is:

$$\mathbf{OUT} = \begin{bmatrix} \theta & u & \alpha & q & \phi & \beta & p & r & \delta_{e_L} & \delta_{e_R} & \delta_{f_L} & \delta_{f_R} & \delta_{a_L} & \delta_{a_R} & \delta_r \end{bmatrix}^T \quad (5.1)$$

The results of these simulations are contained in Appendix G. Simulations are shown for a variety of inputs. Each rate channel is exercised individually for each of the three inputs below

- 15 second duration, 1°/sec rate pulse
- 1 second duration, 45°/sec rate pulse
- 1 second duration, 500°/sec rate pulse

and the resulting state variable and limited effector angle outputs are plotted in the Appendix G figures. Pitch-rate channel simulations do not include the lateral state responses of ϕ and β or the rudder and flap responses since they are all zero. Roll-rate and yaw-rate channel simulations do not include the longitudinal responses of θ, u, and α or the elevator responses since they are zero also. Note that numbers shown on the plots in Appendix G denote plant case numbers. Only those plant cases of particular interest are labeled.

5.5 Hybrid System Coordinated Turn Simulations

The single channel excitation of all the prior simulations serve to demonstrate the successful implementation of a three-axis rate-commanded automatic core flight control system for Lambda. This core system serves as the basic flight control system in allowing many possibilities for outer loop feedback control. The advantage of a noninteracting three-axis flight control system can't be stressed enough. It alone makes many future and versatile Lambda flight control system outer loop enhancements possible.

It is of interest now to see how the design performs in a normal more realistic maneuver. The longitudinal channel is decoupled from the two lateral channels in the linearized EOM system so further longitudinal simulation is basically unexciting. The lateral channel, however, is different. A coordinated turn requires simultaneous roll-rate and yaw-rate channel input. Simulation of an

extended multiple input maneuver like a constant-bank coordinated turn with no effector limiting problems adds further credibility to the design.

Turn coordination will be added to Lambda in the future and it's not known now just exactly how it will be implemented. Many different techniques exist and Blakelock [3] presents some in his book. For this simulation, Equation 4-10 in Blakelock [3:147] is used to provide an appropriate yaw-rate command input for the pilot selected bank angle.

$$r(t) = \frac{g}{V_T} \sin\phi(t) \tag{5.2}$$

A turn is coordinated when β (sideslip angle) remains small. The yaw-rate calculated in Equation 5.2 is approximate and the first simulations showed it is undercalculating r somewhat. Equation 5.2 is modified to correct this as follows:

$$r(t) = a \frac{g}{V_T} \sin\phi(t) \tag{5.3}$$

$$= a' \sin\phi(t) \tag{5.4}$$

The a' in Equation 5.4 is found such that β remains realistically small during the maneuver. The approximate nature of Equation 5.2 justifies the modification. Figure 5.4 shows the Matrix_x simulation block diagram for these simulations and the results are contained in Appendix G. Plant cases #1 and #2 are used for the coordinated turn maneuver simulations. Plant case #1 is the *slow speed* case where the aircraft is flying just above stall at 10° angle-of-attack. Plant case #2 is the other extreme or the *fast speed* case where the aircraft is flying at top speed with a small negative angle-of-attack. These cases represent the extremes of the modeled aircraft dynamics. Template data in Appendix E bears this out. Table 5.1 gives the a' used for Equation 5.4 in the simulations.

Table 5.1. Calculated Yaw-Rate Turn Coordination Gain a' And a For Plant Cases #1 and #2

Plant	a' (rad/sec)	ag/V_T (rad/sec)
1	0.4757	0.54
2	0.19	0.185

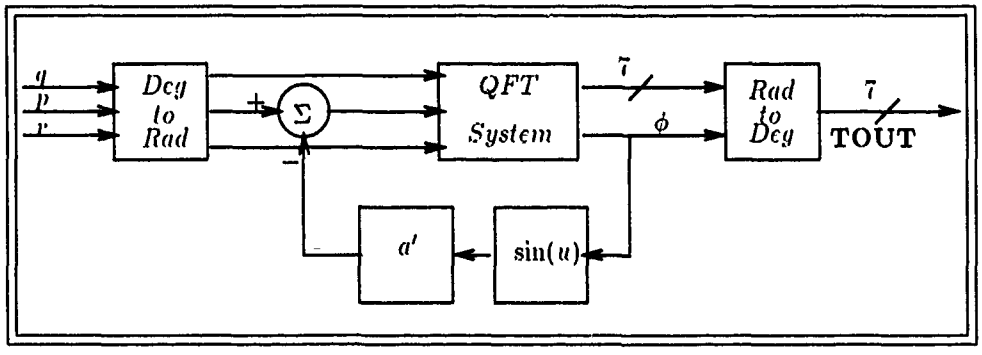

Figure 5.4. Hybrid Nonlinear (Effector Amplitude Limiting) Lambda MIMO System 45° Coordinated Turn Simulation Configuration With z-plane Controllers and Prefilters and s-plane Aircraft Plant, Actuators and Sensors and Approximate Computed Yaw-Rate Turn Coordination

5.6 Simulation Results

5.6.1 MISO Interchannel Disturbance Rejection. MISO interchannel disturbance rejection performance is usually assured in channel loop shaping by synthesizing the loop transmission subject to disturbance bounds in addition to the phase margin bounds and crossover constraints. Again here as mentioned above, the maximum achievable interchannel disturbance performance is subject to the loop gain achieved. For purposes of specifying the design, the worst case interchannel disturbance performance is given. It is derived from the worst case time history of a lateral 5 sec duration, 5°/sec simulation. Due to the decoupled lateral and longitudinal aircraft modes, interchannel responses are only applicable to the lateral system.

Plant case #1 is the worst-case for interchannel disturbance rejection such that all other plant cases have a greater interchannel disturbance rejection performance. The plots in Figure 5.5 show the interchannel disturbance responses to each lateral input for design #1. Tabulation of these

data and also the performance of design #2 are contained in Table 5.2. The figures for design #1 in the table are approximated from the lateral channel response plots in Figure 5.5. The figures for design #2 are generated similarly, however, the plots used are not shown. Approximate steady state performance is used.

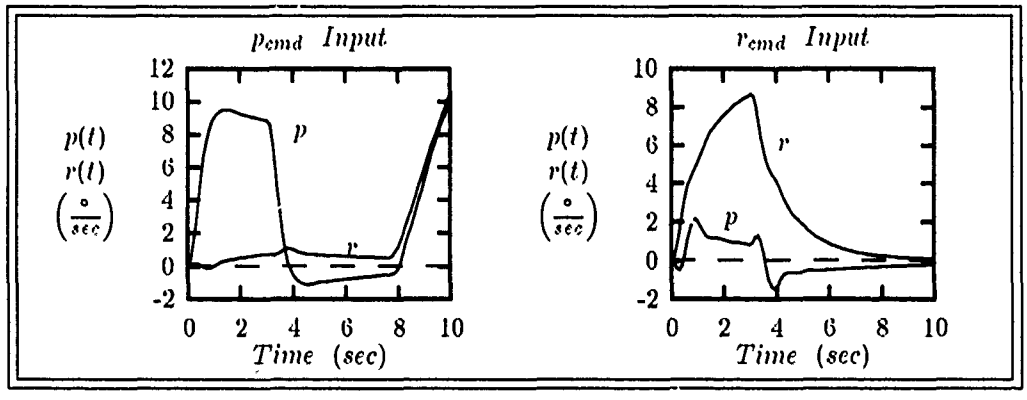

Figure 5.5. Plant #1 (Worst Case) Interchannel Disturbance Rejection Performance for a 3 sec Duration 10°/sec Input to the Lateral Channels

Table 5.2. Plant #1 (Worst Case) Interchannel Disturbance Rejection Performance for a 3 sec Duration 10°/sec Input to the Lateral Channels

Roll-Rate Channel Excitation	
Design #1	Design #2
$-18dB$	$-23dB$
Yaw-Rate Channel Excitation †	
Design #1	Design #2
$-16dB \Rightarrow -24dB$	$-20dB \Rightarrow -54dB$

† For the r_{cmd} input, the disturbance response (p) reaches steady state before r and thus the rejection response changes as r approaches steady state. The figures attempt to show this by giving the rejection specification when p first reaches steady state to when the input (r_{cmd}) is commanded to zero. Figure 5.5 shows that the rejection performance increases from the first steady state p value to the point when the input is commanded to zero.

5.6.2 Tracking Performance. The *a priori* specified tracking performance is achieved for the yaw-rate channel only. Steady state tracking performance is achieved for the pitch-rate and

roll-rate channels, however, the limitations imposed by the NMP transformation zeros, the other high frequency elements, and the desire for low order compensation make it impossible to achieve the gain required to meet the low frequency tracking bounds. Thus, even though maximum loop transmission is synthesized subject to all loop shaping constraints, the tracking bounds are still not met at some low frequencies for the pitch-rate and roll-rate channels.

The pitch-rate and roll-rate channel low frequency problem is a result of the characteristic large magnitude *drooping* present. On the NC, this appears as a large low frequency loop. The *drooping* in these two channels is significantly larger than in the yaw-rate channel where tracking specifications are met. This *drooping* could be removed if compensation order was not a concern. The easiest way to synthesize the loop then would be to include the NMP elements and any unstable poles in the nominal loop transmission synthesis and design the desired loop transmission with no concern for any other elements in the nominal plant $q_{o_{i,i}}$. Thus, g_i is formed by:

$$g_i = \frac{l_{o_i}}{q_{o_{i,i}}} \tag{5.5}$$

The compensator g_i synthesized in this way may be of significantly higher order and thus, for the purposes of this study, would not be implementable. Compensation of the *drooping* in this way does not guarantee that tracking bounds can be met. The maximum loop gain attainable subject to the loop shaping constraints may still be insufficient to ensure compliance with all tracking bounds.

VI. Wing Leveler Autopilot Design

This chapter presents a wing leveler autopilot design and simulation based on the implementation of the rate-commanded automatic flight control system designed for Lambda in this thesis. The specifications, design strategy, and simulation of the wing leveler are presented.

6.1 Background

A wing leveler, for the purposes of this study, is a feedback system designed to keep the aircraft roll attitude level with the horizon ($\phi = 0$) by returning the aircraft to the level roll attitude after a bank angle disturbance. A more complete roll attitude command system may include bank angle command in addition to a wing leveling function. It is natural and possible, due to the noninteracting nature of Lambda's QFT designed automatic flight control system, to use the roll-rate channel and the bank angle signal available to provide the wing leveler function.

A noninteracting system means that inputs to the individual channels do not couple to the other channels and produce responses. Thus, a three channel noninteracting system like Lambda can be represented by three decoupled SISO systems. This is a pleasing situation when considering outer loop feedback control since a MIMO design is much more complex in general. If the system was interacting, then additional feedback loops designed to quell the interaction dynamics may be required. In short, a MIMO design synthesis would be needed. For this wing leveler design, the SISO roll-rate channel is used.

The QFT synthesized Lambda automatic flight control system is depicted in Figure 6.1. On Lambda, bank angle ϕ is available from a vertical gyro sensor and thus it is shown as a secondary output in Figure 6.1. Bank angle ϕ is related to roll-rate p by the relation in Equation 6.1.

$$\dot{\phi}(t) = p(t) \tag{6.1}$$

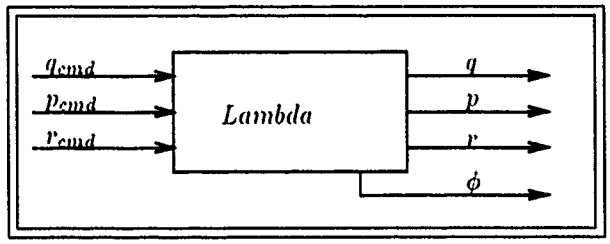

Figure 6.1 Lambda Three-Axis Noninteracting Rate-Commanded Automatic Flight Control System and Aircraft Block Diagram

In the s-plane, Equation 6.1 is:

$$\phi(s) = \frac{1}{s}\, p(s) \tag{6.2}$$

An integration of the roll-rate signal $p(t)$ will produce $\phi(t)$ with the appropriate initial conditions assumed.

Disturbances to ϕ enter the system in the pilot roll-rate p_{cmd} command input channel and at the bank angle output ϕ. External disturbance to bank angle is denoted as ϕ_d. Bank angle disturbances in flight can occur very rapidly and typically result from wind gusts, turbulence, air pockets, etc. In calm air, these disturbances may be small and easily handled by the pilot, but, in rough air, considerable pilot attention may be required to maintain the desired flight attitude. The whole point of a wing leveling function is to reduce pilot workload in maintaining the flight attitude to facilitate timely accomplishment of other cockpit tasks. It is best classified as a pilot assist function and not an aircraft stability augmentation system.

6.2 Performance Requirements

Section 3.1.1.5.2 of MIL-C-18244A [27] contains specifications for the design of various pilot assist functions including the wing leveling or roll attitude hold function. This standard requires that the selected roll attitude be maintained within a static accuracy of $\pm 0.5°$ with respect to the

gyro accuracy. It also requires that the transient roll response to a bank angle disturbance be *smooth* and *rapid* and that the aircraft return to level flight or to the preselected bank angle from a bank angle disturbance of 20° with one overshoot not exceeding 4° or 20% of the initial disturbance [27].

6.3 Design

The wing leveler function is added as outer loop control around the basic QFT automatic three-axis rate-commanded flight control system. The SISO roll-rate channel with a bank angle disturbance input ϕ_d added is shown in Figure 6.2.

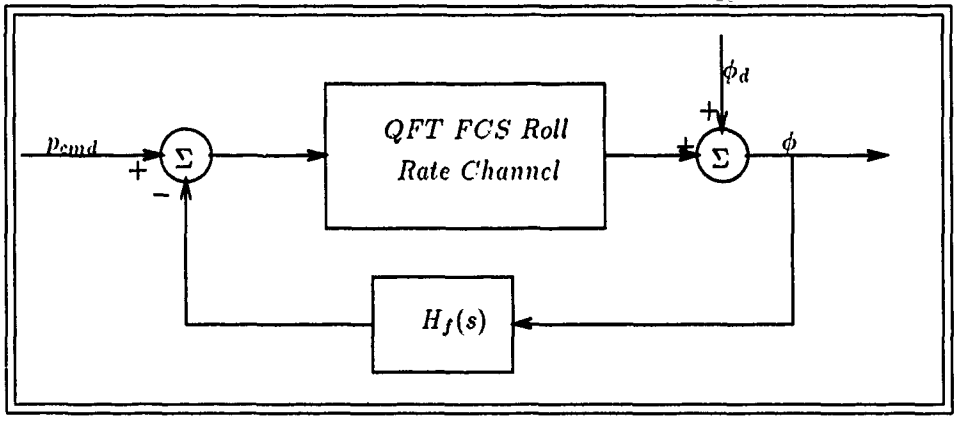

Figure 6.2. Outer Loop Wing Leveler Feedback Control Scheme

The MIL specification does not strictly quantify the value of a *rapid* return to level flight and thus leaves that detail to the designer. It is acceptable multiloop feedback design practice to enclose the higher bandwidth systems in the inner loops by the lower bandwidth outer loops. This design philosophy requires that the wing leveler outer loop be slower than the basic QFT roll-rate command system and the following specifications are established for the design:

- $T_r \approx 2$ sec
- $T_s \approx 6$ sec

- $\zeta > 0.707$

All assumptions and conditions for the s to w′ plane equivalence are the same as for the basic QFT flight control design so that $H_f(w') \approx H_f(s)$. The form of the feedback controller is $H_f(w') = K_\phi H_\phi(w')$ where H_ϕ is chosen to be a proper w′-plane transfer function of first order.

$$\frac{w' - z_1}{w' - p_1} \tag{6.3}$$

z_1 and p_1 in Equation 6.3 denote a stable (negative) zero and pole respectively.

The strategy is to design H_ϕ so that the closed-loop system possesses the second order system characteristics specified by the requirements above. These requirements yield the closed-loop dominant pole pair in Equation 6.4.

$$p_d \;=\; -u_d \pm jv_d \;=\; -0.67 \pm j0.60 \;\; rad/sec \tag{6.4}$$

The roll channel QFT system for all plant cases $\mathbf{P}_i$ is represented as:

$$\frac{p(w')}{p_{cmd}(w')} \;=\; \frac{f_{2,2}(w')g_2(w')q_{i_{2,2}}(w')}{1 + g_2(w')q_{i_{2,2}}(w')} \tag{6.5}$$

In the frequency range associated with the desired closed-loop pair (Equation 6.4), the roll channel QFT system is approximately:

$$\frac{p(w')}{p_{cmd}(w')} \;\approx\; f_{2,2}(w') \tag{6.6}$$

since $g_2(w')q_{i_{2,2}}(w') >> 1$ (see the roll-rate w′ frequency response bounds in Figure D.3 on page D-5 in Appendix D). The roll-rate prefilter dominates the aircraft response in this frequency range.

Lambda has a vertical gyro providing bank angle data from level flight and so, for the design

synthesis, and to satisfy the relation in Equation 6.2, an integrator is added. Figure 6.3 shows the equivalent w'-plane wing leveler design block diagram.

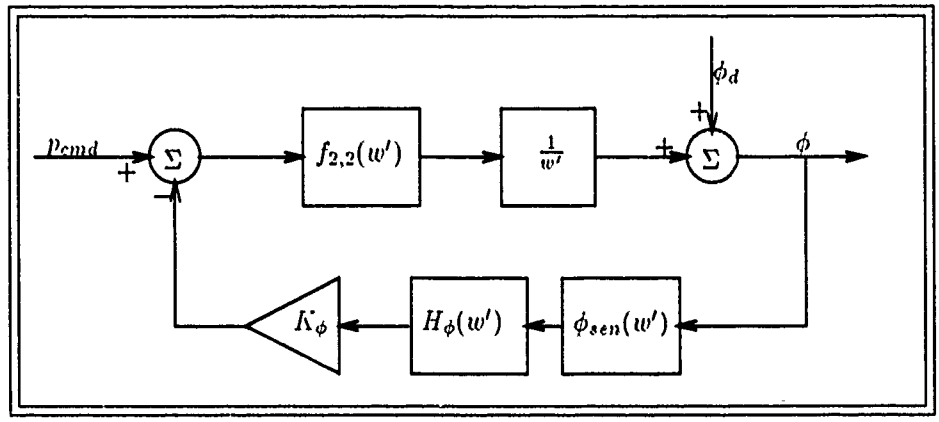

Figure 6.3. w'-plane Wing Leveler System Block Diagram

The elements shown in figure 6.3 are:

$$\phi_{sen}(w') = \frac{20}{w'+20} \tag{6.7}$$

$$\frac{f_{2,2}(w')}{w'} = \frac{0.125(w'+20)}{w'(w'+2.5)} \tag{6.8}$$

$$H_\phi(w') = \frac{w'-z_1}{w'-p_1} \tag{6.9}$$

Proper w'-plane transfer functions are not really needed for the integrator or the sensor in the ensuing design synthesis since, in the frequency range of interest, the difference between the above elements and proper w' transfer functions is insignificant. For the design, the commanded roll-rate input is assumed zero ($p_{cmd} = 0$) so that the feedback transfer function for the roll angle disturbance control ratio $\phi(w')/\phi_d(w')$ is:

$$t_{ol_\phi}(w') = \phi_{sen}(w')\, H_\phi(w')\, K_\phi\, f_{2,2}(w')\, \frac{1}{w'} \tag{6.10}$$

$$= \left[\frac{20}{w'+20}\right]\left[\frac{K_\phi(w'-z_1)}{w'-p_1}\right]\left[\frac{0.125(w'+20)}{w'+2.5}\right]\left[\frac{1}{w'}\right] = \frac{N}{D} \tag{6.11}$$

where

$$\frac{\phi(w')}{\phi_d(w')} = \frac{1}{1+t_{ol_\phi}(w')} = \frac{D}{D+N} \tag{6.12}$$

Standard root locus analysis is used to chose z_1 and p_1 to realize the dominant second-order closed-loop pole pair of Equation 6.4. The $H_\phi(w')$ and K_ϕ synthesized is:

$$H_\phi(w') = \frac{w'+5}{w'+1.5} \tag{6.13}$$

$$K_\phi = 0.2 \tag{6.14}$$

The disturbance control ratio with the H_ϕ and K_ϕ of Equation 6.14 is:

$$\frac{\phi(w')}{\phi_d(w')} = \frac{(w')(w'+1.5)(w'+2.5)}{(w'+0.5993 \pm j0.7303)(w'+2.8015)} \tag{6.15}$$

A few issues are worth mentioning at this point about the design. First, for the specific structure of H_ϕ, it is desirable but not a requirement to achieve a low order compensator. H_ϕ could be more complex and for some problems may have to be to achieve the desired closed-loop system. For Lambda, the first order compensator is enough. Second, the worst case sensor model is used, however, its inclusion had an insignificant effect on the compensator pole/zero placement. Third, wing leveler activation alters the roll-rate input to the aircraft. Instead of a pure pilot roll-rate command, the aircraft roll-rate channel input is an error signal difference between the pilot input and the wing leveler correction signal which is directly proportional to the bank angle. Since the wing leveler dynamics are slower than the inner roll-rate command loop, it is possible for the pilot to *overpower* the wing leveler while it is activated in order to make a heading change or perform some other maneuver. Upon removing the pilot input, the wing leveler returns the aircraft to the level bank angle flight condition. This is a desirable and mandatory requirement for an

attitude pilot assist function.

$H_f(w')$ is transformed to the z-plane with the bilinear transformation of Equation 3.4. The resulting z-plane controller is:

$$H_f(z) = \frac{0.20576(z-0.92)}{(z-0.97531)} \quad (6.16)$$

$$= \frac{0.20576z-0.18930}{z-0.97531} \quad (6.17)$$

$$= \frac{0.20576-0.18930z^{-1}}{1-0.97531z^{-1}} \quad (6.18)$$

For $H_f = Y/R$:

$$Y(z)\left[1-0.97531z^{-1}\right] = R(z)\left[0.20576-0.18930z^{-1}\right] \quad (6.19)$$

The difference equation for implementing H_f is:

$$y(kT) = +0.97531\,y[(k-1)T] + 0.20576\,u(kT) - 0.18930\,u[(k-1)T] \quad (6.20)$$

6.4 Simulation

All simulations of the wing leveler design are performed on Matrix$_X$. Verification of the H_f design is accomplished by simulating the wing leveler w'-plane design in accordance with the block diagram in Figure 6.3. The design verification is accomplished by setting a 20° initial condition on the output integrator to simulate an impulse bank angle disturbance and setting the command input to zero ($p_{cmd} = 0$). Figure 6.4 shows the results of this simulation. The ability to *overpower* the activated wing leveler is simulated in Figure 6.5 by setting a zero integrator initial condition and applying a nonzero roll-rate command p_{cmd}. In this simulation, a 1 second duration, 20°/sec roll-rate input is applied to simulate a pilot command input during wing leveler operation.

Hybrid simulation of the wing leveler is done to verify the z-plane implementation of H_f.

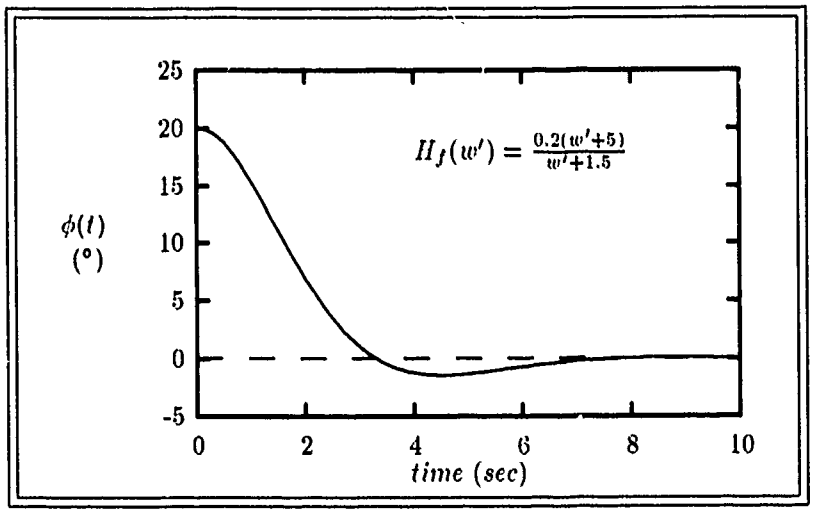

Figure 6.4. w′-plane Wing Leveler Response to a 20° Initial Condition Bank Angle Disturbance

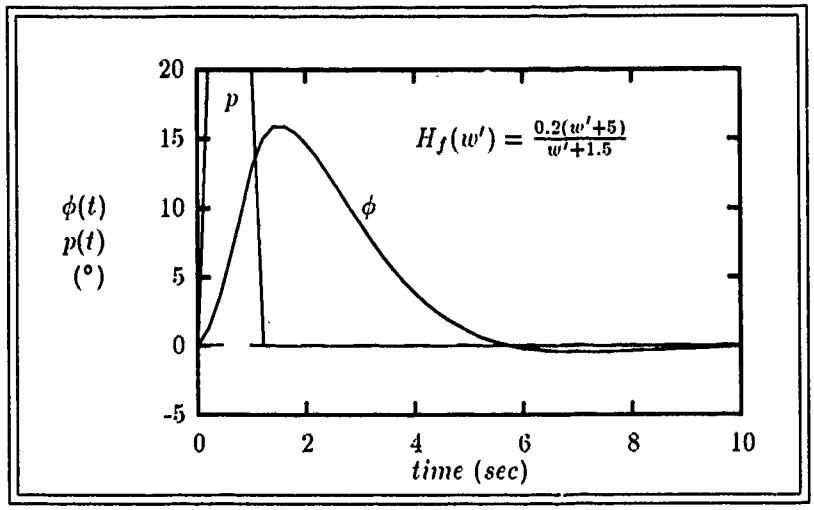

Figure 6.5. w′-plane Wing Leveler Response to a 20° Pilot Input Bank Angle Disturbance

The block diagram for this simulation is shown in Figure 6.6. The aircraft block in Figure 6.6

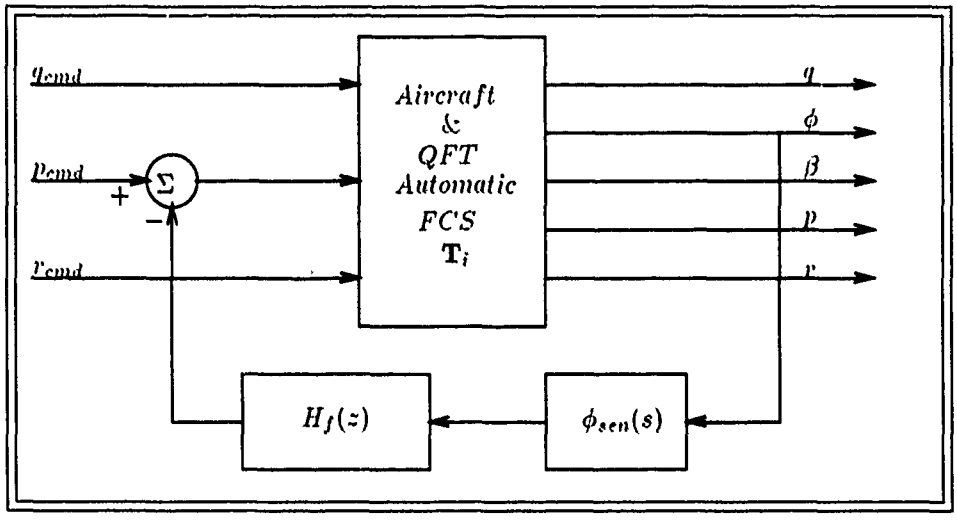

Figure 6.6. Hybrid Wing Leveler Simulation Block Diagram

is labeled with $\mathbf{T}_i$ to denote the closed-loop QFT automatic flight control system associated with the ith plant case $\mathbf{P}_i$. It is a continuous system block; however, discrete system blocks, namely the channel prefilters $f_{i,i}(z)$ and the channel controllers $g_i(z)$ are contained within. The bank angle sensor is continuous and the wing leveler feedback controller is discrete. For the hybrid simulations in Figure 6.7, an initial ϕ condition of 45° is set in the ϕ plant integrator state to provide the initial bank angle disturbance.

6.5 Results and Discussion

The wing leveler system response figures-of-merit are derived approximately from the hybrid simulations in Figure 6.7 and the verification simulation in Figure 6.4.

- $T_r \approx 2\ sec$
- $T_s \approx 6\ sec$
- $\zeta \approx 0.7$

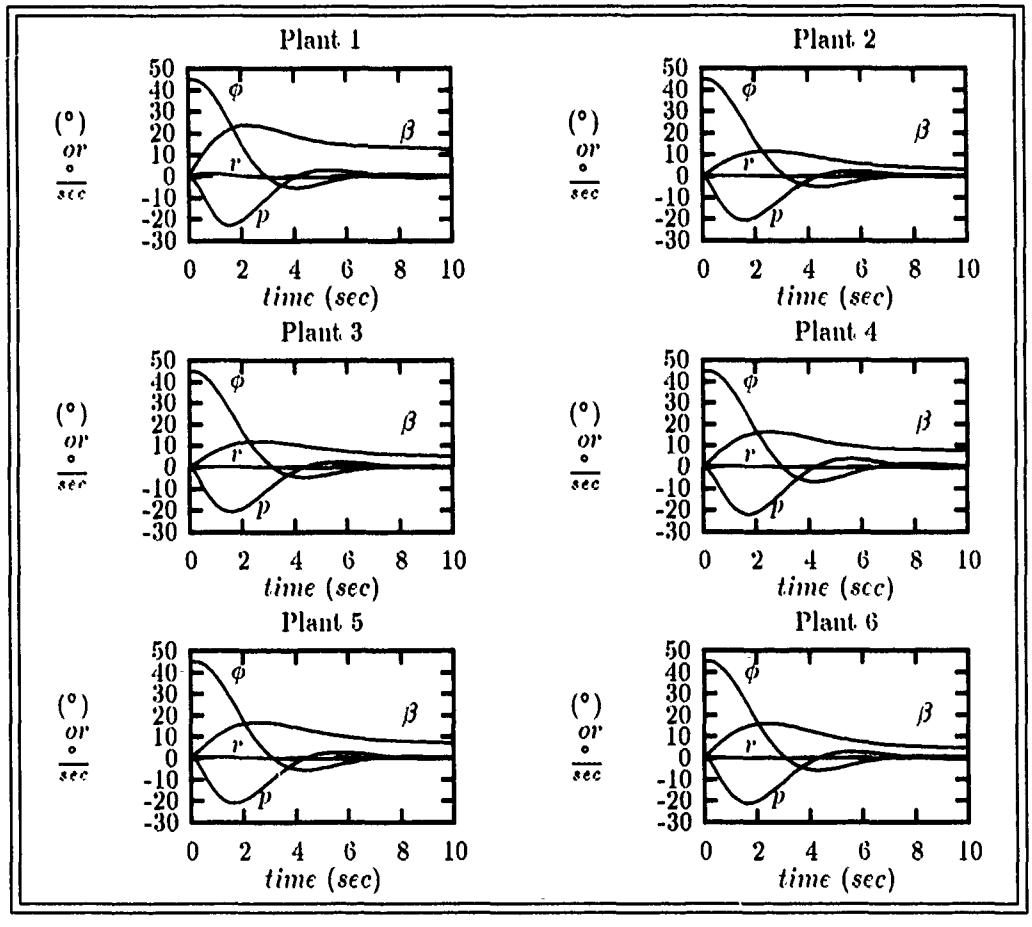

Figure 6.7. Hybrid Wing Leveler Response to a 45° Bank Angle Disturbance For Plant Cases 1-6

The pilot input disturbance simulation in Figure 6.5 demonstrates the ability to overpower the wing leveler when required. The overshoot is 2° for a 20° bank angle disturbance or 10%. The feedback transfer function for the disturbance control ratio is Type 1 as shown in Equation 6.11, and thus the disturbance control ratio has a zero at the origin as in Equation 6.15 yielding zero steady state error to a step input as demonstrated.

This roll-attitude pilot assist autopilot function design meets all the requirements of MIL-C-18244A. It is a very simple design that only levels the wings in response to bank angle disturbances. It does not provide the capability to preset an initial bank angle and hold the roll attitude relative to the preset bank. To provide this feature on this aircraft, turn coordination must be implemented.

Thus, a preset wing leveler bank angle will and should result in a constant coordinated turn.

VII. Conclusions and Recommendations

7.1 Summary

This thesis demonstrates the successful application of discrete MIMO Quantitative Feedback Theory to the design of a three-axis rate-commanded automatic flight control system for the Lambda URV. This study finds that the application of discrete QFT is a straight-forward and systematic design procedure. The experienced control system designer can apply these techniques to many control problems with relative ease. One should, however, be comfortable with all aspects of frequency plane design synthesis and system description and the corresponding time domain implications. That's not to imply that the novice designer should not use QFT. On the contrary, application of QFT to a problem is an excellent way of gaining invaluable experience in frequency plane design.

Most studies at AFIT prior to this have dealt with flight control reconfiguration issues. Typically, for the QFT reconfiguration problem, one basic or nominal aircraft flight condition is selected and failure conditions are generated from that nominal case to quantify the plant uncertainty in the presence of surface failure. It should be obvious that, in a reconfiguration strategy, it is desirable to have a number of the available effectors weighted sufficiently to provide the desired control so that, with the failure of some of the effectors, the desired system response or, at least system stability, is achieved. Due to their physical location on the aircraft and their size and angular displacement, certain effectors are "primary" and are "naturally" the best effectors in generating certain aircraft responses. For example, in a conventional tailed aircraft like Lambda, elevators, ailerons, and rudder are the primary effectors for generating pitch, roll, and yaw respectively. In general, reconfiguration strategy requires heavy weights on "secondary" surfaces so that the weighting matrix $\mathbf{\Delta}$ synthesis, required for blending the effectors to produce a square system plant, becomes quite involved and not so straight-forward.

For this study, a basic flight control system capable of being implemented on Lambda is needed and thus, a reconfiguration strategy is not used. To this author's knowledge, no completely QFT designed flight control systems have, to this point, been implemented for actual flight testing on any Air Force aircraft. The weighting matrix selection in this study is therefore greatly simplified as described in Chapter II and the resulting effective plants have the minimum phase determinants desired.

The numeric difficulties with effective plant discretization documented in past efforts is eliminated with the application of the Hofmann algorithm. The effective plants $\mathbf{P}_e^i(s)$ are quickly discretized in the w'-plane with a Matrix_x macro program.

The effective plants $\mathbf{P}_e^i(s)$ for this study, with a three pole actuator/sensor model, have an excess of four poles. This produces two NMP zeros in $|\mathbf{P}_e^i(w')|$. The phase of these NMP zeros is accounted for by including them in the template generation and in the nominal loop transmission shaping for each MISO channel. In this way, these NMP characteristics are handled *directly* and successful loop transmissions are synthesized for each MISO channel in this study.

Hybrid nonlinear (effector amplitude limited) simulations on Matrix_x of the completed design verify the successful application of discrete QFT in this study. The yaw-rate channel meets all specifications. Due to the large uncertainty at low frequencies in the pitch-rate and roll-rate MISO channels, some low frequency tracking bounds are quite high and not met by the respective loop transmissions. In a strict sense, *a priori* performance specifications are not met by the pitch-rate and roll-rate channels since the low frequency tracking bound violations result in minor sagging of the time responses. It is reasonable to assert that this may not be very noticeable or even detectable to the Lambda pilot. Pilots tend to rate aircraft on transient performance, and so, in that sense, the QFT designs generated in this study meet all *a priori* specifications.

As an added bonus and due to the success of the basic design, an autopilot function design is demonstrated. With a noninteracting three-channel flight control system in place, outer loop

autopilot functions and control enhancements become quite simple to design and implement. A wing leveling function is synthesized that very graphically demonstrates this. Only one difference equation and the appropriate program logic to turn it on and off is required to implement this design.

7.2 Conclusions

The objective of this study was to produce an implementable set of discrete controllers and prefilters to provide a core three-axis rate-commanded automatic flight control system for Lambda. A third order effector actuator/sensor model is used and successful designs are achieved by *directly* handling the inherent NMP transformation elements of the discrete MISO system ($\mathbf{Q}(w')$). It appears that even higher order (more excess poles) effector actuator/sensor models can be handled in a discrete design by this *direct* approach. The NMP elements of $|\mathbf{P}^i_e(w')|$ resulted from transformation to the w'-plane of a MP ($|\mathbf{P}^i_e(s)|$) system and were located no closer than the NMP *sampling* zero at 120 (rad/sec). It is reasonable to assume that, given a MP ($|\mathbf{P}^i_e(s)|$) system, the NMP elements associated with the discrete representation will be no closer than the *sampling* zero and successful loop transmissions should be synthesizable based on the plant dynamics and regardless of the effector actuator/sensor model used. The discrete NMP characteristics of a continuous MP system represent a loss of information between samples of the continuous system dynamics and thus do therefore represent "real" plant dynamics. The time delay inherent in the sampling process for a discrete system manifests itself in these NMP zeros. Continuous system plant NMP properties are another matter and would obviously transform directly to the discrete system creating problems in the design synthesis for QFT or any other robust design technique.

All calculations, manipulations, simulations, etc for this thesis are performed with Matrix_x on a SUN workstation. Just prior to the start of this work, a new version of Matrix_x was installed with claims of major numerical improvements. It appears that this new workstation version is

quite improved since no numerical problems with polynomial convolution and other numerical calculations was noted as was the case in past studies with older versions of $Matrix_x$. The success of this study is partially attributed to the absence of numeric difficulties and the decision to completely handle all data with $Matrix_x$ except for the initial plant case inputs.

7.3 Recommendations

As a consequence of this study, some areas for further attention have surfaced. First, the weighting matrix was simplified in this study to facilitate an implementable design. It was recognized from the start that weighting matrix selection, especially if optimality is considered, is a monumental task and may well be a topic for further independent study as a thesis or dissertation. The weighting matrix employed in this thesis is a natural and acceptable blending of the available Lambda effectors and in no way detracts from the success of the design. More systematic weighting matrix selection should be revisited in future studies building on the results Hamilton [8].

Second, past studies have recommended CAD package development to facilitate the timely and error free design application and this study is no exception. It would be hard at this point to specify the capabilities required of a stand alone discrete QFT CAD package flexible enough to handle the many variations possible in a given problem formulation. It is suggested that a front end package for $Matrix_x$ be designed to ease data entry and maximize the use of $Matrix_x$ for the initial design transfer function manipulations. It is envisioned that $Matrix_x$ could form the core of this QFT design package due to its very flexible command environment.

Third, it is recommended that design #2 controllers and prefilters be implemented for actual flight testing on Lambda. That is the better design in terms of more closely meeting the *a priori* specified performance requirements. Simulation of the design with the nonlinear equations of motion before flight testing is a possible consideration before actual flight testing is attempted. If the design fails in the nonlinear setting, it can only mean that it is operating outside the bounds of

plant uncertainty specified *a priori* or the linearized EOM given for the linearized design are in error. All things considered, it is anticipated that at the very worst, there may be some "flyable" flight conditions in the nonlinear setting that are not contained within the designed for range of plant parameter uncertainty and may not give the specified performance or may be unstable. It is important to remember though that the QFT design is very robust and robustness is enhanced by the overdesign inherent in any higher than required loop transmission synthesis in a loop design. Thus, it is entirely possible that some areas outside the quantified plant parameter uncertainty may also show the specified performance.

Last, given successful flight testing of the design, the wing leveler should be implemented and tested. In addition, a complete attitude command autopilot system should be designed and implemented for Lambda to take full advantage of its unique capabilities.

Appendix A. *Lambda Descriptive Data*

The following data are given for the Lambda URV. It is derived from initial flight testing and the Digital DATCOM CAD package used to design Lambda.

- Wing span — 14 ft
- MAC (mean aerodynamic chord) ($\bar{c}$) — 1.51 ft
- Reference wing area (S) — 21.1 ft^2
- Minimum weight — 150 lbs
- Nominal weight — 168 lbs
- Maximum weight — 200 lbs
- Maximum speed — 100 knots in level flight
- No flap stall speed — 45 knots
- 20° flap stall speed — 35 knots
- Takeoff speed — 60–70 knots
- Landing speed — 50–70 knots
- Nominal CG full fuel — 32% MAC aft of leading edge
- CG range empty fuel — 26–41% MAC aft of leading edge
- CG range full fuel — 32–47% MAC aft of leading edge
- Aileron deflection limit — +15° up −10° down
- Flap deflection limit — −20° down
- Rudder deflection limit — ± 25°
- Elevator deflection limit — ± 15°

Appendix B. *Aircraft Models*

Six flight conditions are used in this design. A short description of how the flight conditions are generated begins on page 2-7. A tabular listing of the flight conditions is reproduced here in the table below.

Table B.1. The Aircraft Flight Conditions

Plant #	Speed (kts)	CG (% MAC)	Weight (lbs)	α	C'_L	$C'_{L_{\dot{\alpha}}}$	C'_m	$C'_{m_{\dot{\alpha}}}$
1	40	50	150	10.4°	1.289	1.091	0.0653	−4.528
2	100	50	150	−1.64°	0.210	1.806	0.0615	−5.266
3	100	25	200	−0.96°	0.280	1.94	−0.0072	−6.133
4	70	50	200	1.9°	0.564	1.554	0.0682	−4.527
5	70	25	150	0.556°	0.427	1.769	−0.0448	−5.595
6 ‡	70	25	150	0.556°	0.427	1.769	−0.0448	−5.595

‡Note that plant #5 and #6 appear to be the same. Their flight parameters shown in table B.1 are identical however changes were made to the stability derivatives such that plant #6 represents the very worst case combination of the derivatives C'_{m_q}, C'_{m_α}, C'_{n_β}, C'_{n_r} and C'_{l_p}.

The Lambda aircraft models for these flight conditions are provided by WRDC/FIGL in the form of the aircraft body axis primed dimensional derivatives. An explanation of this type of aerodynamic derivative is found in references [3, 7].

The aircraft model in state space form used for this design is:

$$\dot{\mathbf{x}}(t) = \mathbf{A}\,\mathbf{x}(t) + \mathbf{B}\,\mathbf{u}(t) \tag{B.1}$$

$$\mathbf{y}(t) = \mathbf{C}\,\mathbf{x}(t) + \mathbf{D}\,\mathbf{u}(t) \tag{B.2}$$

In the aircraft body axis dimensional derivative form, these equations become:

$$\begin{bmatrix} \dot{\theta}(t) \\ \dot{u}(t) \\ \dot{\alpha}(t) \\ \dot{q}(t) \\ \dot{\phi}(t) \\ \dot{\beta}(t) \\ \dot{p}(t) \\ \dot{r}(t) \end{bmatrix} = \begin{bmatrix} 0 & 0 & 0 & 1 & 0 & 0 & 0 & 0 \\ X'_\theta & X'_u & X'_\alpha & X'_q & 0 & 0 & 0 & 0 \\ Z'_\theta & Z'_u & Z'_\alpha & Z'_q & 0 & 0 & 0 & 0 \\ M'_\theta & M'_u & M'_\alpha & M'_q & 0 & 0 & 0 & 0 \\ 0 & 0 & 0 & 0 & 0 & 0 & 1 & 0 \\ 0 & 0 & 0 & 0 & Y'_\phi & Y'_\beta & Y'_p & Y'_r \\ 0 & 0 & 0 & 0 & 0 & L'_\beta & L'_p & L'_r \\ 0 & 0 & 0 & 0 & 0 & N'_\beta & N'_p & N'_r \end{bmatrix} \begin{bmatrix} \theta(t) \\ u(t) \\ \alpha(t) \\ q(t) \\ \phi(t) \\ \beta(t) \\ p(t) \\ r(t) \end{bmatrix}$$

$$+ \begin{bmatrix} 0 & 0 & 0 & 0 & 0 & 0 & 0 \\ X'_{\delta_{e_L}} & X'_{\delta_{e_R}} & X'_{\delta_{f_L}} & X'_{\delta_{f_R}} & X'_{\delta_{a_L}} & X'_{\delta_{a_R}} & 0 \\ Z'_{\delta_{e_L}} & Z'_{\delta_{e_R}} & Z'_{\delta_{f_L}} & Z'_{\delta_{f_R}} & Z'_{\delta_{a_L}} & Z'_{\delta_{a_R}} & 0 \\ M'_{\delta_{e_L}} & M'_{\delta_{e_R}} & M'_{\delta_{f_L}} & M'_{\delta_{f_R}} & M'_{\delta_{a_L}} & M'_{\delta_{a_R}} & 0 \\ 0 & 0 & 0 & 0 & 0 & 0 & 0 \\ 0 & 0 & 0 & 0 & 0 & 0 & Y'_{\delta_r} \\ L'_{\delta_{e_L}} & L'_{\delta_{e_R}} & L'_{\delta_{f_L}} & L'_{\delta_{f_R}} & L'_{\delta_{a_L}} & L'_{\delta_{a_R}} & L'_{\delta_r} \\ N'_{\delta_{e_L}} & N'_{\delta_{e_R}} & N'_{\delta_{f_L}} & N'_{\delta_{f_R}} & N'_{\delta_{a_L}} & N'_{\delta_{a_R}} & N'_{\delta_r} \end{bmatrix} \begin{bmatrix} \delta_{e_L}(t) \\ \delta_{e_R}(t) \\ \delta_{f_L}(t) \\ \delta_{f_R}(t) \\ \delta_{a_L}(t) \\ \delta_{a_R}(t) \\ \delta_r(t) \end{bmatrix} \tag{B.3}$$

$$\begin{bmatrix} p(t) \\ q(t) \\ r(t) \end{bmatrix} = \begin{bmatrix} 0 & 0 & 0 & 1 & 0 & 0 & 0 & 0 \\ 0 & 0 & 0 & 0 & 0 & 0 & 1 & 0 \\ 0 & 0 & 0 & 0 & 0 & 0 & 0 & 1 \end{bmatrix} \begin{bmatrix} \theta(t) & (rad) \\ u(t) & (ft/sec) \\ \alpha(t) & (rad) \\ q(t) & (rad/sec) \\ \phi(t) & (rad) \\ \beta(t) & (rad) \\ p(t) & (rad/sec) \\ r(t) & (rad/sec) \end{bmatrix} \tag{B.4}$$

Table B.2 and B.3 are tabular listings of the body axis primed dimensional derivatives in units of $1/sec$.

Table B.2. Aircraft Model Lateral Dimensional Derivative Data

	Flight Condition					
	# 1	# 2	# 3	# 4	# 5	# 6
	40 kts	100 kts	100 kts	70 kts	70 kts	70 kts
	CG 50%	CG 50%	CG 25%	CG 50%	CG 25%	CG 25%
	150 lbs	150 lbs	200 lbs	200 lbs	150 lbs	150 lbs
	α = 10.4°	α =-1.64°	α =-0.96°	α = 1.9°	α = 0.556°	α = 0.556°
Y'_0	0.475676	0.190265	0.190265	0.271798	0.271798	0.271798
Y'_β	−0.0979	−0.247452	−0.185589	−0.129427	−0.17257	−0.17257
Y'_p	0.18076	−0.0286309	−0.0167993	0.0329826	0.0095594	0.0095594
Y'_r	−0.993786	−0.993707	−0.995281	−0.995258	−0.993712	−0.993712
Y'_{δ_r}	0.0735538	0.184001	0.138001	0.0965949	0.128793	0.128793
L'_β	−4.42851	−5.23061	−8.84221	−6.58808	−4.38385	−4.30435
L'_p	−2.89123	−12.467	−11.1274	−7.68487	−8.58997	−10.205
L'_r	3.3633	1.84869	2.00065	2.39331	2.10875	2.10248
$L'_{\delta_{e_L}}$	0.582036	3.3515	3.01717	1.47777	1.63497	1.63497
$L'_{\delta_{e_R}}$	−0.582036	−3.3515	−3.01717	−1.47777	−1.63497	−1.63497
$L'_{\delta_{f_L}}$	6.55765	40.8274	36.7615	18.0489	20.0038	20.0038
$L'_{\delta_{f_R}}$	−6.55765	−40.8274	−36.7615	−18.0489	−20.0038	−20.0038
$L'_{\delta_{a_L}}$	11.8798	73.663	66.3312	32.4528	36.0059	36.0059
$L'_{\delta_{a_R}}$	−11.8798	−73.9822	−66.3312	−32.4528	−36.0059	−36.0059
L'_{δ_r}	1.26732	−1.25659	−0.662067	0.641964	0.208767	0.208767
N'_β	1.53915	11.532	12.8746	5.31588	9.55164	3.40761
N'_p	−0.823552	−0.0941559	−0.226784	−0.552717	−0.54654	−0.551241
N'_r	−0.187398	−0.779109	−0.864736	−0.503889	−0.901531	−1.62835
$N'_{\delta_{e_L}}$	0.0565537	−0.0508011	−0.0280877	0.0272348	0.0118997	0.0118997
$N'_{\delta_{e_R}}$	−0.0565537	0.0508011	0.0280877	−0.0272348	−0.0118997	−0.0118997
$N'_{\delta_{f_L}}$	0.205708	−1.15497	−0.979359	−0.240337	−0.523322	−0.523322
$N'_{\delta_{f_R}}$	−0.205708	1.15497	0.979359	0.240337	0.523322	0.523322
$N'_{\delta_{a_L}}$	0.111915	−2.41373	−2.15844	−0.787371	−1.35742	−1.35742
$N'_{\delta_{a_R}}$	−0.111915	2.41856	2.15844	0.787371	1.35742	1.35742
N'_{δ_r}	−3.65563	−23.2352	−21.9503	−10.751	−16.1346	−16.1346

Table B.3. Aircraft Model Longitudinal Dimensional Derivative Data

	Flight Condition					
	# 1	# 2	# 3	# 4	# 5	# 6
	40 kts	100 kts	100 kts	70 kts	70 kts	70 kts
	CG 50%	CG 50%	CG 25%	CG 50%	CG 25%	CG 25%
	150 lbs	150 lbs	200 lbs	200 lbs	150 lbs	150 lbs
	α = 10.4°	α =-1.64°	α =-0.96°	α = 1.9°	α = 0.556°	α = 0.556°
X'_θ	−32.17	−32.17	−32.17	−32.17	−32.17	−32.17
X'_u	0.00385506	−0.0574517	−0.0413963	−0.0243532	−0.0360561	−1.30833
X'_α	38.0952	−6.35954	4.51655	31.4246	22.9839	21.5225
X'_q	−12.0748	4.75225	2.76989	−3.87661	−1.11515	−1.11515
$X'_{\delta_{eL}}$	−1.15621	0.0146258	−0.300342	−0.763416	−0.635744	−0.635744
$X'_{\delta_{eR}}$	−1.15621	0.0146258	−0.300342	−0.763416	−0.635744	−0.635744
$X'_{\delta_{fL}}$	−3.53819	0.303286	−0.743093	−2.36357	−1.89333	−1.89333
$X'_{\delta_{fR}}$	−3.53819	0.303286	−0.743093	−2.36357	−1.89333	−1.89333
$X'_{\delta_{aL}}$	−2.10141	0.944603	0.0970785	−1.20335	−0.820593	−0.820593
$X'_{\delta_{aR}}$	−2.10141	0.944603	0.0970785	−1.20335	−0.820593	−0.820593
Z'_θ	0	0	0	0	0	0
Z'_u	−0.014259	−0.00314731	−0.0026521	−0.00376754	−0.00428808	−0.0043924
Z'_α	−1.32638	−5.29872	−4.01458	−2.81562	−3.72577	−3.72589
Z'_q	0.983807	0.981947	0.97774	0.987683	0.970904	0.970904
$Z'_{\delta_{eL}}$	−0.081291	−0.20285	−0.150277	−0.103929	−0.14037	−0.14037
$Z'_{\delta_{eR}}$	−0.081291	−0.20285	−0.150277	−0.103929	−0.14037	−0.14037
$Z'_{\delta_{fL}}$	−0.250987	−0.647605	−0.487936	−0.339101	−0.448443	−0.448443
$Z'_{\delta_{fR}}$	−0.250987	−0.647605	−0.487936	−0.339101	−0.448443	−0.448443
$Z'_{\delta_{aL}}$	−0.157063	−0.405856	−0.304528	−0.211861	−0.282525	−0.282525
$Z'_{\delta_{aR}}$	−0.157063	−0.405856	−0.304528	−0.211861	−0.282525	−0.282525
M'_θ	0	0	0	0	0	0
M'_u	0.0141923	0.00402177	−0.00228065	0.000253322	0.00563355	0.00625911
M'_α	−3.3774	9.66986	−45.4757	7.38835	−24.5418	−31.1685
M'_q	−1.29817	−3.64553	−3.38135	−1.83395	−2.8509	−3.69636
$M'_{\delta_{eL}}$	−4.41083	−26.9074	−23.2027	−10.5787	−14.1915	−14.1915
$M'_{\delta_{eR}}$	−4.41083	−26.9074	−23.2027	−10.5787	−14.1915	−14.1915
$M'_{\delta_{fL}}$	0.00321951	−0.204912	−5.9655	−0.140934	−3.59539	−3.59539
$M'_{\delta_{fR}}$	0.00321951	−0.204912	−5.9655	−0.140934	−3.59539	−3.59539
$M'_{\delta_{aL}}$	0.0335753	0.0555291	−3.91485	−0.0134475	−2.35926	−2.35926
$M'_{\delta_{aR}}$	0.0335753	0.0555291	−3.91485	−0.0134475	−2.35926	−2.35926

Equation B.3 shows the longitudinal and lateral mode decoupling present in this model. The sections below present the **A** and **B** matrices of the state space models used in this study. They are derived by inserting the data presented in Tables B.2 and B.3 into Equation B.3. For ease of presetation the matrices are displayed in the form of **A1**, **A2**, **B1**, **B2** where:

$$\mathbf{A} = \begin{bmatrix} \mathbf{A1} & \mathbf{0} \\ \mathbf{0} & \mathbf{A2} \end{bmatrix} \tag{B.5}$$

$$\mathbf{B} = \begin{bmatrix} \mathbf{B1} \\ \mathbf{B2} \end{bmatrix} \tag{B.6}$$

B.1 Flight Condition #1 — Speed 40 kts, CG 50% MAC, Weight 150 lbs, $\alpha = 10.4°$

$$\mathbf{A1} = \begin{bmatrix} 0 & 0 & 0 & 1.0 \\ -32.17 & .00385506 & 38.0952 & -12.0748 \\ 0 & -.0104259 & -1.32638 & 0.983807 \\ 0 & .0141923 & -3.3774 & -1.29817 \end{bmatrix} \tag{B.7}$$

$$\mathbf{A2} = \begin{bmatrix} 0 & 0 & 1.0 & 0 \\ .475676 & -0.0979 & .18076 & -.993786 \\ 0 & -4.42851 & -2.89123 & 3.3633 \\ 0 & 1.53915 & -.823552 & -.187398 \end{bmatrix} \tag{B.8}$$

$$\mathbf{B1} = \begin{bmatrix} 0 & -1.15621 & -.0812910 & -4.41083 \\ 0 & -1.15621 & -.0812910 & -4.41083 \\ 0 & -3.53819 & -.2509870 & .00321951 \\ 0 & -3.53819 & -.2509870 & .00321951 \\ 0 & -2.10141 & -.1570630 & .0335753 \\ 0 & -2.10141 & -.1570630 & .0335753 \\ 0 & 0 & 0 & 0 \end{bmatrix}^T \tag{B.9}$$

$$\mathbf{B2} = \begin{bmatrix} 0 & 0 & .5820360 & .0565537 \\ 0 & 0 & -.5820360 & -.0565537 \\ 0 & 0 & 6.55765 & .2057080 \\ 0 & 0 & -6.55765 & -.2057080 \\ 0 & 0 & 11.8798 & .1119150 \\ 0 & 0 & -11.8798 & -.1119150 \\ 0 & .0735538 & 1.26732 & -3.65563 \end{bmatrix}^T \tag{B.10}$$

B.2 Flight Condition #2 — Speed 100 kts, CG 50% MAC, Weight 150 lbs, $\alpha = -1.64°$

$$\mathbf{A1} = \begin{bmatrix} 0 & 0 & 0 & 1.0 \\ -32.17 & -0.057451 & -6.35954 & 4.75225 \\ 0 & -0.00314731 & -5.29872 & 0.981947 \\ 0 & 0.00402177 & 9.66986 & -3.64553 \end{bmatrix} \tag{B.11}$$

$$\mathbf{A2} = \begin{bmatrix} 0 & 0 & 1.0 & 0 \\ 0.190265 & -0.247452 & -0.0286309 & -0.993707 \\ 0 & -5.23061 & -12.467 & 1.84869 \\ 0 & 11.532 & -0.0941559 & -0.779109 \end{bmatrix} \tag{B.12}$$

$$\mathbf{B1} = \begin{bmatrix} 0 & 0.0146258 & -0.20285 & -26.9074 \\ 0 & 0.0146258 & -0.20285 & -26.9074 \\ 0 & 0.303286 & -0.647605 & -0.204912 \\ 0 & 0.303286 & -0.647605 & -0.204912 \\ 0 & 0.944603 & -0.405856 & 0.0555291 \\ 0 & 0.944603 & -0.405856 & 0.0555291 \\ 0 & 0 & 0 & 0 \end{bmatrix}^T \tag{B.13}$$

$$\mathbf{B2} = \begin{bmatrix} 0 & 0 & 3.3515 & -0.0508011 \\ 0 & 0 & -3.3515 & 0.0508011 \\ 0 & 0 & 40.8274 & -1.15497 \\ 0 & 0 & -40.8274 & 1.15497 \\ 0 & 0 & \boxed{73.663} & \boxed{-2.41373} \\ 0 & 0 & \boxed{-73.9822} & \boxed{2.41856} \\ 0 & 0.184001 & -1.25659 & -23.2352 \end{bmatrix}^T \tag{B.14}$$

B.3 Flight Condition #3 — Speed 100 kts, CG 25% MAC, Weight 200 lbs, $\alpha = -0.96°$

$$\mathbf{A1} = \begin{bmatrix} 0 & 0 & 0 & 1.0 \\ -32.17 & -0.0413963 & 4.51655 & 2.76989 \\ 0 & -0.0026521 & -4.01458 & 0.97774 \\ 0 & -0.00228065 & -45.4757 & -3.38135 \end{bmatrix} \tag{B.15}$$

$$\mathbf{A2} = \begin{bmatrix} 0 & 0 & 1.0 & 0 \\ 0.190265 & -0.185589 & -0.0167993 & -0.995281 \\ 0 & -8.84221 & -11.1274 & 2.00065 \\ 0 & 12.8746 & -0.226784 & -0.864736 \end{bmatrix} \tag{B.16}$$

$$\mathbf{B1} = \begin{bmatrix} 0 & -0.300342 & -0.150277 & -23.2027 \\ 0 & -0.300342 & -0.150277 & -23.2027 \\ 0 & -0.743093 & -0.487936 & -5.9655 \\ 0 & -0.743093 & -0.487936 & -5.9655 \\ 0 & 0.0970785 & -0.304528 & -3.91485 \\ 0 & 0.0970785 & -0.304528 & -3.91485 \\ 0 & 0 & 0 & 0 \end{bmatrix}^T \tag{B.17}$$

$$\mathbf{B2} = \begin{bmatrix} 0 & 0 & 3.01717 & -0.0280877 \\ 0 & 0 & -3.01717 & 0.0280877 \\ 0 & 0 & 36.7615 & -0.979359 \\ 0 & 0 & -36.7615 & 0.979359 \\ 0 & 0 & 66.3312 & -2.15844 \\ 0 & 0 & -66.3312 & 2.15844 \\ 0 & 0.138001 & -0.662067 & -21.9503 \end{bmatrix}^T \tag{B.18}$$

B.4 Flight Condition #4 — Speed 70 kts, CG 50% MAC, Weight 200 lbs, α = 1.90°

$$\mathbf{A1} = \begin{bmatrix} 0 & 0 & 0 & 1.0 \\ -32.17 & -0.0243532 & 31.4246 & -3.87661 \\ 0 & -0.00376754 & -2.81562 & 0.987683 \\ 0 & 0.000253322 & 7.38835 & -1.83395 \end{bmatrix} \tag{B.19}$$

$$\mathbf{A2} = \begin{bmatrix} 0 & 0 & 1.0 & 0 \\ 0.271798 & -0.129427 & 0.0329826 & -0.995258 \\ 0 & -6.58808 & -7.68487 & 2.39331 \\ 0 & 5.31588 & -0.552717 & -0.503889 \end{bmatrix} \tag{B.20}$$

$$\mathbf{B1} = \begin{bmatrix} 0 & -0.763416 & -0.103929 & -10.5787 \\ 0 & -0.763416 & -0.103929 & -10.5787 \\ 0 & -2.36357 & -0.339101 & -0.140934 \\ 0 & -2.36357 & -0.339101 & -0.140934 \\ 0 & -1.20335 & -0.211861 & -0.0134475 \\ 0 & -1.20335 & -0.211861 & -0.0134475 \\ 0 & 0 & 0 & 0 \end{bmatrix}^T \tag{B.21}$$

$$\mathbf{B2} = \begin{bmatrix} 0 & 0 & 1.47777 & 0.0272348 \\ 0 & 0 & -1.47777 & -0.0272348 \\ 0 & 0 & 18.0489 & -0.240337 \\ 0 & 0 & -18.0489 & 0.240337 \\ 0 & 0 & 32.4528 & -0.787371 \\ 0 & 0 & -32.4528 & 0.787371 \\ 0 & 0.0965949 & 0.641964 & -10.751 \end{bmatrix}^T \tag{B.22}$$

B.5 Flight Condition #5 — Speed 70 kts, CG 25% MAC, Weight 150 lbs. $\alpha = 0.556°$

$$\mathbf{A1} = \begin{bmatrix} 0 & 0 & 0 & 1.0 \\ -32.17 & -0.0360561 & 22.9839 & -1.11515 \\ 0 & -0.00428808 & -3.72577 & 0.970904 \\ 0 & 0.0[illegible]355 & -24.5418 & -2.8509 \end{bmatrix} \tag{B.23}$$

$$\mathbf{A2} = \begin{bmatrix} 0 & 0 & 1.0 & 0 \\ 0.271798 & -0.17257 & 0.0095594 & -0.993712 \\ 0 & -4.38385 & -8.58997 & 2.10875 \\ 0 & 9.55164 & -0.54654 & -0.901531 \end{bmatrix} \tag{B.24}$$

$$\mathbf{B1} = \begin{bmatrix} 0 & -0.635744 & -0.14037 & -14.1915 \\ 0 & -0.635744 & -0.14037 & -14.1915 \\ 0 & -1.89333 & -0.448443 & -3.59539 \\ 0 & -1.89333 & -0.448443 & -3.59539 \\ 0 & -0.820593 & -0.282525 & -2.35926 \\ 0 & -0.820593 & -0.282525 & -2.35926 \\ 0 & 0 & 0 & 0 \end{bmatrix}^T \tag{B.25}$$

$$\mathbf{B2} = \begin{bmatrix} 0 & 0 & 1.63497 & 0.0118997 \\ 0 & 0 & -1.63497 & -0.0118997 \\ 0 & 0 & 20.0038 & -0.523322 \\ 0 & 0 & -20.0038 & 0.523322 \\ 0 & 0 & 36.0059 & -1.35742 \\ 0 & 0 & -36.0059 & 1.35742 \\ 0 & 0.128793 & 0.208767 & -16.1346 \end{bmatrix}^T \tag{B.26}$$

B.6 Flight Condition #6 — Speed 70 kts, CG 25% MAC, Weight 150 lbs, α = 0.556°

$$\mathbf{A1} = \begin{bmatrix} 0 & 0 & 0 & 1.0 \\ -32.17 & -1.30833 & 21.5225 & -1.11515 \\ 0 & -0.0043924 & -3.72589 & 0.970904 \\ 0 & 0.00625911 & -31.1685 & -3.69636 \end{bmatrix} \tag{B.27}$$

$$\mathbf{A2} = \begin{bmatrix} 0 & 0 & 1.0 & 0 \\ 0.271798 & -0.17257 & 0.0095594 & -0.993712 \\ 0 & -4.30435 & -10.205 & 2.10248 \\ 0 & 3.40761 & -0.551241 & -1.62835 \end{bmatrix} \tag{B.28}$$

$$\mathbf{B1} = \begin{bmatrix} 0 & -0.635744 & -0.14037 & -14.1915 \\ 0 & -0.635744 & -0.14037 & -14.1915 \\ 0 & -1.89333 & -0.448443 & -3.59539 \\ 0 & -1.89333 & -0.448443 & -3.59539 \\ 0 & -0.820593 & -0.282525 & -2.35926 \\ 0 & -0.820593 & -0.282525 & -2.35926 \\ 0 & 0 & 0 & 0 \end{bmatrix}^T \tag{B.29}$$

$$\mathbf{B2} = \begin{bmatrix} 0 & 0 & 1.63497 & 0.0118997 \\ 0 & 0 & -1.63497 & -0.0118997 \\ 0 & 0 & 20.0038 & -0.523322 \\ 0 & 0 & -20.0038 & 0.523322 \\ 0 & 0 & 36.0059 & -1.35742 \\ 0 & 0 & -36.0059 & 1.35742 \\ 0 & 0.128793 & 0.208767 & -16.1346 \end{bmatrix}^T \tag{B.30}$$

Appendix C. *Transfer Functions*

The sections of this appendix present listings of all the transfer functions used at the various stages of this thesis. Elements of $\mathbf{P}_e(s)$, $\mathbf{P}_e(w')$ and $\mathbf{Q}(w')$ are listed. The following tabular listings of transfer functions are presented in factored numerator/denominator form with the complex frequency variable s or w' omitted. Left-half plane roots are preceeded by a negative sign. Where the sign is omitted, a plus sign (right-half plane) is assumed. All roots are presented within a set of parentheses. Gain is not enclosed in parentheses and will have either sign.

C.1 *Effective Plant Transfer Functions* $\mathbf{P}_e(s)$

This section contains listings of the s-plane effective plant transfer functions. Each table presents all the nonzero elements of the $3x3$ $\mathbf{P}_e(s)$ for a given flight condition. Equation C.1 shows the notation used for the elements of $\mathbf{P}_e(s)$ in the tables.

$$\mathbf{P}_e(s) = \begin{bmatrix} \frac{q(s)}{\delta_q(s)} & 0 & 0 \\ 0 & \frac{p(s)}{\delta_p(s)} & \frac{p(s)}{\delta_r(s)} \\ 0 & \frac{r(s)}{\delta_p(s)} & \frac{r(s)}{\delta_r(s)} \end{bmatrix} = \begin{bmatrix} p_{e_{1,1}} & 0 & 0 \\ 0 & p_{e_{2,2}} & p_{e_{2,3}} \\ 0 & p_{e_{3,2}} & p_{e_{3,3}} \end{bmatrix} \tag{C.1}$$

Table C.1. $\mathbf{P}_e(s)$ Transfer Functions-Plant # 1

Element	Plant # 1
$p_{e_{1,1}}$	$\frac{1.4280e5\ (0)(-0.6263 \pm j0.1696)}{(-0.0198 \pm j0.5799)(-1.2906 \pm j1.8705)(-12.7003 \pm j12.7559)(-50.0007)}$
$p_{e_{2,2}}$	$\frac{3.8562e5\ (0)(-0.4265 \pm j1.4600)}{(0.1891)(-0.4389 \pm j2.0502)(-2.4878)(-12.7003 \pm j12.7559)(-50.0007)}$
$p_{e_{3,2}}$	$\frac{6.3514e4\ (-1.1390)(1.5895 \pm j1.7960)}{(0.1891)(-0.4389 \pm j2.0502)(-2.4878)(-12.7003 \pm j12.7559)(-50.0007)}$
$p_{e_{2,3}}$	$\frac{-2.9511e5\ (0)(-0.7821)(3.9402)}{(0.1891)(-0.4389 \pm j2.0502)(-2.4878)(-12.7003 \pm j12.7559)(-50.0007)}$
$p_{e_{3,3}}$	$\frac{2.9429e5\ (-0.0474 \pm j0.6081)(-3.6891)}{(0.1891)(-0.4389 \pm j2.0502)(-2.4878)(-12.7003 \pm j12.7559)(-50.0007)}$

Table C.2. $\mathbf{P}_e(s)$ Transfer Functions–Plant # 2

Element	Plant # 2
$p_{e_{1,1}}$	$\frac{8.7162e5\ (0)(-0.0537)(-5.3900)}{(0.1325)(-0.2352)(-1.2270)(-7.6720)(-12.7003 \pm j12.7559)(-50.0007)}$
$p_{e_{2,2}}$	$\frac{2.5445e6\ (0)(-0.6233 \pm j3.4493)}{(0.0222)(-0.5180 \pm j3.4026)(-12.4798)(-12.7003 \pm j12.7559)(-50.0007)}$
$p_{e_{3,2}}$	$\frac{2.9439e5\ (0.1343 \pm j1.2799)(-12.0524)}{(0.0222)(-0.5180 \pm j3.4026)(-12.4798)(-12.7003 \pm j12.7559)(-50.0007)}$
$p_{e_{2,3}}$	$\frac{-1.0941e6\ (0)(1.1454 \pm j0.8033)}{(0.0222)(-0.5180 \pm j3.4026)(-12.4798)(-12.7003 \pm j12.7559)(-50.0007)}$
$p_{e_{3,3}}$	$\frac{1.9212e6\ (0.0828)(-0.2456)(-12.5158)}{(0.0222)(-0.5180 \pm j3.4026)(-12.4798)(-12.7003 \pm j12.7559)(-50.0007)}$

Table C.3. $\mathbf{P}_e(s)$ Transfer Functions–Plant # 3

Element	Plant # 3
$p_{e_{1,1}}$	$\frac{7.6445e5\ (0)(-0.0451)(-3.6625)}{(-0.0139 \pm j0.2480)(-3.7048 \pm j6.6611)(-12.7003 \pm j12.7559)(-50.0007)}$
$p_{e_{2,2}}$	$\frac{2.2790e6\ (0)(-0.6535 \pm j3.6968)}{(0.0231)(-0.5328 \pm j3.6193)(-11.1352)(-12.7003 \pm j12.7559)(-50.0007)}$
$p_{e_{3,2}}$	$\frac{2.8249e5\ (0.1806 \pm j1.4726)(-9.7427)}{(0.0231)(-0.5328 \pm j3.6193)(-11.1352)(-12.7003 \pm j12.7559)(-50.0007)}$
$p_{e_{2,3}}$	$\frac{-1.0209e6\ (0)(-0.8920)(3.4912)}{(0.0231)(-0.5328 \pm j3.6193)(-11.1352)(-12.7003 \pm j12.7559)(-50.0007)}$
$p_{e_{3,3}}$	$\frac{1.8129e6\ (-0.0506 \pm j0.1560)(-11.2601)}{(0.0231)(-0.5328 \pm j3.6193)(-11.1352)(-12.7003 \pm j12.7559)(-50.0007)}$

Table C.4. $\mathbf{P}_e(s)$ Transfer Functions–Plant # 4

Element	Plant # 4
$p_{e_{1,1}}$	$\frac{3.4279e5\ (0)(-0.0653)(-2.8621)}{(-0.1501 \pm j0.4787)(0.6851)(-5.0588)(-12.7003 \pm j12.7559)(-50.0007)}$
$p_{e_{2,2}}$	$\frac{1.0995e6\ (0)(-0.4823 \pm j2.4563)}{(0.0543)(-0.3960 \pm j2.4610)(-7.5804)(-12.7003 \pm j12.7559)(-50.0007)}$
$p_{e_{3,2}}$	$\frac{1.4788e5\ (0.1965 \pm j1.7501)(-4.0413)}{(0.0543)(-0.3960 \pm j2.4610)(-7.5804)(-12.7003 \pm j12.7559)(-50.0007)}$
$p_{e_{2,3}}$	$\frac{-5.7773e5\ (0)(-1.1707)(4.2869)}{(0.0543)(-0.3960 \pm j2.4610)(-7.5804)(-12.7003 \pm j12.7559)(-50.0007)}$
$p_{e_{3,3}}$	$\frac{8.8359e5\ (-0.0401 \pm j0.3217)(8.0485)}{(0.0543)(-0.3960 \pm j2.4610)(-7.5804)(-12.7003 \pm j12.7559)(-50.0007)}$

Table C.5. $\mathbf{P}_e(s)$ Transfer Functions–Plant # 5

Element	Plant # 5
$p_{e_{1,1}}$	$\frac{4.6745e5\ (0)(-0.0676)(-3.4077)}{(-0.0137 \pm j0.3428)(-3.2927 \pm j4.8633)(-12.7003 \pm j12.7559)(-50.0007)}$
$p_{e_{2,2}}$	$\frac{1.2280e6\ (0)(-0.7260 \pm j3.1499)}{(0.0503)(-0.6035 \pm j3.1501)(-8.5073)(-12.7003 \pm j12.7559)(-50.0007)}$
$p_{e_{3,2}}$	$\frac{2.1570e5\ (0.1709 \pm j1.6363)(-5.9004)}{(0.0503)(-0.6035 \pm j3.1501)(-8.5073)(-12.7003 \pm j12.7559)(-50.0007)}$
$p_{e_{2,3}}$	$\frac{-6.0021e5\ (0)(-0.1371)(3.8081)}{(0.0503)(-0.6035 \pm j3.1501)(-8.5073)(-12.7003 \pm j12.7559)(-50.0007)}$
$p_{e_{3,3}}$	$\frac{1.3289e6\ (-0.0337)(-0.0637)(-8.8370)}{(0.0503)(-0.6035 \pm j3.1501)(-8.5073)(-12.7003 \pm j12.7559)(-50.0007)}$

Table C.6. $\mathbf{P}_e(s)$ Transfer Functions–Plant # 6

Element	Plant # 6
$p_{e_{1,1}}$	$\frac{4.6745e5\ (0)(-1.3601)(-3.3101)}{(-0.0971)(-1.2042)(-3.7146 \pm j5.5011)(-12.7003 \pm j12.7559)(-50.0007)}$
$p_{e_{2,2}}$	$\frac{1.2280e6\ (0)(-1.0888 \pm j1.8156)}{(0.0010)(-0.9489 \pm j1.7812)(-10.1092)(-12.7003 \pm j12.7559)(-50.0007)}$
$p_{e_{3,2}}$	$\frac{2.1570e5\ (-0.0132 \pm j0.9472)(-7.1800)}{(0.0010)(-0.9489 \pm j1.7812)(-10.1092)(-12.7003 \pm j12.7559)(-50.0007)}$
$p_{e_{2,3}}$	$\frac{-6.0021e5\ (0)(-1.4933)(4.4222)}{(0.0010)(-0.9489 \pm j1.7812)(-10.1092)(-12.7003 \pm j12.7559)(-50.0007)}$
$p_{e_{3,3}}$	$\frac{1.3289e6\ (-0.0701 \pm j0.2587)(-10.4595)}{(0.0010)(-0.9489 \pm j1.7812)(-10.1092)(-12.7003 \pm j12.7559)(-50.0007)}$

C.2 *Effective Plant Transfer Functions* $\mathbf{P}_e(w')$

This section contains listings of the w'-plane effective plant transfer functions used in this study. Each table presents all the nonzero elements of the 3x3 $\mathbf{P}_e(w')$ for a given flight condition. Equation C.2 shows the notation used for the elements of $\mathbf{P}_e(w')$ in the tables.

$$\mathbf{P}_e(w') = \begin{bmatrix} \frac{q(w')}{\delta_q(w')} & 0 & 0 \\ 0 & \frac{p(w')}{\delta_p(w')} & \frac{p(w')}{\delta_r(w')} \\ 0 & \frac{r(w')}{\delta_p(w')} & \frac{r(w')}{\delta_r(w')} \end{bmatrix} = \begin{bmatrix} p_{e_{1,1}} & 0 & 0 \\ 0 & p_{e_{2,2}} & p_{e_{2,3}} \\ 0 & p_{e_{3,2}} & p_{e_{3,3}} \end{bmatrix} \tag{C.2}$$

Table C.7. $\mathbf{P}_e(w')$ Transfer Functions–Plant # 1

Element	Plant # 1
$p_{e_{1,1}}$	$\frac{5.4517e-5\ (0)(-0.6263 \pm j0.1696)(120)(-140.1131)(155.5707)(-947.3232)}{(-0.0198 \pm j0.5799)(-1.2908 \pm j1.8704)(-12.7956 \pm j12.6603)(-47.2948)}$
$p_{e_{2,2}}$	$\frac{1.4900e-4\ (0)(-0.4265 \pm j1.4601)(120)(-140.0479)(155.7088)(-935.7121)}{(0.1891)(-0.4390 \pm j2.0503)(-2.4875)(-12.7956 \pm j12.6600)(-47.2950)}$
$p_{e_{3,2}}$	$\frac{2.5406e-5\ (-1.1390)(1.5897 \pm j1.7959)(120)(-139.8569)(156.1404)(-902.3886)}{(0.1891)(-0.4390 \pm j2.0503)(-2.4875)(-12.7956 \pm j12.6600)(-47.2950)}$
$p_{e_{2,3}}$	$\frac{-1.1963e-4\ (0)(-0.7821)(3.9388)(120)(-139.7862)(156.3146)(-890.2361)}{(0.1891)(-0.4390 \pm j2.0503)(-2.4875)(-12.7956 \pm j12.6600)(-47.2950)}$
$p_{e_{3,3}}$	$\frac{1.0959e-4\ (-0.0474 \pm j0.6081)(-3.6879)(120)(-140.2478)(155.2860)(-972.2681)}{(0.1891)(-0.4390 \pm j2.0503)(-2.4875)(-12.7956 \pm j12.6600)(-47.2950)}$

Table C.8. $\mathbf{P}_e(w')$ Transfer Functions-Plant # 2

Element	Plant # 2
$p_{e_{1,1}}$	$\frac{3.4165e-4\ (0)(-0.0537)(-5.3864)(120)(-139.9607)(155.8809)(-921.0612)}{(0.1325)(-0.2352)(-1.2269)(-7.6616)(-12.7956 \pm j12.6603)(-47.2948)}$
$p_{e_{2,2}}$	$\frac{1.0989e-3\ (0)(-0.6238 \pm j3.4502)(120)(-139.3744)(157.1567)(-830.1928)}{(0.0222)(-0.5184 \pm j3.4035)(-12.4350)(-12.7956 \pm j12.6600)(-47.2950)}$
$p_{e_{3,2}}$	$\frac{1.1287e-4\ (0.1343 \pm j1.2799)(-12.0121)(120)(-140.0909)(155.6224)(-943.1903)}{(0.0222)(-0.5184 \pm j3.4035)(-12.4350)(-12.7956 \pm j12.6600)(-47.2950)}$
$p_{e_{2,3}}$	$\frac{-4.9059e-4\ (0)(1.1454 \pm j0.8033)(120)(-139.1551)(157.7230)(-798.5383)}{(0.0222)(-0.5184 \pm j3.4035)(-12.4350)(-12.7956 \pm j12.6600)(-47.2950)}$
$p_{e_{3,3}}$	$\frac{7.2857e-4\ (0.0828)(-0.2456)(-12.4706)(120)(-140.1535)(155.4964)(-954.2558)}{(0.0222)(-0.5184 \pm j3.4035)(-12.4350)(-12.7956 \pm j12.6600)(-47.2950)}$

Table C.9. $\mathbf{P}_e(w')$ Transfer Functions-Plant # 3

Element	Plant # 3
$p_{e_{1,1}}$	$\frac{3.0075e-4\ (0)(-0.0451)(-3.6614)(120)(-139.9680)(155.9448)(-919.4859)}{(-0.0139 \pm j0.2480)(-3.7150 \pm j6.6615)(-12.7956 \pm j12.6600)(-47.2950)}$
$p_{e_{2,2}}$	$\frac{9.7022e-4\ (0)(-0.6541 \pm j3.6979)(120)(-139.4677)(156.9547)(-843.3652)}{(0.0231)(-0.5333 \pm j3.6203)(-11.1034)(-12.7956 \pm j12.6600)(-47.2950)}$
$p_{e_{3,2}}$	$\frac{1.0974e-4\ (0.1806 \pm j1.4726)(-9.7213)(120)(-140.0154)(155.7766)(-930.1079)}{(0.0231)(-0.5333 \pm j3.6203)(-11.1034)(-12.7956 \pm j12.6600)(-47.2950)}$
$p_{e_{2,3}}$	$\frac{-4.5335e-4\ (0)(-0.8920)(3.4902)(120)(-139.2261)(157.5809)(-807.4862)}{(0.0231)(-0.5333 \pm j3.6203)(-11.1034)(-12.7956 \pm j12.6600)(-47.2950)}$
$p_{e_{3,3}}$	$\frac{6.8758e-4\ (-0.0506 \pm j0.1560)(-11.2272)(120)(-140.1542)(155.4983)(-954.2588)}{(0.0231)(-0.5333 \pm j3.6203)(-11.1034)(-12.7956 \pm j12.6600)(-47.2950)}$

Table C.10. $\mathbf{P}_e(w')$ Transfer Functions-Plant # 4

Element	Plant # 4
$p_{e_{1,1}}$	$\frac{1.3144e-4\ (0)(-0.0653)(-2.8615)(120)(-140.0838)(155.6183)(-942.5994)}{(-0.1501 \pm j0.4788)(0.6851)(-5.0558)(-12.7956 \pm j12.6600)(-47.2950)}$
$p_{e_{2,2}}$	$\frac{4.5052e-4\ (0)(-0.4825 \pm j2.4566)(120)(-139.7067)(156.4401)(-879.0487)}{(0.0543)(-0.3962 \pm j2.4613)(-7.5703)(-12.7956 \pm j12.6600)(-47.2950)}$
$p_{e_{3,2}}$	$\frac{5.8738e-5\ (0.1966 \pm j1.7502)(-4.0398)(120)(-139.8864)(156.0451)(-908.3511)}{(0.0543)(-0.3962 \pm j2.4613)(-7.5703)(-12.7956 \pm j12.6600)(-47.2950)}$
$p_{e_{2,3}}$	$\frac{-2.4784e-4\ (0)(-1.1706)(4.2851)(120)(-139.4485)(157.0792)(-838.3336)}{(0.0543)(-0.3962 \pm j2.4613)(-7.5703)(-12.7956 \pm j12.6600)(-47.2950)}$
$p_{e_{3,3}}$	$\frac{3.3242e-4\ (-0.0401 \pm j0.3217)(-8.0364)(120)(-140.1948)(155.4034)(-962.0808)}{(0.0543)(-0.3962 \pm j2.4613)(-7.5703)(-12.7956 \pm j12.6600)(-47.2950)}$

Table C.11. $\mathbf{P}_e(w')$ Transfer Functions-Plant # 5

Element	Plant # 5
$p_{e_{1,1}}$	$\frac{1.8248e-4\ (0)(-0.0676)(-3.4068)(120)(-140.0000)(155.8433)(-926.2329)}{(-0.0137 \pm j0.3428)(-3.2973 \pm j4.8623)(-12.7956 \pm j12.6600)(-47.2950)}$
$p_{e_{2,2}}$	$\frac{5.0799e-4\ (0)(-0.7265 \pm j3.1505)(120)(-139.6483)(156.5661)(-870.0592)}{(0.0503)(-0.6040 \pm j3.1508)(-8.4930)(-12.7956 \pm j12.6600)(-47.2950)}$
$p_{e_{3,2}}$	$\frac{8.5117e-5\ (0.1709 \pm j1.6364)(-5.8957)(120)(-139.9257)(155.9651)(-914.8122)}{(0.0503)(-0.6040 \pm j3.1508)(-8.4930)(-12.7956 \pm j12.6600)(-47.2950)}$
$p_{e_{2,3}}$	$\frac{-2.6272e-4\ (0)(-0.1371)(3.8069)(120)(-139.3252)(157.3713)(-820.5649)}{(0.0503)(-0.6040 \pm j3.1508)(-8.4930)(-12.7956 \pm j12.6600)(-47.2950)}$
$p_{e_{3,3}}$	$\frac{5.0342e-4\ (-0.0337)(-0.0637)(-8.8211)(120)(-140.1595)(155.4844)(-955.3193)}{(0.0503)(-0.6040 \pm j3.1508)(-8.4930)(-12.7956 \pm j12.6600)(-47.2950)}$

Table C.12. $\mathbf{P}_e(w')$ Transfer Functions-Plant # 6

Element	Plant # 6
$p_{e_{1,1}}$	$\frac{1.8455e-4\ (0)(-1.3601)(-3.3093)(120)(-139.9407)(155.9830)(-915.5680)}{(-0.0971)(-1.2042)(3.7212 \pm j5.4997)(-12.7956 \pm j12.6600)(-47.2950)}$
$p_{e_{2,2}}$	$\frac{5.1703e-4\ (0)(-1.0890 \pm j1.8156)(120)(-139.5386)(156.8025)(-853.6338)}{(0.0010)(-0.9491 \pm j1.1781)(-10.0853)(-12.7953 \pm j12.6596)(-47.2946)}$
$p_{e_{3,2}}$	$\frac{8.5794e-5\ (-0.0132 \pm j0.9472)(-7.1714)(120)(-139.8756)(156.0593)(-906.8621)}{(0.0010)(-0.9491 \pm j1.1781)(-10.0853)(-12.7953 \pm j12.6596)(-47.2946)}$
$p_{e_{2,3}}$	$\frac{-2.6700e-4\ (0)(-1.4932)(4.4202)(120)(-139.2179)(157.6095)(-806.1144)}{(0.0010)(-0.9491 \pm j1.1781)(-10.0853)(-12.7953 \pm j12.6596)(-47.2946)}$
$p_{e_{3,3}}$	$\frac{5.0762e-4\ (-0.0701 \pm j0.2587)(-10.4331)(120)(-140.1117)(155.5787)(-946.8793)}{(0.0010)(-0.9491 \pm j1.1781)(-10.0853)(-12.7953 \pm j12.6596)(-47.2946)}$

C.3 *Design Transfer Functions* $\mathbf{Q}(w')$

This section contains listings of the w'-plane effective plant design transfer functions used in this study. Each table presents all the nonzero elements of $\mathbf{Q}(w')$ for a given flight condition. Equation C.3 shows the notation used for the elements of $\mathbf{Q}(w')$ in the tables.

$$\mathbf{Q}(w') = \begin{bmatrix} q_{1,1}(w') & \infty & \infty \\ \infty & q_{2,2}(w') & q_{2,3}(w') \\ \infty & q_{3,2}(w') & q_{3,3}(w') \end{bmatrix} \tag{C.3}$$

Table C.13. $\mathbf{Q}(w')$ Transfer Functions–Plant # 1

Element	Plant # 1
$q_{1,1}$	$\frac{5.4517e-5\ (0)(-0.6263 \pm j0.1696)(120)(-140.1131)(155.5707)(-947.3232)}{(-0.0198 \pm j0.5799)(-1.2908 \pm j1.8704)(-12.7956 \pm j12.6603)(-47.2948)}$
$q_{2,2}$	$\frac{1.7669e-4\ (0)(-0.0661)(120)(-140.0997)(155.5963)(-972.2681)}{(-0.0474 \pm j0.6081)(-3.6879)(-12.8491 \pm j12.6632)(-47.1230)}$
$q_{3,2}$	$\frac{-8.0711e-4\ (0)(-0.0661)(120)(-140.0997)(155.5963)(-944.8428)}{(-1.1390)(1.5897 \pm j1.7959)(-12.8289 \pm j12.7042)(-47.4427)}$
$q_{2,3}$	$\frac{1.7141e-4\ (-0.0661)(120)(-140.1008)(155.5963)(-944.8400)}{(-0.7821)(3.9388)(-12.8130 \pm j12.7074)(-47.1581)}$
$q_{3,3}$	$\frac{1.2999e-4\ (0)(-0.0661)(120)(-140.9967)(155.5963)(-935.7121)}{(0)(-0.4265 \pm j1.4601)(-12.8472 \pm j12.6911)(-47.3705)}$

Table C.14. $\mathbf{Q}(w')$ Transfer Functions-Plant # 2

Element	Plant # 2
$q_{1,1}$	$\frac{3.4165e-4\ (0)(-0.0537)(-5.3864)(120)(-139.9607)(155.8809)(-921.0612)}{(0.1325)(-0.2352)(-1.2269)(-7.6616)(-12.7956 \pm j12.6603)(-47.2948)}$
$q_{2,2}$	$\frac{1.1750e-3\ (0)(-0.1576)(120)(-139.3616)(157.1885)(-828.3031)}{(0.0828)(-0.2456)(-12.4706)(-12.8582 \pm j12.6983)(-47.4953)}$
$q_{3,2}$	$\frac{-7.5845e-3\ (0)(-0.1576)(120)(-139.3616)(157.1885)(-828.3031)}{(0.1343 \pm j1.2799)(-12.0121)(-12.8388 \pm j12.7237)(-47.5038)}$
$q_{2,3}$	$\frac{1.8479e-3\ (-0.1576)(120)(-140.1485)(155.5064)(-953.3663)}{(1.1454 \pm j0.8033)(-12.8665 \pm j12.6758)(-47.4853)}$
$q_{3,3}$	$\frac{7.7895e-4\ (0)(-0.1576)(120)(-140.1485)(155.5064)(-953.3663)}{(0)(-0.6238 \pm j3.4502)(-12.8500 \pm j12.7167)(-47.1625)}$

Table C.15. $\mathbf{Q}(w')$ Transfer Functions-Plant # 3

Element	Plant # 3
$q_{1,1}$	$\frac{3.0075e-4\ (0)(-0.0451)(-3.6614)(120)(-139.9680)(155.9448)(-919.4859)}{(-0.0139 \pm j0.2480)(-3.7150 \pm j6.6615)(-12.7956 \pm j12.6600)(-47.2950)}$
$q_{2,2}$	$\frac{1.0426e-3\ (0)(-0.1065)(120)(-139.4546)(156.9874)(-841.3625)}{(-0.0506 \pm j0.1560)(-11.2272)(-12.8748 \pm j12.6823)(-47.4210)}$
$q_{3,2}$	$\frac{-6.5323e-3\ (0)(-0.1065)(120)(-139.4546)(156.9874)(-841.3625)}{(0.1806 \pm j1.4726)(-9.7213)(-12.8617 \pm j12.7206)(-47.1282)}$
$q_{2,3}$	$\frac{1.6745e-3\ (-0.1065)(120)(-140.1419)(155.5230)(-952.0646)}{(-0.8920)(3.4902)(-12.8356 \pm j12.7142)(-47.1076)}$
$q_{3,3}$	$\frac{7.3886e-4\ (0)(-0.1065)(120)(-140.1419)(155.5230)(-952.0646)}{(0)(-0.6541 \pm j3.6979)(-12.8412 \pm j12.7109)(-47.1565)}$

Table C.16. $\mathbf{Q}(w')$ Transfer Functions-Plant # 4

Element	Plant # 4
$q_{1,1}$	$\frac{1.3144e-4\ (0)(-0.0653)(-2.8615)(120)(-140.0838)(155.6183)(-942.5994)}{(-0.1501 \pm j0.4788)(0.6851)(-5.0558)(-12.7956 \pm j12.6600)(-47.2950)}$
$q_{2,2}$	$\frac{4.9431e-4\ (0)(-0.0830)(120)(-139.6980)(156.4615)(-877.6426)}{(-0.0401 \pm j0.3217)(-8.0364)(-12.8498 \pm j12.6991)(-47.1429)}$
$q_{3,2}$	$\frac{-2.7975e-3\ (0)(-0.0830)(120)(-140.1558)(155.4822)(-955.0356)}{(0.1966 \pm j1.7502)(-4.0398)(-12.8538 \pm j12.6931)(-47.1554)}$
$q_{2,3}$	$\frac{7.0212e-4\ (-0.0830)(120)(-140.1558)(155.4822)(-955.0356)}{(-1.1706)(4.2851)(-12.8134 \pm j12.7222)(-47.1643)}$
$q_{3,3}$	$\frac{3.6473e-4\ (0)(-0.0830)(120)(-140.1558)(155.4822)(-955.0356)}{(0)(-0.4825 \pm j2.4566)(-12.8281 \pm j12.7080)(-47.1357)}$

Table C.17. Q(w') Transfer Functions-Plant # 5

Element	Plant # 5
$q_{1,1}$	$\frac{1.8248e-4\ (0)(-0.0676)(-3.4068)(120)(-140.0000)(155.8433)(-926.2329)}{(-0.0137 \pm j0.3428)(-3.2973 \pm j4.8623)(-12.7956 \pm j12.6600)(-47.2950)}$
$q_{2,2}$	$\frac{5.5241e-4\ (0)(-0.0976)(120)(-139.6341)(156.5994)(-867.8138)}{(-0.0337)(-0.0637)(-8.8211)(-12.8540 \pm j12.6876)(-47.4875)}$
$q_{3,2}$	$\frac{-3.2672e-3\ (0)(-0.0976)(120)(-140.1311)(156.5994)(-950.2532)}{(0.1709 \pm j1.6364)(-5.8957)(-12.8834 \pm j12.6775)(-47.4973)}$
$q_{2,3}$	$\frac{1.1210e-3\ (-0.0976)(120)(-140.1311)(155.5417)(-950.2532)}{(-0.1371)(3.8069)(-12.8382 \pm j12.6938)(-47.4333)}$
$q_{3,3}$	$\frac{5.4744e-4\ (0)(-0.0976)(120)(-140.1311)(155.5417)(-950.2532)}{(0)(-0.7265 \pm j3.1505)(-12.8398 \pm j12.7029)(-47.3843)}$

Table C.18. Q(w') Transfer Functions-Plant # 6

Element	Plant # 6
$q_{1,1}$	$\frac{1.8455e-4\ (0)(-1.3601)(-3.3093)(120)(-139.9407)(155.9830)(-915.5680)}{(-0.0971)(-1.2042)(-3.7212 \pm j5.4997)(-12.7956 \pm j12.6600)(-47.2950)}$
$q_{2,2}$	$\frac{5.6216e-4\ (0)(-0.1466)(120)(-139.5234)(156.8387)(-851.3130)}{(-0.0701 \pm j0.2587)(-10.4331)(-12.8653 \pm j12.7141)(-47.1209)}$
$q_{3,2}$	$\frac{-3.3261e-3\ (0)(-0.1466)(120)(-140.0843)(155.6334)(-851.3130)}{(-0.0132 \pm j0.9472)(-7.1714)(-12.8833 \pm j12.6763)(-47.4618)}$
$q_{2,3}$	$\frac{1.2702e-3\ (-0.1466)(120)(-140.0843)(155.6334)(-851.3130)}{(-1.4932)(4.4202)(-12.8215 \pm j12.7387)(-47.4669)}$
$q_{3,3}$	$\frac{5.5193e-4\ (0)(-0.1466)(120)(-140.0843)(155.6334)(-942.1000)}{(0)(-1.0890 \pm j1.8156)(-12.8341 \pm j12.7253)(-47.4609)}$

Appendix D. *QFT Design Response Models*

This appendix presents the QFT design response models used in this thesis. The roll-rate response model (p) and the yaw-rate response model (r) are the same as those used by Hamilton [8]. The pitch-rate response model (q) is synthesized to provide desirable pitch-rate time-domain figures-of-merit. Table D.1 lists the figures-of-merit for all the response models. The w'-plane and s-plane response models are presented.

D.1 s-plane Models

D.1.1 Lower Bound Pitch-Rate (q)

$$\frac{q_{LB}(s)}{q_{cmd_{LB}}(s)} = \frac{270}{(s+3)(s+9)(s+10)} \tag{D.1}$$

D.1.2 Upper Bound Pitch-Rate (q)

$$\frac{q_{UB}(s)}{q_{cmd_{UB}}(s)} = \frac{100}{s^2+8s+100} \tag{D.2}$$

D.1.3 Lower Bound Roll-Rate (p)

$$\frac{p_{LB}(s)}{p_{cmd_{LB}}(s)} = \frac{192}{(s+4)(s+4)(s+12)} \tag{D.3}$$

D.1.4 Upper Bound Roll-Rate (p)

$$\frac{p_{UB}(s)}{p_{cmd_{UB}}(s)} = \frac{5}{s+5} \tag{D.4}$$

D.1.5 Lower Bound Yaw-Rate (r)

$$\frac{r_{LB}(s)}{r_{cmd_{LB}}(s)} = \frac{3}{(s+1)(s+1)(s+3)} \tag{D.5}$$

D.1.6 Upper Bound Yaw-Rate (r)

$$\frac{r_{UB}(s)}{r_{cmd_{UB}}(s)} = \frac{1.25}{s+1.25} \tag{D.6}$$

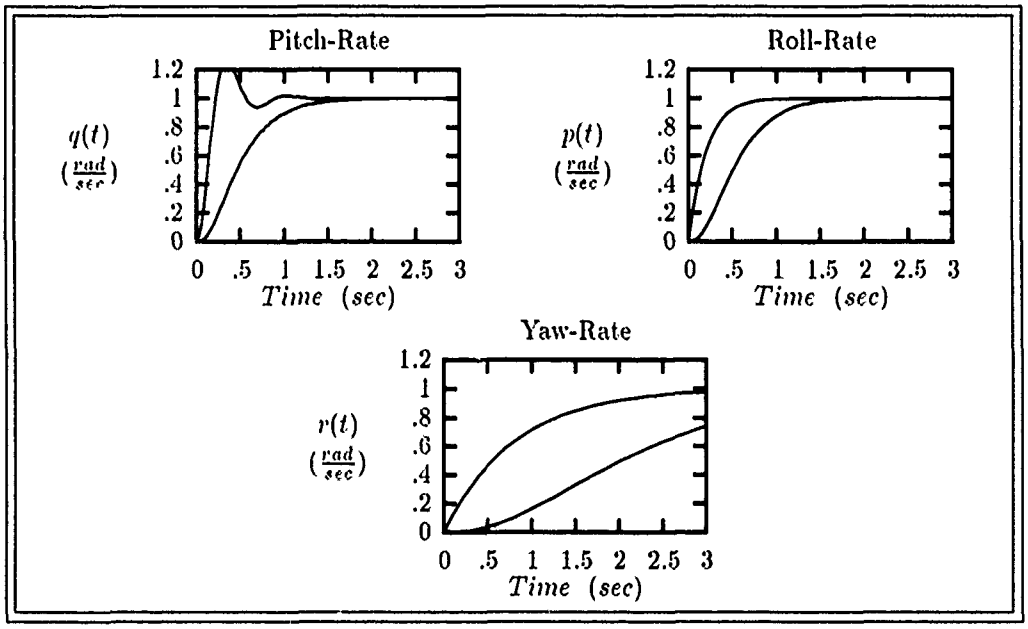

Figure D.1. s-plane QFT Closed-Loop Channel Design Model Step Response Bounds

Table D.1 presents the s-plane response model figures-of-merit. For this study, the s and w′-plane models are approximately equal and thus the figures in Table D.1 also apply to the w′-plane models presented next.

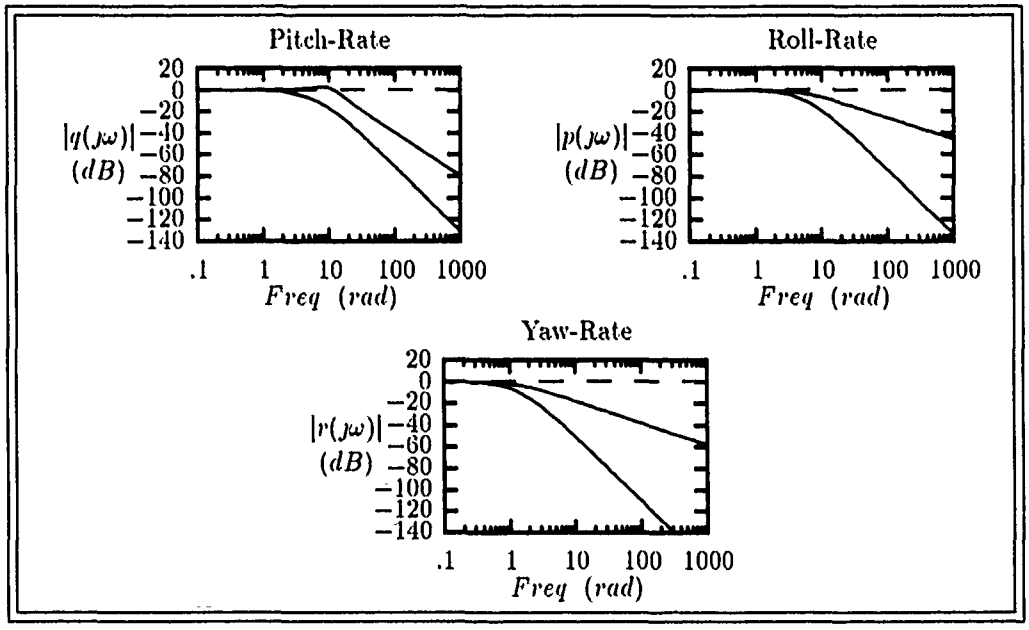

Figure D.2. s-plane QFT Closed-Loop Channel Design Model Frequency Response Bounds

Table D.1. Figures-of-Merit for the QFT Response Models

Model	T_r (sec)	T_s (sec)	M_p $\frac{rad}{sec}$	FV $\frac{rad}{sec}$
$\frac{q_{LB}(s)}{q_{cmd_{LB}}(s)}$	0.84	1.56	1.0	1.0
$\frac{q_{UB}(s)}{q_{cmd_{UB}}(s)}$	0.15	0.34	1.25	1.0
$\frac{p_{LB}(s)}{p_{cmd_{LB}}(s)}$	0.87	1.56	1.0	1.0
$\frac{p_{UB}(s)}{p_{cmd_{UB}}(s)}$	0.44	0.78	1.0	1.0
$\frac{r_{LB}(s)}{r_{cmd_{LB}}(s)}$	3.48	6.22	1.0	1.0
$\frac{r_{UB}(s)}{r_{cmd_{UB}}(s)}$	1.76	3.13	1.0	1.0

The notation used in Table D.1 is as follows:

- T_r—rise time
- T_s—settling time
- M_p—maximum peak value
- FV—final value

D.2 w'-plane Models

D.2.1 Lower Bound Pitch-Rate (q)

$$\frac{q_{LB}(w')}{q_{cmd_{LB}}(w')} = \frac{5.16e-5(w'-120)(w'+197.6)(w'-219.7)}{(w'+3.00)(w'+8.98)(w'+9.98)} \tag{D.7}$$

D.2.2 Upper Bound Pitch-Rate (q)

$$\frac{q_{UB}(w')}{q_{cmd_{UB}}(w')} = \frac{1.55e-4(w'-120)(w'+5396)}{w'+4.02\pm j9.17} \tag{D.8}$$

D.2.3 Lower Bound Roll-Rate (p)

$$\frac{p_{LB}(w')}{p_{cmd_{LB}}(w')} = \frac{0.37e-4(w'-120)(w'+198.5)(w'-218.5)}{(w'+3.99)(w'+3.99)(w'+11.96)} \tag{D.9}$$

D.2.4 Upper Bound Roll-Rate (p)

$$\frac{p_{UB}(w')}{p_{cmd_{UB}}(w')} = \frac{-0.0416(w'-120)}{w'+4.997} \tag{D.10}$$

D.2.5 Lower Bound Yaw-Rate (r)

$$\frac{r_{LB}(w')}{r_{cmd_{LB}}(w')} = \frac{5.78e-5(w'-120)(w'+205.4)(w'-210.4)}{(w'+1.00)(w'+1.00)(w'+2.99)} \tag{D.11}$$

D.2.6 Upper Bound Yaw-Rate (r)

$$\frac{r_{UB}(w')}{r_{cmd_{UB}}(w')} = \frac{-0.0104(w'-120)}{w'+1.25} \tag{D.12}$$

Since this is a w'-plane design, the frequency response plots in Figure D.3 describe the QFT loop transmission performance frequency bounds for each MISO equivalent loop synthesis.

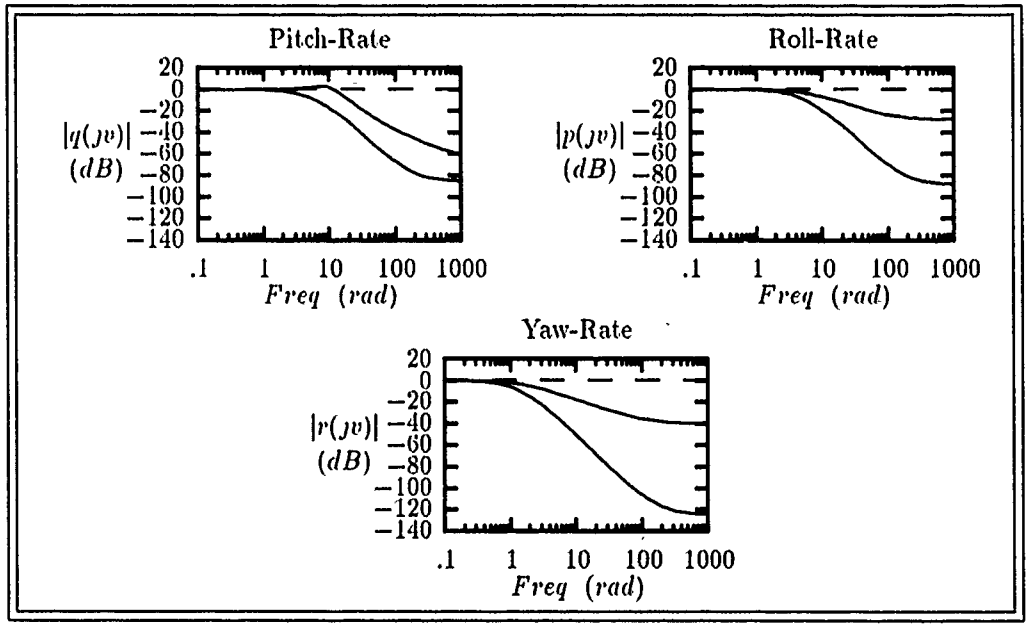

Figure D.3. w'-plane QFT Closed-Loop Channel Design Model Frequency Response Bounds

Appendix E. *Template Data*

These tables contain all w′-plane template data generated by Matrix$_x$ for potential use in this design. Templates are not necessarily generated for each v_k shown in the tables below. The actual templates used in the design are shown graphically on the NC in the figures in each section below. The scales on each NC are identical so the relative uncertainty between the loops is easily seen.

E.1 Pitch-Loop ($q_{1,1}$) SISO

Table E.1. Pitch-Loop ($q_{1,1}$) Templates for $v_k = 0.001, 0.01$ *rad/sec*

Frequency	v_k = 0.001 rad/sec		v_k = 0.01 rad/sec	
Plant #	Phase (°)	Magnitude (dB)	Phase (°)	Magnitude (dB)
1	90.1290	−53.4132	91.2897	−33.4088
2	−88.7934	−25.5107	−78.0601	−5.3964
3	91.2477	−53.2603	102.2761	−33.0397
4	−89.1049	−46.8717	−81.1163	−26.7702
5	90.8340	−55.7196	98.2795	−35.6192
6	89.4063	−31.9721	84.0835	−12.0174

Table E.2. Pitch-Loop ($q_{1,1}$) Templates for $v_k = 0.05, 0.1$ *rad/sec*

Frequency	v_k = 0.05 rad/sec		v_k = 0.1 rad/sec	
Plant #	Phase (°)	Magnitude (dB)	Phase (°)	Magnitude (dB)
1	96.4339	−19.3233	102.7767	−12.9691
2	−40.8366	10.4051	−19.1720	18.2878
3	136.7410	−15.4400	152.8898	−4.0088
4	−51.7072	−10.8412	−31.6676	−1.4318
5	125.7974	−19.6589	144.4628	−9.9118
6	62.5694	0.9867	43.7806	4.8887

Table E.3. Pitch-Loop ($q_{1,1}$) Templates for $v_k = 0.2, 0.3$ *rad/sec*

Frequency	v_k = 0.2 rad/sec		v_k = 0.3 rad/sec	
Plant #	Phase (°)	Magnitude (dB)	Phase (°)	Magnitude (dB)
1	114.8213	−5.5800	125.3567	0.3810
2	−8.7745	24.6102	−10.5059	26.8080
3	153.3925	14.7307	8.5278	19.2945
4	−17.1351	10.1351	−16.9942	18.0533
5	157.2437	3.7952	150.7141	19.2176
6	25.1437	6.8502	16.8347	7.3304

Table E.4. Pitch-Loop ($q_{1,1}$) Templates for $v_k = 0.33, 0.4$ *rad/sec*

Frequency	v_k = 0.33 rad/sec		v_k = 0.4 rad/sec	
Plant #	Phase (°)	Magnitude (dB)	Phase (°)	Magnitude (dB)
1	128.0800	2.2009	133.2567	6.8416
2	−11.6684	27.1566	−14.7582	27.6807
3	3.9344	16.6967	0.8804	13.7654
4	−19.3985	20.0837	−30.6330	24.2390
5	122.6531	28.0415	4.7889	20.5733
6	15.1989	7.4005	12.2360	7.5080

Table E.5. Pitch-Loop ($q_{1,1}$) Templates for $v_k = 0.5, 0.6$ *rad/sec*

Frequency	v_k = 0.5 rad/sec		v_k = 0.6 rad/sec	
Plant #	Phase (°)	Magnitude (dB)	Phase (°)	Magnitude (dB)
1	134.0831	16.0384	19.2829	27.4963
2	−19.4357	28.0101	−24.0086	28.0744
3	0.1202	12.0428	0.1334	11.2563
4	−59.4491	27.5827	−84.5982	27.2255
5	−1.9954	14.7752	−2.8370	12.7383
6	9.3163	7.5914	7.2967	7.6396

Table E.6. Pitch-Loop ($q_{1,1}$) Templates for $v_k = 0.7, 1$ *rad/sec*

Frequency	v_k = 0.7 rad/sec		v_k = 1 rad/sec	
Plant #	Phase (°)	Magnitude (dB)	Phase (°)	Magnitude (dB)
1	−10.6740	16.8365	−9.6879	11.4462
2	−28.3315	27.9923	−39.5995	27.3354
3	0.3093	10.8410	0.8732	10.4163
4	−96.7143	25.7123	−104.3307	22.1122
5	−2.9637	11.7376	−2.9783	10.6496
6	5.8178	7.6750	3.0686	7.7845

Table E.7. Pitch-Loop ($q_{1,1}$) Templates for $v_k = 2, 3$ *rad/sec*

Frequency	v_k = 2 rad/sec		v_k = 3 rad/sec	
Plant #	Phase (°)	Magnitude (dB)	Phase (°)	Magnitude (dB)
1	−33.3024	11.9721	−67.6693	10.3740
2	−63.6075	24.3334	−77.5413	21.8380
3	0.5694	11.0366	−3.8257	12.3916
4	−100.5699	16.6084	−101.0169	13.8952
5	−6.3436	10.9673	−15.6318	12.2704
6	−1.8577	8.6273	−9.3776	9.9729

Table E.8. Pitch-Loop ($q_{1,1}$) Templates for $v_k = 4, 5$ *rad/sec*

Frequency	v_k = 4 rad/sec		v_k = 5 rad/sec	
Plant #	Phase (°)	Magnitude (dB)	Phase (°)	Magnitude (dB)
1	−88.3494	7.7882	−101.8639	5.5817
2	−87.9296	19.9241	96.9799	18.3982
3	−12.5966	13.9224	−25.7130	15.3475
4	−104.9436	12.0677	−110.6245	10.6270
5	−30.6432	13.4875	−49.7038	14.1147
6	−21.6016	11.3378	−37.9630	12.3410

Table E.9. Pitch-Loop ($q_{1,1}$) Templates for $v_k = 6, 7$ *rad/sec*

Frequency	v_k = 6 rad/sec		v_k = 7 rad/sec	
Plant #	Phase (°)	Magnitude (dB)	Phase (°)	Magnitude (dB)
1	−112.4236	3.7712	−121.6310	2.2414
2	−105.4883	17.1193	−113.7610	15.9981
3	−42.6400	16.3937	−61.8551	16.8283
4	−117.1782	9.3902	−124.1775	8.2766
5	−69.6567	13.9568	−87.8154	13.1929
6	−56.6280	12.7289	−75.2257	12.4780

Table E.10. Pitch-Loop ($q_{1,1}$) Templates for $v_k = 8, 9$ *rad/sec*

Frequency	v_k = 8 rad/sec		v_k = 9 rad/sec	
Plant #	Phase (°)	Magnitude (dB)	Phase (°)	Magnitude (dB)
1	−130.1526	0.9032	−138.2962	−0.3046
2	−121.9198	14.9779	−130.0103	14.0211
3	−81.1098	16.6033	−98.6838	15.8825
4	−131.4138	7.2435	−138.7793	6.2636
5	−103.3595	12.1261	−116.6558	10.9623
6	−92.1459	11.7688	−106.9826	10.8158

Table E.11. Pitch-Loop ($q_{1,1}$) Templates for $v_k = 10, 11$ *rad/sec*

Frequency	v_k = 10 rad/sec		v_k = 11 rad/sec	
Plant #	Phase (°)	Magnitude (dB)	Phase (°)	Magnitude (dB)
1	−146.2100	−1.4247	−153.9606	−2.4880
2	−138.0419	13.1016	−146.0033	12.2006
3	−114.0488	14.8874	−127.4377	13.7753
4	−146.2087	5.3169	−153.6522	4.3880
5	−128.3148	9.7945	−138.8260	8.6527
6	−120.0054	9.7626	−131.6320	8.6804

Table E.12. Pitch-Loop ($q_{1,1}$) Templates for $v_k = 20, 50$ *rad/sec*

Frequency	v_k = 20 rad/sec		v_k = 50 rad/sec	
Plant #	Phase (°)	Magnitude (dB)	Phase (°)	Magnitude (dB)
1	−214.8461	−11.5620	57.6596	−34.5012
2	−209.2264	3.7806	60.2514	−18.8587
3	−205.6883	3.7277	60.6808	−19.7953
4	−214.0567	−4.1965	58.0944	−26.9385
5	−208.7152	−0.9308	59.8731	−24.1392
6	−205.6163	−0.8727	61.0215	−24.1266

Table E.13. Pitch-Loop ($q_{1,1}$) Templates for $v_k = 100, 1000$ *rad/sec*

Frequency	v_k = 100 rad/sec		v_k = 1000 rad/sec	
Plant #	Phase (°)	Magnitude (dB)	Phase (°)	Magnitude (dB)
1	9.9142	−52.6413	−31.4884	−82.2471
2	11.4105	−36.9516	−30.5339	−66.4199
3	11.5687	−38.0249	−30.4704	−67.5335
4	10.1705	−45.0493	−31.3196	−74.6236
5	11.1445	−42.3207	−30.7213	−71.8443
6	11.7858	−42.3163	−30.3263	−71.7924

Table E.14. Pitch-Loop ($q_{1,1}$) Template for $v_k = 10000$ *rad/sec*

Frequency	v_k = 10000 rad/sec	
Plant #	Phase (°)	Magnitude (dB)
1	−4.2101	−85.2281
2	−4.0458	−69.2894
3	−4.0354	−70.3968
4	−4.1807	−77.5845
5	−4.0779	−74.7360
6	−4.0109	−74.6390

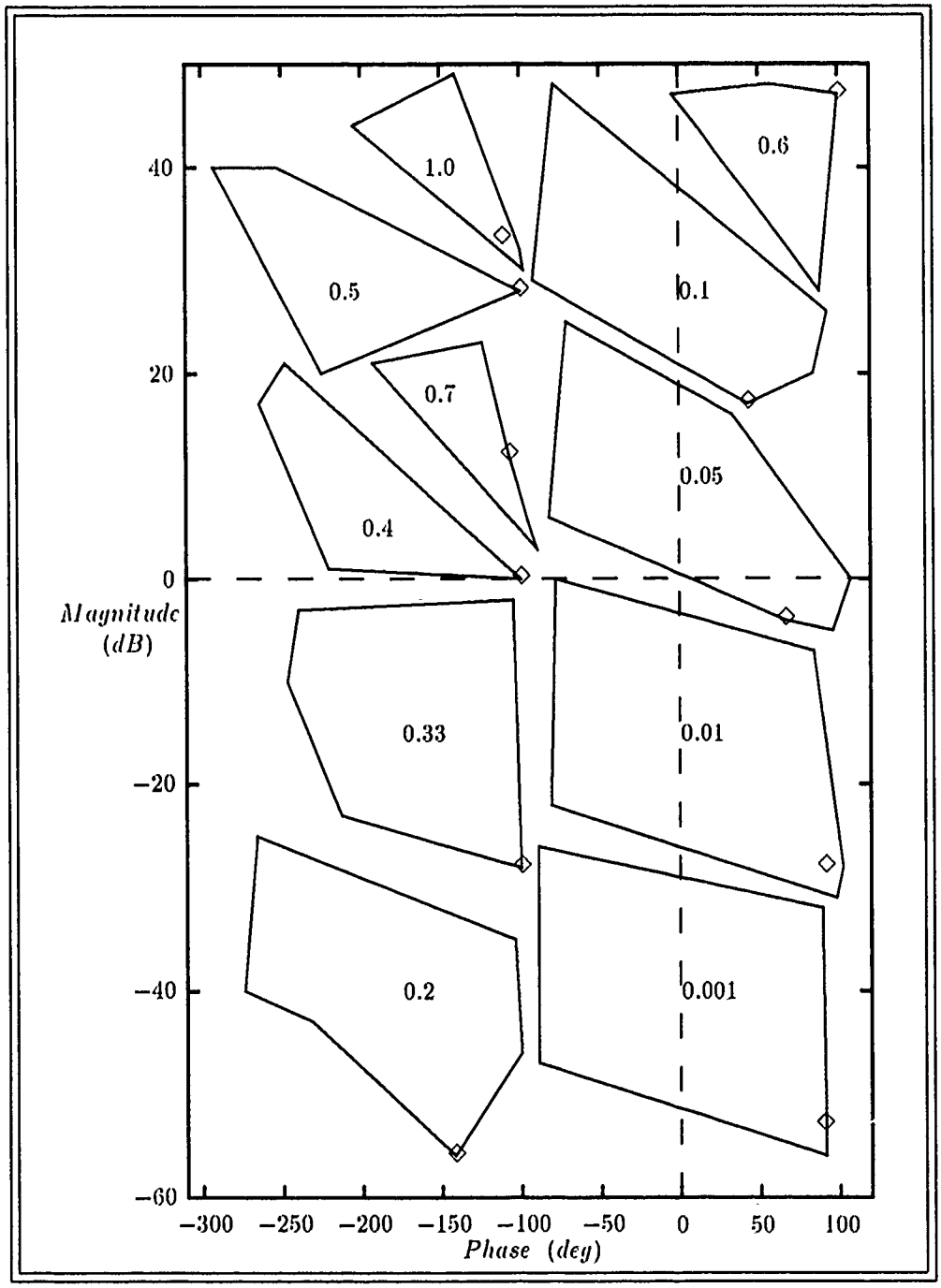

Figure E.1. Pitch-Rate Channel Plant Templates ($q_{1,1}$) $v_k = 0.001, 0.01, 0.05, 0.1, 0.2, 0.33, 0.4, 0.5, 0.6, 0.7, 1$ rad/sec With Plant Case # 1 Nominal

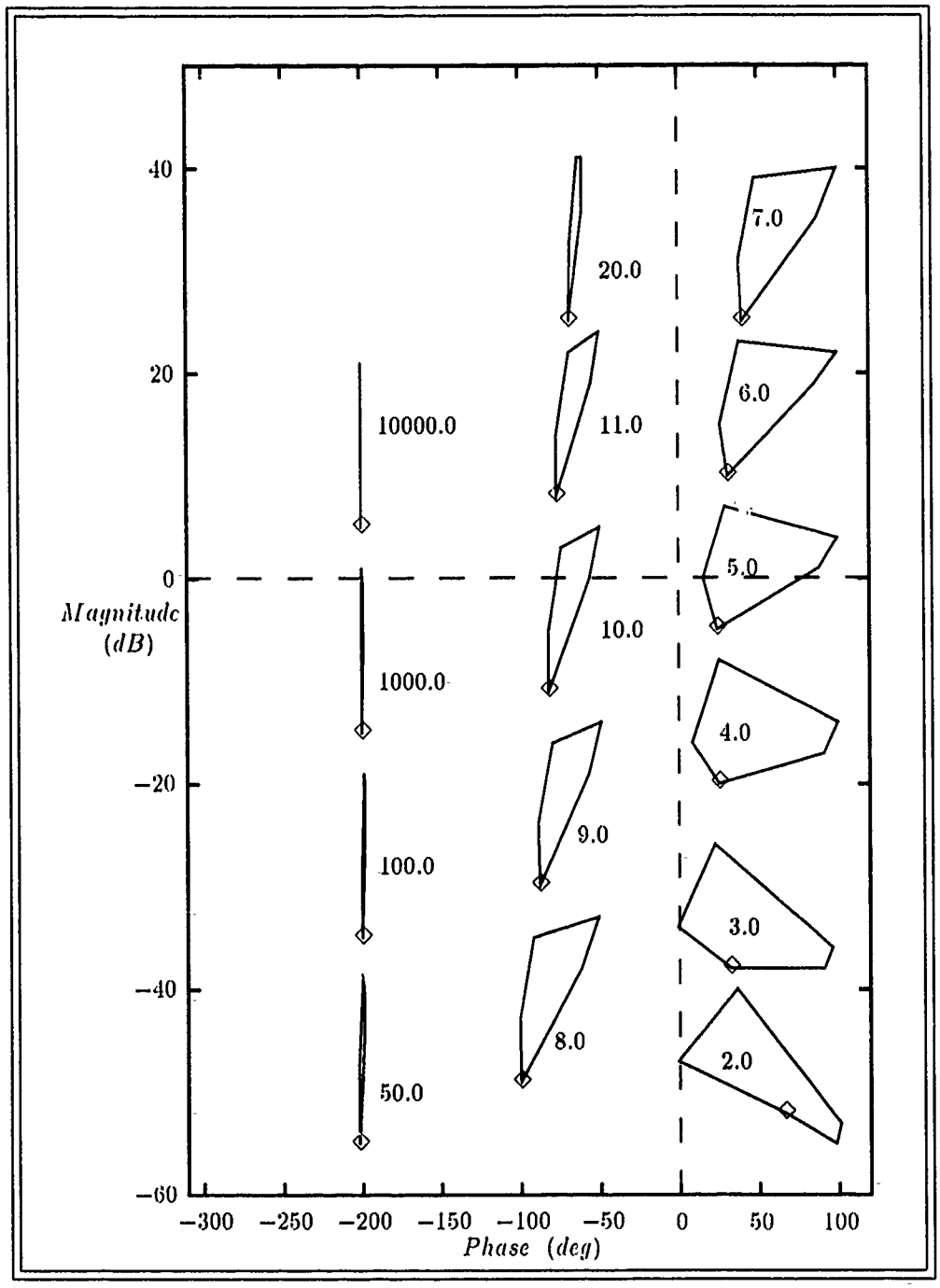

Figure E.2. Pitch-Rate Channel Plant Templates ($q_{1,1}$) v_k = 2, 3, 4, 5, 6, 7, 8, 9, 10, 11, 20, 50, 100, 1000, 10000 rad/sec With Plant Case # 1 Nominal

E.2 *Roll-Loop ($q_{2,2_e}$) MIMO Loop #2*

Table E.15. Roll-Loop ($q_{2,2_e}$) Templates for $v_k = 0.001, 0.01$ *rad/sec*

Frequency	v_k = 0.001 rad/sec		v_k = 0.01 rad/sec	
Plant #	Phase (°)	Magnitude (dB)	Phase (°)	Magnitude (dB)
1	90.7523	−56.9995	97.4645	−36.9175
2	−89.2106	−19.7787	−82.1399	0.1691
3	90.2570	−25.5991	92.5530	−5.5459
4	90.5743	−42.7704	95.7203	−22.7117
5	87.7931	−7.5672	68.7308	11.8917
6	90.2520	−35.9475	92.5138	−15.9192

Table E.16. Roll-Loop ($q_{2,2_e}$) Templates for $v_k = 0.1, 0.2$ *rad/sec*

Frequency	v_k = 0.1 rad/sec		v_k = 0.2 rad/sec	
Plant #	Phase (°)	Magnitude (dB)	Phase (°)	Magnitude (dB)
1	140.2571	−12.1416	151.7614	−0.7328
2	−31.4986	17.0747	−12.5905	19.7684
3	99.5682	19.0677	32.1140	27.9816
4	131.7544	1.4646	139.4120	14.4413
5	7.6783	20.0248	−0.0158	19.6298
6	109.3726	6.6410	100.1964	18.7606

Table E.17. Roll-Loop ($q_{2,2_e}$) Templates for $v_k = 0.3, 0.4$ *rad/sec*

Frequency	v_k = 0.3 rad/sec		v_k = 0.4 rad/sec	
Plant #	Phase (°)	Magnitude (dB)	Phase (°)	Magnitude (dB)
1	152.7362	7.1874	148.6616	13.9461
2	−7.2371	20.8732	−5.9491	21.4342
3	4.2932	25.3234	−1.8212	24.0692
4	114.9942	27.5544	18.5220	28.1894
5	−2.5597	19.4643	−4.2738	19.3911
6	39.9568	24.6016	8.7278	22.1924

Table E.18. Roll-Loop ($q_{2,2_e}$) Templates for $v_k = 0.5, 0.6$ *rad/sec*

Frequency	v_k = 0.5 rad/sec		v_k = 0.6 rad/sec	
Plant #	Phase (°)	Magnitude (dB)	Phase (°)	Magnitude (dB)
1	138.0419	20.4708	131.2190	31.6977
2	−6.0386	21.7472	−6.6602	21.9347
3	−4.4861	23.4783	−6.2288	23.1552
4	1.1636	24.1820	−4.2191	22.4195
5	−5.7555	19.3510	−7.1463	19.3247
6	−0.2175	20.5846	−4.1867	19.7097

Table E.19. Roll-Loop ($q_{2,2_e}$) Templates for $v_k = 0.7, 0.8$ *rad/sec*

Frequency	v_k = 0.7 rad/sec		v_k = 0.8 rad/sec	
Plant #	Phase (°)	Magnitude (dB)	Phase (°)	Magnitude (dB)
1	22.9545	30.9076	0.4182	26.2881
2	−7.5116	22.0534	−8.4711	22.1317
3	−7.6418	22.9582	−8.9139	22.8280
4	−7.1552	21.4723	−9.2712	20.8941
5	−8.4929	19.3046	−9.8146	19.2874
6	−6.6098	19.1887	−8.4192	18.8524

Table E.20. Roll-Loop ($q_{2,2_e}$) Templates for $v_k = 0.9, 1$ *rad/sec*

Frequency	v_k = 0.9 rad/sec		v_k = 1 rad/sec	
Plant #	Phase (°)	Magnitude (dB)	Phase (°)	Magnitude (dB)
1	−8.3412	23.8790	−13.6224	22.4193
2	−9.4851	22.1847	−10.5277	22.2213
3	−10.1183	22.7361	−11.2869	22.6676
4	−11.0363	20.5098	−12.6271	20.2378
5	−11.1205	19.2713	−12.4155	19.2556
6	−9.9439	18.6212	−11.3215	18.4539

Table E.21. Roll-Loop ($q_{2,2_e}$) Templates for $v_k = 2,3$ *rad/sec*

Frequency	v_k = 2 rad/sec		v_k = 3 rad/sec	
Plant #	Phase (°)	Magnitude (dB)	Phase (°)	Magnitude (dB)
1	−40.6369	18.1635	−60.9379	16.3383
2	−21.2353	22.2631	−31.8631	22.1279
3	−22.5070	22.3544	−33.5133	22.1264
4	−26.3222	19.2367	−39.1286	18.7502
5	−25.0665	19.0591	−37.3349	18.7637
6	−23.2522	17.8177	−34.5979	17.5066

Table E.22. Roll-Loop ($q_{2,2_e}$) Templates for $v_k = 4,5$ *rad/sec*

Frequency	v_k = 4 rad/sec		v_k = 5 rad/sec	
Plant #	Phase (°)	Magnitude (dB)	Phase (°)	Magnitude (dB)
1	−77.6062	14.3518	−88.6470	12.1610
2	−42.3421	21.9189	−52.6733	21.6527
3	−44.3488	21.8561	−54.9928	21.5334
4	−51.3990	18.2435	−63.0911	17.6744
5	−49.2046	18.3770	−60.6460	17.9146
6	−45.7003	17.1810	−56.5462	16.8077

Table E.23. Roll-Loop ($q_{2,2_e}$) Templates for $v_k = 6,7$ *rad/sec*

Frequency	v_k = 6 rad/sec		v_k = 7 rad/sec	
Plant #	Phase (°)	Magnitude (dB)	Phase (°)	Magnitude (dB)
1	−93.2302	10.4139	−96.4219	9.6352
2	−62.8581	21.3354	−72.8960	20.9694
3	−65.4353	21.1596	−75.6725	20.7370
4	−74.1854	17.0491	−84.6915	16.3809
5	−71.6560	17.3911	−82.2501	16.8178
6	−67.1226	16.3840	−77.4254	15.9127

Table E.24. Roll-Loop ($q_{2,2_c}$) Templates for $v_k = 8, 10$ *rad/sec*

Frequency	v_k = 8 rad/sec		v_k = 10 rad/sec	
Plant #	Phase (°)	Magnitude (dB)	Phase (°)	Magnitude (dB)
1	−102.6791	9.3311	−120.9144	8.5005
2	−82.7829	20.5558	−102.0588	19.5865
3	−85.7021	20.2677	−105.1125	19.1929
4	−94.6343	15.6834	−112.9846	14.2534
5	−92.4509	16.2029	−111.7460	14.8689
6	−87.4542	15.3972	−106.6803	14.2448

Table E.25. Roll-Loop ($q_{2,2_c}$) Templates for $v_k = 50, 100$ *rad/sec*

Frequency	v_k = 50 rad/sec		v_k = 100 rad/sec	
Plant #	Phase (°)	Magnitude (dB)	Phase (°)	Magnitude (dB)
1	62.3476	−22.6602	11.8040	−40.8156
2	74.4709	−8.3109	17.3221	−26.4089
3	73.0468	−9.1261	16.5375	−27.2566
4	67.4457	−15.1776	14.6238	−33.3137
5	69.3868	−14.3269	15.2006	−32.4663
6	71.0242	−14.3882	16.1511	−32.4945

Table E.26. Roll-Loop ($q_{2,2_c}$) Templates for $v_k = 1000, 10000$ *rad/sec*

Frequency	v_k = 1000 rad/sec		v_k = 10000 rad/sec	
Plant #	Phase (°)	Magnitude (dB)	Phase (°)	Magnitude (dB)
1	−32.0288	−70.6453	−4.3250	−73.7139
2	−26.8791	−55.6551	−3.4412	−58.0973
3	−27.4059	−56.5969	−3.5236	−59.0924
4	−28.8258	−62.7452	−3.7563	−65.4039
5	−28.4372	−61.9070	−3.6909	−64.5171
6	−27.8051	−61.8395	−3.5885	−64.3812

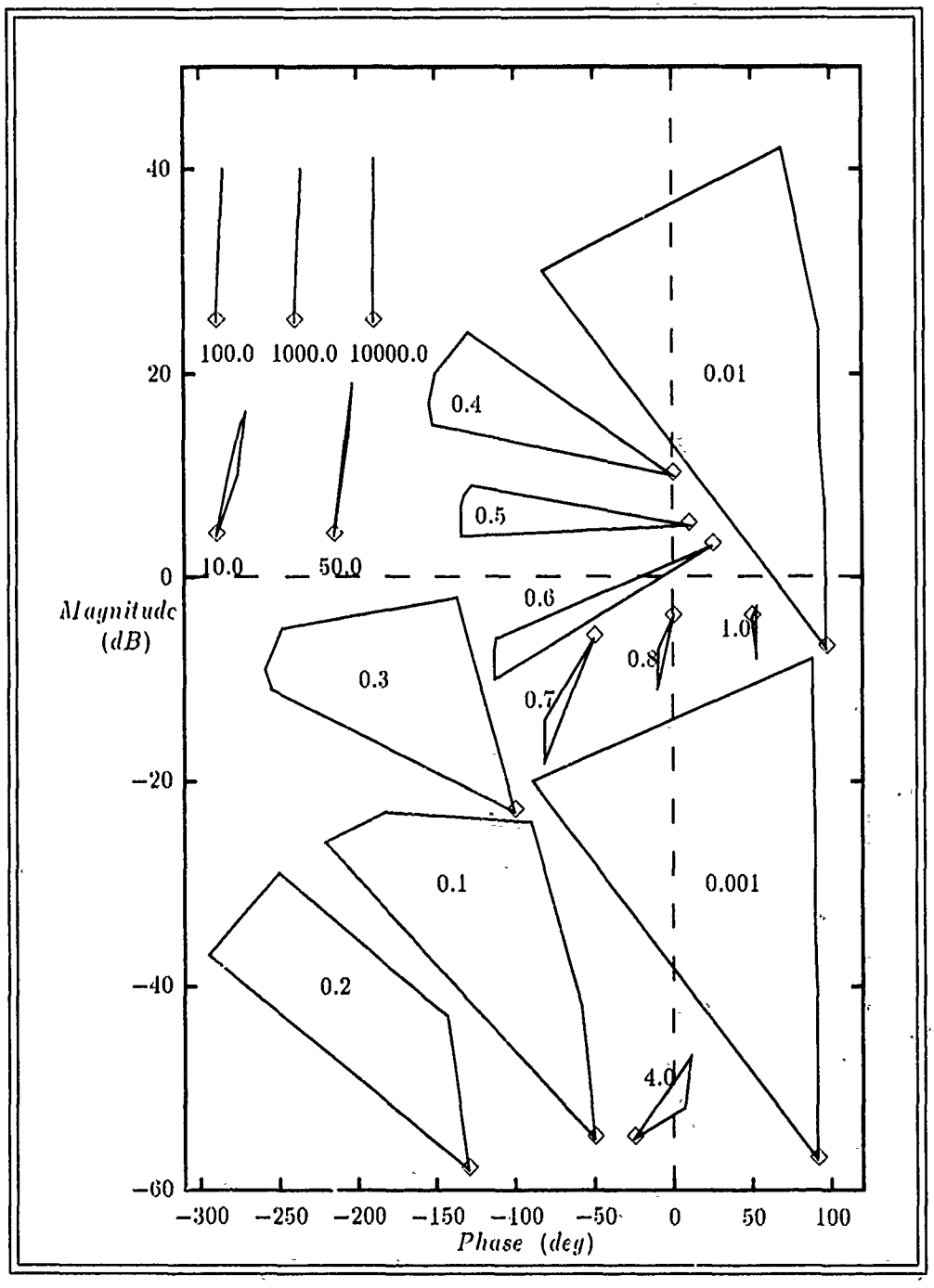

Figure E.3. Roll-Rate Channel Plant Templates ($q_{2,2_e}$) v_k = 0.001, 0.01, 0.1, 0.2, 0.3, 0.4, 0.5, 0.6, 0.7, 0.8, 1, 4, 10, 50, 100, 1000, 10000 rad/sec With Plant Case # 1 Nominal

E.3 Yaw-Loop ($q_{3,3}$) MIMO Loop #1

Table E.27. Yaw-Loop ($q_{3,3}$) Templates for $v_k = 0.001, 0.01$ *rad/sec*

Frequency	v_k = 0.001 rad/sec		v_k = 0.01 rad/sec	
Plant #	Phase (°)	Magnitude (dB)	Phase (°)	Magnitude (dB)
1	0.8391	−4.6009	8.3260	−4.5034
2	0.3515	4.1680	3.5105	4.1853
3	0.5264	−0.8880	5.2485	−0.8502
4	0.6752	−2.1014	6.7192	−2.0393
5	0.5729	−1.7032	5.7090	−1.6583
6	0.3568	9.1597	3.5620	9.1797

Table E.28. Yaw-Loop ($q_{3,3}$) Templates for $v_k = 0.1, 0.3$ *rad/sec*

Frequency	v_k = 0.1 rad/sec		v_k = 0.3 rad/sec	
Plant #	Phase (°)	Magnitude (dB)	Phase (°)	Magnitude (dB)
1	53.7907	0.5968	69.1733	9.0253
2	31.1966	5.6430	58.6926	10.8751
3	42.0471	1.8617	67.0157	8.6724
4	48.8073	1.8041	70.0182	9.4933
5	44.2871	1.4205	67.7400	8.5534
6	30.8953	10.8271	53.6640	16.3883

Table E.29. Yaw-Loop ($q_{3,3}$) Templates for $v_k = 1, 1.4$ *rad/sec*

Frequency	v_k = 1 rad/sec		v_k = 1.4 rad/sec	
Plant #	Phase (°)	Magnitude (dB)	Phase (°)	Magnitude (dB)
1	47.1169	22.3950	5.2465	27.2975
2	68.6356	21.0035	65.4331	24.5746
3	72.1137	19.2054	68.5201	22.7088
4	68.7680	20.9091	60.6407	25.2990
5	69.5871	19.3183	63.9972	23.0085
6	43.5452	26.6843	25.0882	29.8838

Table E.30. Yaw-Loop ($q_{3,3}$) Templates for $v_k = 2, 3$ *rad/sec*

Frequency	v_k = 2 rad/sec		v_k = 3 rad/sec	
Plant #	Phase (°)	Magnitude (dB)	Phase (°)	Magnitude (dB)
1	−58.7904	24.6947	−88.7306	18.7059
2	56.5189	29.2975	19.9272	37.5911
3	60.1978	27.2038	31.9858	34.9052
4	34.9865	32.0002	−63.3488	32.9863
5	50.7380	27.9185	−1.8267	35.1767
6	−10.0789	32.0675	−55.8294	30.4009

Table E.31. Yaw-Loop ($q_{3,3}$) Templates for $v_k = 4, 5$ *rad/sec*

Frequency	v_k = 4 rad/sec		v_k = 5 rad/sec	
Plant #	Phase (°)	Magnitude (dB)	Phase (°)	Magnitude (dB)
1	−101.6119	15.2956	−111.1172	12.9260
2	−63.5194	38.1493	−96.6556	32.9092
3	−46.1249	38.6460	−91.2554	33.3831
4	−94.2284	27.0666	−107.5268	23.6437
5	−69.7125	32.8026	−95.5725	28.5875
6	−79.6051	27.6861	−94.6622	25.4662

Table E.32. Yaw-Loop ($q_{3,3}$) Templates for $v_k = 6, 7$ *rad/sec*

Frequency	v_k = 6 rad/sec		v_k = 7 rad/sec	
Plant #	Phase (°)	Magnitude (dB)	Phase (°)	Magnitude (dB)
1	−119.4478	11.0835	−127.2691	9.5523
2	−111.4239	29.5564	−121.9087	27.2074
3	−108.7536	29.6728	−120.1871	27.1358
4	−117.2446	21.2883	−125.7336	19.4677
5	−109.5281	25.7245	−120.0151	23.6128
6	−106.2563	23.6664	−116.2214	22.1500

Table E.33. Yaw-Loop ($q_{3,3}$) Templates for $v_k = 8, 9$ *rad/sec*

Frequency	v_k = 8 rad/sec		v_k = 9 rad/sec	
Plant #	Phase (°)	Magnitude (dB)	Phase (°)	Magnitude (dB)
1	−134.8498	8.2204	−142.3113	7.0203
2	−130.8759	25.3823	−139.1670	23.8607
3	−129.6099	25.2033	−138.1653	23.6142
4	−133.6931	17.9557	−141.3951	16.6358
5	−129.1197	21.9211	−137.5614	20.4826
6	−125.3215	20.8239	−133.9192	19.6268

Table E.34. Yaw-Loop ($q_{3,3}$) Templates for $v_k = 10, 50$ *rad/sec*

Frequency	v_k = 10 rad/sec		v_k = 50 rad/sec	
Plant #	Phase (°)	Magnitude (dB)	Phase (°)	Magnitude (dB)
1	−149.7059	5.9077	57.2032	−27.0711
2	−147.1066	22.5262	57.3718	−11.3061
3	−146.2775	22.2344	57.4828	−11.7696
4	−148.9555	15.4393	57.0524	−17.8987
5	−145.6388	19.2036	57.7987	−14.4238
6	−142.1980	18.5160	58.6515	−14.4553

Table E.35. Yaw-Loop ($q_{3,3}$) Templates for $v_k = 100, 1000$ *rad/sec*

Frequency	v_k = 100 rad/sec		v_k = 1000 rad/sec	
Plant #	Phase (°)	Magnitude (dB)	Phase (°)	Magnitude (dB)
1	9.7573	−45.2026	−31.1566	−74.7497
2	9.7018	−29.4760	−31.6932	−59.1212
3	9.7650	−29.9446	−31.6478	−59.5858
4	9.5283	−36.0561	−31.7610	−65.7047
5	9.9743	−32.5762	−31.5699	−62.1982
6	10.4672	−32.5860	−31.2733	−62.1628

Table E.36. Yaw-Loop ($y_{3,3}$) Template for $v_k = 10000$ *rad/sec*

Frequency	v_k = 10000 rad/sec	
Plant #	Phase (°)	Magnitude (dB)
1	−4.1462	−77.6813
2	−4.2467	−62.1280
3	−4.2387	−62.5872
4	−4.2580	−68.7187
5	−4.2261	−65.1917
6	−4.1747	−65.1216

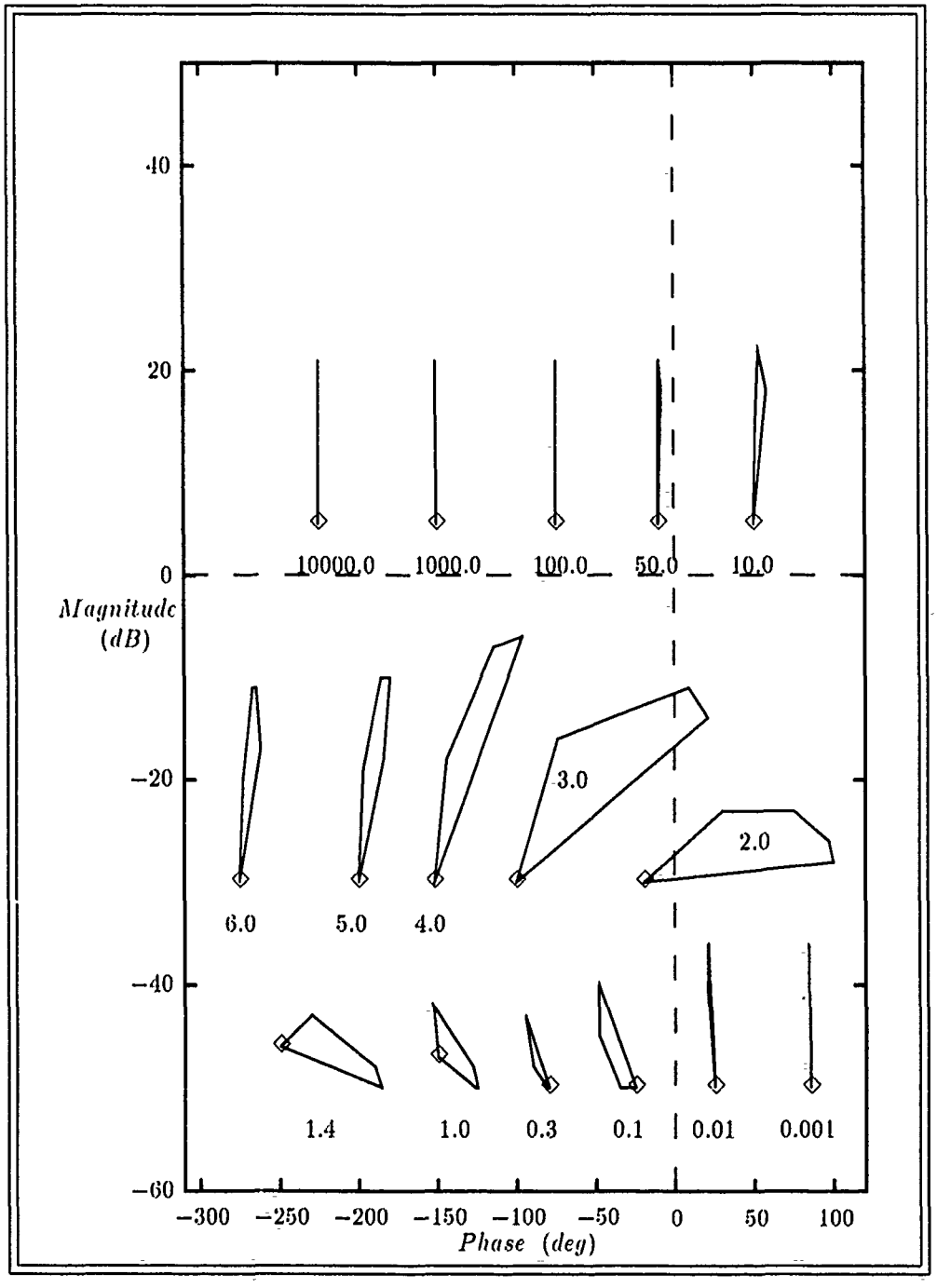

Figure E.4. Yaw-Rate Channel Plant Templates ($q_{3,3}$) v_k = 0.001, 0.01, 0.1, 0.3, 1, 1.4, 2, 3, 4, 5, 6, 10, 50, 100, 1000, 10000 rad/sec With Plant Case # 1 Nominal

Appendix F. *Z-Plane Compensator Listings*

This appendix contains all the listings of the compensator and prefilter transfer functions designed in this thesis. The w'-plane and various forms of the z-plane representations are given. The difference equations required to implement each are also given.

For a proper z-plane transfer function of the form:

$$G(z) = \frac{Y(z)}{U(z)} = \frac{c_m z^m + c_{m-1} z^{m-1} + \cdots + c_1 z + c_0}{d_n z^n + d_{n-1} z^{n-1} + \cdots + d_1 z + d_0}$$

where

$$n \geq m$$

$$d_n = 1$$

the system difference equation is written as:

$$y[(k+n)T] + d_{n-1}y[(k+n-1)T] + \cdots + d_1 y[(k+1)T] + d_0 y(kT) =$$

$$c_m u[(k+m)T] + c_{n-1}u[(k+m-1)T] + \cdots + c_1 u[(k+1)T] + c_0 u(kT) \qquad \text{(F.1)}$$

Equation F.1 can be rearranged and rewritten such that:

$$\begin{aligned} y(kT) = & -d_{n-1}y[(k-1)T] - \cdots - d_1 y[(k+1-n)T] - d_0 y[(k-n)T] \\ & + c_m u[(k+m-n)T] + c_{m-1}u[(k+m-n-1)T] + \cdots + c_1 u[(k+1-n)T] \\ & + c_0 u[(k-n)T] \end{aligned} \qquad \text{(F.2)}$$

The difference equations provided in the following sections are written in the form of equation F.2.

F.1 Pitch-Rate Channel Type 0

$$
\begin{aligned}
g_1(w') &= \frac{562(w'+6)(w'^2+20w'+324)}{w'(w'^2+500w'+250000)} \\
g_1(z) &= \frac{31.149422(z-0.822004 \pm j0.2097646)(z-0.904762)}{(z+0.726264 \pm j0.320355)(z-1)} \\
g_1(z) &= \frac{31.149422z^3-79.392721z^2+68.750756z-20.282933}{z^3+0.452528z^2-0.822441z-0.630086} \\
g_1(z) &= \frac{31.149422-79.392721z^{-1}+68.750756z^{-2}-20.282933z^{-3}}{1+0.452528z^{-1}-0.822441z^{-2}-0.630086z^{-3}} \\
f_{1,1}(w') &= \frac{0.003(w'+1000)}{(w'+3)} \\
f_{1,1}(z) &= \frac{0.027317(z+0.785714)}{z-0.951220} \\
f_{1,1}(z) &= \frac{0.027317z+0.021463}{z-0.951220} \\
f_{1,1}(z) &= \frac{0.027317+0.021463z^{-1}}{1-0.951220z^{-1}}
\end{aligned}
$$

The difference equations to implement this type 0 design for $f_{1,1}$ and g_1 are:

$$
\begin{aligned}
g_1 \Rightarrow y(kT) &= -0.452528\, y[(k-1)T] + 0.822441\, y[(k-2)T] \\
&\quad + 0.630086\, y[(k-3)T] + 31.149422\, u(kT) \\
&\quad - 79.392721\, u[(k-1)T] + 68.750756\, u[(k-2)T] \\
&\quad - 20.282933\, u[(k-3)T] \qquad \text{(F.3)} \\
f_{1,1} \Rightarrow y(kT) &= +0.951220\, y[(k-1)T] + 0.027317\, u(kT) \\
&\quad + 0.021463\, u[(k-1)T] \qquad \text{(F.4)}
\end{aligned}
$$

F.2 Pitch-Rate Channel Type 1 Design # 1

$$
\begin{aligned}
g_1(w') &= \frac{562(w'+0.3)(w'+6)(w'^2+20w'+324)}{w'^2(w'^2+500w'+250000)} \\
g_1(z) &= \frac{31.227295(z-0.822004\pm j0.209764)(z-0.904762)(z-0.995012)}{(z+0.726264\pm j0.320355)(z-1)(z-1)} \\
g_1(z) &= \frac{31.227295z^4-110.662751z^3+148.116872z^2-88.912520z+20.232226}{z^4-0.547472z^3-1.274969z^2+0.192355z+0.630086} \\
g_1(z) &= \frac{31.227295-110.662751z^{-1}+148.116872z^{-2}-88.912520z^{-3}+20.232226z^{-4}}{1-0.547472z^{-1}-1.274969z^{-2}+0.192355z^{-3}+0.630086z^{-4}} \\
f_{1,1}(w') &= \frac{0.0012(w'+100)(w'+500)}{(w'+4)(w'+15)} \\
f_{1,1}(z) &= \frac{0.009778(z-0.090909)(z+0.612903)}{(z-0.777778)(z-0.935484)} \\
f_{1,1}(z) &= \frac{0.009778z^2+0.005104z-0.000545}{z^2-1.713262z+0.727599} \\
f_{1,1}(z) &= \frac{0.009778+0.005104z^{-1}-0.000545z^{-2}}{1-1.713262z^{-1}+0.727599z^{-2}}
\end{aligned}
$$

The difference equations to implement the type 1 design # 1 for $f_{1,1}$ and g_1 are:

$$
\begin{aligned}
g_1 \Rightarrow y(kT) &= +\,0.547472\,y[(k-1)T] + 1.274969\,y[(k-2)T] \\
&\quad -\,0.192355\,y[(k-3)T] - 0.630086\,y[(k-4)T] \\
&\quad +\,31.227295\,u(kT) - 110.662751\,u[(k-1)T] \\
&\quad +\,148.116872\,u[(k-2)T] - 88.912520\,u[(k-3)T] \\
&\quad +\,20.232226\,u[(k-4)T] \qquad \text{(F.5)} \\
f_{1,1} \Rightarrow y(kT) &= +\,1.713262\,y[(k-1)T] - 0.727599y[(k-2)T] \\
&\quad +\,0.009778\,u(kT) + 0.005104\,u[(k-1)T] \\
&\quad -\,0.000545\,u[(k-2)T] \qquad \text{(F.6)}
\end{aligned}
$$

F.3 Pitch-Rate Channel Type 1 Design # 2

The prefilter for design # 2 is identical to design # 1.

$$
\begin{aligned}
g_1(w') &= \frac{562(w'+0.2)(w'+0.3)(w'+6)(w'^2+20w'+324)}{w'^2(w'+0.02)(w'^2+500w'+250000)} \\
g_1(z) &= \frac{31.227295(z-0.822004 \pm j0.209764)(z-0.904762)(z-0.995012)(z-0.996672)}{(z+0.726264 \pm j0.320355)(z-1)(z-1)(z-0.999667)} \\
g_1(z) &= \frac{31.274128z^5-141.998772z^4+258.798914z^3-236.891236z^2+109.012110z-20.195140}{z^5-1.547139z^4-0.727679z^3+1.466899z^2+0.437795z-0.629876} \\
g_1(z) &= \frac{31.274128-141.998772z^{-1}+258.798914z^{-2}-236.891236z^{-3}+109.012110z^{-4}-20.195140z^{-5}}{1-1.547139z^{-1}-0.727679z^{-2}+1.466899z^{-3}+0.437795z^{-4}-0.629876z^{-5}}
\end{aligned}
$$

The difference equation to implement the type 1 design # 2 for g_1 is:

$$
\begin{aligned}
g_1 \Rightarrow y(kT) = &+ 1.547139\, y[(k-1)T] + 0.727679\, y[(k-2)T] \\
&- 1.466899\, y[(k-3)T] - 0.437795\, y[(k-4)T] \\
&+ 0.629876\, y[(k-5)T] + 31.274128\, u(kT) \\
&- 141.998772u[(k-1)T] + 258.798914\, u[(k-2)T] \\
&- 236.891236\, u[(k-3)T] + 109.012110\, u[(k-4)T] \\
&- 20.195140\, u[(k-5)T] \qquad \text{(F.7)}
\end{aligned}
$$

F.4 Roll-Rate Channel Design # 1

$$
\begin{aligned}
g_2(w') &= \frac{3.55(w'+0.1)(w'^2+16w'+100)}{w'^2(w'+500)} \\
g_2(z) &= \frac{0.784134(z-0.870889 \pm j0.087698)(z-0.998335)}{(z+0.612903)(z-1)(z-1)} \\
g_2(z) &= \frac{0.784134z^3-2.148616z^2+1.964269z-0.599755}{z^3-1.387097z^2-0.225806z+0.612903} \\
g_2(z) &= \frac{0.784134-2.148616z^{-1}+1.964269z^{-2}-0.599755z^{-3}}{1-1.387097z^{-1}-0.225806z^{-2}+0.612903z^{-3}}
\end{aligned}
$$

$$
\begin{aligned}
f_{2,2}(w') &= \frac{0.125(w'+20)}{w'+2.5} \\
f_{2,2}(z) &= \frac{0.142857(z-0.714286)}{z-0.959184} \\
f_{2,2}(z) &= \frac{0.142857z-0.102041}{z-0.959184} \\
f_{2,2}(z) &= \frac{0.142857-0.102041z^{-1}}{1-0.959184z^{-1}}
\end{aligned}
$$

The difference equations to implement the type 1 design # 1 for $f_{2,2}$ and g_2 are:

$$
\begin{aligned}
g_2 \Rightarrow y(kT) &= +\,1.387097\, y[(k-1)T] + 0.225806\, y[(k-2)T] \\
&\quad -\,0.612903\, y[(k-3)T] + 0.784134\, u(kT) \\
&\quad -\,2.148616\, u[(k-1)T] + 1.964269\, u[(k-2)T] \\
&\quad -\,0.599755\, u[(k-3)T] \qquad \text{(F.8)} \\
f_{2,2} \Rightarrow y(kT) &= +\,0.959184\, y[(k-1)T] + 0.142857\, u(kT) \\
&\quad -\,0.102041\, u[(k-1)T] \qquad \text{(F.9)}
\end{aligned}
$$

F.5 Roll-Rate Channel Design # 2

The prefilter for design # 2 is identical to design # 1.

$$
\begin{aligned}
g_2(w') &= \frac{3.55(w'+0.1)(w'+0.3)(w'^2+16w'+100)}{w'^2(w'+0.009)(w'+500)} \\
g_2(z) &= \frac{0.786035(z-0.870889\pm j0.087698)(z-0.998335)(z-0.995012)}{(z+0.612903)(z-0.999850)(z-1)(z-1)} \\
g_2(z) &= \frac{0.786035z^4-2.935941z^3+4.112116z^2-2.560421z+0.598211}{z^4-2.386947z^3+1.161082z^2+0.838676z-0.612811} \\
g_2(z) &= \frac{0.786035-2.935941z^{-1}+4.112116z^{-2}-2.560421z^{-3}+0.598211z^{-4}}{1-2.386947z^{-1}+1.161082z^{-2}+0.838676z^{-3}-0.612811z^{-4}}
\end{aligned}
$$

The difference equation to implement the type 1 design # 2 for g_2 is:

$$
g_2 \Rightarrow y(kT) = +\,2.386947\, y[(k-1)T] - 1.161082\, y[(k-2)T]
$$

$$
\begin{aligned}
&- 0.838676\ y[(k-3)T] \ + \ 0.612811\ y[(k-4)T] \\
&+ 0.786035\ u(kT) \ - \ 2.935941\ u[(k-1)T] \\
&+ 4.112116\ u[(k-2)T] \ - \ 2.560421\ u[(k-3)T] \\
&+ 0.598211 y[(k-4)T] \qquad \text{(F.10)}
\end{aligned}
$$

F.6 Yaw-Rate Channel Design # 1

$$
\begin{aligned}
g_3(w') &= \frac{223(w'+4.5)(w'^2+20w'+324)}{w'(w'^2+500w'+250000)} \\
g_3(z) &= \frac{12.212859(z-0.822004 \pm j0.209764)(z-0.927711)}{(z+0.726264 \pm j0.320355)(z-1)} \\
g_3(z) &= \frac{12.212859z^3-31.408045z^2+27.416111z-8.154108}{z^3+0.452528z^2-0.822441z-0.630086} \\
g_3(z) &= \frac{12.212859-31.408045z^{-1}+27.416111z^{-2}-8.154108z^{-3}}{1+0.452528z^{-1}-0.822441z^{-2}-0.630086z^{-3}} \\
f_{3,3}(w') &= \frac{0.004(w'+200)}{w'+0.8} \\
f_{3,3}(z) &= \frac{0.010596(z+0.250000)}{z-0.986755} \\
f_{3,3}(z) &= \frac{0.010596z+0.002649}{z-0.986755} \\
f_{3,3}(z) &= \frac{0.010596+0.002649z^{-1}}{1-0.986755z^{-1}}
\end{aligned}
$$

The difference equations to implement the type 1 design # 1 for $f_{3,3}$ and g_3 are:

$$
\begin{aligned}
g_3 \Rightarrow y(kT) &= - 0.452528\ y[(k-1)T] \ + \ 0.822441\ y[(k-2)T] \\
&+ 0.630086\ y[(k-3)T] \ + \ 12.212859\ u(kT) \\
&- 31.408045\ u[(k-1)T] \ + \ 27.416111\ u[(k-2)T] \\
&- 8.154108\ u[(k-3)T] \qquad \text{(F.11)} \\
f_{3,3} \Rightarrow y(kT) &= + 0.986755\ y[(k-1)T] \ + \ 0.010596\ u(kT)
\end{aligned}
$$

$$+ 0.002649\, u[(k-1)T] \qquad \text{(F.12)}$$

F.7 Yaw-Rate Channel Design # 2

The prefilter for design # 2 is identical to design # 1.

$$\begin{aligned}
g_3(w') &= \frac{223(w'+0.3)(w'+4.5)(w'^2+20w'+324)}{w'(w'+0.009)(w'^2+500w'+250000)} \\
g_3(z) &= \frac{12.242473(z-0.822004 \pm j0.209764)(z-0.927711)(z-0.995012)}{(z+0.726264 \pm j0.320355)(z-0.999850)(z-1)} \\
g_3(z) &= \frac{12.242473z^4 - 43.665617z^3 + 58.809765z^2 - 35.519400z + 8.133112}{z^4 - 0.547322z^3 - 1.274901z^2 + 0.192232z + 0.629992} \\
g_3(z) &= \frac{12.242473 - 43.665617z^{-1} + 58.809765z^{-2} - 35.519400z^{-3} + 8.133112z^{-4}}{1 - 0.547322z^{-1} - 1.274901z^{-2} + 0.192232z^{-3} + 0.629992z^{-4}}
\end{aligned}$$

The difference equation to implement the type 1 design # 2 for g_3 is:

$$\begin{aligned}
g_3 \Rightarrow y(kT) = {} & + 0.547322\, y[(k-1)T] + 1.274901\, y[(k-2)T] \\
& - 0.192232\, y[(k-3)T] - 0.629992\, y[(k-4)T] \\
& + 12.242473\, u(kT) - 43.665617\, u[(k-1)T] \\
& + 58.809765\, u[(k-2)T] - 35.519400\, u[(k-3)T] \\
& + 8.133112\, u[(k-4)T] \qquad \text{(F.13)}
\end{aligned}$$

Appendix G. *Design Simulations*

G.1 w'-plane Loop Design Simulations

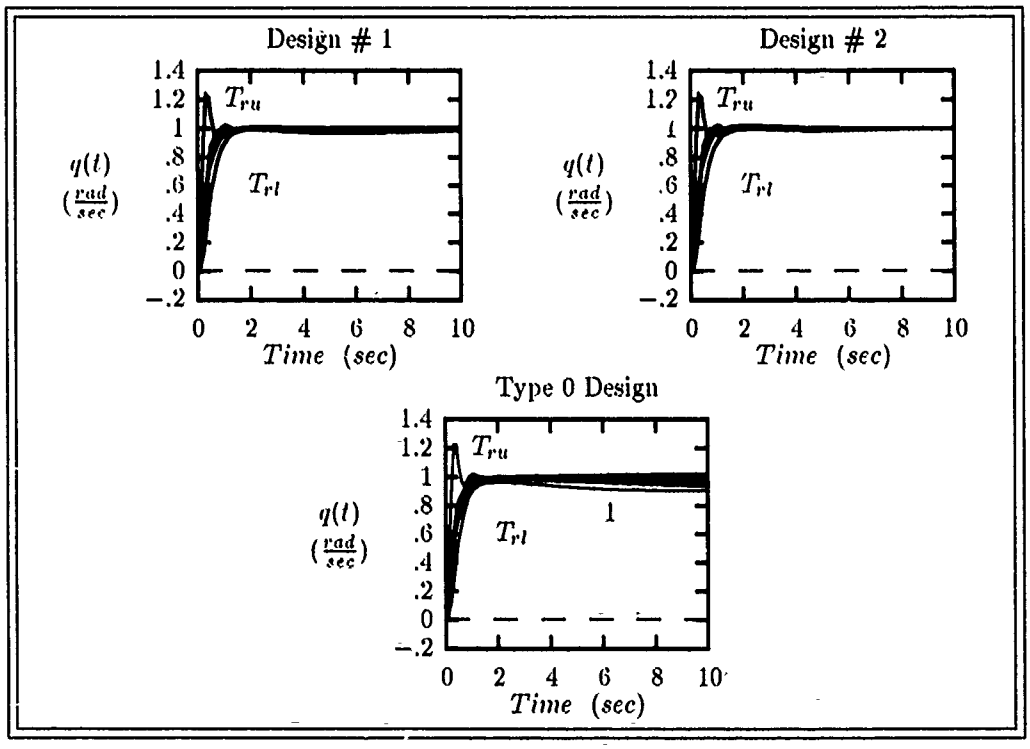

Figure G.1. Pitch-Loop ($q_{1,1}$) Plant and Tracking Model (T_{ru}, T_{rl}) Responses to a Step q_{cmd} Input

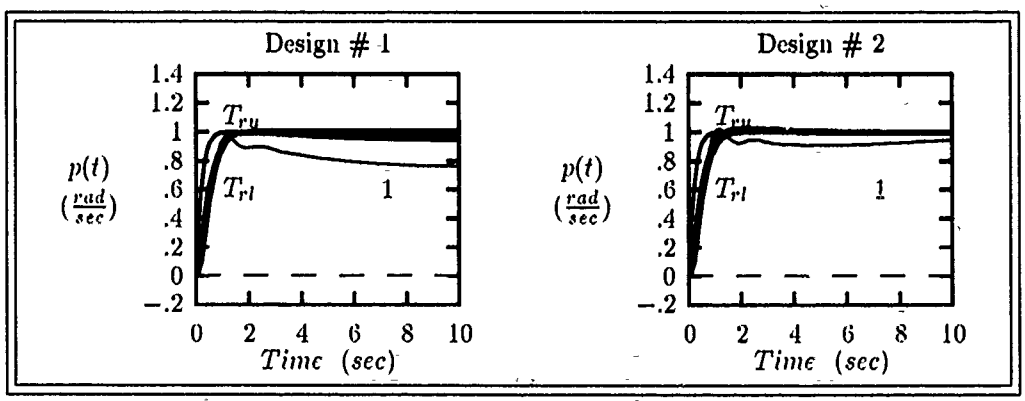

Figure G.2. Roll-Loop ($q_{2,2}$) Plant and Tracking Model (T_{ru}, T_{rl}) Responses to a Step p_{cmd} Input

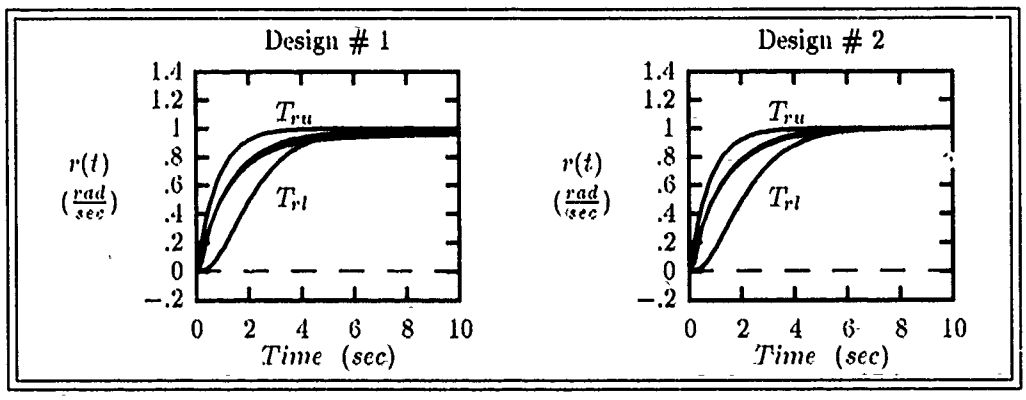

Figure G.3. Yaw-Loop ($q_{3,3}$) Plant and Tracking Model (T_{ru}, T_{rl}) Responses to a Step r_{cmd} Input

G.2 Hybrid Single Channel Input Simulations

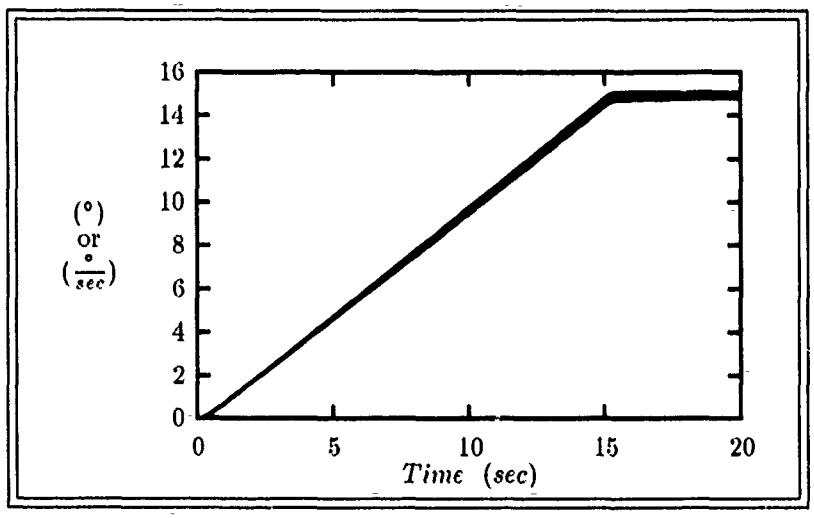

Figure G.4. θ Responses For Plants 1–6 to a 15 *sec* Duration 1°/*sec* Pitch-Rate (q) Input to Design #1

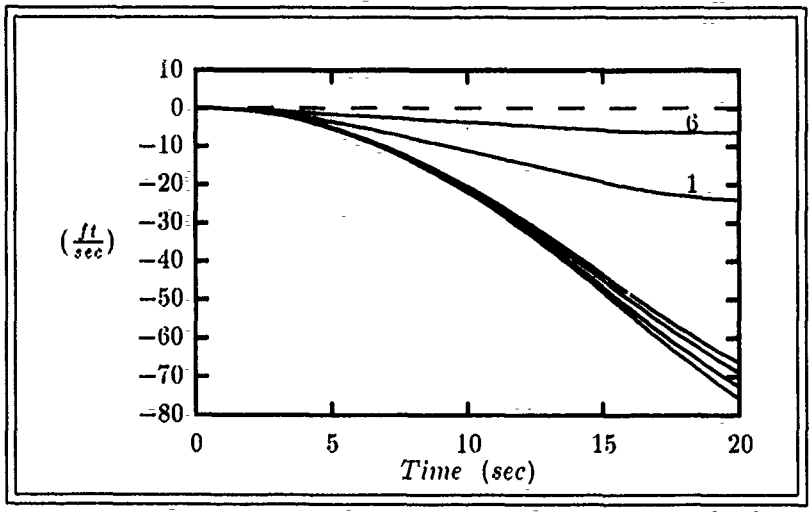

Figure G.5. u Responses For Plants 1–6 to a 15 *sec* Duration 1°/*sec* Pitch-Rate (q) Input to Design #1

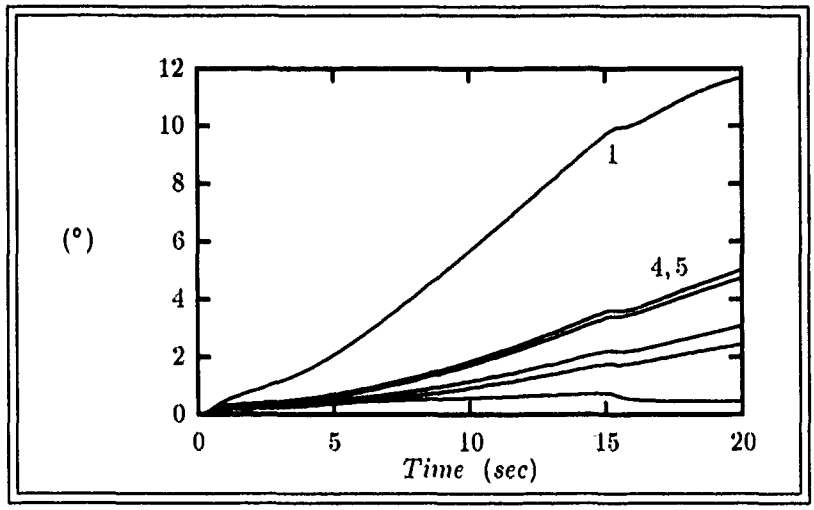

Figure G.6. α Responses For Plants 1–6 to a 15 *sec* Duration 1°/*sec* Pitch-Rate (q) Input to Design #1

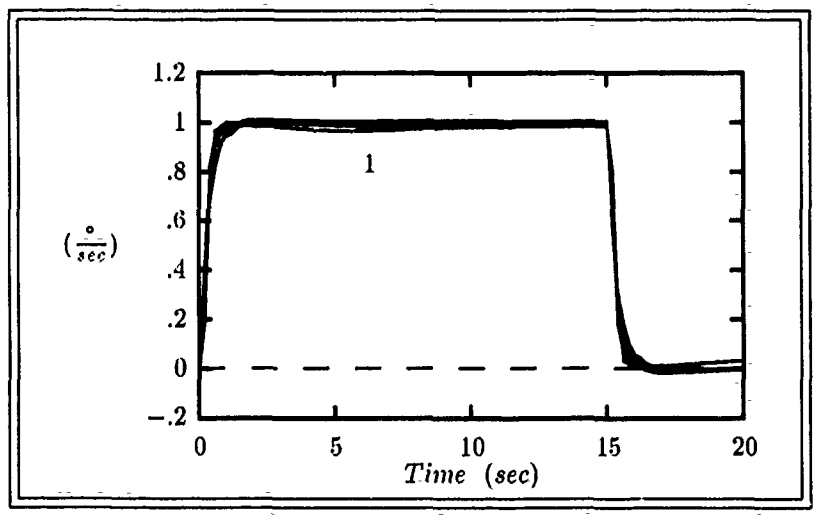

Figure G.7. q Responses For Plants 1–6 to a 15 *sec* Duration 1°/*sec* Pitch-Rate (q) Input to Design #1

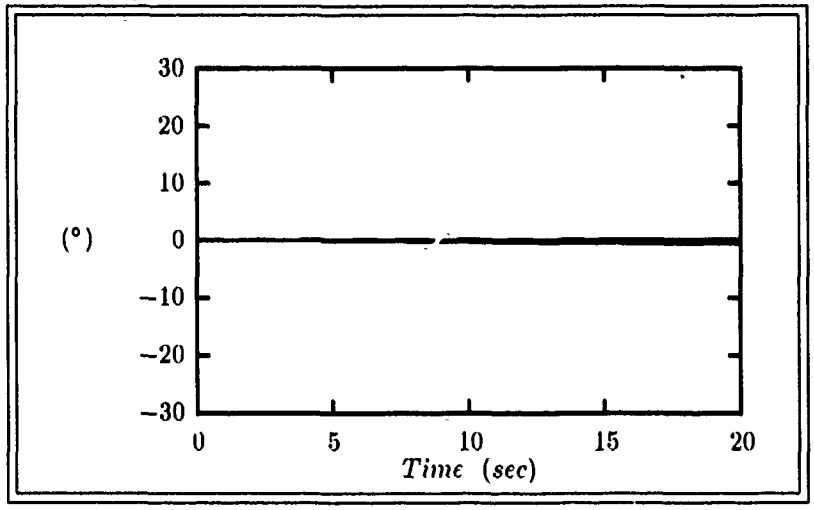

Figure G.8. δ_{a_L} Responses For Plants 1–6 to a 15 *sec* Duration 1°/*sec* Pitch-Rate (q) Input to Design #1 (amplitude limited at +15° and −10°)

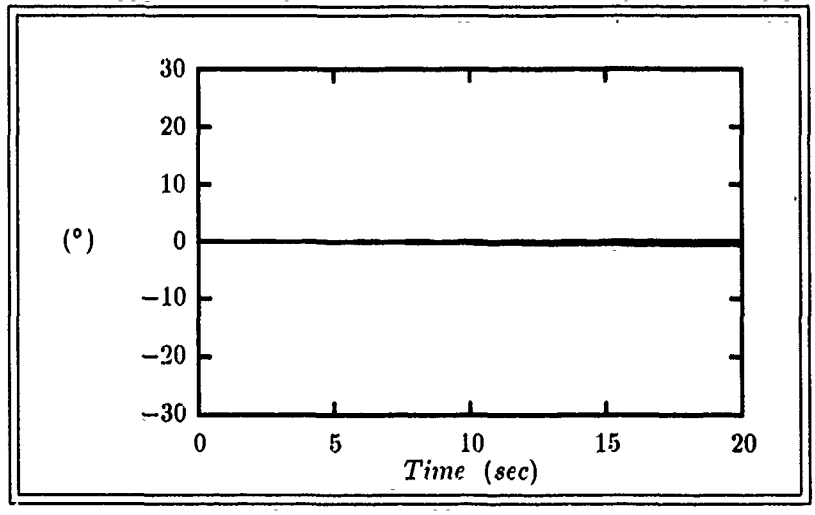

Figure G.9. δ_{a_R} Responses For Plants 1–6 to a 15 *sec* Duration 1°/*sec* Pitch-Rate (q) Input to Design #1 (amplitude limited at +15° and −10°)

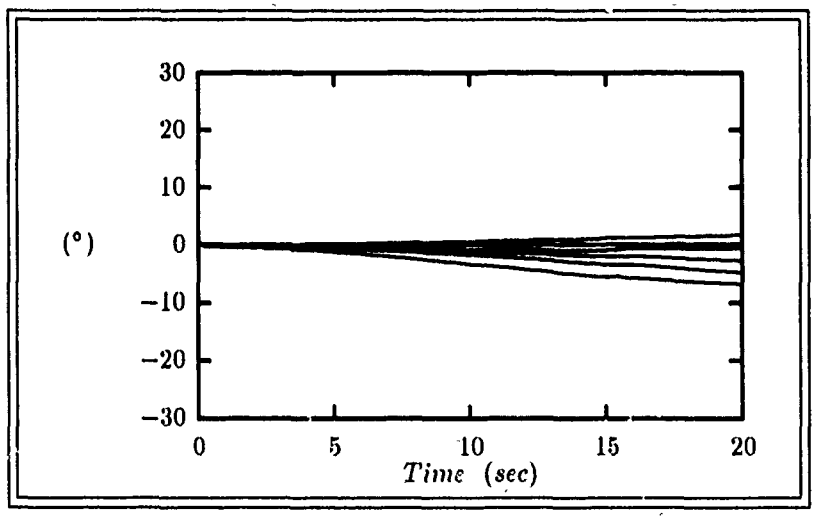

Figure G.10. δ_{e_L} Responses For Plants 1–6 to a 15 *sec* Duration 1°/*sec* Pitch-Rate (q) Input to Design #1 (amplitude limited at ±15°)

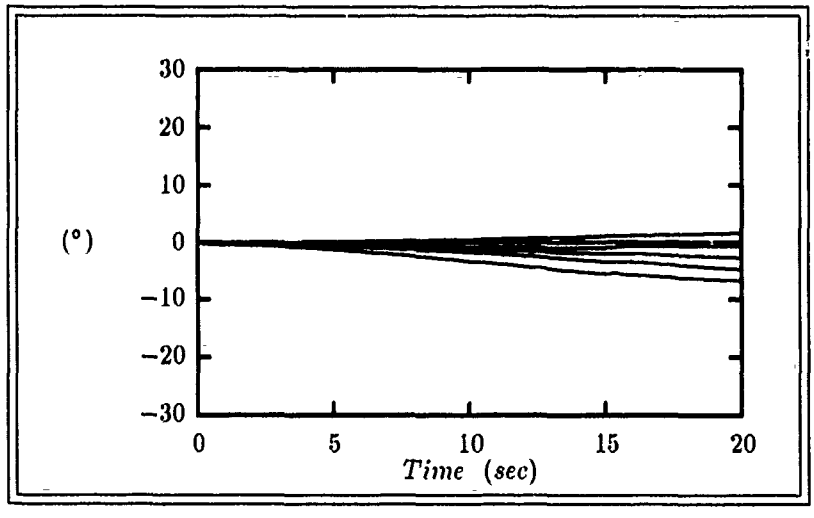

Figure G.11. δ_{e_R} Responses For Plants 1–6 to a 15 *sec* Duration 1°/*sec* Pitch-Rate (q) Input to Design #1 (amplitude limited at ±15°)

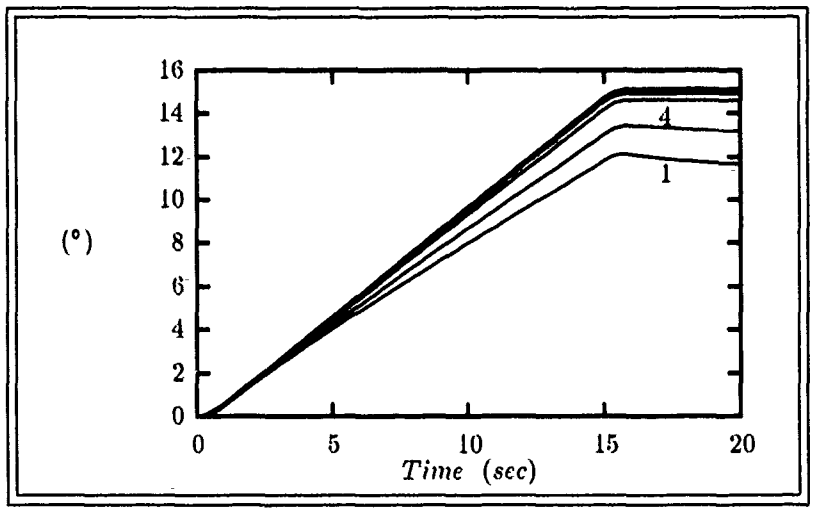

Figure G.12. ϕ Responses For Plants 1–6 to a 15 *sec* Duration 1°/*sec* Roll-Rate (p) Input to Design #1

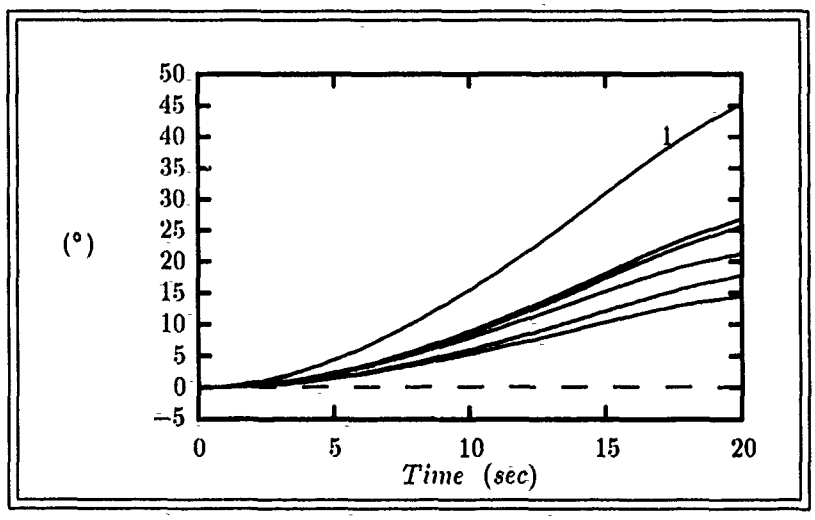

Figure G.13. β Responses For Plants 1–6 to a 15 *sec* Duration 1°/*sec* Roll-Rate (p) Input to Design #1

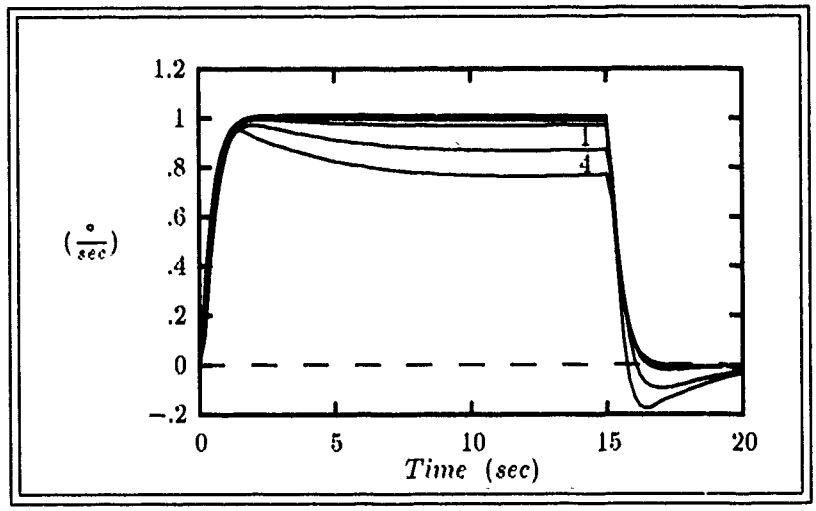

Figure G.14. p Responses For Plants 1–6 to a 15 *sec* Duration 1°/*sec* Roll-Rate (p) Input to Design #1

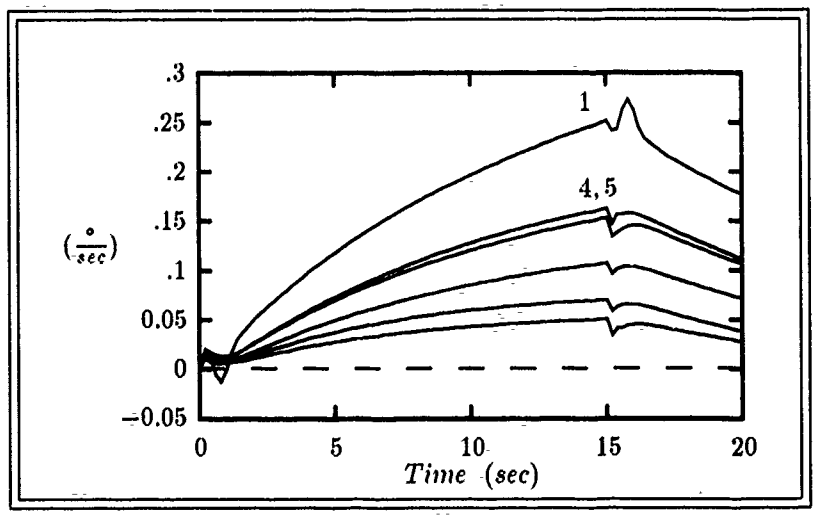

Figure G.15. r Responses For Plants 1–6 to a 15 *sec* Duration 1°/*sec* Roll-Rate (p) Input to Design #1

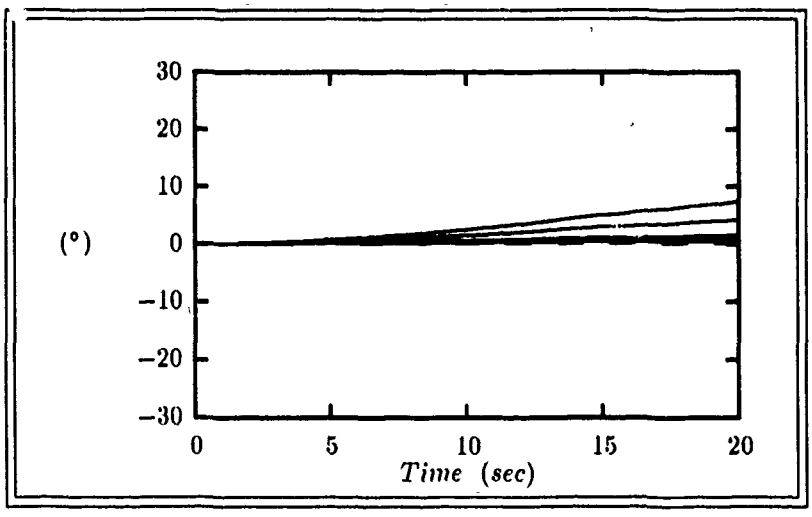

Figure G.16. δ_{a_L} Responses For Plants 1-6 to a 15 *sec* Duration 1°/*sec* Roll-Rate (p) Input to Design #1 (amplitude limited at +15° and −10°)

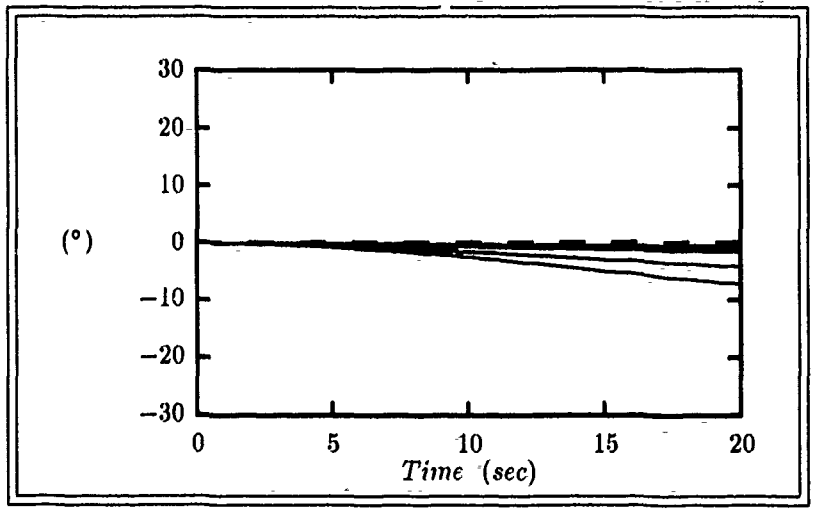

Figure G.17. δ_{a_R} Responses For Plants 1-6 to a 15 *sec* Duration 1°/*sec* Roll-Rate (p) Input to Design #1 (amplitude limited at +15° and −10°)

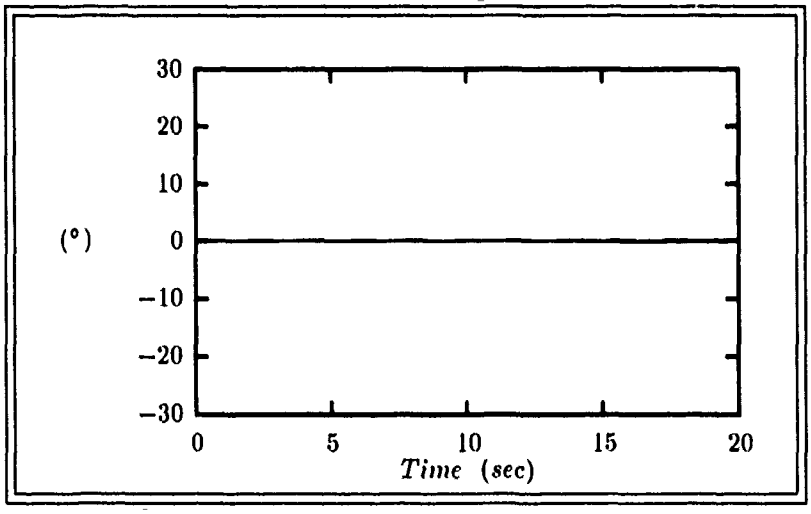

Figure G.18. δ_{f_L} Responses For Plants 1–6 to a 15 *sec* Duration 1°/*sec* Roll-Rate (p) Input to Design #1 (amplitude limited at 0° and −20°)

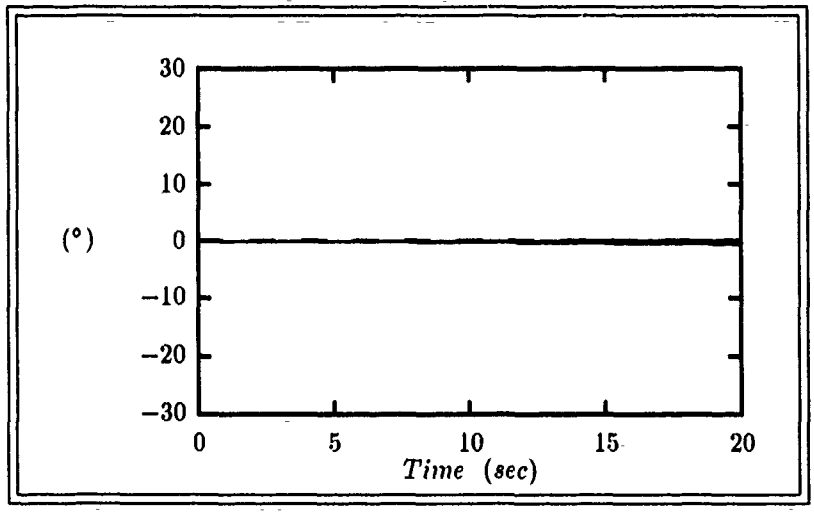

Figure G.19. δ_{f_R} Responses For Plants 1–6 to a 15 *sec* Duration 1°/*sec* Roll-Rate (p) Input to Design #1 (amplitude limited at 0° and −20°)

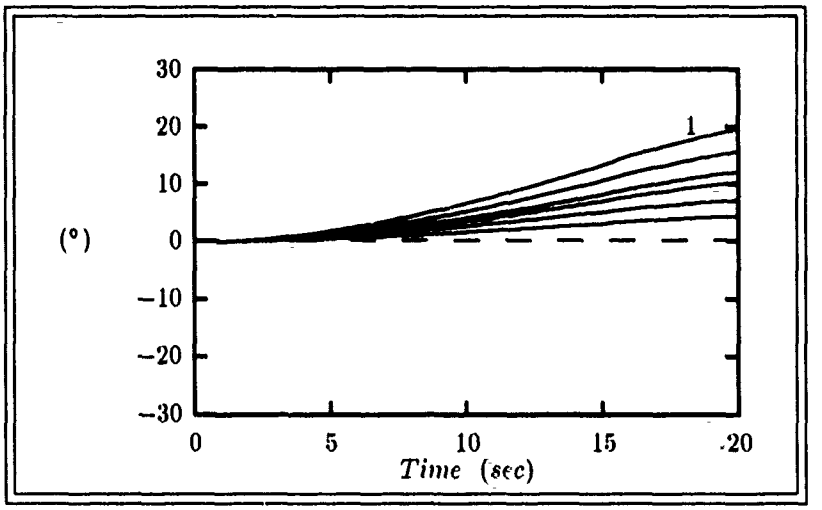

Figure G.20. δ_R Responses For Plants 1–6 to a 15 *sec* Duration 1°/*sec* Roll-Rate (p) Input to Design #1 (amplitude limited at ±25°)

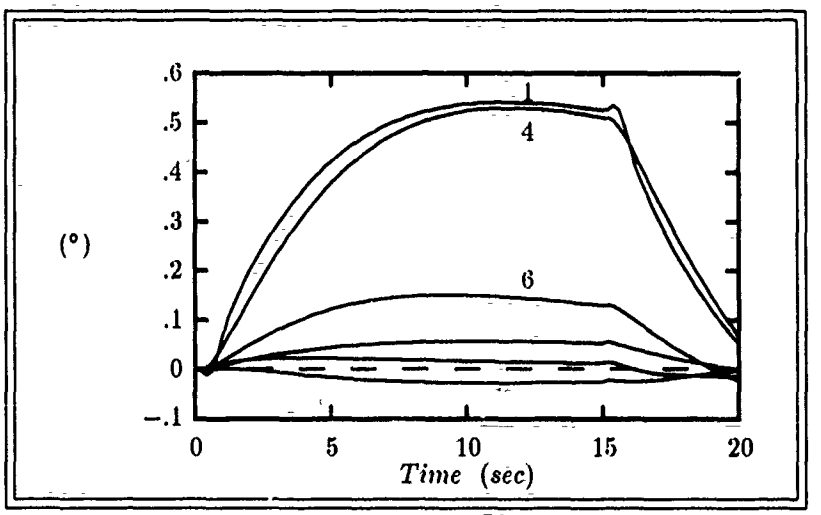

Figure G.21. ϕ Responses For Plants 1–6 to a 15 *sec* Duration 1°/*sec* Yaw-Rate (r) Input to Design #1

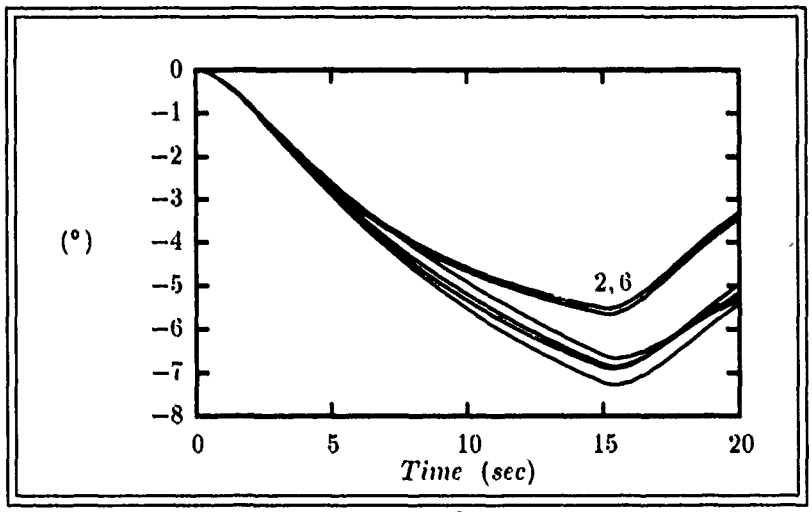

Figure G.22. β Responses For Plants 1–6 to a 15 *sec* Duration 1°/*sec* Yaw-Rate (r) Input to Design #1

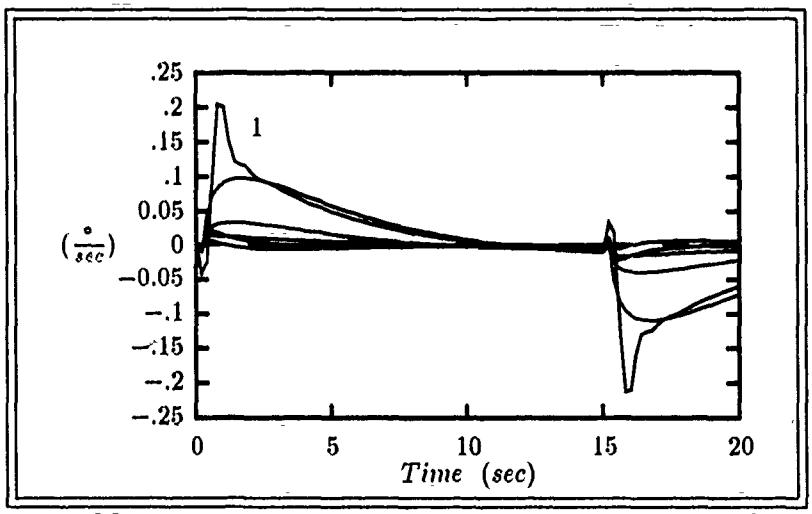

Figure G.23. p Responses For Plants 1–6 to a 15 *sec* Duration 1°/*sec* Yaw-Rate (r) Input to Design #1

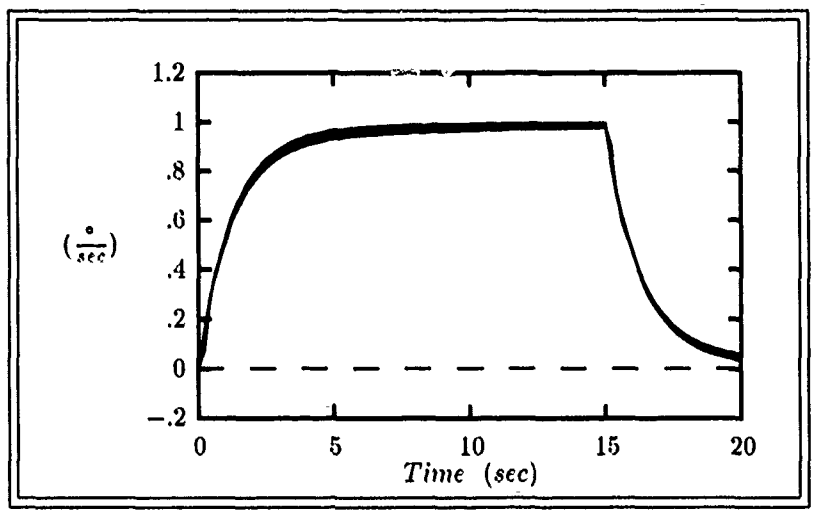

Figure G.24. r Responses For Plants 1–6 to a 15 *sec* Duration 1°/*sec* Yaw-Rate (r) Input to Design #1

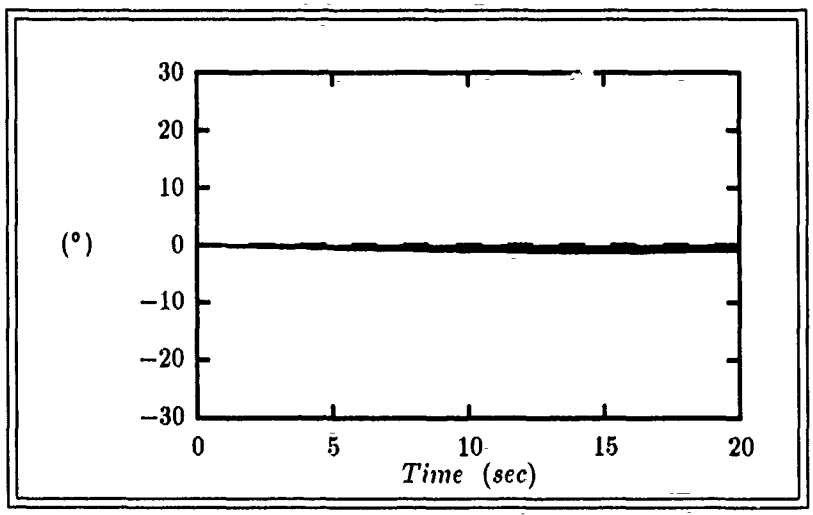

Figure G.25. δ_{a_L} Responses For Plants 1–6 to a 15 *sec* Duration 1°/*sec* Yaw-Rate (r) Input to Design #1 (amplitude limited at +15° and −10°)

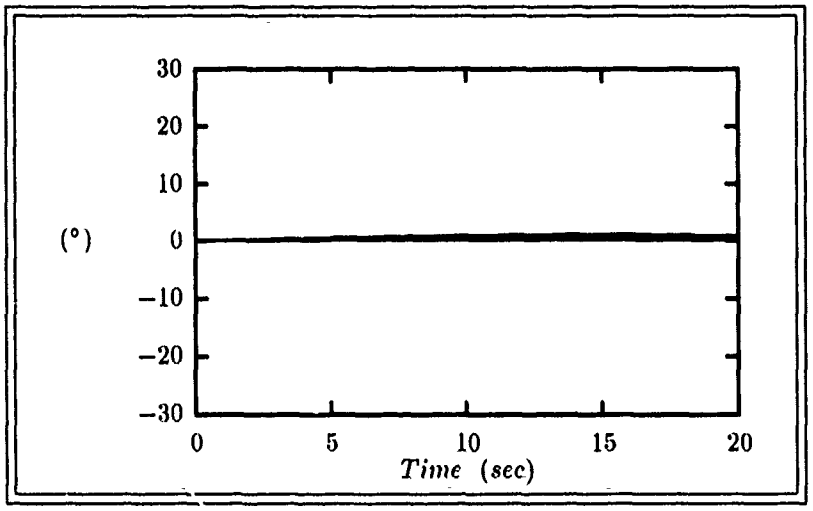

Figure G.26. δ_{a_R} Responses For Plants 1–6 to a 15 *sec* Duration 1°/*sec* Yaw-Rate (r) Input to Design #1 (amplitude limited at +15° and −10°)

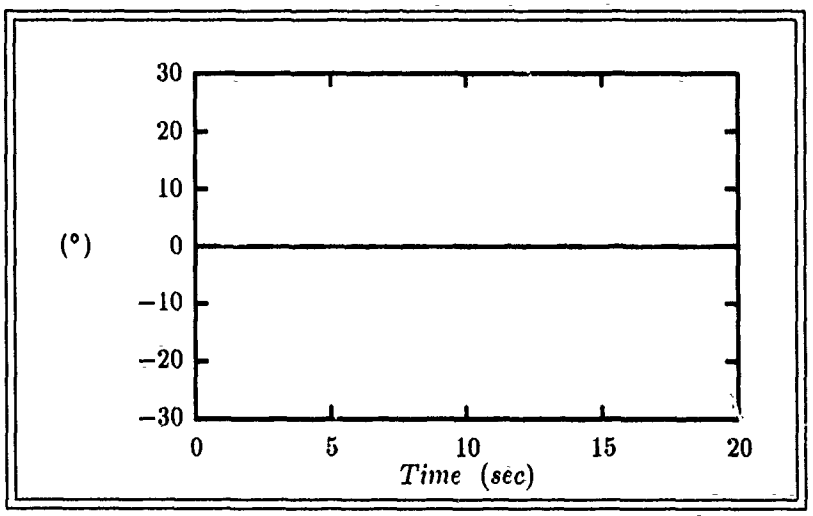

Figure G.27. δ_{f_L} Responses For Plants 1–6 to a 15 *sec* Duration 1°/*sec* Yaw-Rate (r) Input to Design #1 (amplitude limited at 0° and −20°)

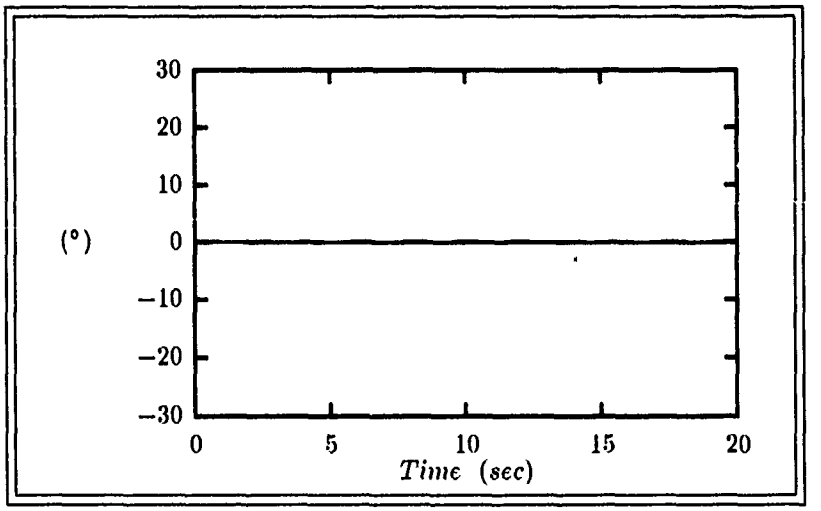

Figure G.28. δ_{f_R} Responses For Plants 1–6 to a 15 *sec* Duration 1°/*sec* Yaw-Rate (r) Input to Design #1 (amplitude limited at 0° and −20°)

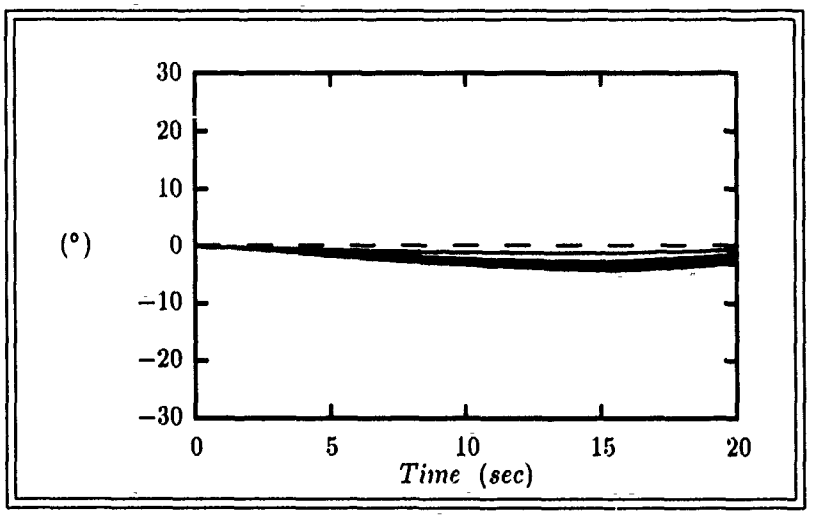

Figure G.29. δ_R Responses For Plants 1–6 to a 15 *sec* Duration 1°/*sec* Yaw-Rate (r) Input to Design #1 (amplitude limited at ±25°)

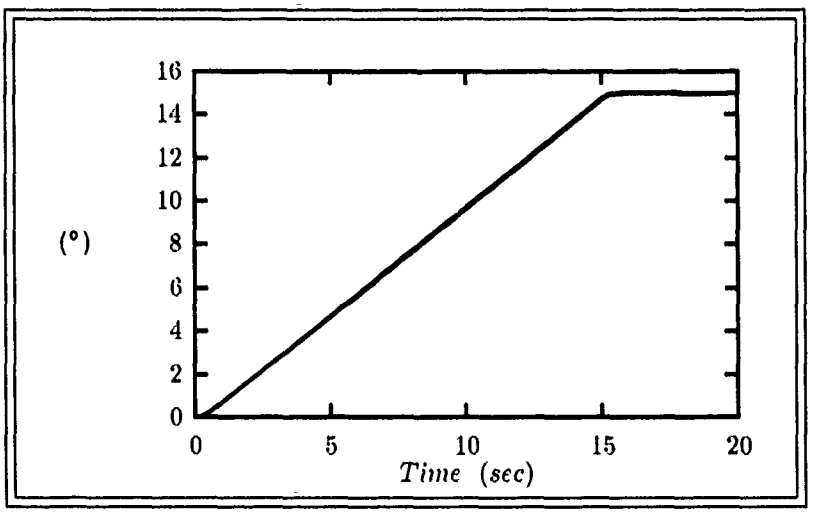

Figure G.30. θ Responses For Plants 1–6 to a 15 *sec* Duration 1°/*sec* Pitch-Rate (q) Input to Design #2

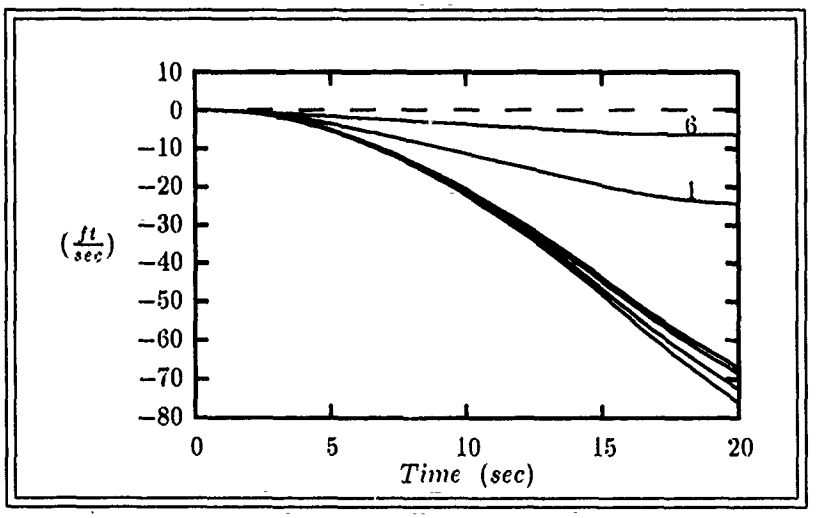

Figure G.31. u Responses For Plants 1–6 to a 15 *sec* Duration 1°/*sec* Pitch-Rate (q) Input to Design #2

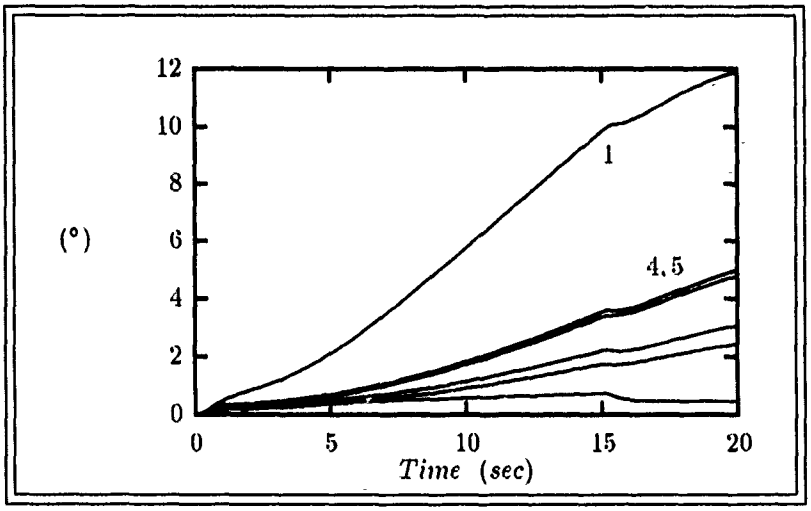

Figure G.32. α Responses For Plants 1–6 to a 15 *sec* Duration 1°/*sec* Pitch-Rate (q) Input to Design #2

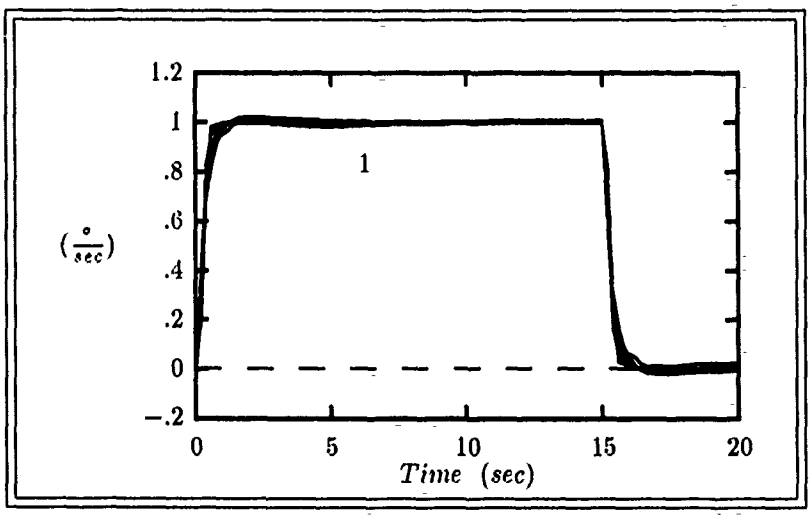

Figure G.33. q Responses For Plants 1–6 to a 15 *sec* Duration 1°/*sec* Pitch-Rate (q) Input to Design #2

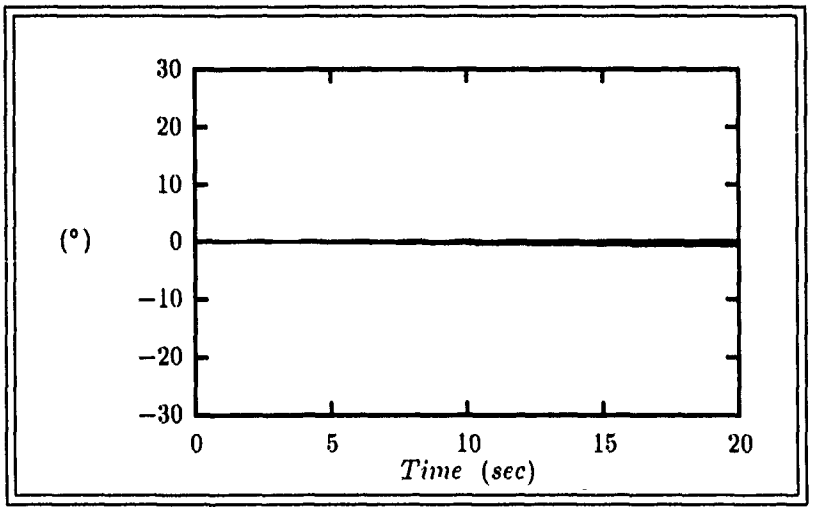

Figure G.34. δ_{a_L} Responses For Plants 1–6 to a 15 *sec* Duration 1°/*sec* Pitch-Rate (q) Input to Design #2 (amplitude limited at +15° and −10°)

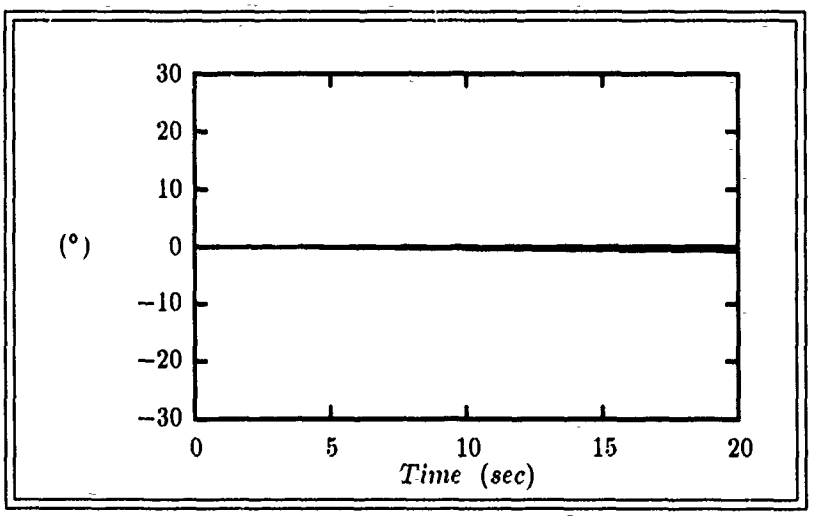

Figure G.35. δ_{a_R} Responses For Plants 1–6 to a 15 *sec* Duration 1°/*sec* Pitch-Rate (q) Input to Design #2 (amplitude limited at +15° and −10°)

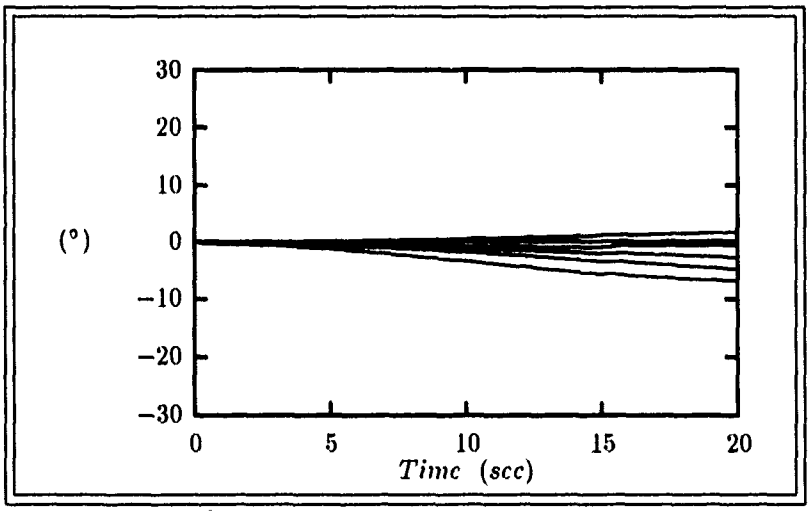

Figure G.36. δ_{e_L} Responses For Plants 1–6 to a 15 *sec* Duration 1°/*sec* Pitch-Rate (q) Input to Design #2 (amplitude limited at ±15°)

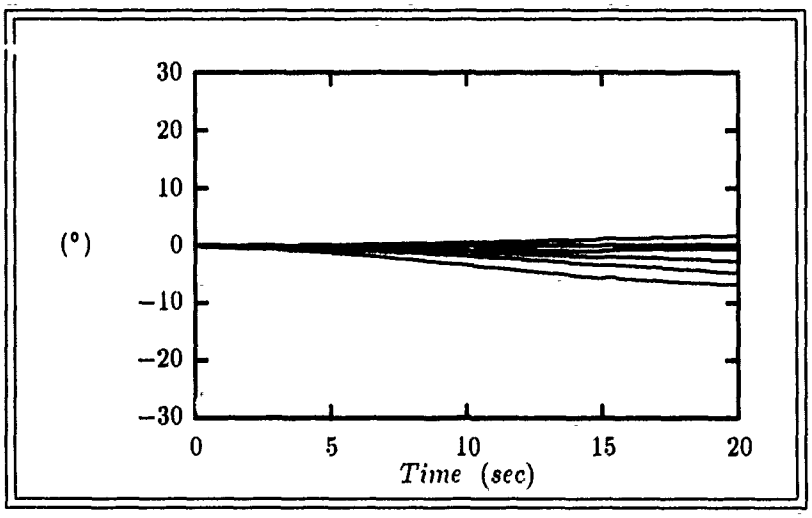

Figure G.37. δ_{e_R} Responses For Plants 1–6 to a 15 *sec* Duration 1°/*sec* Pitch-Rate (q) Input to Design #2 (amplitude limited at ±15°)

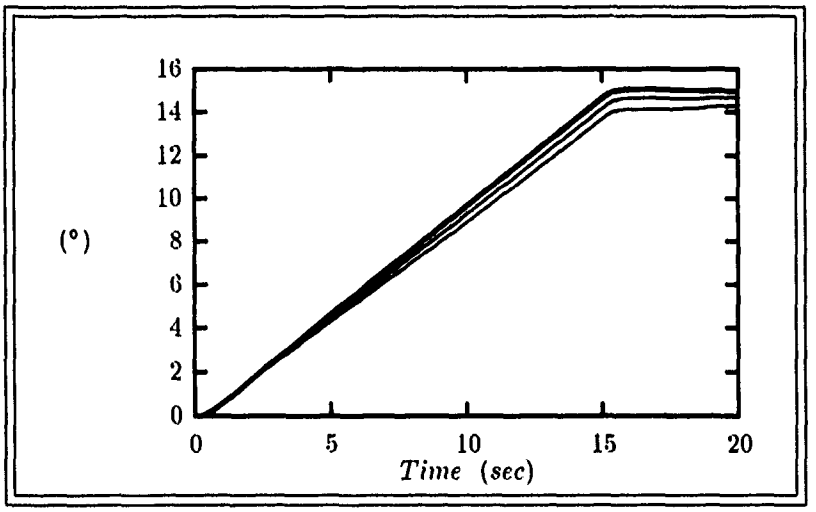

Figure G.38. ϕ Responses For Plants 1–6 to a 15 *sec* Duration 1°/*sec* Roll-Rate (p) Input to Design #2

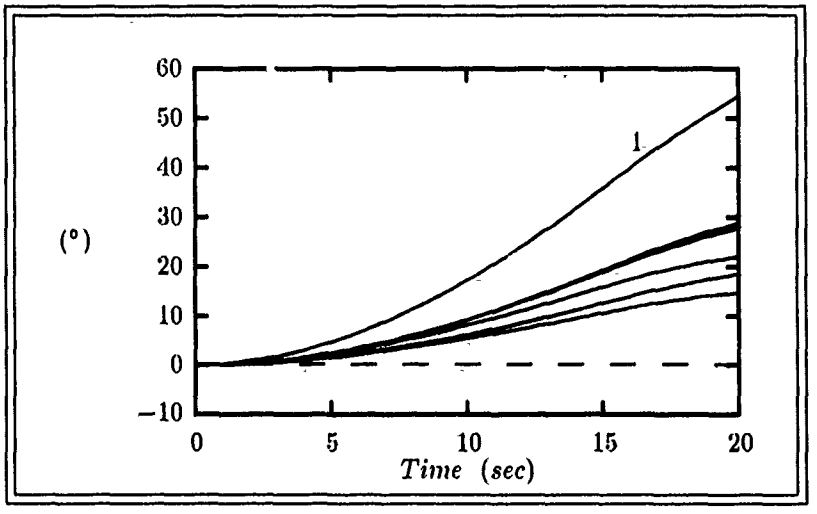

Figure G.39. β Responses For Plants 1–6 to a 15 *sec* Duration 1°/*sec* Roll-Rate (p) Input to Design #2

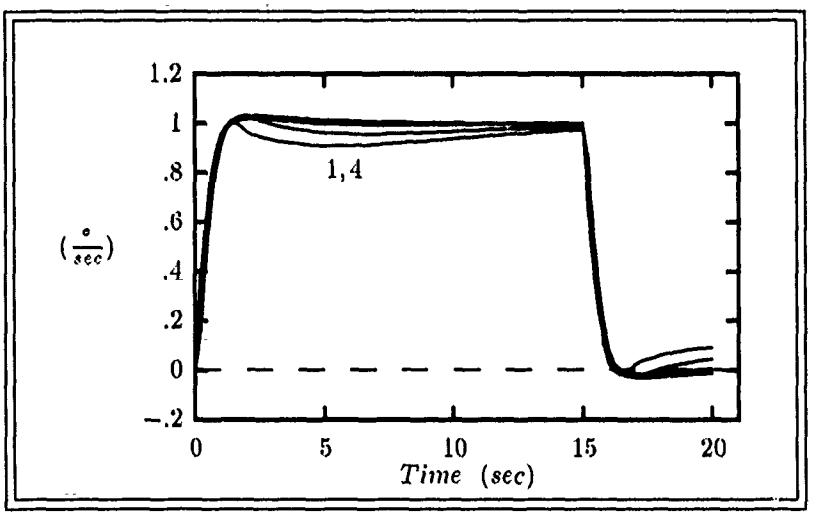

Figure G.40. p Responses For Plants 1-6 to a 15 *sec* Duration 1°/*sec* Roll-Rate (p) Input to Design #2

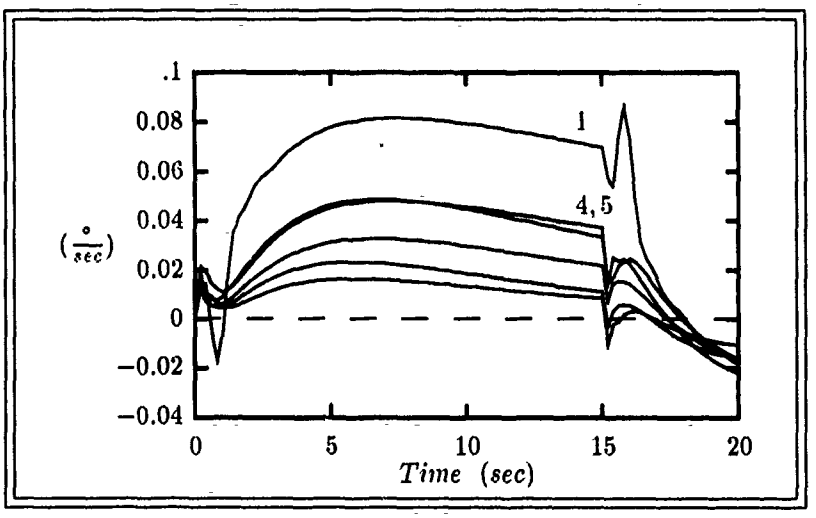

Figure G.41. r Responses For Plants 1-6 to a 15 *sec* Duration 1°/*sec* Roll-Rate (p) Input to Design #2

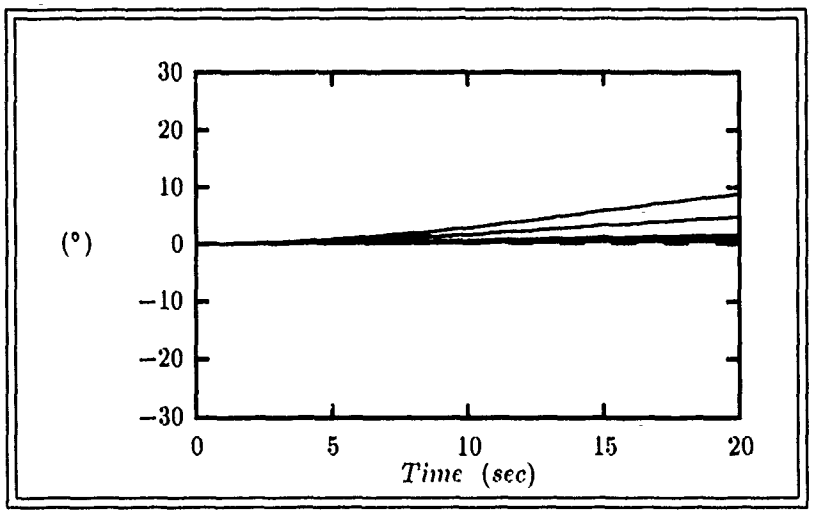

Figure G.42. δ_{a_L} Responses For Plants 1–6 to a 15 *sec* Duration 1°/*sec* Roll-Rate (p) Input to Design #2 (amplitude limited at +15° and −10°)

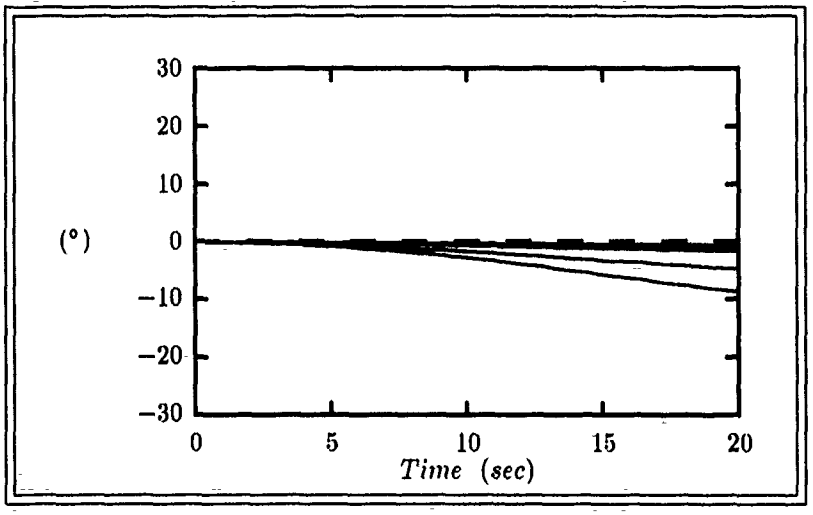

Figure G.43. δ_{a_R} Responses For Plants 1–6 to a 15 *sec* Duration 1°/*sec* Roll-Rate (p) Input to Design #2 (amplitude limited at +15° and −10°)

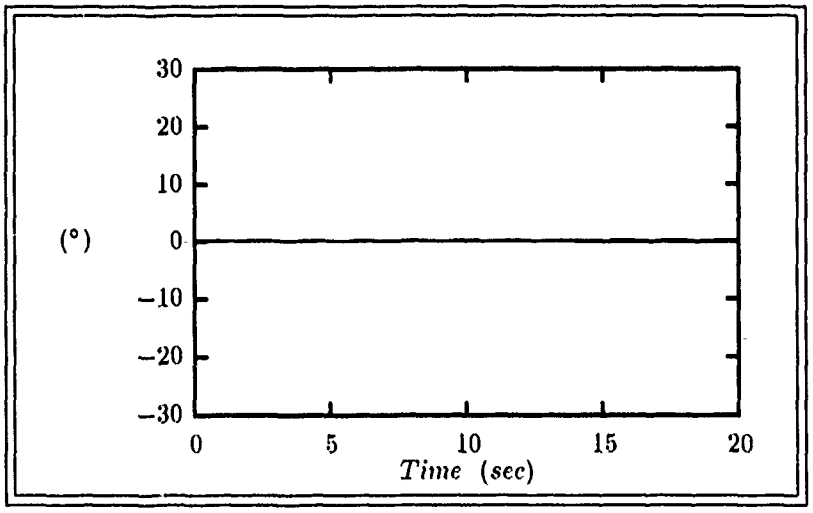

Figure G.44. δ_{f_L} Responses For Plants 1–6 to a 15 *sec* Duration 1°/*sec* Roll-Rate (p) Input to Design #2 (amplitude limited at 0° and −20°)

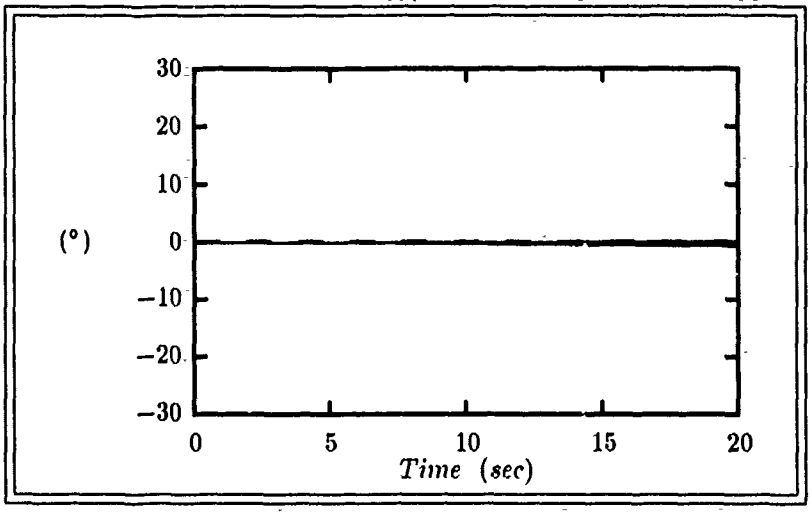

Figure G.45. δ_{f_R} Responses For Plants 1–6 to a 15 *sec* Duration 1°/*sec* Roll-Rate (p) Input to Design #2 (amplitude limited at 0° and −20°)

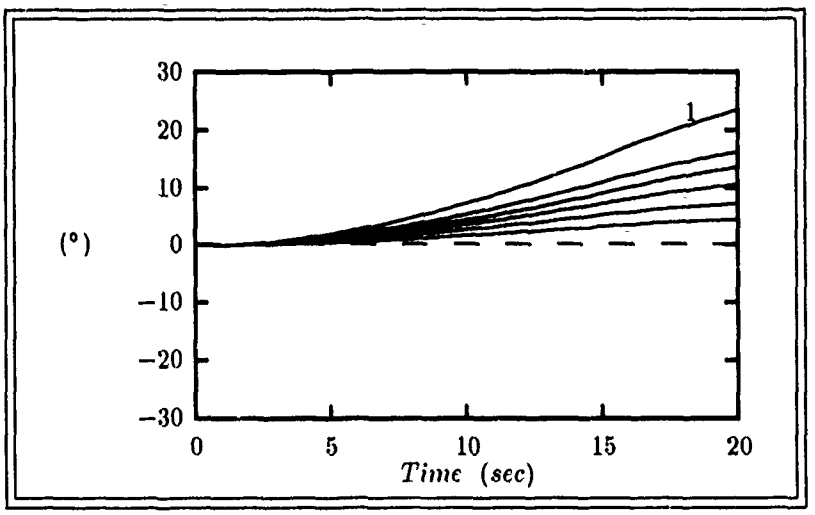

Figure G.46. δ_R Responses For Plants 1–6 to a 15 *sec* Duration 1°/*sec* Roll-Rate (p) Input to Design #2 (amplitude limited at ±25°)

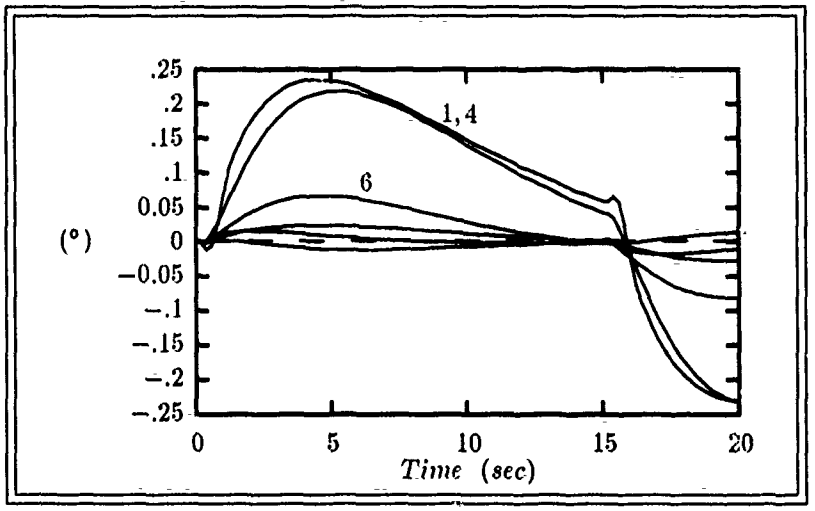

Figure G.47. ϕ Responses For Plants 1–6 to a 15 *sec* Duration 1°/*sec* Yaw-Rate (r) Input to Design #2

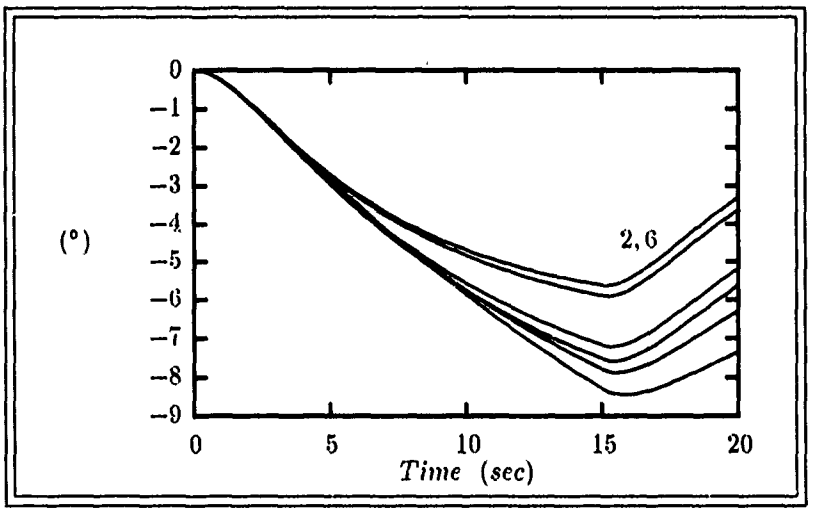

Figure G.48. β Responses For Plants 1–6 to a 15 *sec* Duration 1°/*sec* Yaw-Rate (r) Input to Design #2

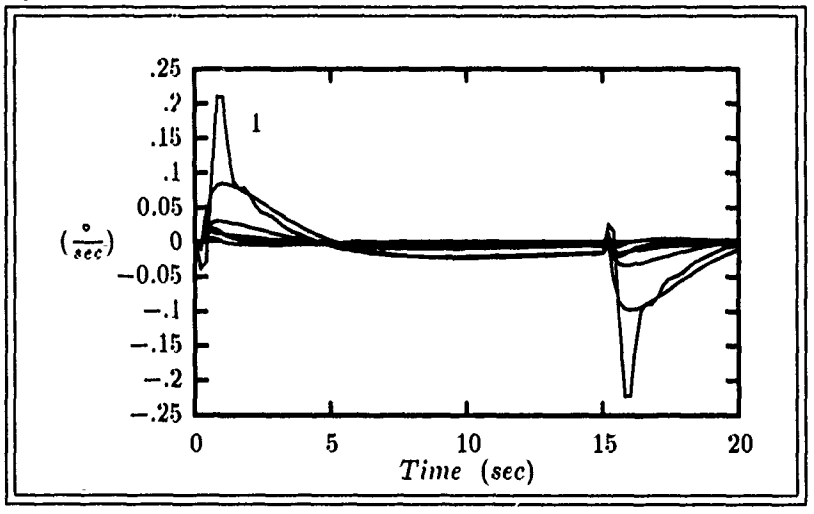

Figure G.49. p Responses For Plants 1–6 to a 15 *sec* Duration 1°/*sec* Yaw-Rate (r) Input to Design #2

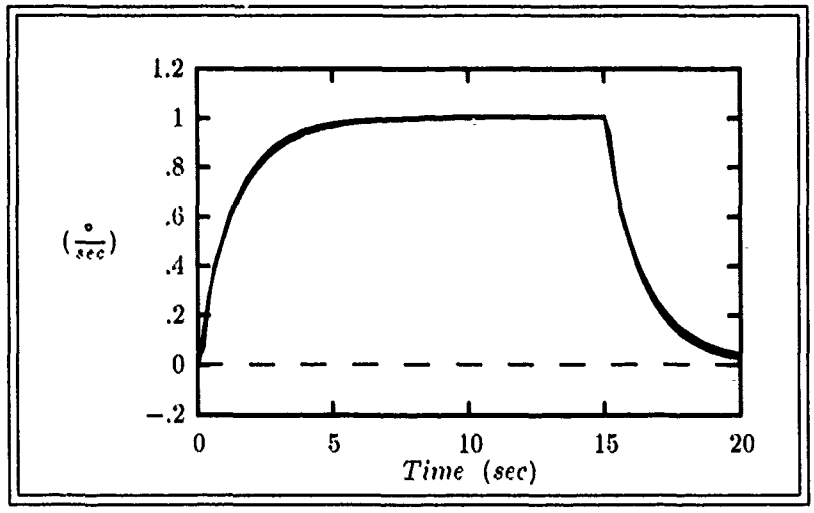

Figure G.50. r Responses For Plants 1–6 to a 15 *sec* Duration 1°/*sec* Yaw-Rate (r) Input to Design #2

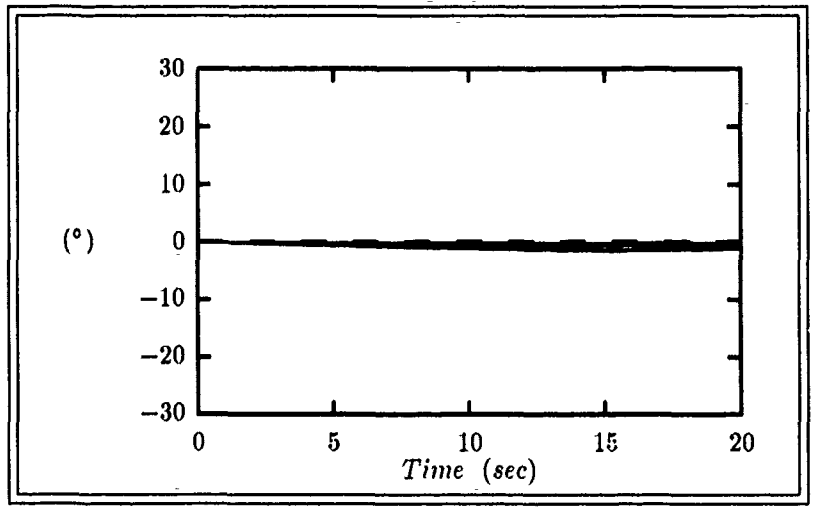

Figure G.51. δ_{a_L} Responses For Plants 1–6 to a 15 *sec* Duration 1°/*sec* Yaw-Rate (r) Input to Design #2 (amplitude limited at +15° and −10°)

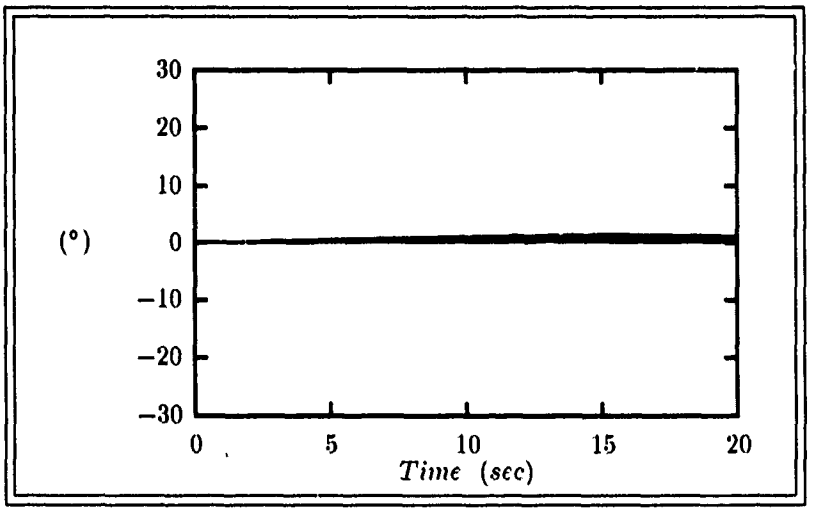

Figure G.52. δ_{a_R} Responses For Plants 1-6 to a 15 *sec* Duration 1°/*sec* Yaw-Rate (r) Input to Design #2 (amplitude limited at +15° and −10°)

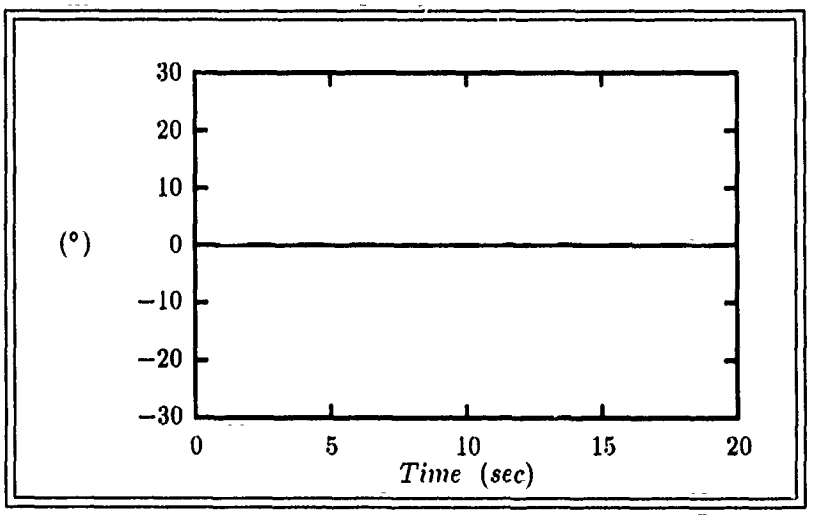

Figure G.53. δ_{f_L} Responses For Plants 1-6 to a 15 *sec* Duration 1°/*sec* Yaw-Rate (r) Input to Design #2 (amplitude limited at +15° and −10°)

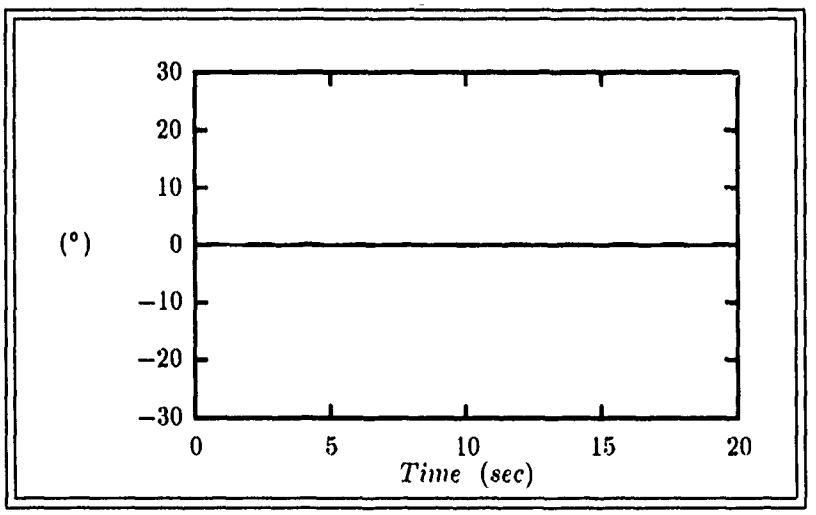

Figure G.54. δ_{f_R} Responses For Plants 1–6 to a 15 *sec* Duration 1°/*sec* Yaw-Rate (r) Input to Design #2 (amplitude limited at 0° and −20°)

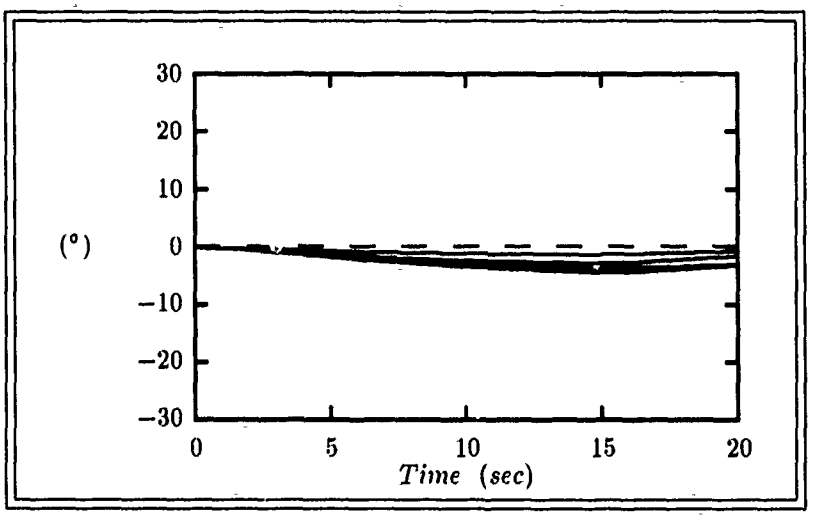

Figure G.55. δ_R Responses For Plants 1–6 to a 15 *sec* Duration 1°/*sec* Yaw-Rate (r) Input to Design #2 (amplitude limited at ±25°)

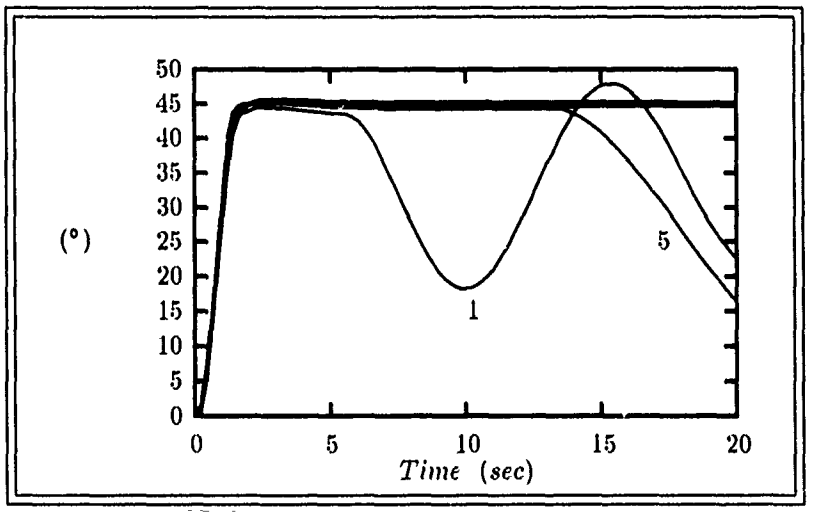

Figure G.56. θ Responses For Plants 1-6 to a 1 *sec* Duration 45°/*sec* Pitch-Rate (q) Input to Design #1

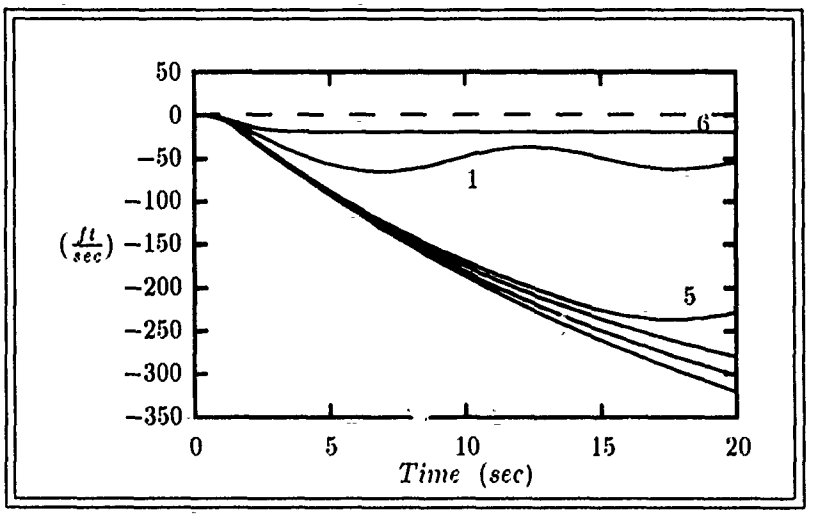

Figure G.57. u Responses For Plants 1-6 to a 1 *sec* Duration 45°/*sec* Pitch-Rate (q) Input to Design #1

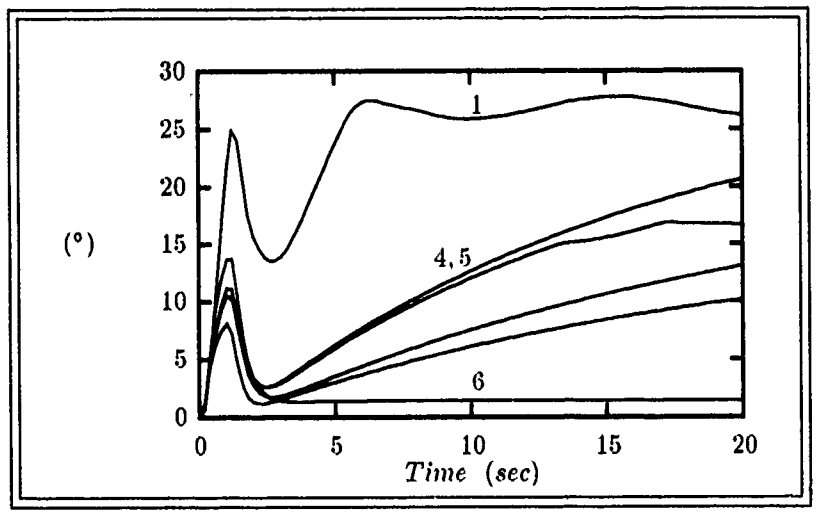

Figure G.58. α Responses For Plants 1–6 to a 1 *sec* Duration 45°/*sec* Pitch-Rate (q) Input to Design #1

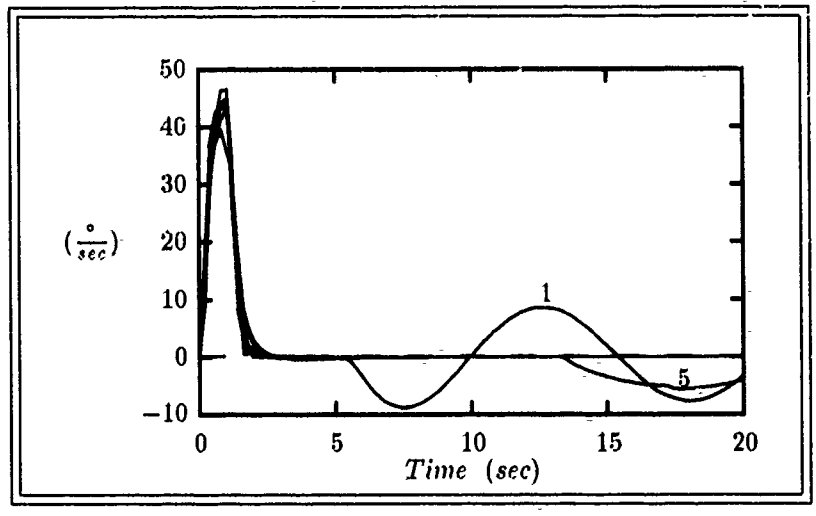

Figure G.59. q Responses For Plants 1–6 to a 1 *sec* Duration 45°/*sec* Pitch-Rate (q) Input to Design #1

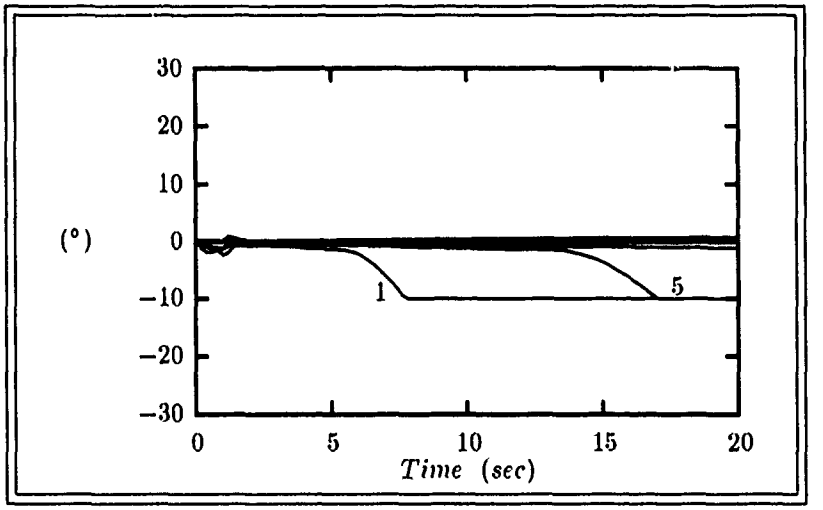

Figure G.60. δ_{a_L} Responses For Plants 1-6 to a 1 *sec* Duration 45°/*sec* Pitch-Rate (q) Input to Design #1 (amplitude limited at +15° and −10°)

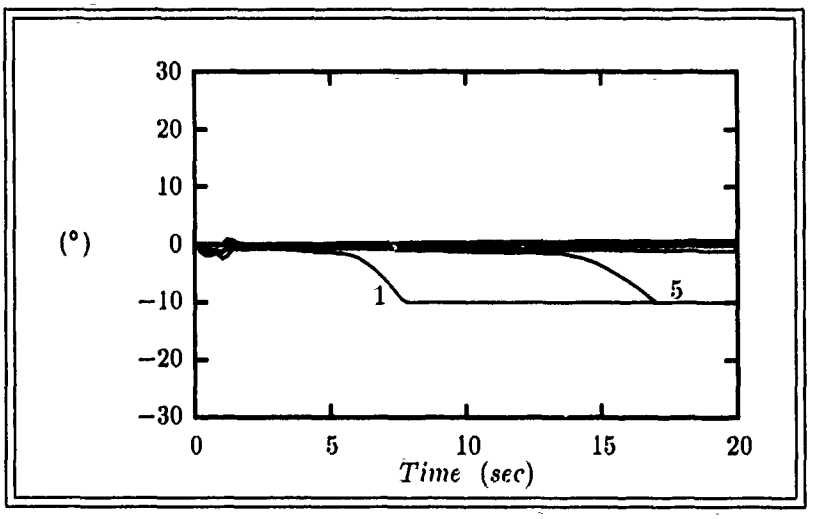

Figure G.61. δ_{a_R} Responses For Plants 1-6 to a 1 *sec* Duration 45°/*sec* Pitch-Rate (q) Input to Design #1 (amplitude limited at +15° and −10°)

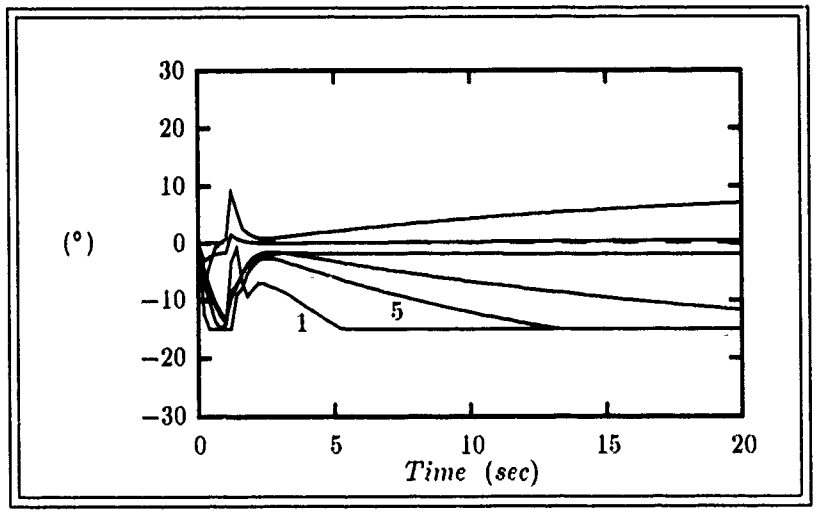

Figure G.62. δ_{e_L} Responses For Plants 1–6 to a 1 *sec* Duration 45°/*sec* Pitch-Rate (q) Input to Design #1 (amplitude limited at ±15°)

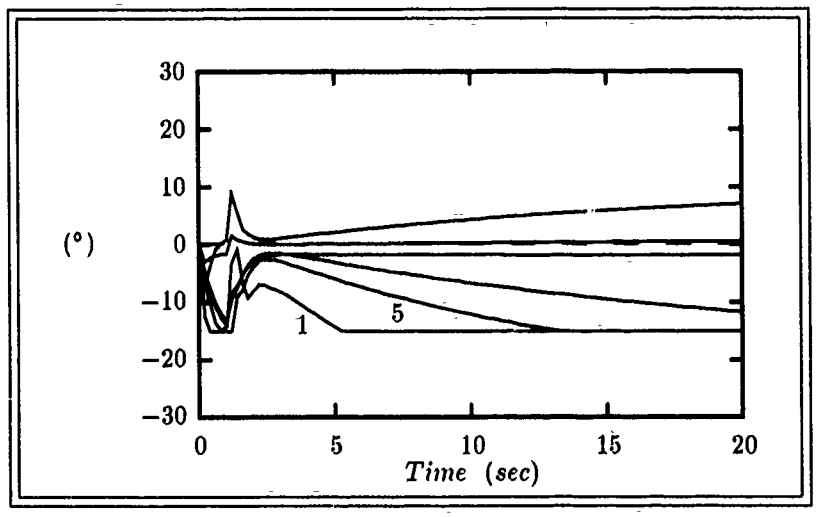

Figure G.63. δ_{e_R} Responses For Plants 1–6 to a 1 *sec* Duration 45°/*sec* Pitch-Rate (q) Input to Design #1 (amplitude limited at ±15°)

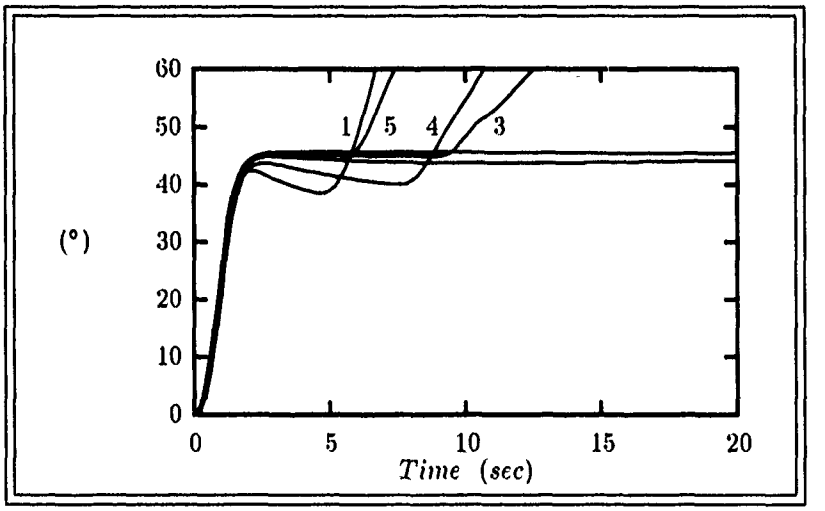

Figure G.64. ϕ Responses For Plants 1-6 to a 1 *sec* Duration 45°/*sec* Roll-Rate (p) Input to Design #1

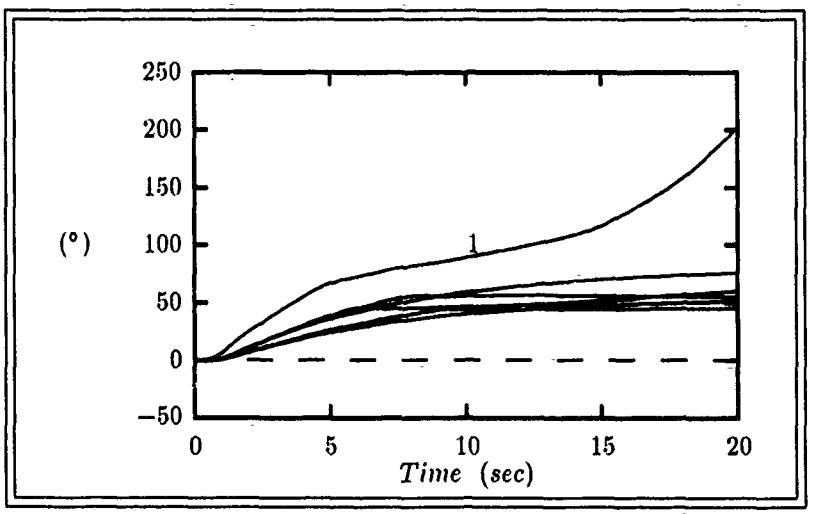

Figure G.65. β Responses For Plants 1-6 to a 1 *sec* Duration 45°/*sec* Roll-Rate (p) Input to Design #1

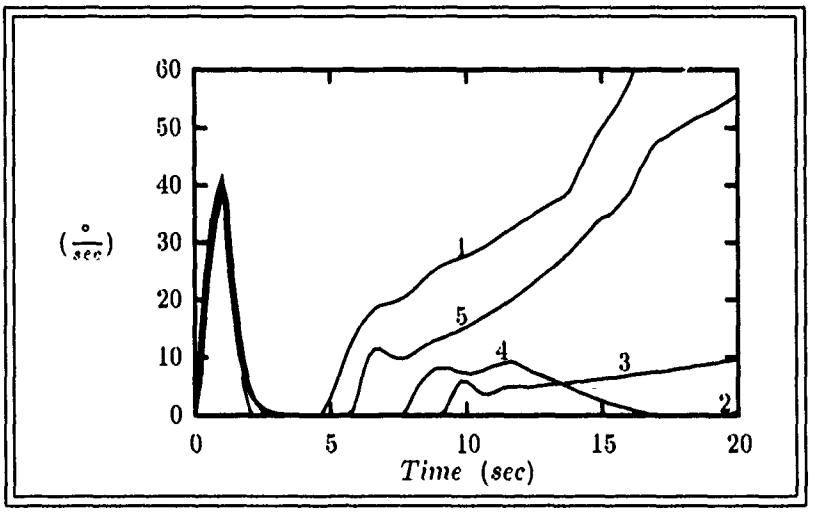

Figure G.66. p Responses For Plants 1–6 to a 1 *sec* Duration 45°/*sec* Roll-Rate (p) Input to Design #1

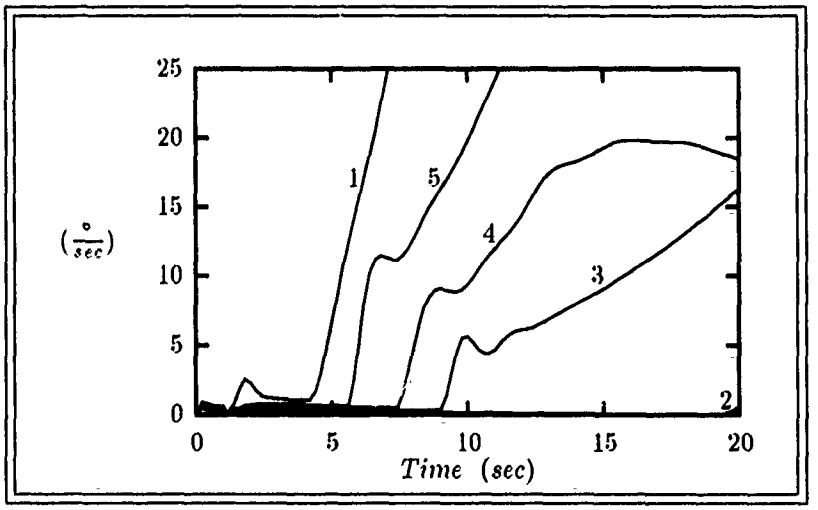

Figure G.67. r Responses For Plants 1–6 to a 1 *sec* Duration 45°/*sec* Roll-Rate (p) Input to Design #1

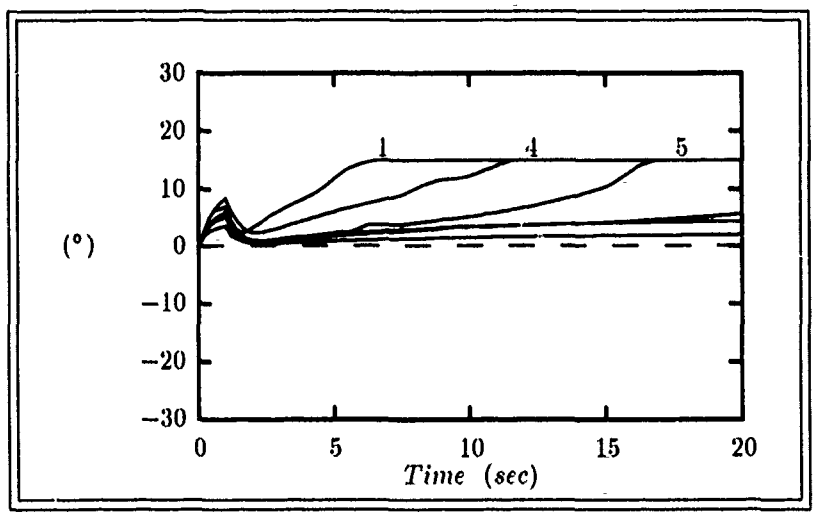

Figure G.68. δ_{a_L} Responses For Plants 1–6 to a 1 *sec* Duration 45°/*sec* Roll-Rate (p) Input to Design #1 (amplitude limited at +15° and −10°)

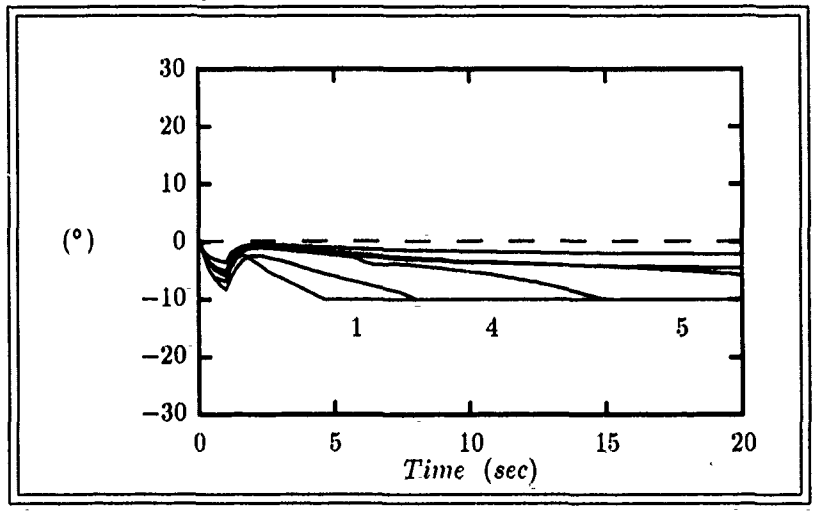

Figure G.69. δ_{a_R} Responses For Plants 1–6 to a 1 *sec* Duration 45°/*sec* Roll-Rate (p) Input to Design #1 (amplitude limited at +15° and −10°)

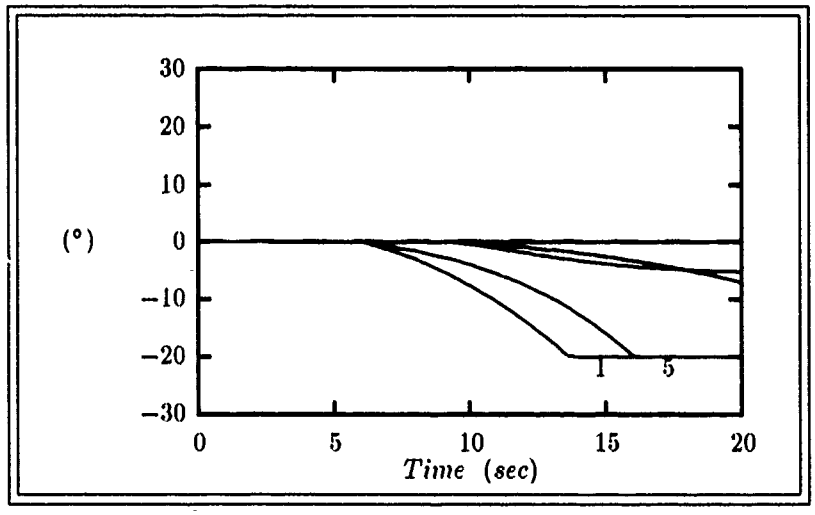

Figure G.70. δ_{f_L} Responses For Plants 1–6 to a 1 *sec* Duration 45°/*sec* Roll-Rate (p) Input to Design #1 (amplitude limited at 0° and −20°)

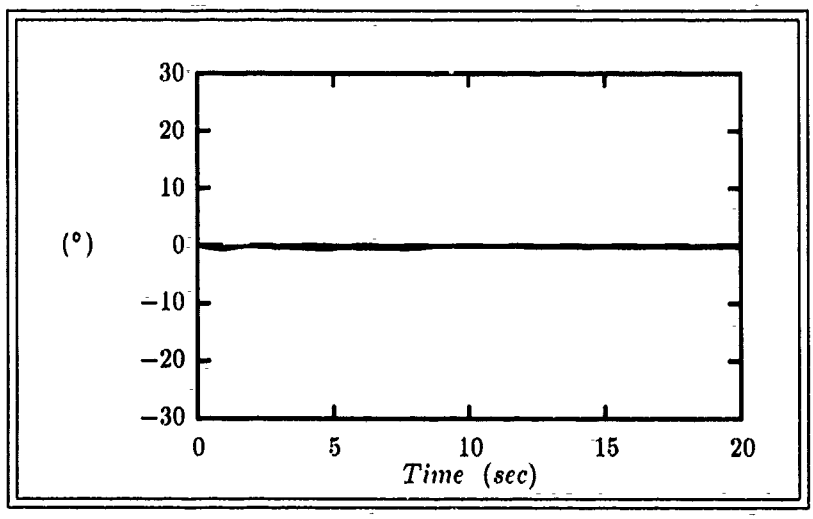

Figure G.71. δ_{f_R} Responses For Plants 1–6 to a 1 *sec* Duration 45°/*sec* Roll-Rate (p) Input to Design #1 (amplitude limited at 0° and −20°)

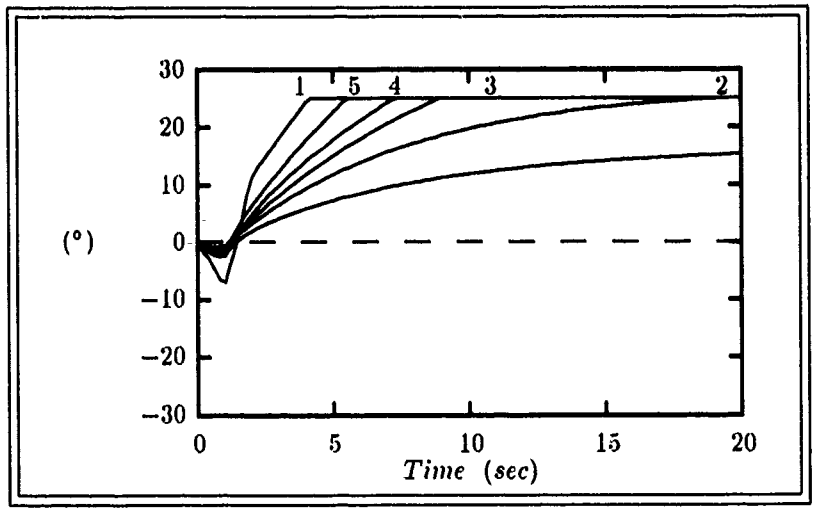

Figure G.72. δ_R Responses For Plants 1–6 to a 1 *sec* Duration 45°/*sec* Roll-Rate (p) Input to Design #1 (amplitude limited at ±25°)

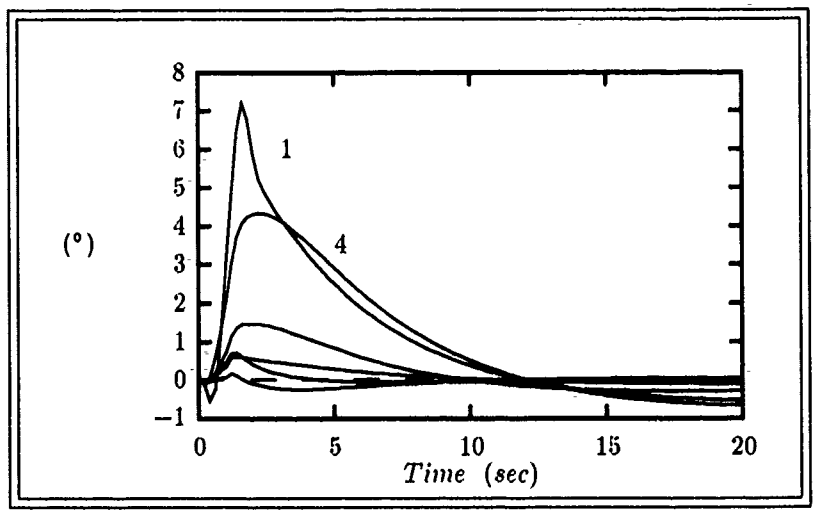

Figure G.73. ϕ Responses For Plants 1–6 to a 1 *sec* Duration 45°/*sec* Yaw-Rate (r) Input to Design #1

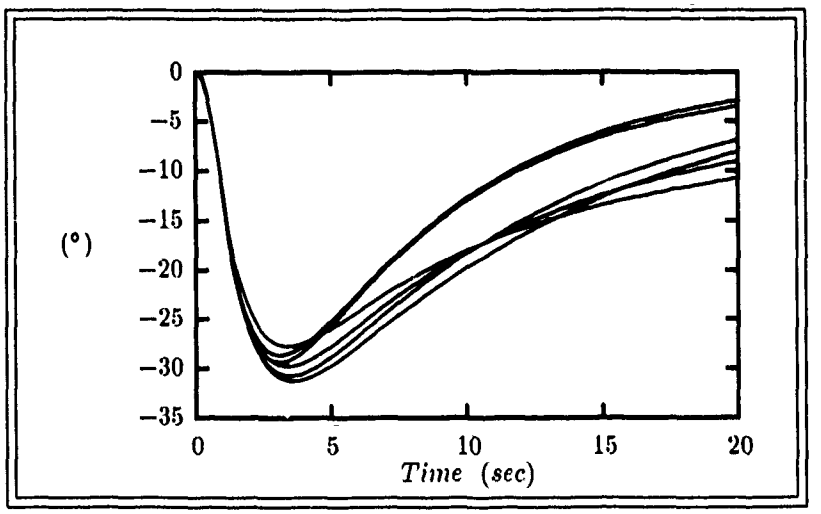

Figure G.74. β Responses For Plants 1–6 to a 1 *sec* Duration 45°/*sec* Yaw-Rate (r) Input to Design #1

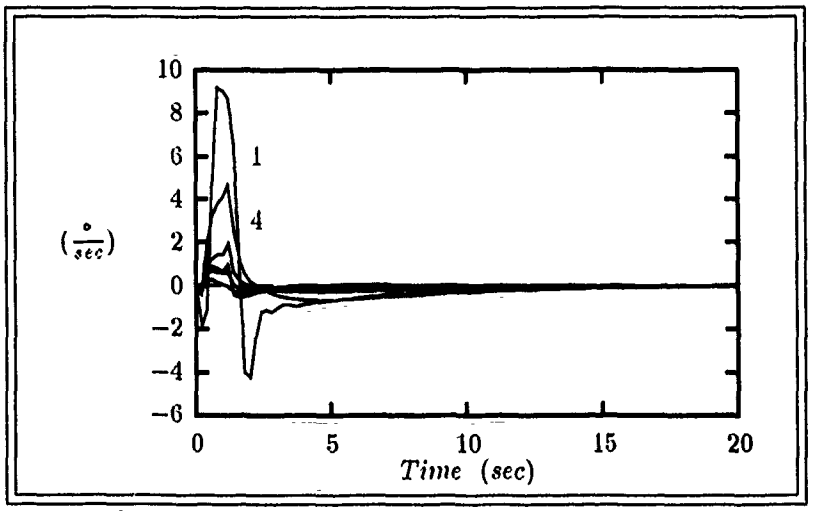

Figure G.75. p Responses For Plants 1–6 to a 1 *sec* Duration 45°/*sec* Yaw-Rate (r) Input to Design #1

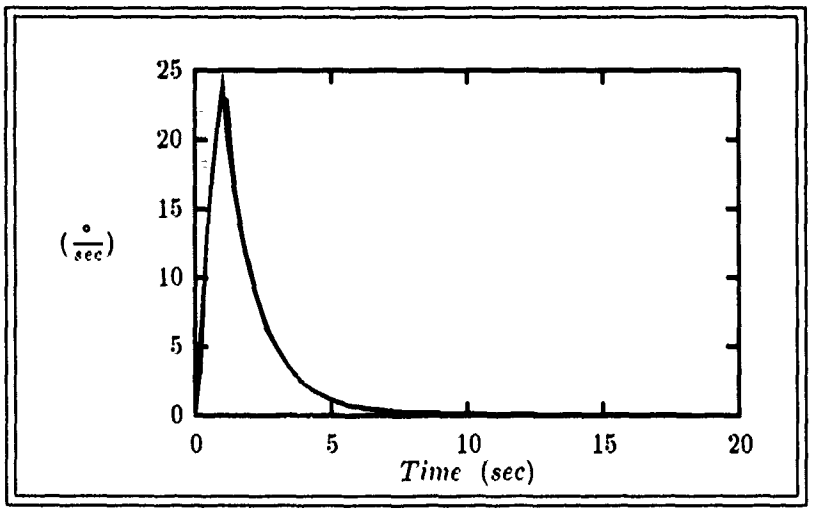

Figure G.76. r Responses For Plants 1–6 to a 1 *sec* Duration 45°/*sec* Yaw-Rate (r) Input to Design #1

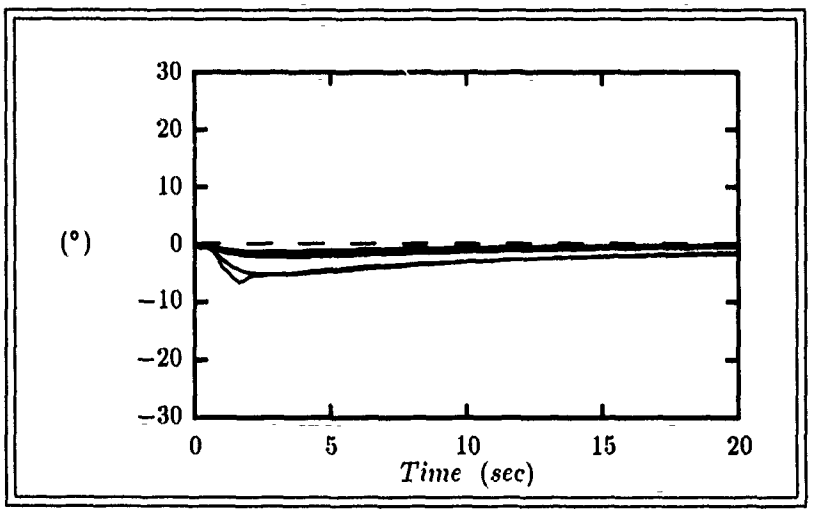

Figure G.77. δ_{a_L} Responses For Plants 1–6 to a 1 *sec* Duration 45°/*sec* Yaw-Rate (r) Input to Design #1 (amplitude limited at +15° and −10°)

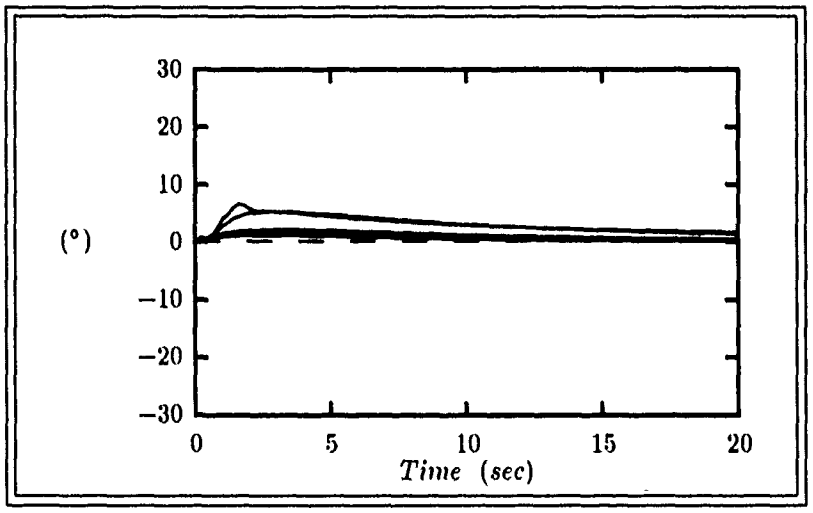

Figure G.78. δ_{a_R} Responses For Plants 1–6 to a 1 *sec* Duration 45°/*sec* Yaw-Rate (r) Input to Design #1 (amplitude limited at +15° and −10°)

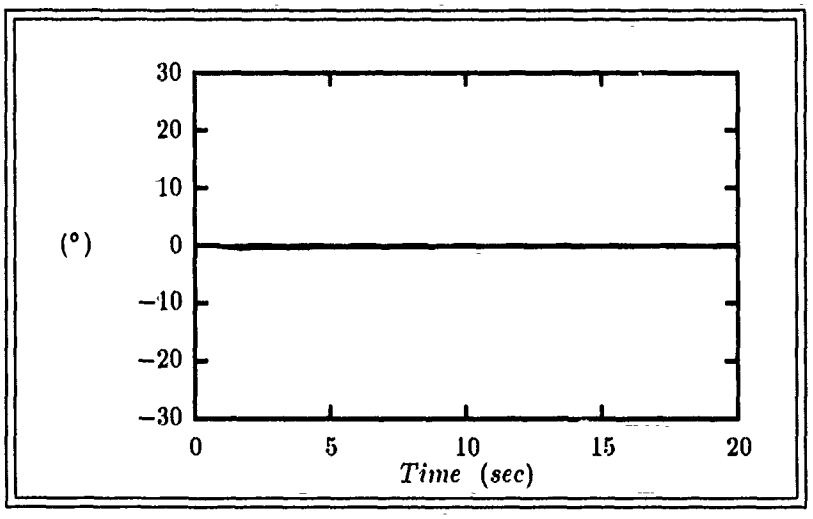

Figure G.79. δ_{f_L} Responses For Plants 1–6 to a 1 *sec* Duration 45°/*sec* Yaw-Rate (r) Input to Design #1 (amplitude limited at 0° and −20°)

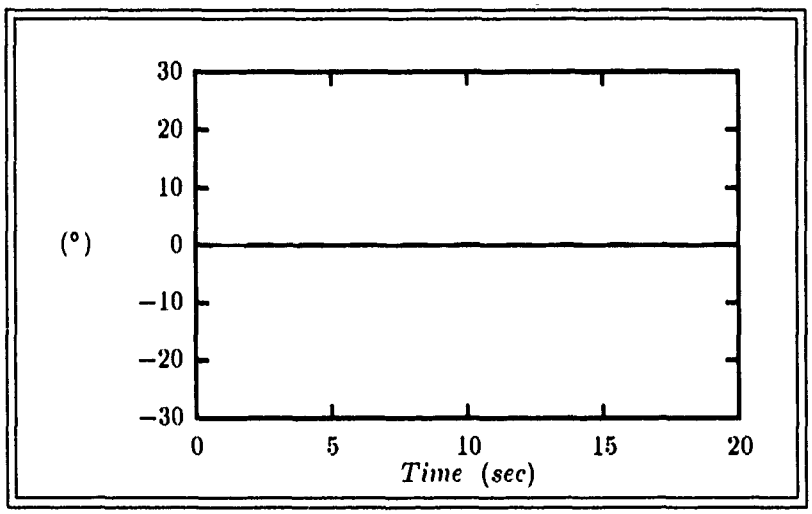

Figure G.80. δ_{f_R} Responses For Plants 1-6 to a 1 *sec* Duration 45°/*sec* Yaw-Rate (r) Input to Design #1 (amplitude limited at 0° and −20°)

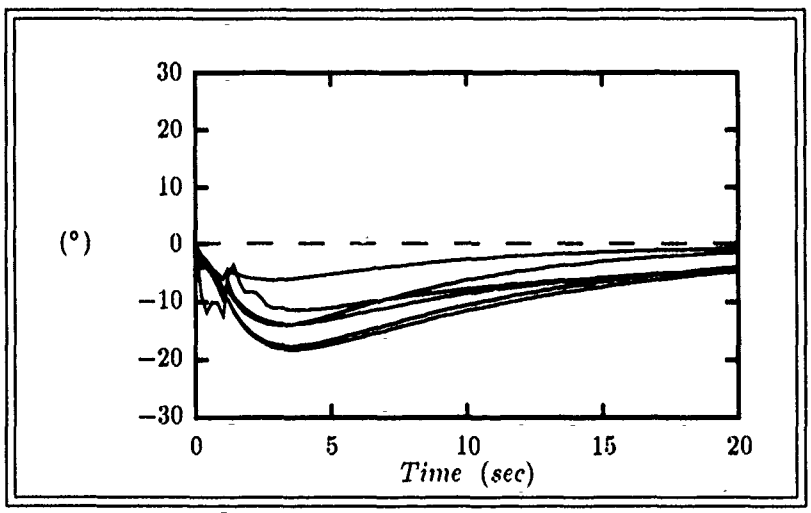

Figure G.81. δ_R Responses For Plants 1-6 to a 1 *sec* Duration 45°/*sec* Yaw-Rate (r) Input to Design #1 (amplitude limited at ±25°)

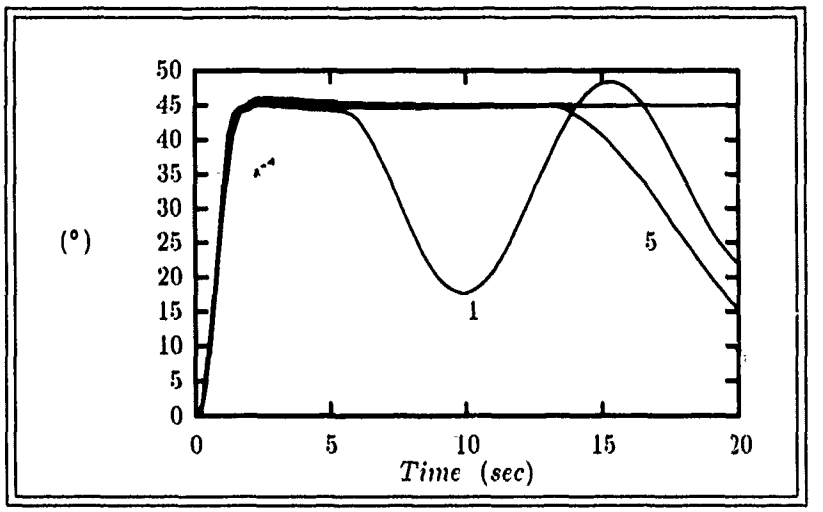

Figure G.82. θ Responses For Plants 1–6 to a 1 *sec* Duration 45°/*sec* Pitch-Rate (q) Input to Design #2

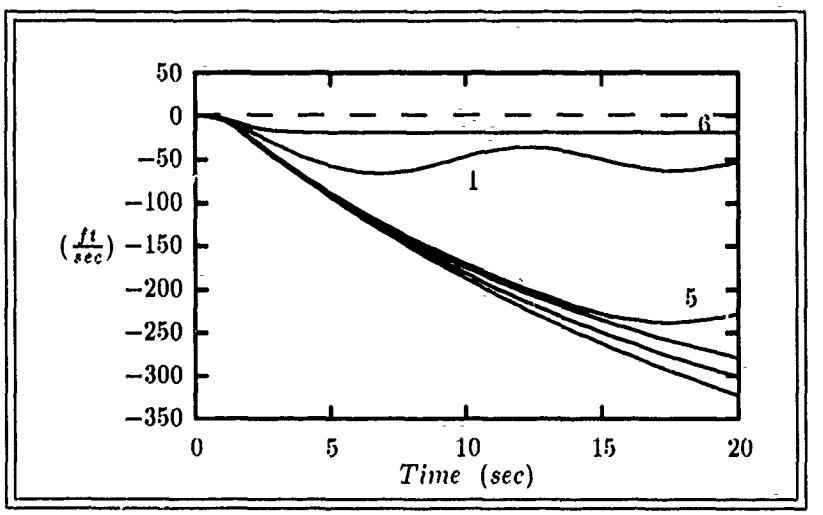

Figure G.83. u Responses For Plants 1–6 to a 1 *sec* Duration 45°/*sec* Pitch-Rate (q) Input to Design #2

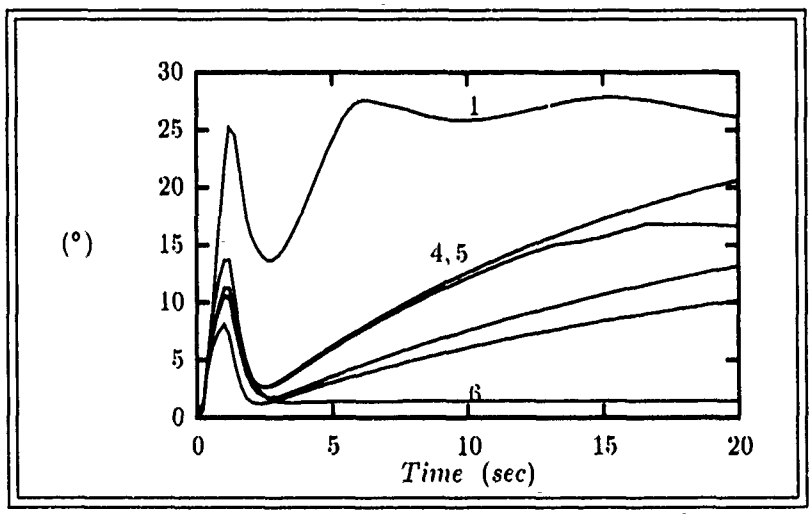

Figure G.84. α Responses For Plants 1–6 to a 1 *sec* Duration 45°/*sec* Pitch-Rate (q) Input to Design #2

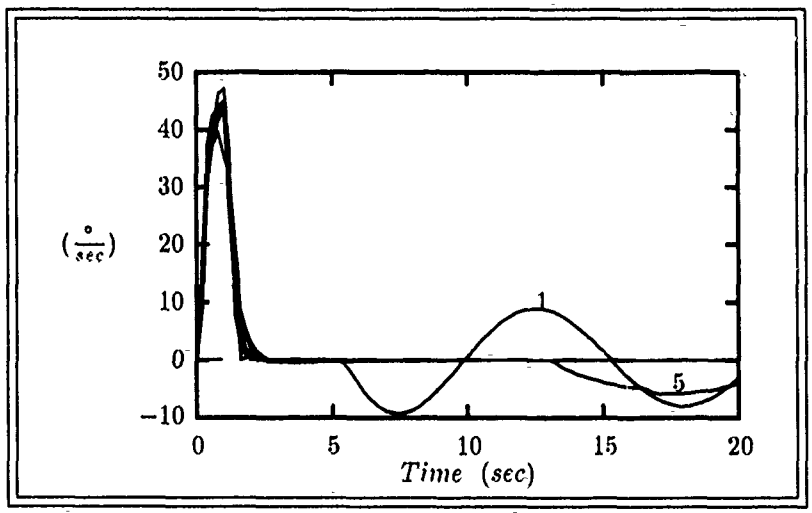

Figure G.85. q Responses For Plants 1–6 to a 1 *sec* Duration 45°/*sec* Pitch-Rate (q) Input to Design #2

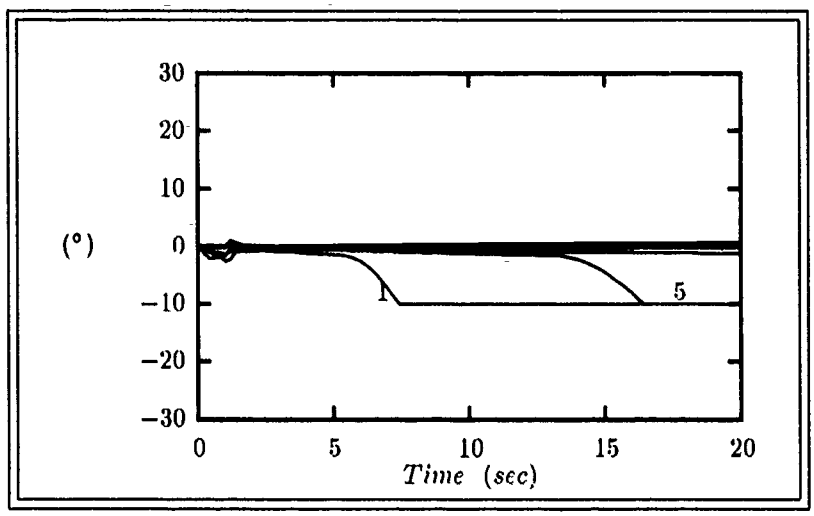

Figure G.86. δ_{a_L} Responses For Plants 1–6 to a 1 *sec* Duration 45°/*sec* Pitch-Rate (q) Input to Design #2 (amplitude limited at +15° and −10°)

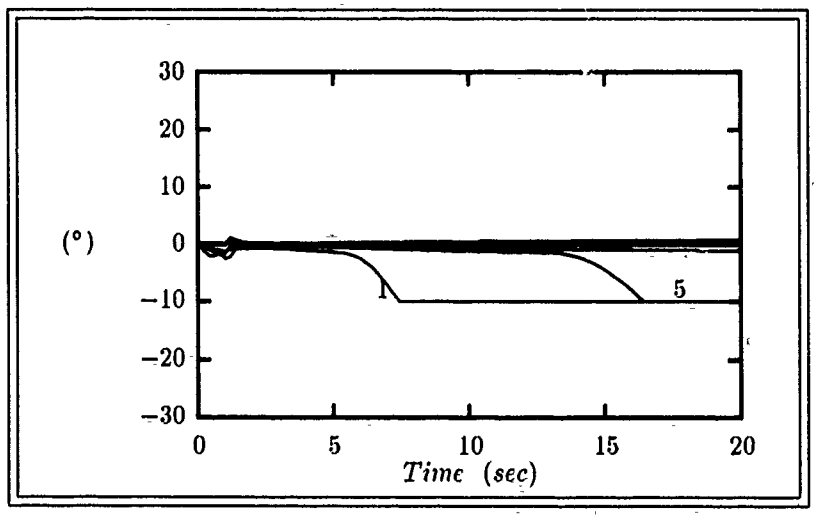

Figure G.87. δ_{a_R} Responses For Plants 1–6 to a 1 *sec* Duration 45°/*sec* Pitch-Rate (q) Input to Design #2 (amplitude limited at +15° and −10°)

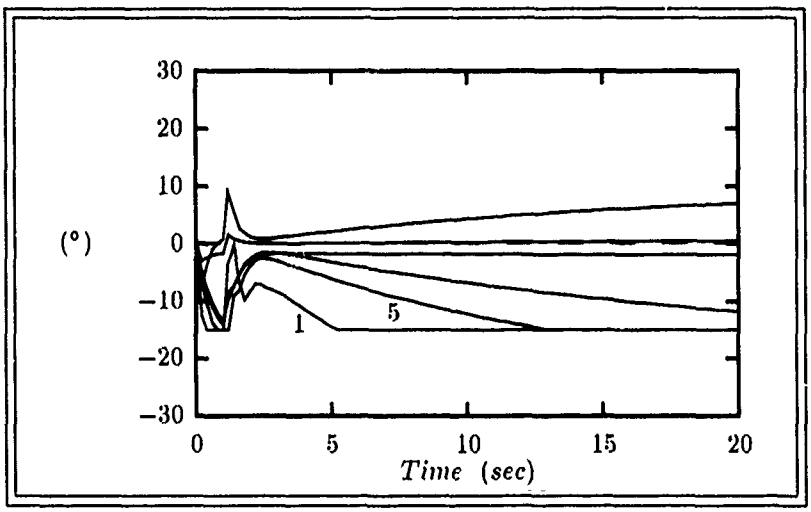

Figure G.88. δ_{e_L} Responses For Plants 1–6 to a 1 *sec* Duration 45°/*sec* Pitch-Rate (q) Input to Design #2 (amplitude limited at ±15°)

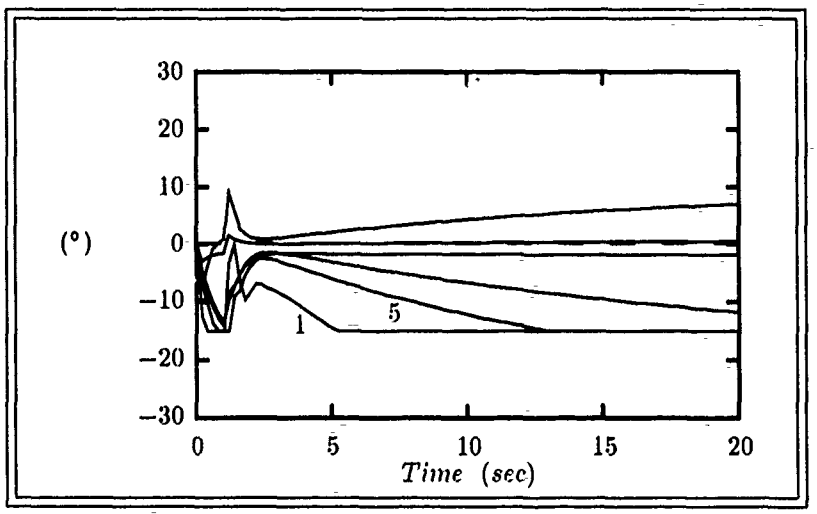

Figure G.89. δ_{e_R} Responses For Plants 1–6 to a 1 *sec* Duration 45°/*sec* Pitch-Rate (q) Input to Design #2 (amplitude limited at ±15°)

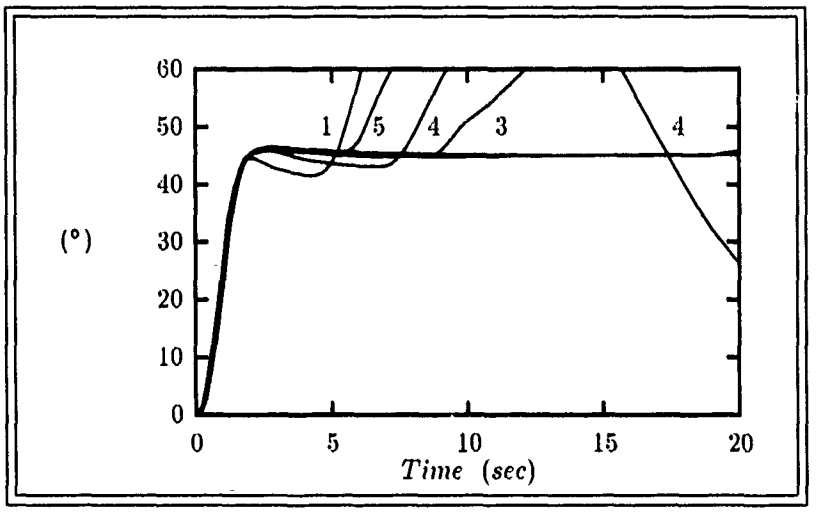

Figure G.90. ϕ Responses For Plants 1–6 to a 1 *sec* Duration 45°/*sec* Roll-Rate (p) Input to Design #2

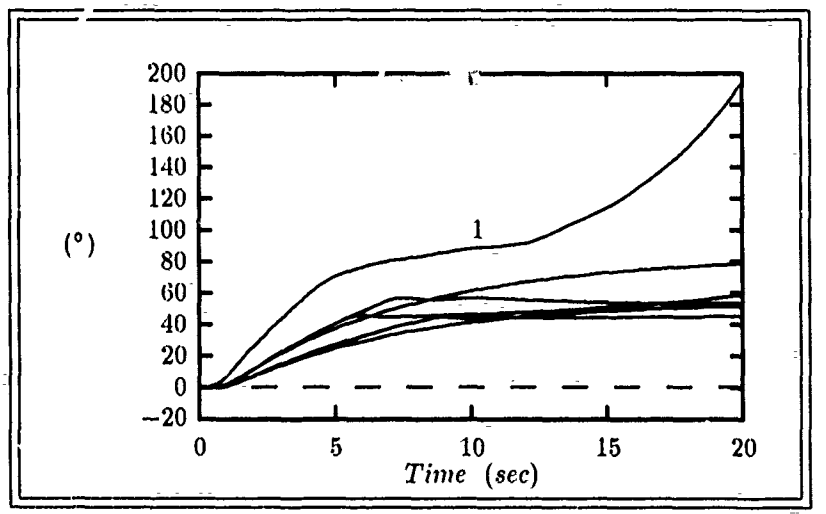

Figure G.91. β Responses For Plants 1–6 to a 1 *sec* Duration 45°/*sec* Roll-Rate (p) Input to Design #2

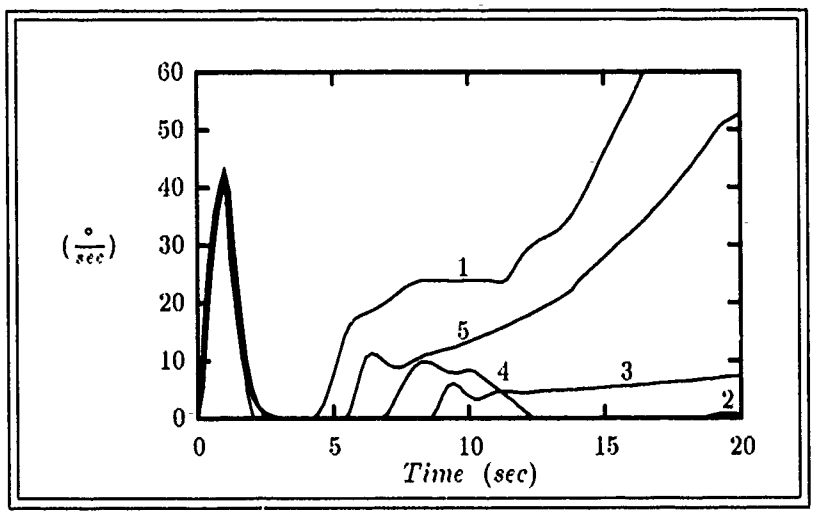

Figure G.92. p Responses For Plants 1–6 to a 1 *sec* Duration 45°/*sec* Roll-Rate (p) Input to Design #2

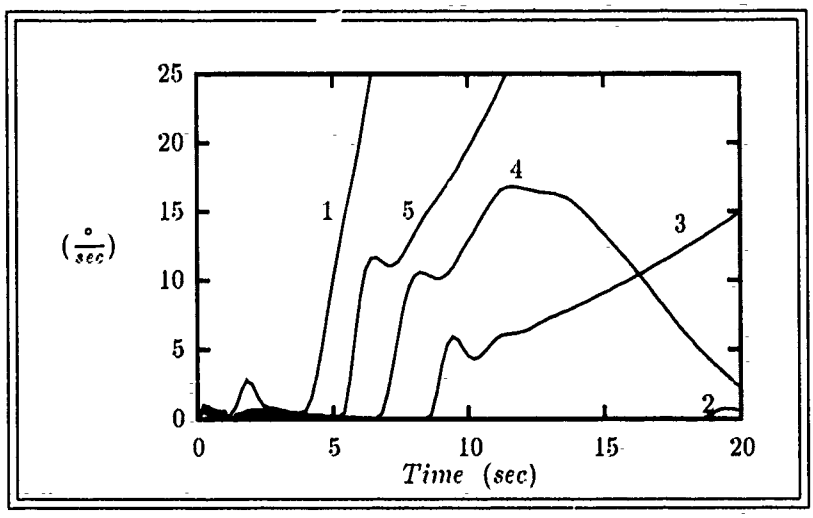

Figure G.93. r Responses For Plants 1–6 to a 1 *sec* Duration 45°/*sec* Roll-Rate (p) Input to Design #2

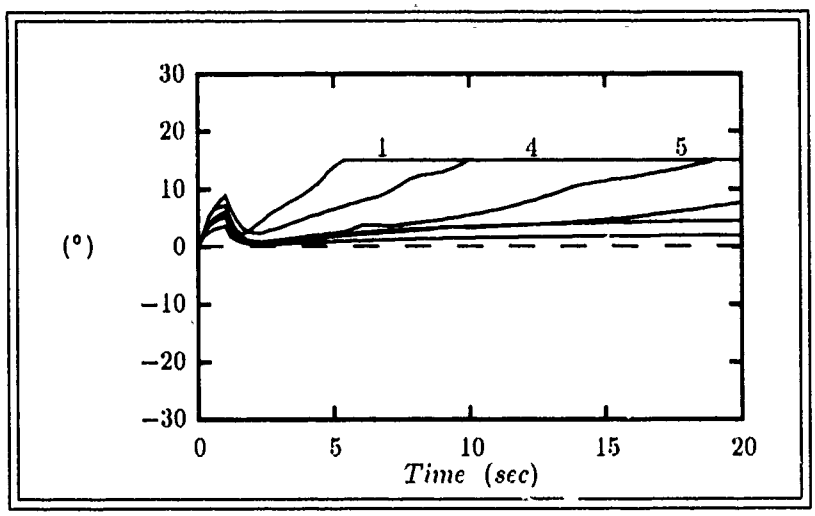

Figure G.94. δ_{a_L} Responses For Plants 1–6 to a 1 *sec* Duration 45°/*sec* Roll-Rate (p) Input to Design #2 (amplitude limited at +15° and −10°)

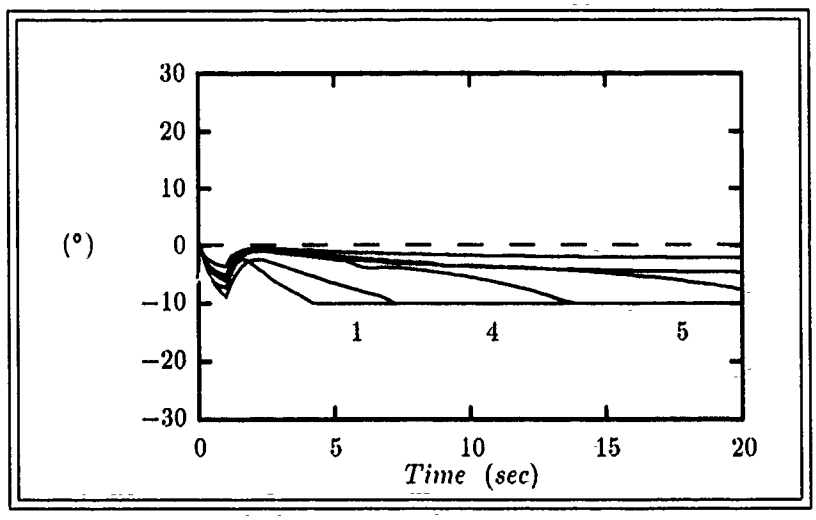

Figure G.95. δ_{a_R} Responses For Plants 1–6 to a 1 *sec* Duration 45°/*sec* Roll-Rate (p) Input to Design #2 (amplitude limited at +15° and −10°)

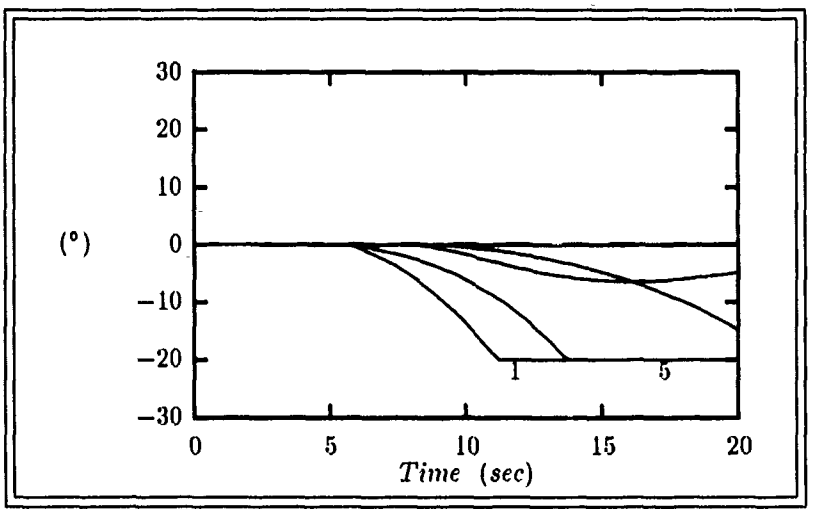

Figure G.96. δ_{f_L} Responses For Plants 1-6 to a 1 *sec* Duration 45°/*sec* Roll-Rate (p) Input to Design #2 (amplitude limited at 0° and −20°)

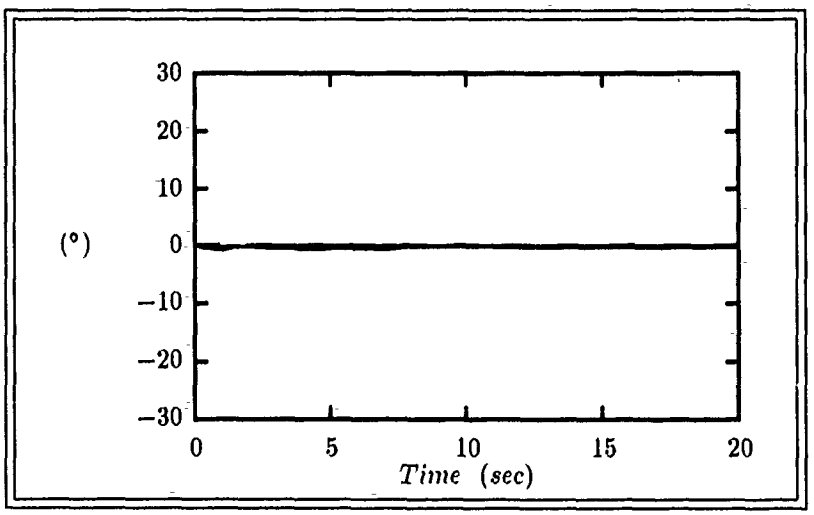

Figure G.97. δ_{f_R} Responses For Plants 1-6 to a 1 *sec* Duration 45°/*sec* Roll-Rate (p) Input to Design #2 (amplitude limited at 0° and −20°)

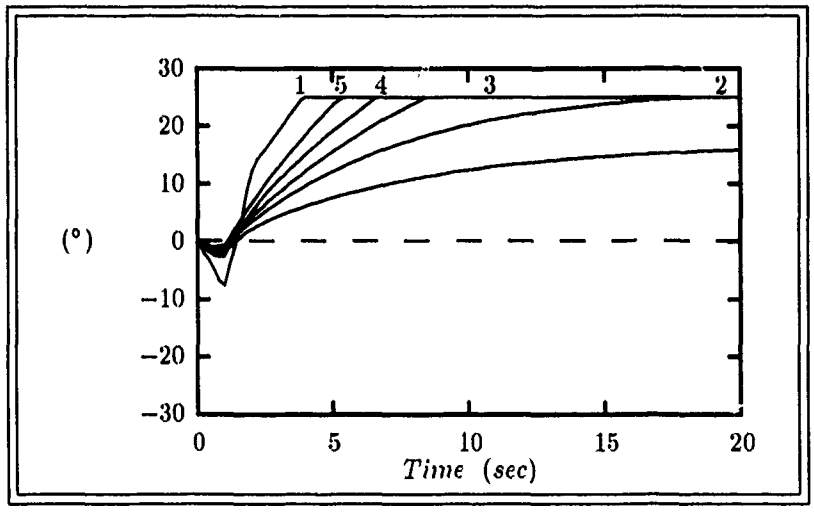

Figure G.98. δ_R Responses For Plants 1–6 to a 1 *sec* Duration 45°/*sec* Roll-Rate (p) Input to Design #2 (amplitude limited at ±25°)

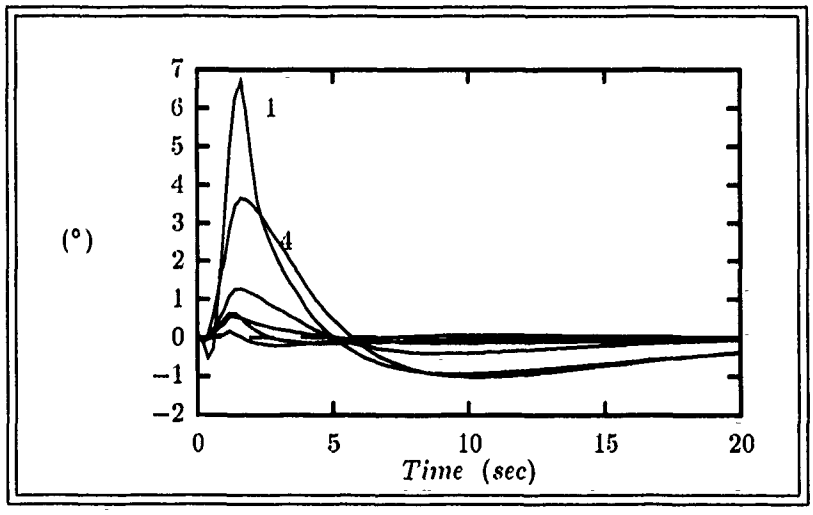

Figure G.99. ϕ Responses For Plants 1–6 to a 1 *sec* Duration 45°/*sec* Yaw-Rate (r) Input to Design #2

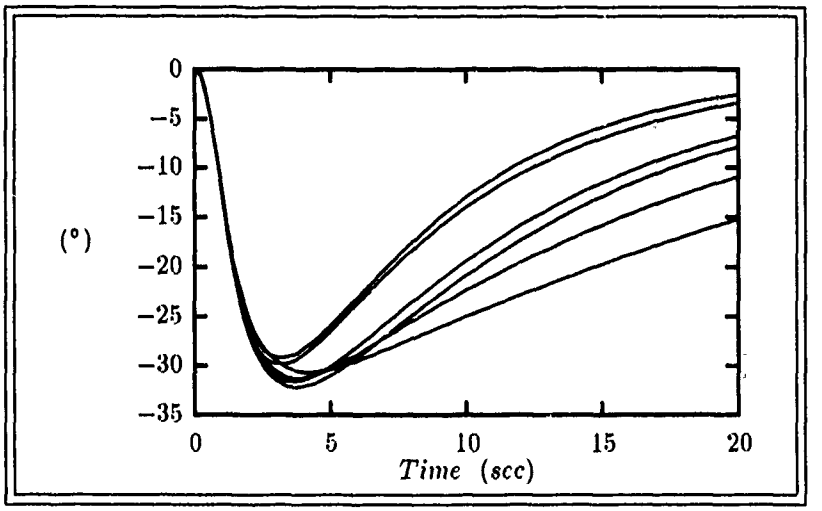

Figure G.100. β Responses For Plants 1–6 to a 1 *sec* Duration 45°/*sec* Yaw-Rate (r) Input to Design #2

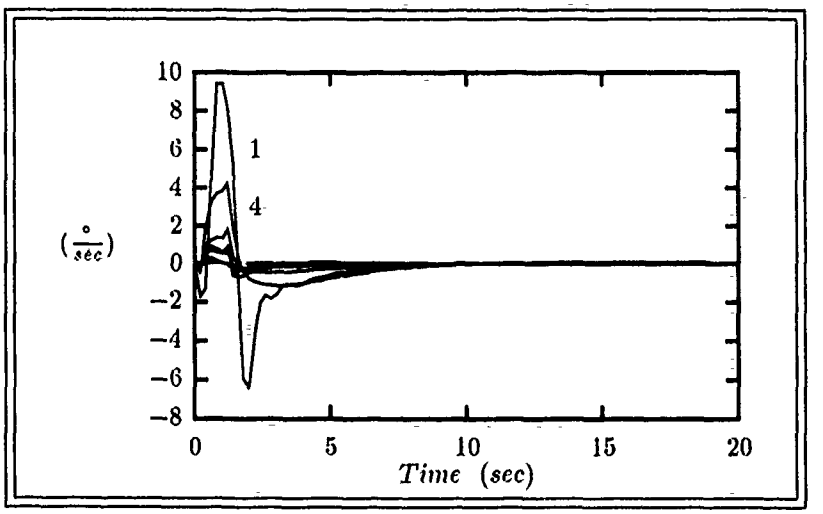

Figure G.101. p Responses For Plants 1–6 to a 1 *sec* Duration 45°/*sec* Yaw-Rate (r) Input to Design #2

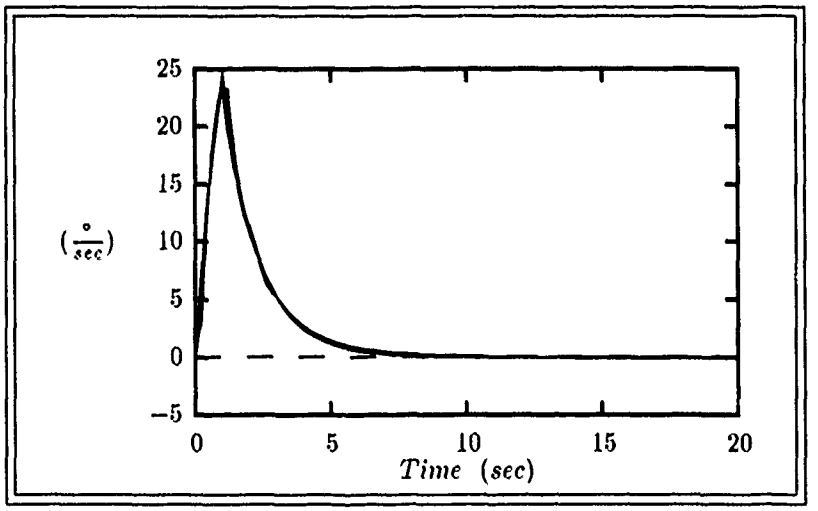

Figure G.102. r Responses For Plants 1–6 to a 1 *sec* Duration 45°/*sec* Yaw-Rate (r) Input to Design #2

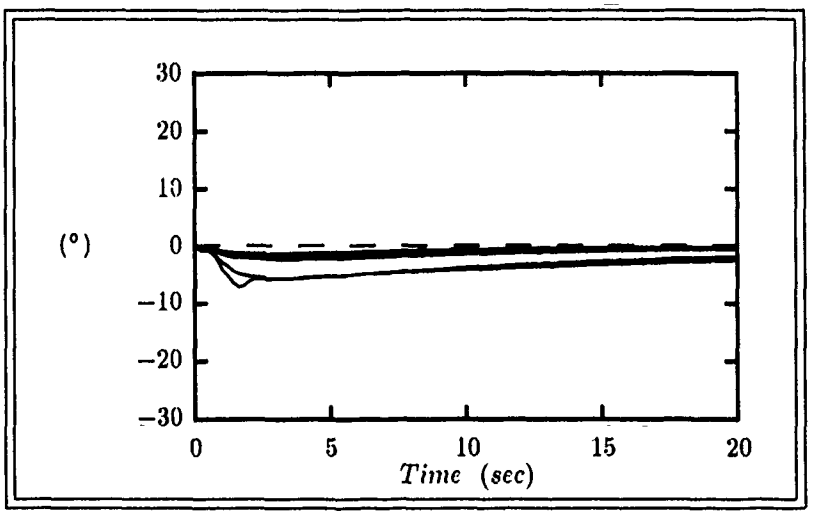

Figure G.103. δ_{a_L} Responses For Plants 1–6 to a 1 *sec* Duration 45°/*sec* Yaw-Rate (r) Input to Design #2 (amplitude limited at +15° and −10°)

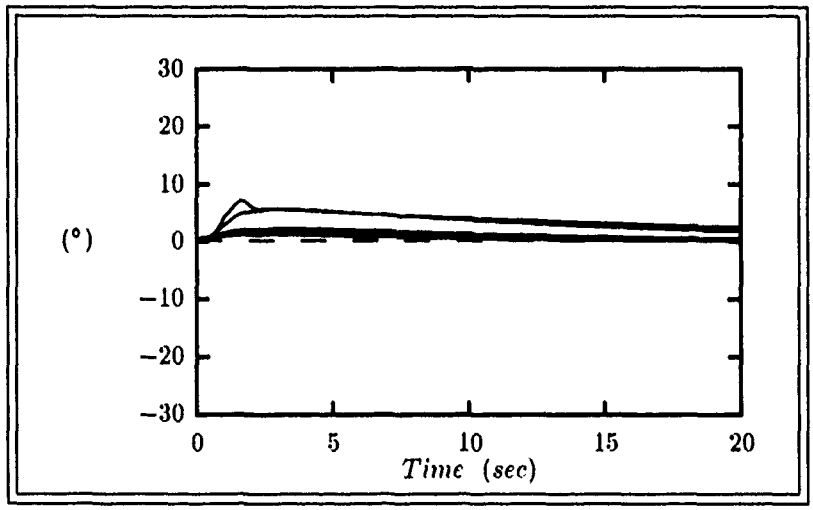

Figure G.104. δ_{a_R} Responses For Plants 1–6 to a 1 *sec* Duration 45°/*sec* Yaw-Rate (r) Input to Design #2 (amplitude limited at +15° and −10°)

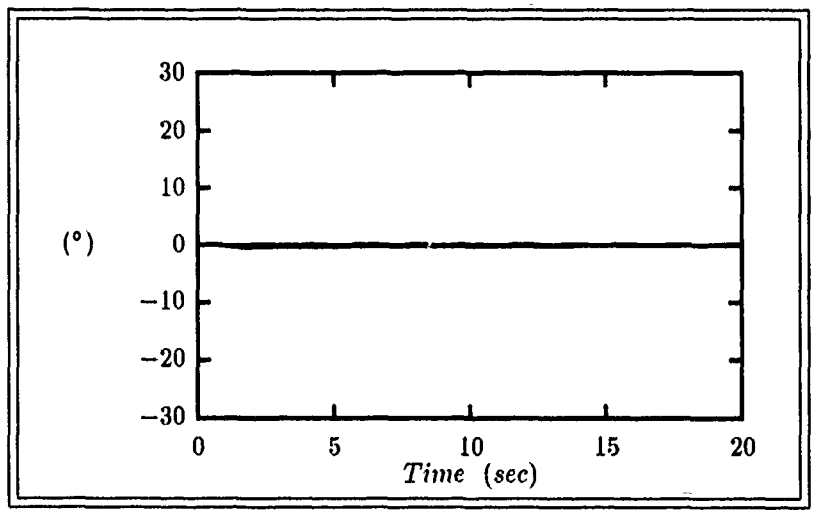

Figure G.105. δ_{f_L} Responses For Plants 1–6 to a 1 *sec* Duration 45°/*sec* Yaw-Rate (r) Input to Design #2 (amplitude limited at 0° and −20°)

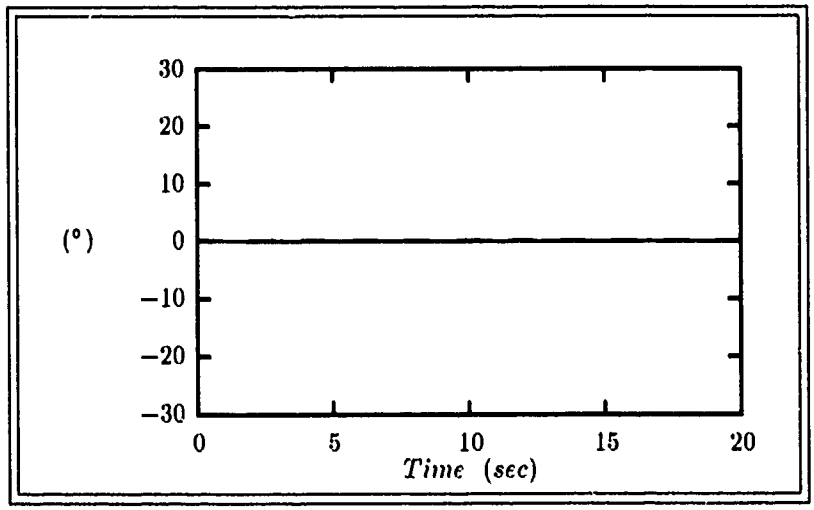

Figure G.106. δ_{f_R} Responses For Plants 1–6 to a 1 *sec* Duration 45°/*sec* Yaw-Rate (r) Input to Design #2 (amplitude limited at 0° and −20°)

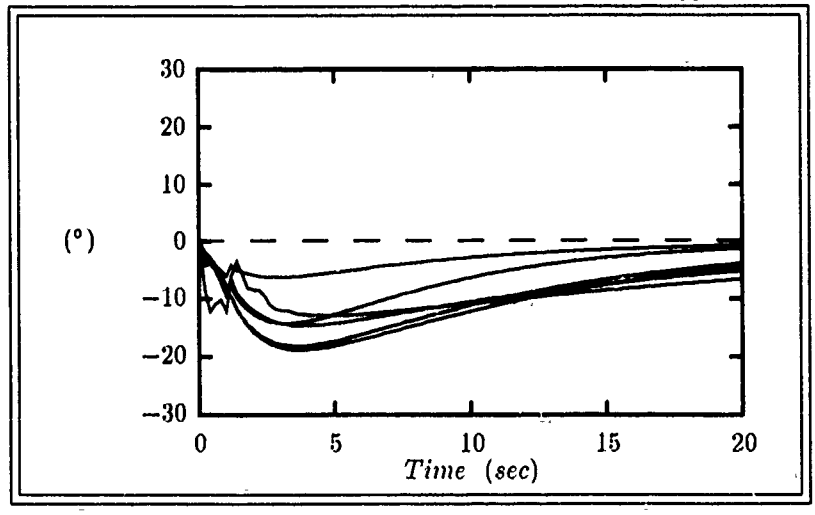

Figure G.107. δ_R Responses For Plants 1–6 to a 1 *sec* Duration 45°/*sec* Yaw-Rate (r) Input to Design #2 (amplitude limited at ±25°)

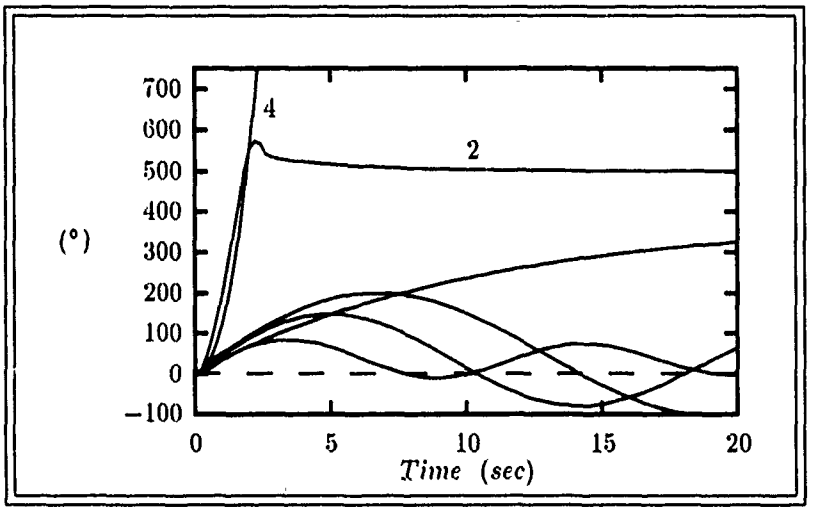

Figure G.108. θ Responses For Plants 1–6 to a 1 *sec* Duration 500°/*sec* Pitch-Rate (q) Input to Design #1

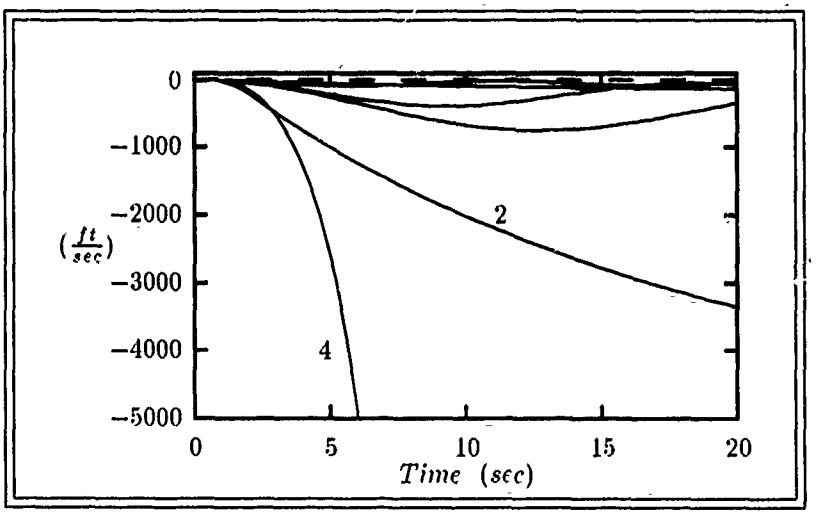

Figure G.109. u Responses For Plants 1–6 to a 1 *sec* Duration 500°/*sec* Pitch-Rate (q) Input to Design #1

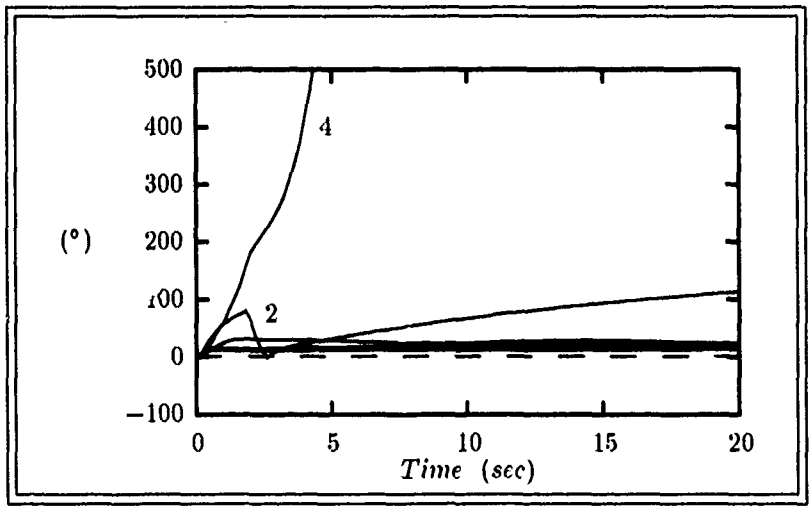

Figure G.110. α Responses For Plants 1–6 to a 1 *sec* Duration 500°/*sec* Pitch-Rate (q) Input to Design #1

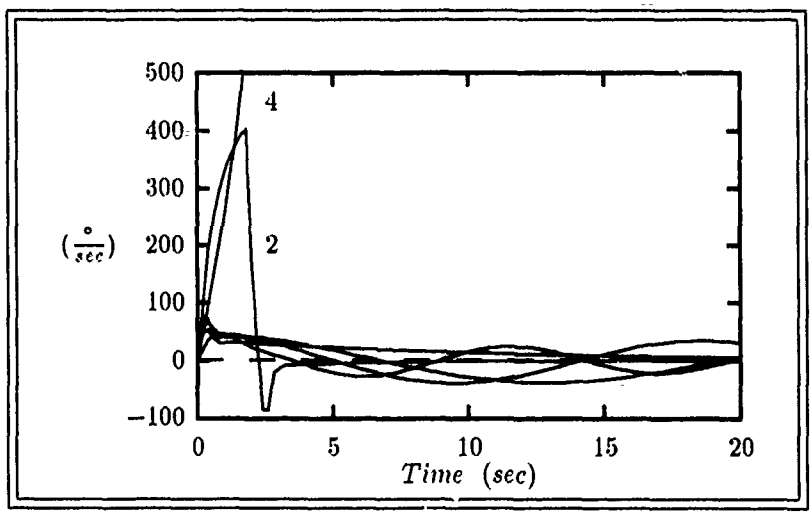

Figure G.111. q Responses For Plants 1–6 to a 1 *sec* Duration 500°/*sec* Pitch-Rate (q) Input to Design #1

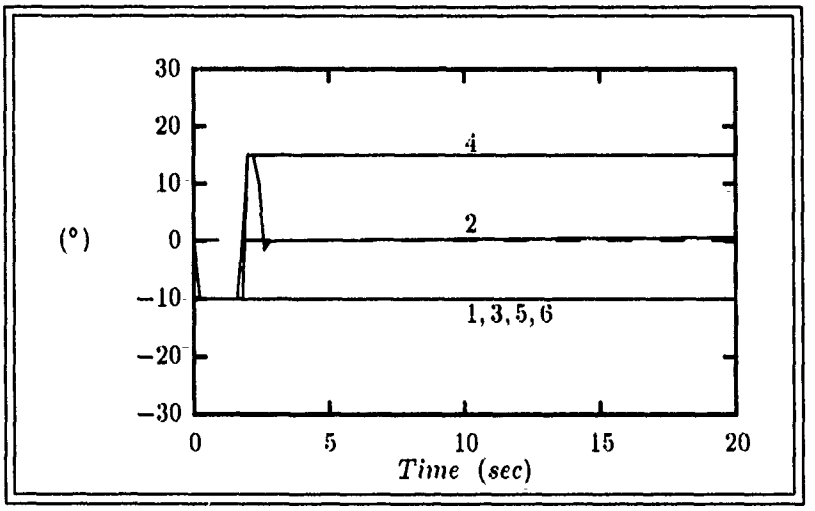

Figure G.112. δ_{a_L} Responses For Plants 1–6 to a 1 *sec* Duration 500°/*sec* Pitch-Rate (q) Input to Design #1 (amplitude limited at +15° and −10°)

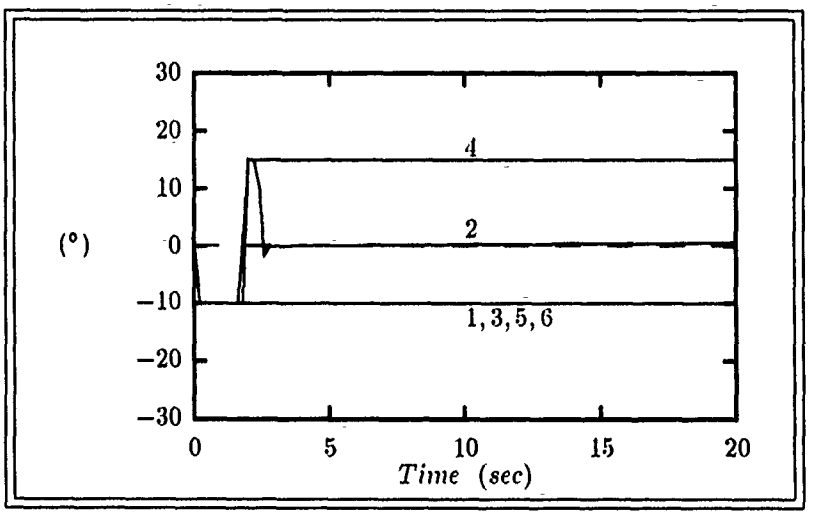

Figure G.113. δ_{a_R} Responses For Plants 1–6 to a 1 *sec* Duration 500°/*sec* Pitch-Rate (q) Input to Design #1 (amplitude limited at +15° and −10°)

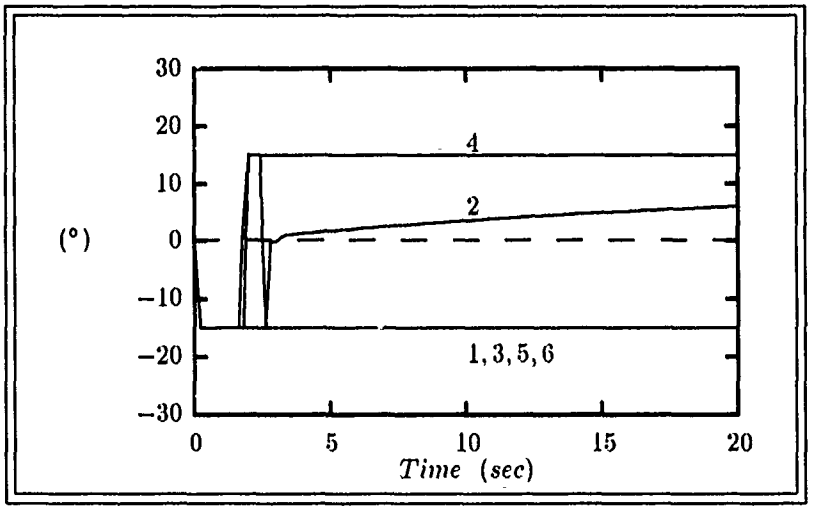

Figure G.114. δ_{e_L} Responses For Plants 1–6 to a 1 *sec* Duration 500°/*sec* Pitch-Rate (q) Input to Design #1 (amplitude limited at ±15°)

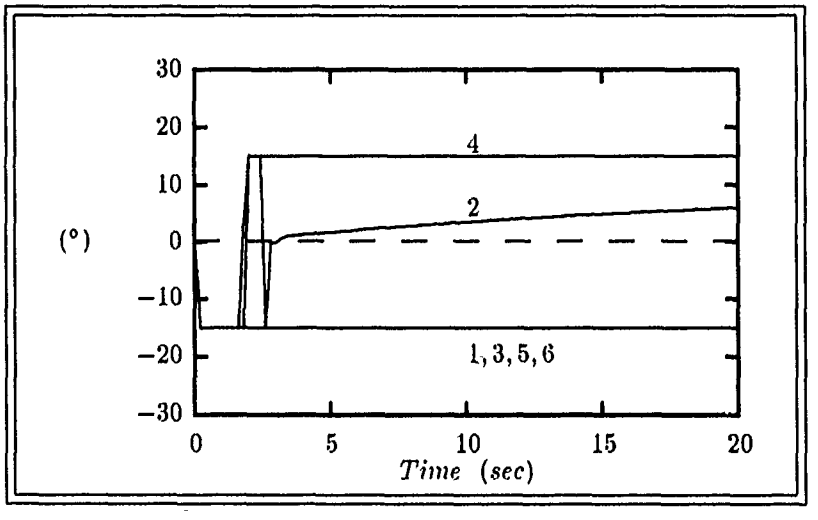

Figure G.115. δ_{e_R} Responses For Plants 1–6 to a 1 *sec* Duration 500°/*sec* Pitch-Rate (q) Input to Design #1 (amplitude limited at ±15°)

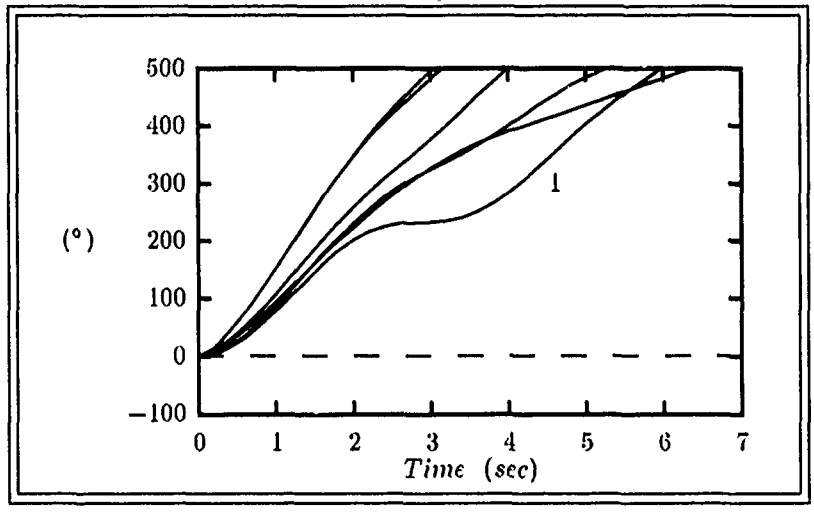

Figure G.116. ϕ Responses For Plants 1–6 to a 1 *sec* Duration 500°/*sec* Roll-Rate (p) Input to Design #1

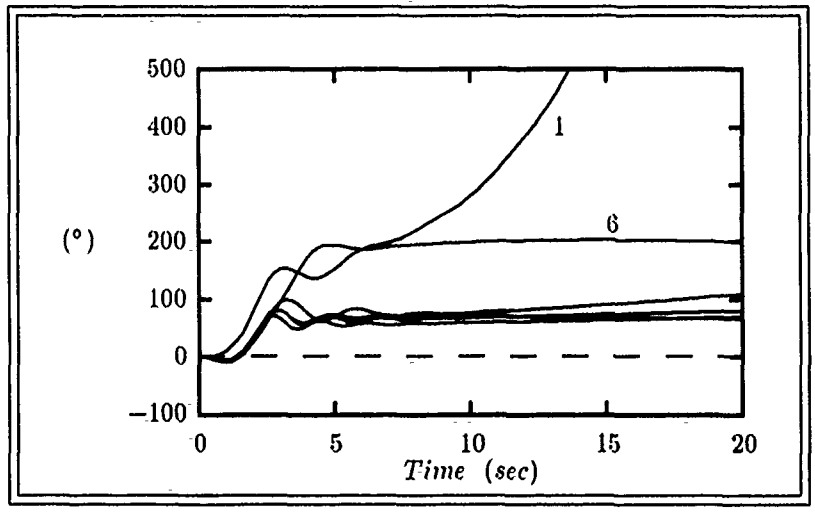

Figure G.117. β Responses For Plants 1–6 to a 1 *sec* Duration 500°/*sec* Roll-Rate (p) Input to Design #1

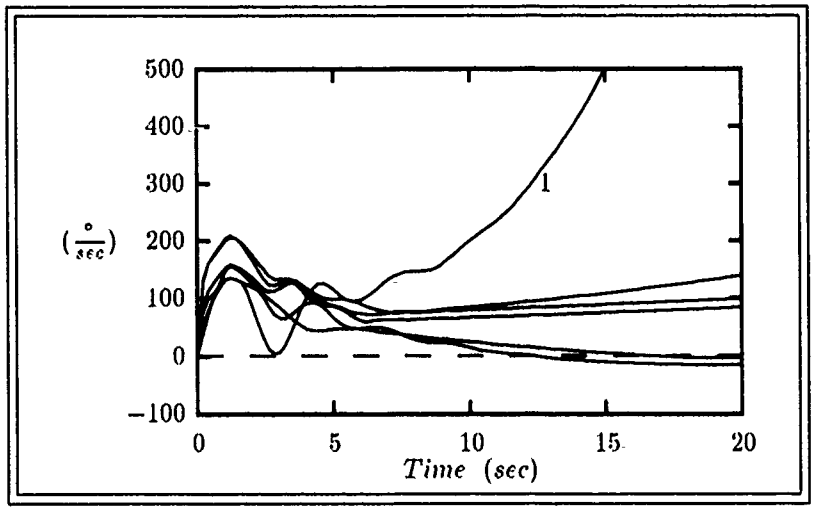

Figure G.118. p Responses For Plants 1–6 to a 1 *sec* Duration 500°/*sec* Roll-Rate (p) Input to Design #1

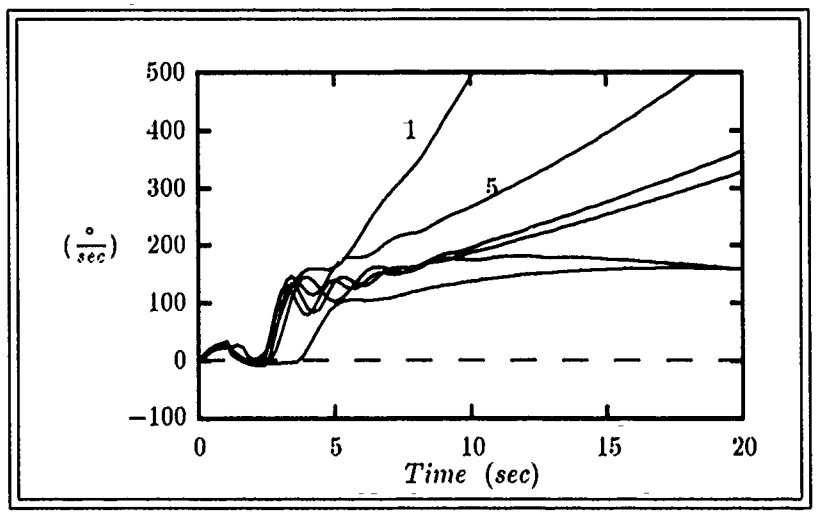

Figure G.119. r Responses For Plants 1–6 to a 1 *sec* Duration 500°/*sec* Roll-Rate (p) Input to Design #1

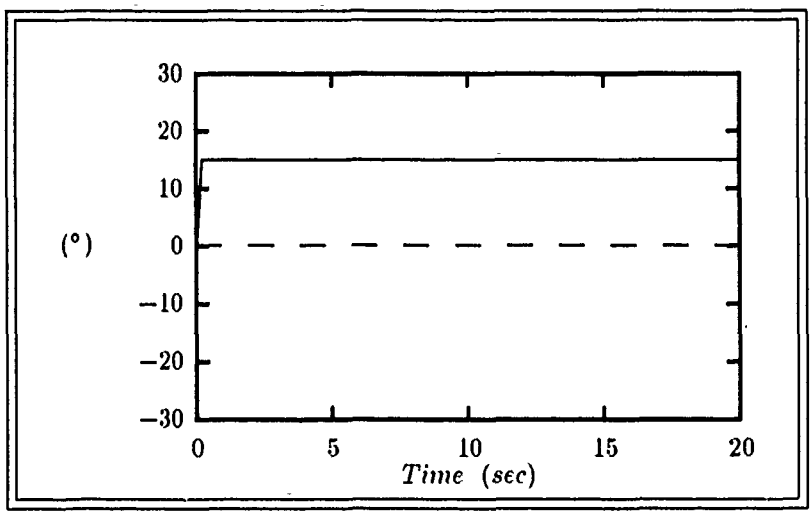

Figure G.120. δ_{a_L} Responses For Plants 1–6 to a 1 *sec* Duration 500°/*sec* Roll-Rate (p) Input to Design #1 (amplitude limited at +15° and −10°)

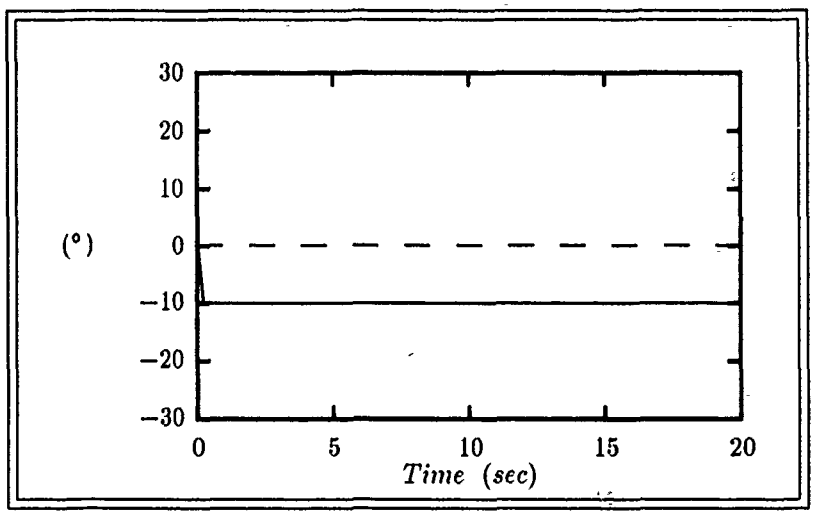

Figure G.121. δ_{a_R} Responses For Plants 1–6 to a 1 *sec* Duration 500°/*sec* Roll-Rate (p) Input to Design #1 (amplitude limited at +15° and −10°)

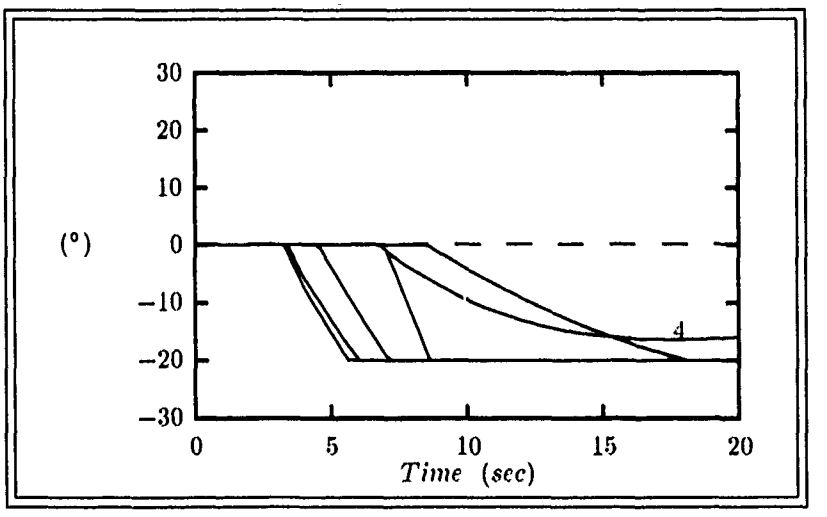

Figure G.122. δ_{f_L} Responses For Plants 1–6 to a 1 *sec* Duration 500°/*sec* Roll-Rate (p) Input to Design #1 (amplitude limited at 0° and −20°)

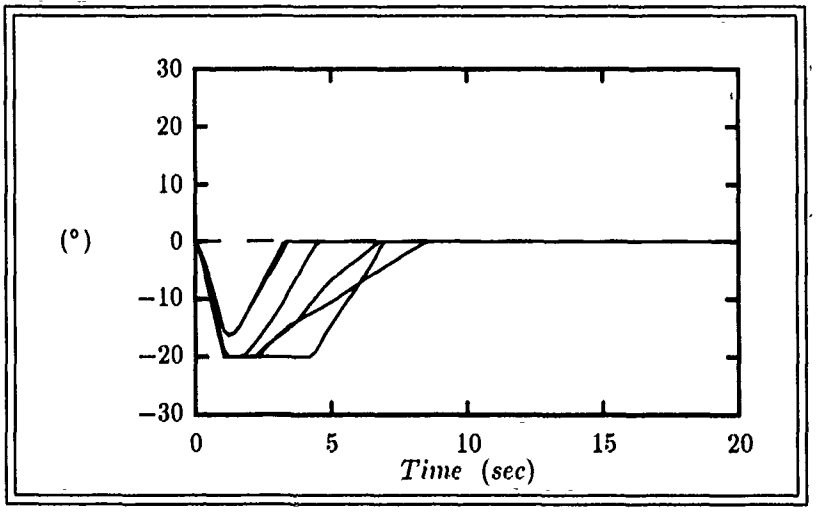

Figure G.123. δ_{f_R} Responses For Plants 1–6 to a 1 *sec* Duration 500°/*sec* Roll-Rate (p) Input to Design #1 (amplitude limited at 0° and −20°)

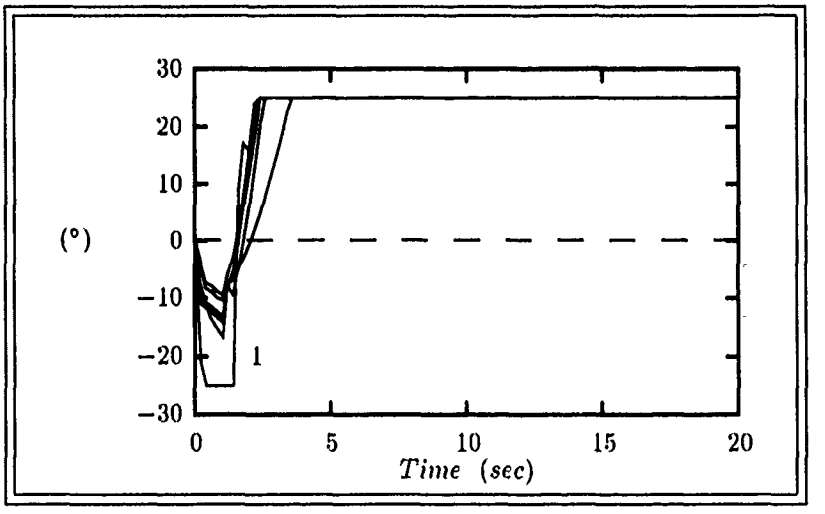

Figure G.124. δ_R Responses For Plants 1–6 to a 1 *sec* Duration 500°/*sec* Roll-Rate (p) Input to Design #1 (amplitude limited at ±25°)

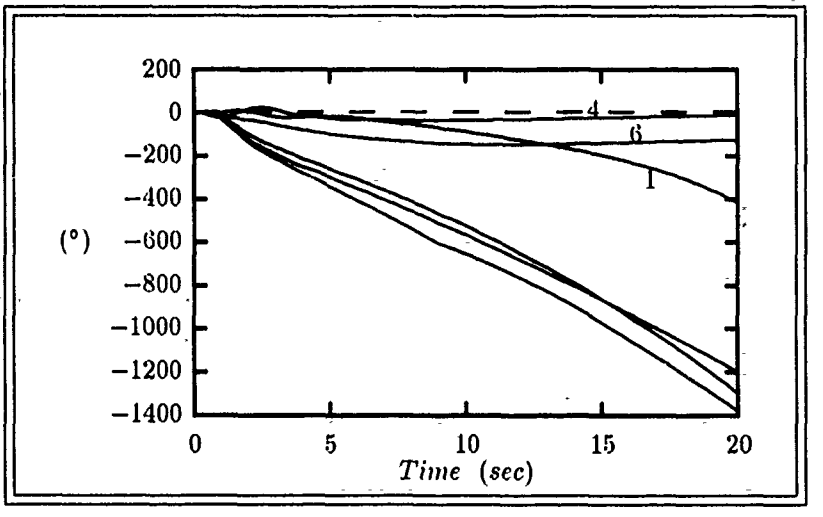

Figure G.125. ϕ Responses For Plants 1–6 to a 1 *sec* Duration 500°/*sec* Yaw-Rate (r) Input to Design #1

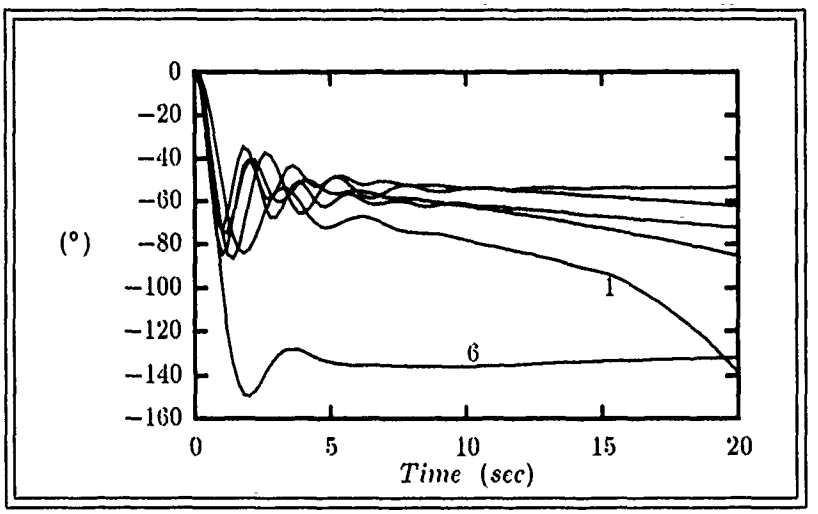

Figure G.126. β Responses For Plants 1–6 to a 1 *sec* Duration 500°/*sec* Yaw-Rate (r) Input to Design #1

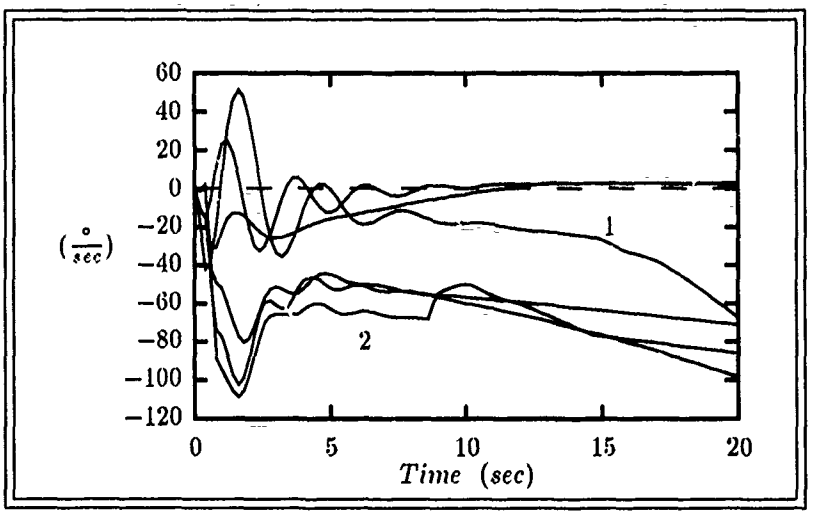

Figure G.127. p Responses For Plants 1–6 to a 1 *sec* Duration 500°/*sec* Yaw-Rate (r) Input to Design #1

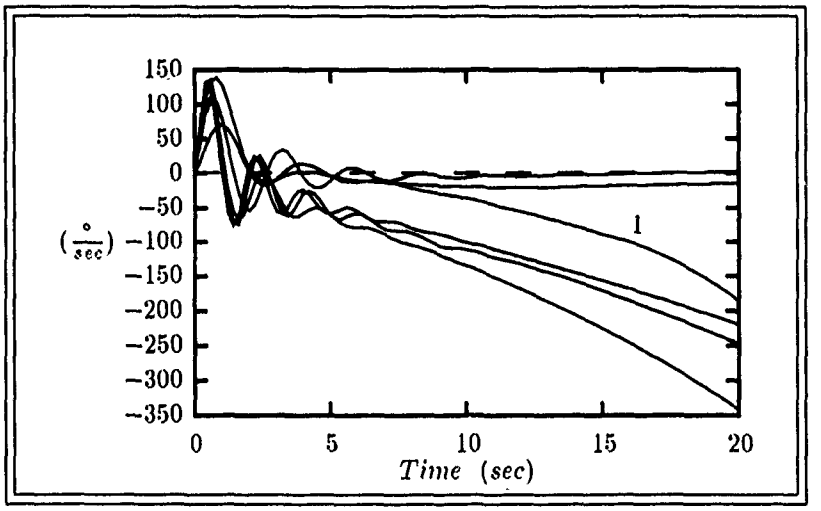

Figure G.128. r Responses For Plants 1–6 to a 1 *sec* Duration 500°/*sec* Yaw-Rate (r) Input to Design #1

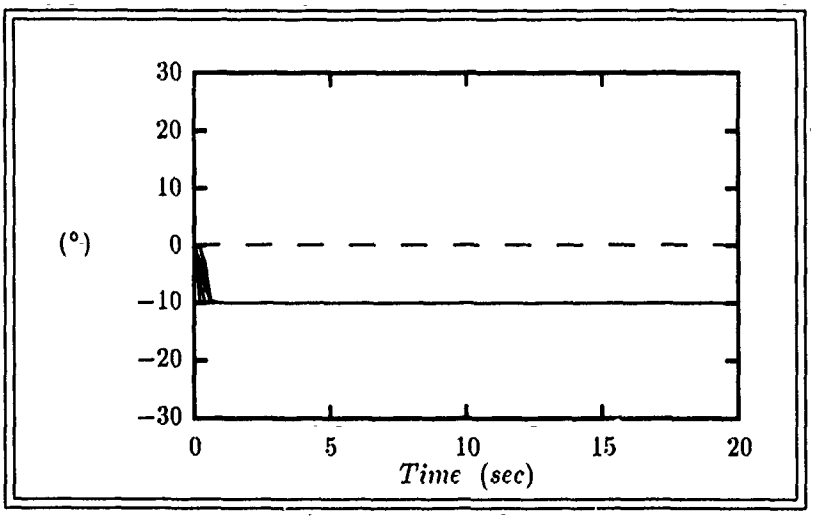

Figure G.129. δ_{a_L} Responses For Plants 1–6 to a 1 *sec* Duration 500°/*sec* Yaw-Rate (r) Input to Design #1 (amplitude limited at +15° and −10°)

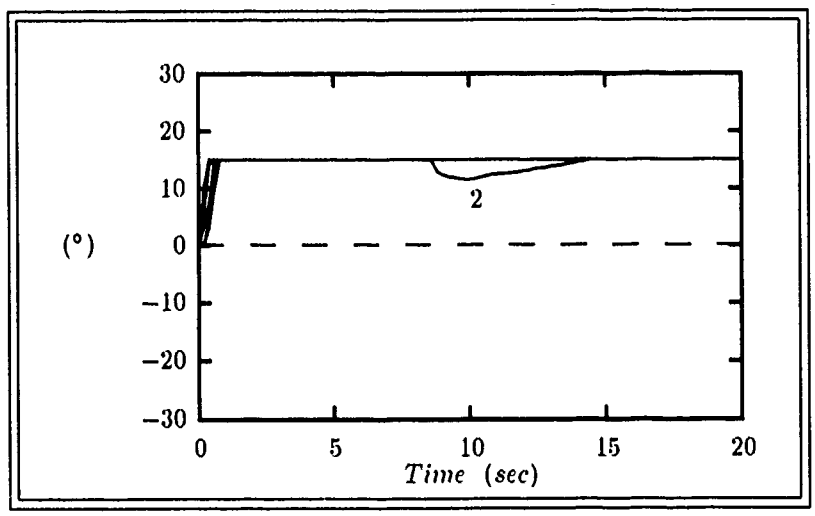

Figure G.130. δ_{a_R} Responses For Plants 1–6 to a 1 *sec* Duration 500°/*sec* Yaw-Rate (r) Input to Design #1 (amplitude limited at +15° and −10°)

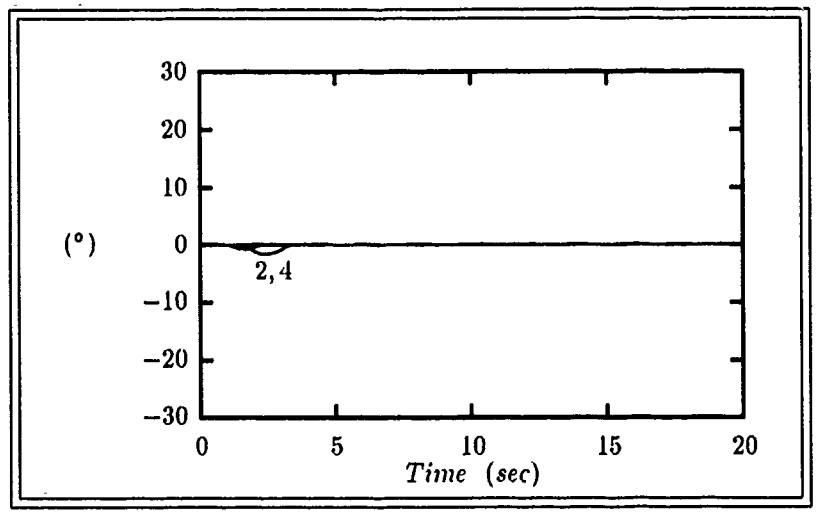

Figure G.131. δ_{f_L} Responses For Plants 1–6 to a 1 *sec* Duration 500°/*sec* Yaw-Rate (r) Input to Design #1 (amplitude limited at 0° and −20°)

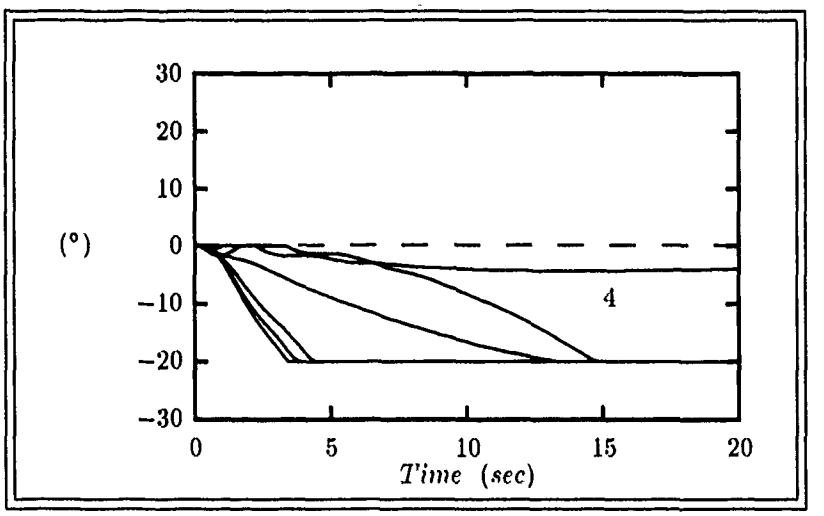

Figure G.132. δ_{J_R} Responses For Plants 1–6 to a 1 *sec* Duration 500°/*sec* Yaw-Rate (r) Input to Design #1 (amplitude limited at 0° and −20°)

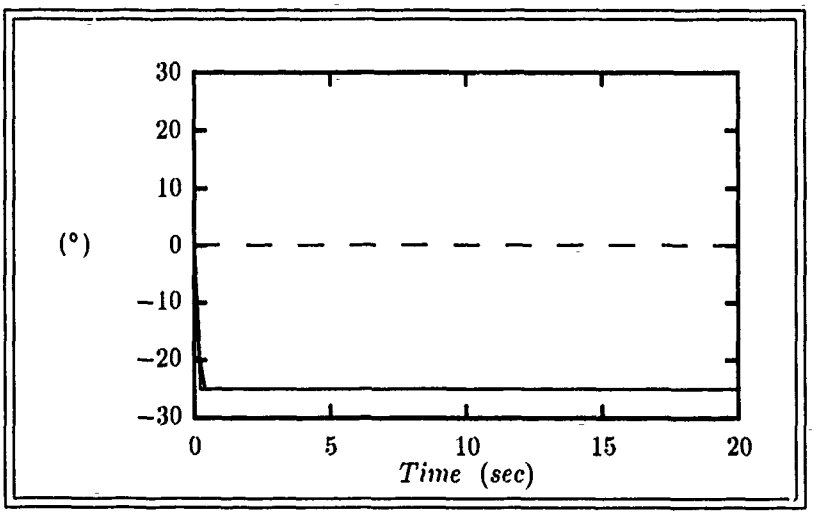

Figure G.133. δ_R Responses For Plants 1–6 to a 1 *sec* Duration 500°/*sec* Yaw-Rate (r) Input to Design #1 (amplitude limited at ±25°)

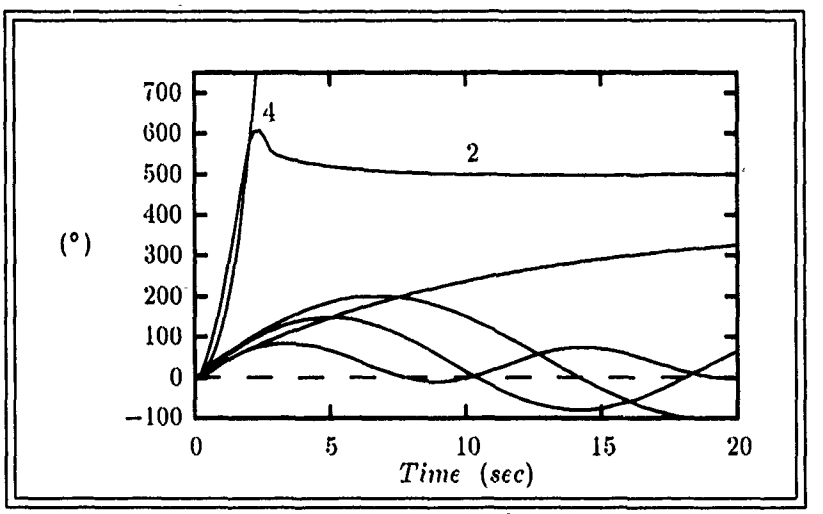

Figure G.134. θ Responses For Plants 1–6 to a 1 *sec* Duration 500°/*sec* Pitch-Rate (q) Input to Design #2

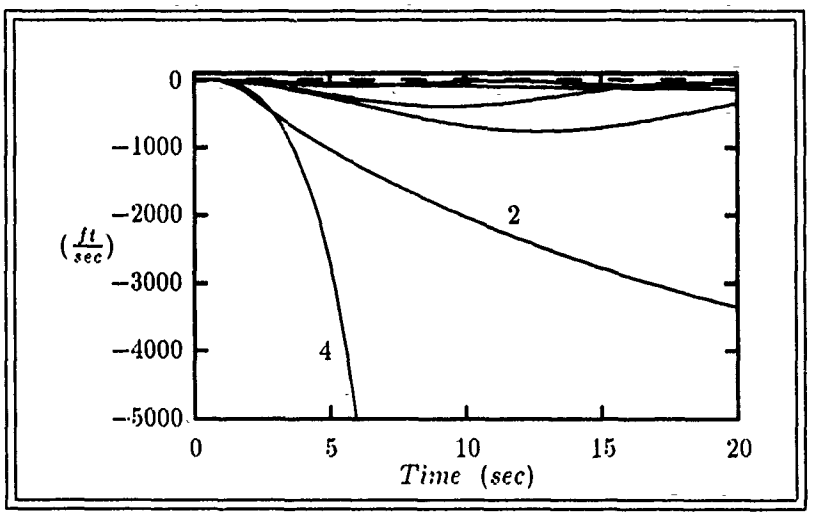

Figure G.135. u Responses For Plants 1–6 to a 1 *sec* Duration 500°/*sec* Pitch-Rate (q) Input to Design #2

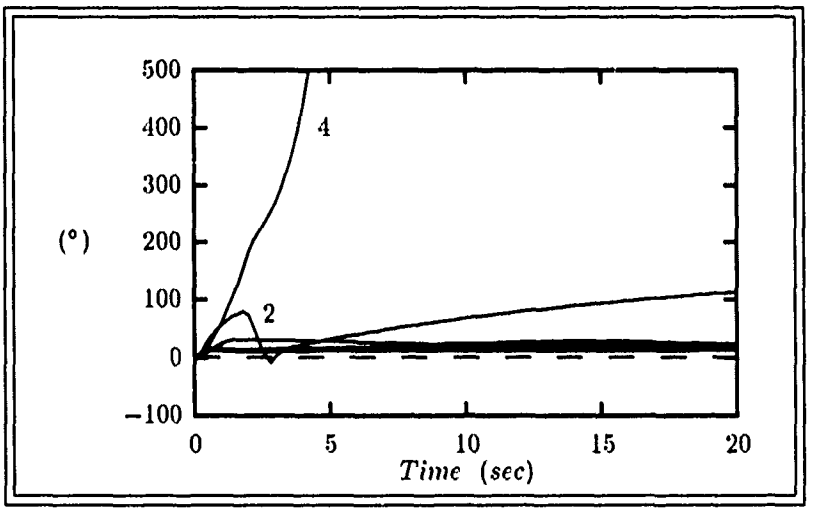

Figure G.136. α Responses For Plants 1-6 to a 1 *sec* Duration 500°/*sec* Pitch-Rate (q) Input to Design #2

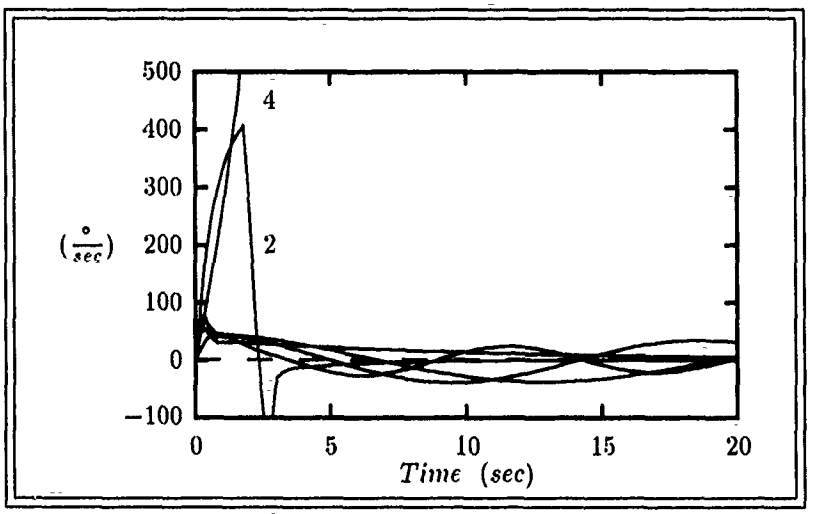

Figure G.137. q Responses For Plants 1-6 to a 1 *sec* Duration 500°/*sec* Pitch-Rate (q) Input to Design #2

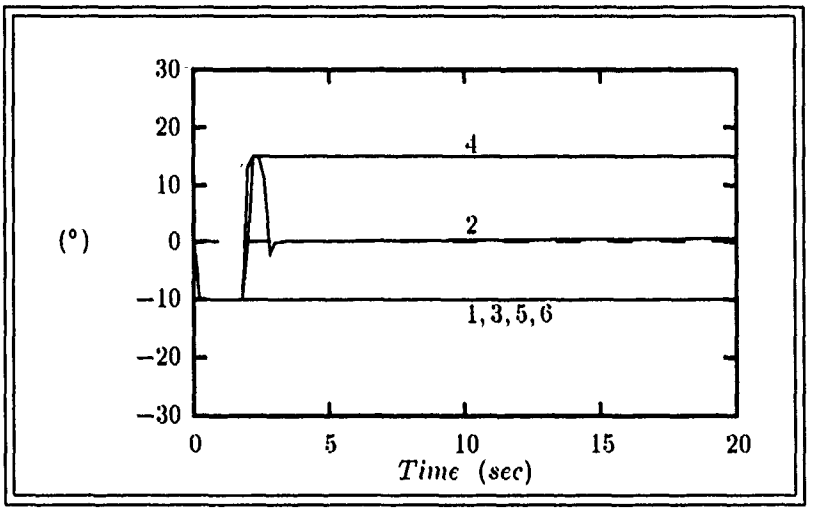

Figure G.138. δ_{a_L} Responses For Plants 1–6 to a 1 *sec* Duration 500°/*sec* Pitch-Rate (q) Input to Design #2 (amplitude limited at +15° and −10°)

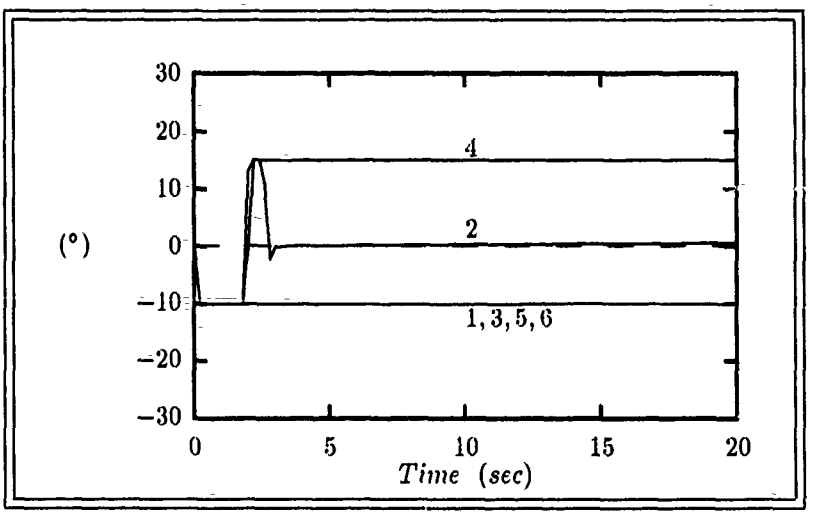

Figure G.139. δ_{a_R} Responses For Plants 1–6 to a 1 *sec* Duration 500°/*sec* Pitch-Rate (q) Input to Design #2 (amplitude limited at +15° and −10°)

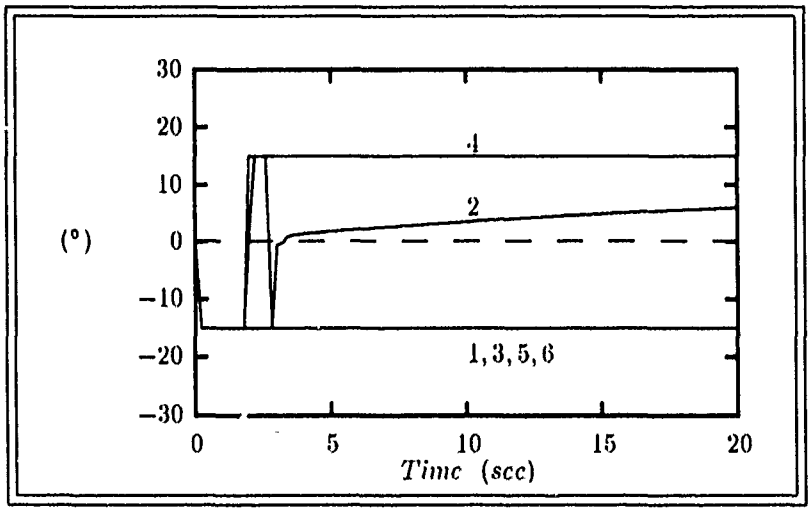

Figure G.140. δ_{e_L} Responses For Plants 1-6 to a 1 *sec* Duration 500°/*sec* Pitch-Rate (q) Input to Design #2 (amplitude limited at ±15°)

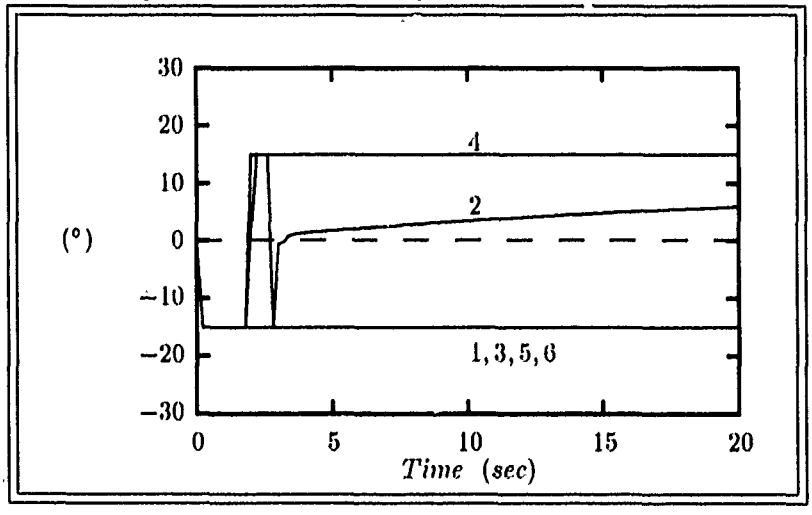

Figure G.141. δ_{e_R} Responses For Plants 1-6 to a 1 *sec* Duration 500°/*sec* Pitch-Rate (q) Input to Design #2 (amplitude limited at ±15°)

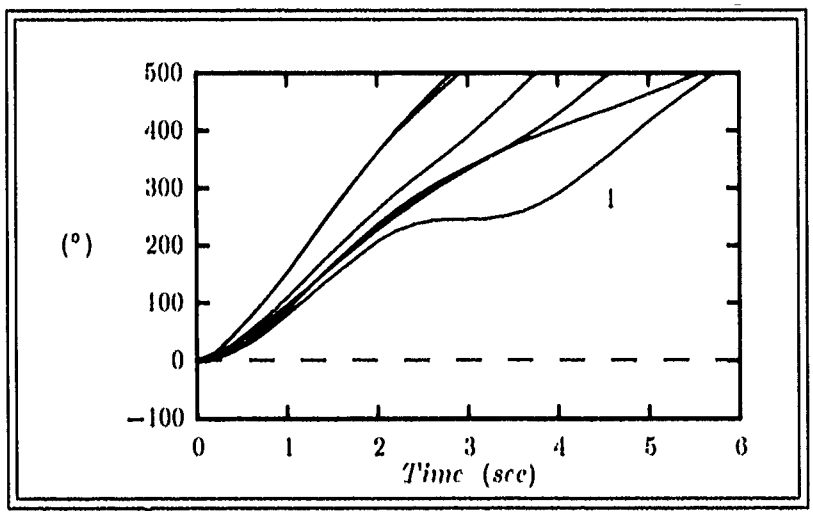

Figure G.142. ϕ Responses For Plants 1-6 to a 1 *sec* Duration 500°/*sec* Roll-Rate (p) Input to Design #2

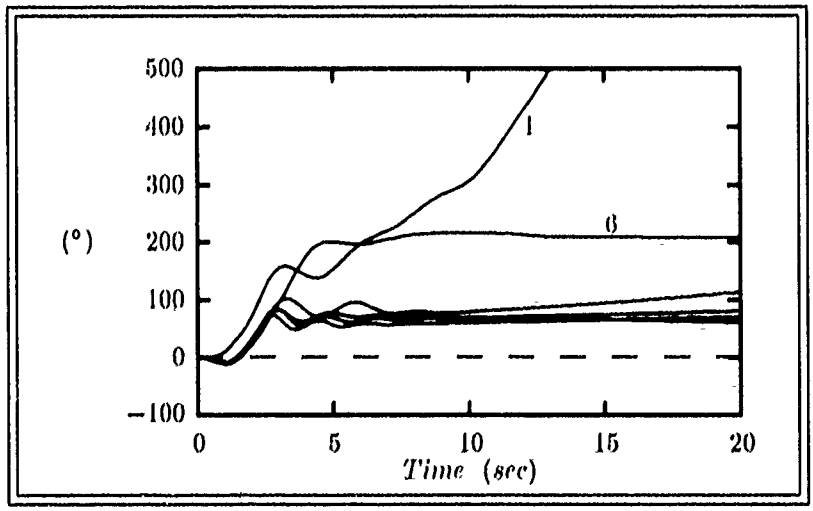

Figure G.143. β Responses For Plants 1-6 to a 1 *sec* Duration 500°/*sec* Roll-Rate (p) Input to Design #2

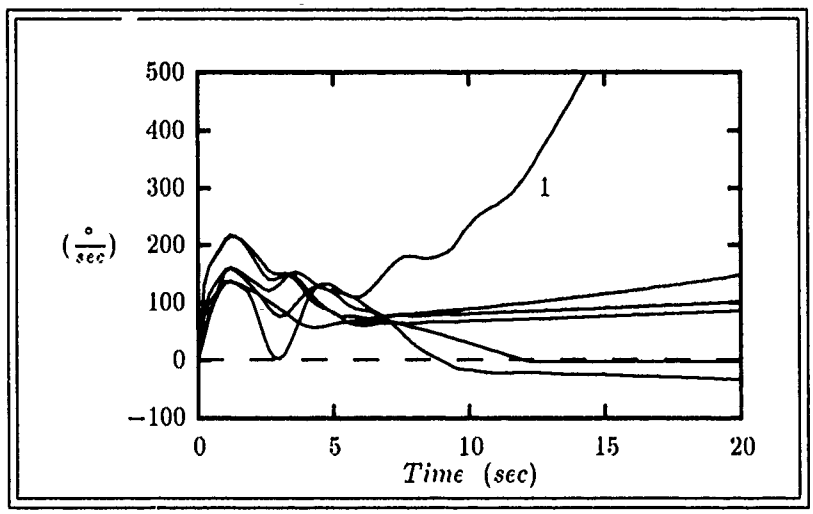

Figure G.144. p Responses For Plants 1–6 to a 1 *sec* Duration 500°/*sec* Roll-Rate (p) Input to Design #2

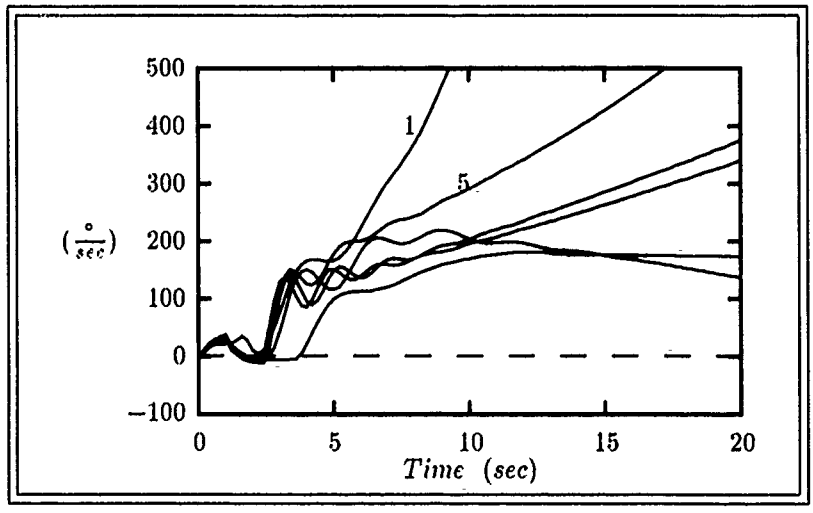

Figure G.145. r Responses For Plants 1–6 to a 1 *sec* Duration 500°/*sec* Roll-Rate (p) Input to Design #2

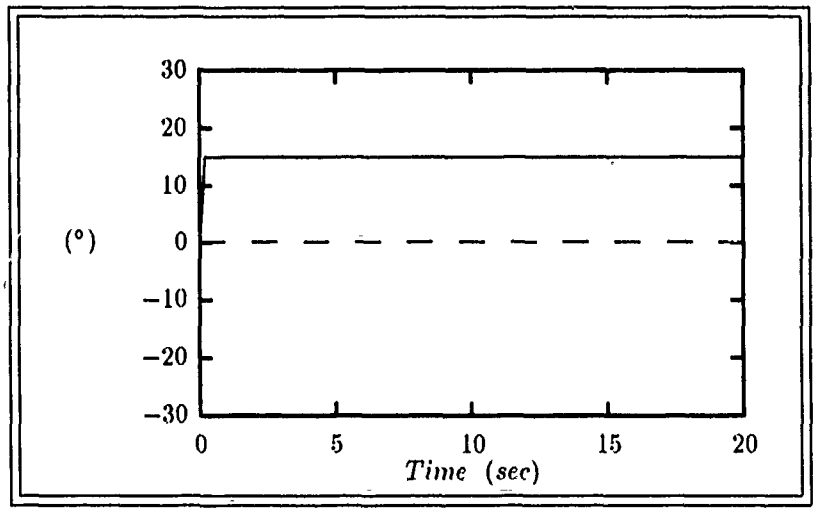

Figure G.146. δ_{a_L} Responses For Plants 1–6 to a 1 *sec* Duration 500°/*sec* Roll-Rate (p) Input to Design #2 (amplitude limited at +15° and −10°)

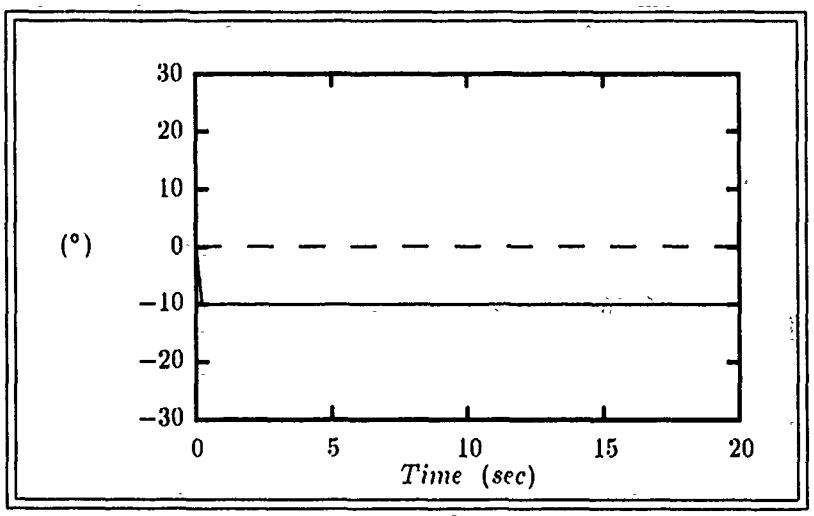

Figure G.147. δ_{a_R} Responses For Plants 1–6 to a 1 *sec* Duration 500°/*sec* Roll-Rate (p) Input to Design #2 (amplitude limited at +15° and −10°)

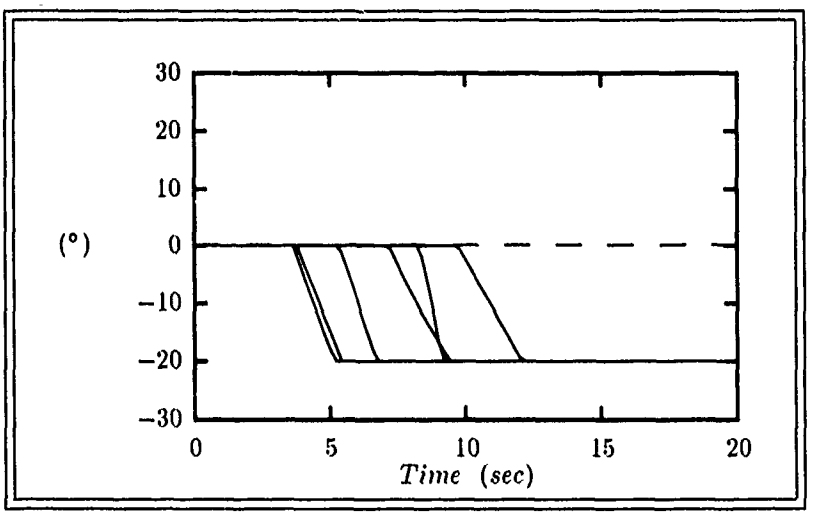

Figure G.148. δ_{f_L} Responses For Plants 1–6 to a 1 *sec* Duration 500°/*sec* Roll-Rate (p) Input to Design #2 (amplitude limited at 0° and −20°)

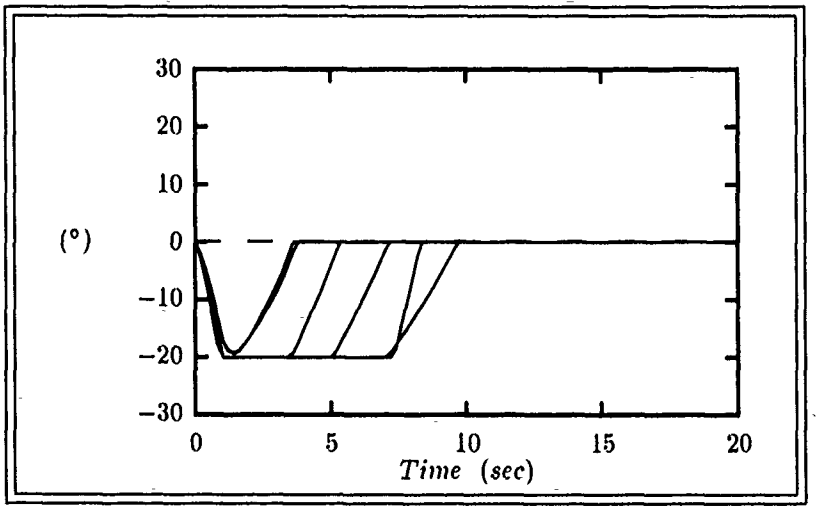

Figure G.149. δ_{f_R} Responses For Plants 1–6 to a 1 *sec* Duration 500°/*sec* Roll-Rate (p) Input to Design #2 (amplitude limited at 0° and −20°)

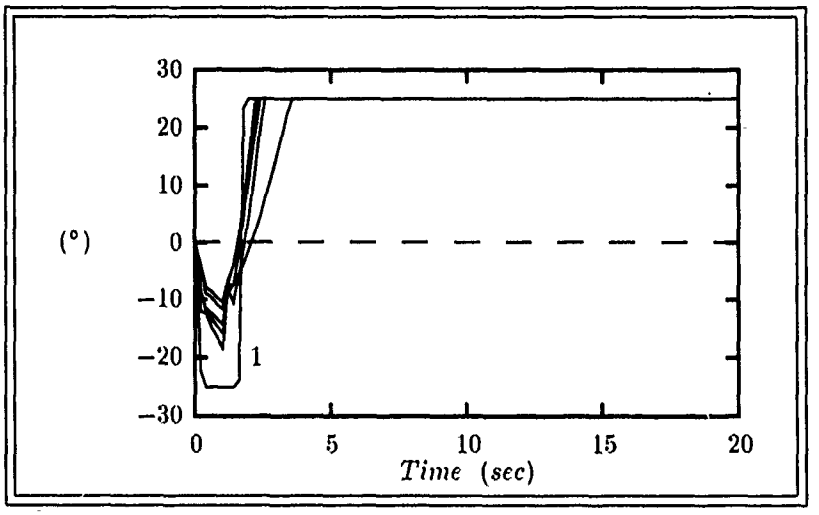

Figure G.150. δ_R Responses For Plants 1–6 to a 1 *sec* Duration 500°/*sec* Roll-Rate (p) Input to Design #2 (amplitude limited at ±25°)

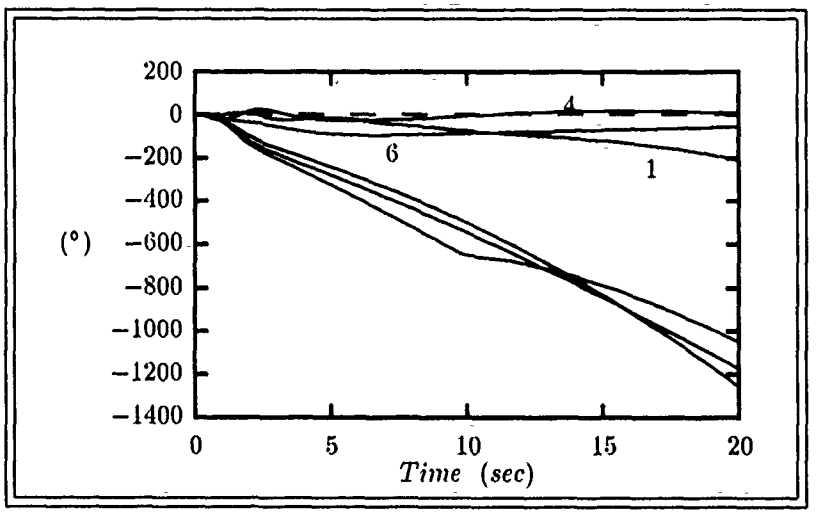

Figure G.151. ϕ Responses For Plants 1–6 to a 1 *sec* Duration 500°/*sec* Yaw-Rate (r) Input to Design #2

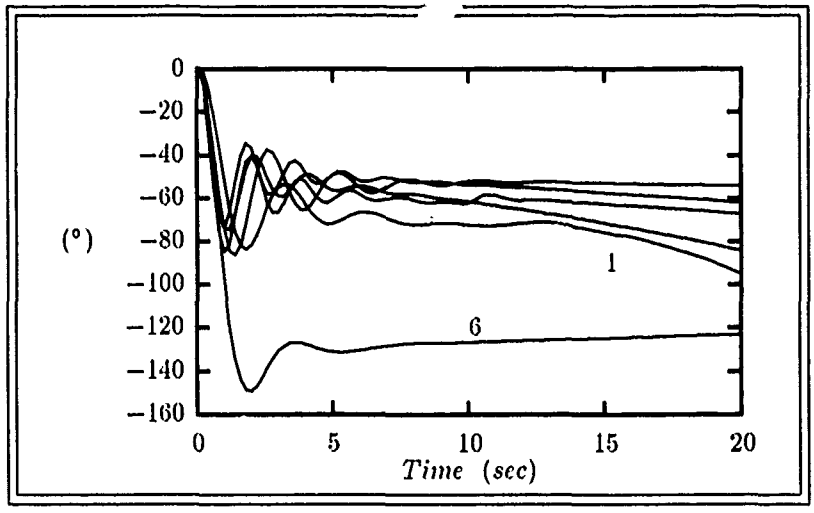

Figure G.152. β Responses For Plants 1–6 to a 1 *sec* Duration 500°/*sec* Yaw-Rate (r) Input to Design #2

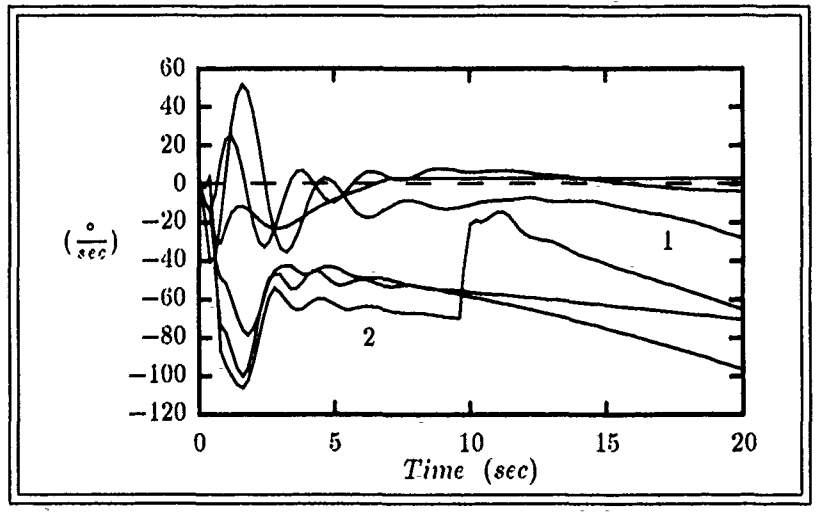

Figure G.153. p Responses For Plants 1–6 to a 1 *sec* Duration 500°/*sec* Yaw-Rate (r) Input to Design #2

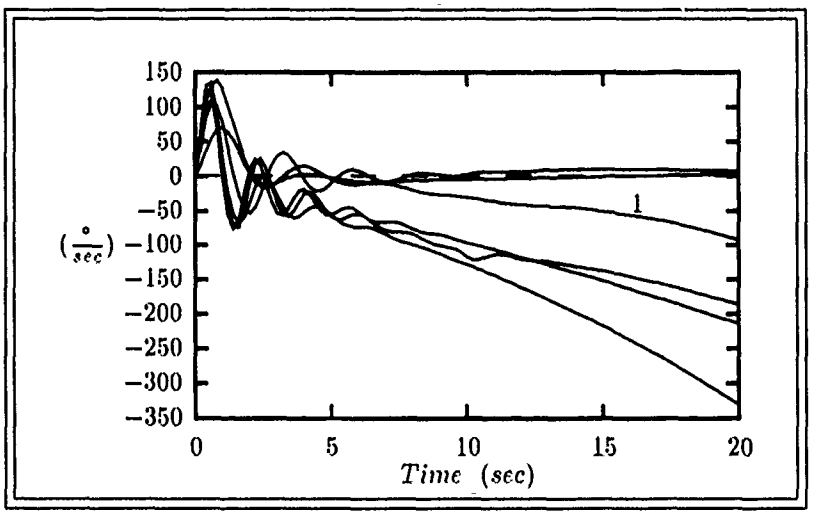

Figure G.154. r Responses For Plants 1–6 to a 1 *sec* Duration 500°/*sec* Yaw-Rate (r) Input to Design #2

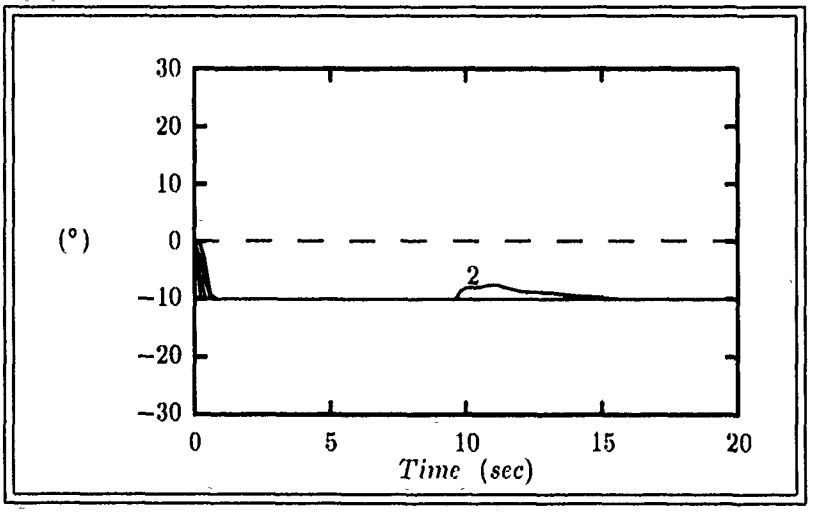

Figure G.155. δ_{a_L} Responses For Plants 1–6 to a 1 *sec* Duration 500°/*sec* Yaw-Rate (r) Input to Design #2 (amplitude limited at +15° and −10°)

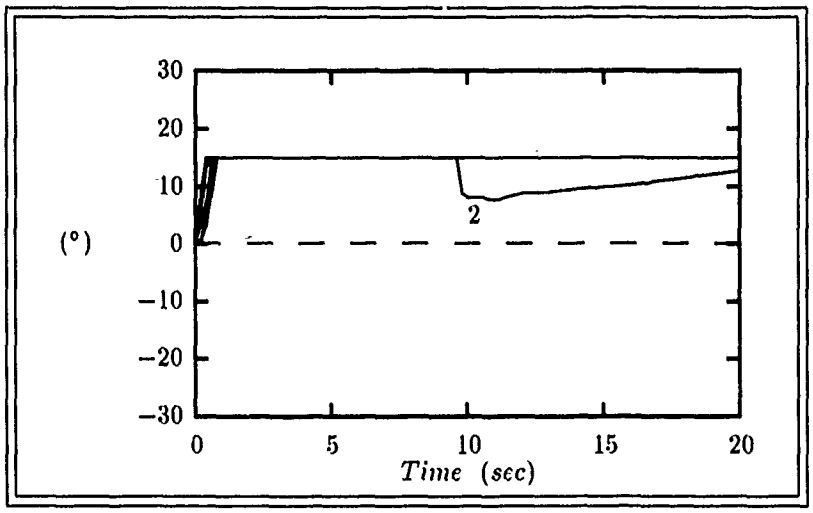

Figure G.156. δ_{a_R} Responses For Plants 1–6 to a 1 *sec* Duration 500°/*sec* Yaw-Rate (r) Input to Design #2 (amplitude limited at +15° and −10°)

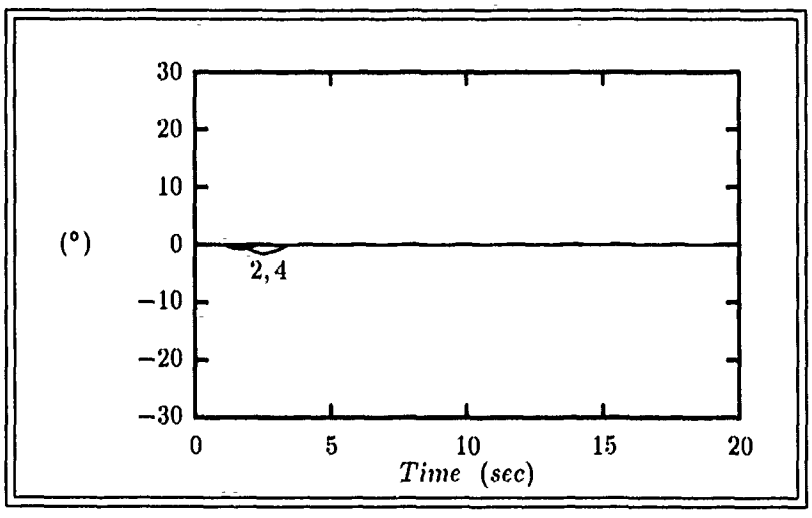

Figure G.157. δ_{f_L} Responses For Plants 1–6 to a 1 *sec* Duration 500°/*sec* Yaw-Rate (r) Input to Design #2 (amplitude limited at 0° and −20°)

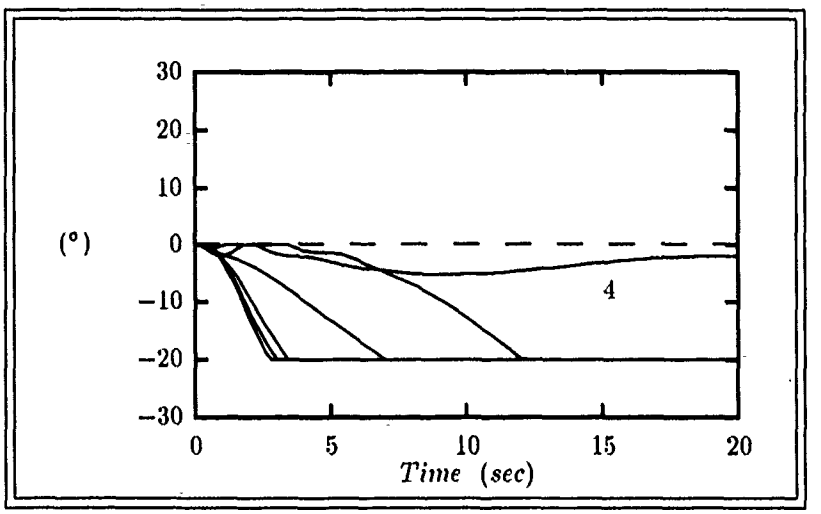

Figure G.158. δ_{f_R} Responses For Plants 1-6 to a 1 *sec* Duration 500°/*sec* Yaw-Rate (r) Input to Design #2 (amplitude limited at 0° and −20°)

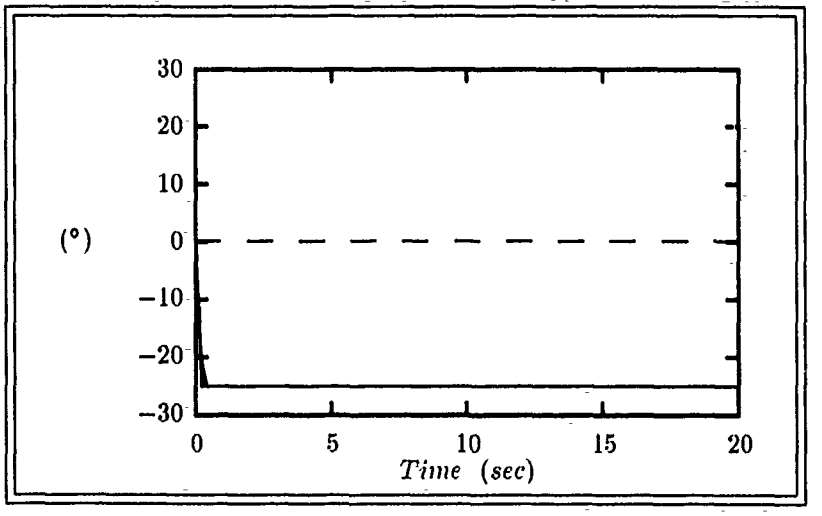

Figure G.159. δ_R Responses For Plants 1-6 to a 1 *sec* Duration 500°/*sec* Yaw-Rate (r) Input to Design #2 (amplitude limited at ±25°)

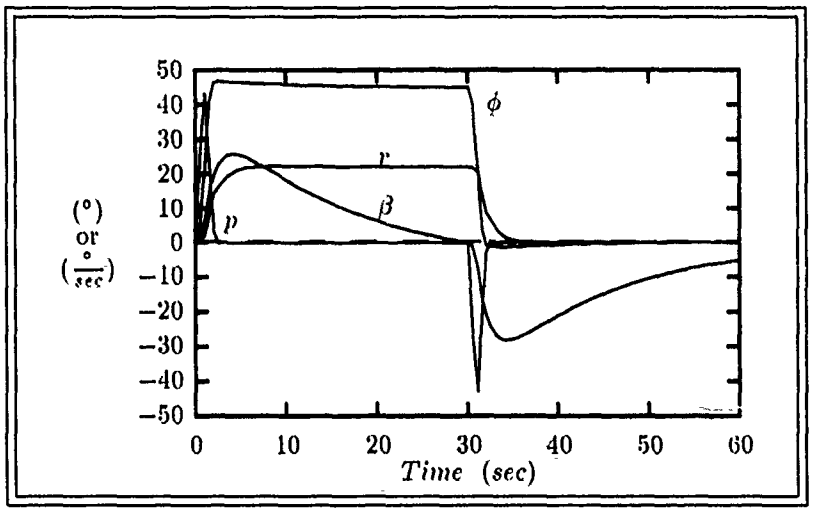

Figure G.160. Lambda Lateral State Responses For Plant #1 to a 45° Steep Bank Coordinated Turn Input

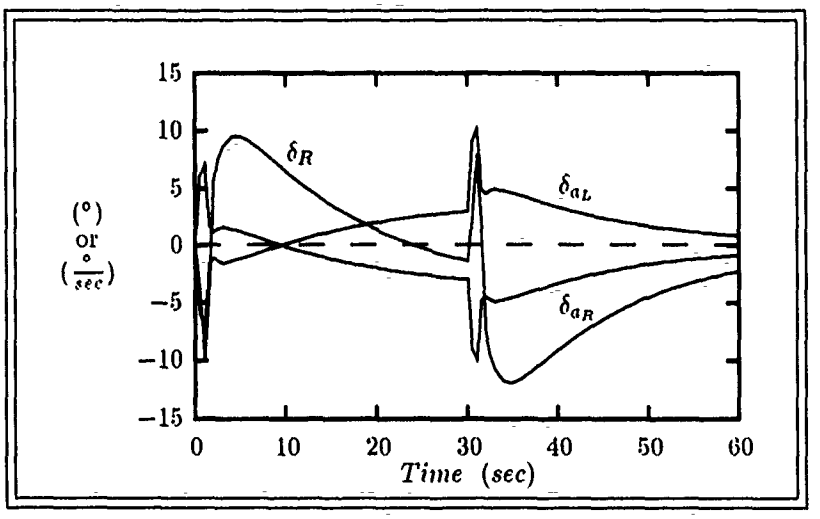

Figure G.161. Lambda Aileron And Rudder Responses For Plant #1 to a 45° Steep Bank Coordinated Turn Input

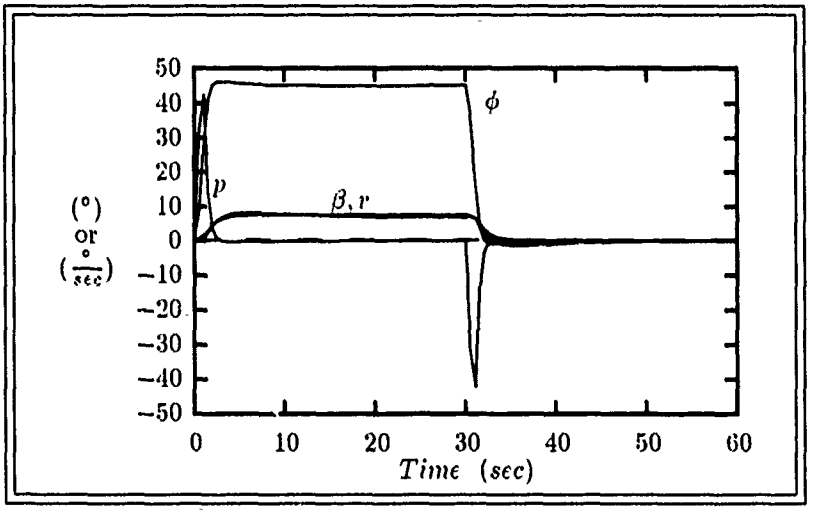

Figure G.162. Lambda Lateral State Responses For Plant #2 to a 45° Steep Bank Coordinated Turn Input

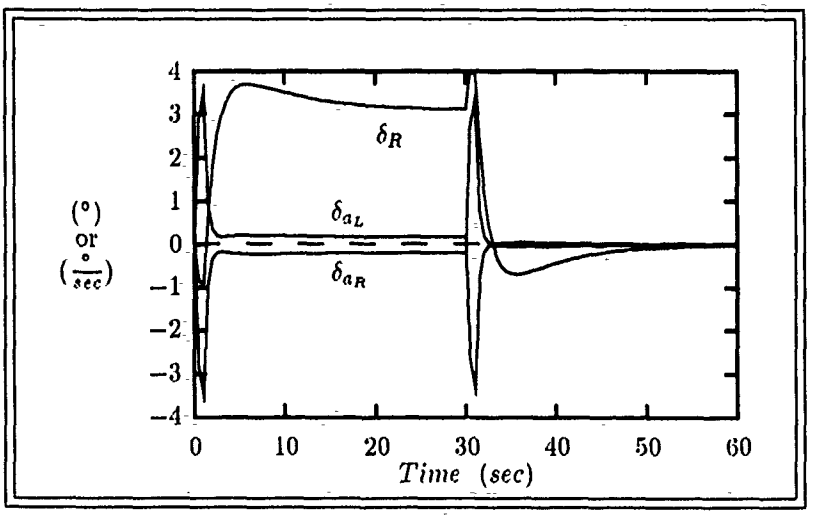

Figure G.163. Lambda Aileron And Rudder Responses For Plant #2 to a 45° Steep Bank Coordinated Turn Input

Bibliography

1. Adams, James M. *QFT Design Of A Robust Longitudinal Digital Controller For The AFTI/F-16 Using Matrix$_x$*. MS thesis, Air Force Institute of Technology, Wright-Patterson AFB, OH, March 1988.
2. Arnold, Phillip B. *Flight Control System Reconfiguration Design Using Quantitative Feedback Theory*. MS thesis, Air Force Institute of Technology, Wright-Patterson AFB, OH, December 1984.
3. Blakelock, John H. *Automatic Control of Aircraft and Missiles*. Wiley & Sons, 1965.
4. Clough, Bruce T. *Reconfigurable Flight Control System For A STOL Aircraft Using Quantitative Feedback Theory*. MS thesis, Air Force Institute of Technology, Wright-Patterson AFB, OH, December 1985.
5. Coucoules, John S. *Study of the Effects of Discretizing Quantitative Feedback Theory Analog Control System Designs*. MS thesis, Air Force Institute of Technology, Wright-Patterson AFB, OH, December 1985.
6. D'Azzo, John J. and Constantine H. Houpis. *Linear Control System Analysis & Design — Conventional and Modern* (Third Edition). McGraw-Hill, 1988.
7. Etkin, Bernard. *Dynamics of Atmospheric Flight*. Wiley & Sons, 1972.
8. Hamilton, Steven W. *QFT Digital Controller For An Unmanned Research Vehicle With An Improved Method For Choosing The Control Weightings*. MS thesis, Air Force Institute of Technology, Wright-Patterson AFB, OH, December 1987.
9. Hofmann, L. G. and R. E. Michael. "Technique for Analysis of Digital Control Systems." General Electric Company, Avionic and Electronic Systems Division. Binghamton, New York.
10. Horowitz, Isaac. *Synthesis of Feedback Systems*. Academic Press, 1963.
11. Horowitz, Isaac. "Optimum Loop Transfer Function in Single-Loop Minimum Phase Feedback Systems." *International Journal of Control, Vol. 22*:pp 97–113 (1973).
12. Horowitz, Isaac. "Quantitative Synthesis Of Uncertain Multiple Input-Output Feedback System," *International Journal of Control, Vol. 30*(No. 1):pp 81–106 (1979).
13. Horowitz, Isaac. "Improved Design Technique For Uncertain Multiple-Input-Multiple-Output Feedback Systems," *International Journal of Control, Vol. 36*(No. 6):pp 977–988 (1982).
14. Horowitz, Isaac. and Clayton Loecher. "Design of a 3x3 Multivariable Feedback System With Large Plant Uncertainty," *International Journal of Control, Vol. 33*(No. 4):pp 677–699 (1981).
15. Horowitz, Isaac and M. Sidi. "Optimum Synthesis Of Nonminimum-Phase Feedback Systems with Parameter Uncertainty," *International Journal of Control, Vol. 27*:pp 361–386 (1978).
16. Horowitz, Isaac and Yin-Kuei Liao. "Limitations of Non-minimum-phase feedback systems," *International Journal of Control, Vol. 40*(No. 5):pp 1003–1013 (1984).
17. Horowitz, Isaac M.. "Personal Conversation and Correspondance." Professor of Electrical Engineering, University of C...fornia Davis, May 1990 through December 1990.
18. Houpis, Constantine H., "Personal Conversation, Correspondance and Class Notes." Professor of Electrical Engineering, Air Force Institute of Technology, Wright-Patterson AFB, OH, May 1989 through December 1990.

19. Houpis, Constantine H. *Quantitative Feedback Theory (QFT)—Technique for Designing Multivariable Control Systems*. Technical Report AFWAL-TR-86-3107, Wright-Patterson AFB, OH: Flight Dynamics Laboratory, January 1987.

20. Houpis Constantine H. and Gary B. Lamont. *Digital Control Systems—Theory, Hardware, Software*. McGraw-Hill, 1985.

21. Jong, M. T. *Methods of Discrete Signal and System Analysis*. McGraw-Hill, 1982.

22. Lancaster, P. *Theory of Matrices*. Academic Press, 1969.

23. Matrix$_x$ CAD/CAE Program, Integrated Systems Inc., Santa Clara, CA, 95054-1215.

24. Maybeck, Peter S. *Stochastic Models, Estimation, and Control Volume I*. Academic Press, 1979.

25. Migyanko, Barry S. *Design of Integrated Flight/Propulsion Control Laws of a STOL Aircraft During Approach and Landing Using Quantitative Feedback Theory*. MS thesis, Air Force Institute of Technology, Wright-Patterson AFB, OH, December 1986.

26. Military Specification—Flying Qualities of Piloted Aircraft. MIL-STD-1797A. 30 January 1990.

27. Military Specification—Control and Stabilization Systems: Automatic, Piloted Aircraft, General Specification For. MIL-C-18244A. 1 December 1962.

28. Neumann, Kurt N. *The Control Reconfigurable Combat Aircraft Designed Using Quantitative Feedback Theory*. MS thesis, Air Force Institute of Technology, Wright-Patterson AFB, OH, December 1988.

29. Ott, Paul T. *QFT Digital Design For Inherent Reconfiguration of the Flight Control System of An Unmanned Research Vehicle*. MS thesis, Air Force Institute of Technology, Wright-Patterson AFB, OH, June 1988.

30. Russell, Harvey H. *Design of Robust Controllers For a Multiple Input-Multiple Output Control System With Uncertain Parameters Application to the Lateral and Longitudinal Modes of the KC-135 Transport Aircraft*. MS thesis, Air Force Institute of Technology, Wright-Patterson AFB, OH, December 1984.

31. Schneider, Dean L. *QFT Digital Flight Control Design As Applied to the AFTI/F16*. MS thesis, Air Force Institute of Technology, Wright-Patterson AFB, OH, December 1986.

32. Tischler, Mark B. "Assessment of Digital Flight-Control Technology for Advanced Combat Rotorcraft," *Journal of the American Helicopter Society*, pages 66-76 (1989).

REPORT DOCUMENTATION PAGE

Form Approved
OMB No 0704-0188

1. AGENCY USE ONLY (Leave blank)	2. REPORT DATE	3. REPORT TYPE AND DATES COVERED
	December 1990	Master's Thesis

4. TITLE AND SUBTITLE

Automatic Flight Control Design For An Unmanned Research Vehicle Using Discrete Quantitative Feedback Theory

5. FUNDING NUMBERS

6. AUTHOR(S)

David G. Wheaton, Captain, USAF

7. PERFORMING ORGANIZATION NAME(S) AND ADDRESS(ES)

Air Force Institute of Technology, WPAFB OH 45433-6583

8. PERFORMING ORGANIZATION REPORT NUMBER

AFIT/GE/ENG/90D-66

9. SPONSORING/MONITORING AGENCY NAME(S) AND ADDRESS(ES)

10. SPONSORING/MONITORING AGENCY REPORT NUMBER

11. SUPPLEMENTARY NOTES

12a. DISTRIBUTION/AVAILABILITY STATEMENT

Approved for Public Release; Distribution Unlimited.

12b. DISTRIBUTION CODE

13. ABSTRACT *(Maximum 200 words)*

This thesis presents the application of non-minimum phase (NMP) w'-plane discrete MIMO Quantitative Feedback Theory (QFT) to the design of a three-axis rate-commanded automatic flight control system for an unmanned research vehicle (URV). The URV model is a seven input three output perturbation equation set. Six flight conditions provide the plant uncertainty expressed with plant templates $\mathcal{P} = \{\mathbf{P}(jv)\}$. A weighting matrix Δ is used to blend the seven inputs into three resulting in an *effective* plant $\mathbf{P}_e = \mathbf{P}\Delta$. A three-pole effector/sensor model is also used. A robust time-scaled recursive algorithm is used for transformation to the w'-plane. All URV plant elements are minimum phase, but the w'-plane plants are NMP. NMP elements limit the available loop bandwidth ($l_i(jv)$). Standard QFT design is used, but due to the loop bandwidth limitations, only stability bounds are derived. The loop transmissions ($l_i(jv)$) are then shaped to achieve the maximum levels subject to the stability bounds. The design is verified by hybrid (effector amplitude limiting) simulations. Hard limiting and nominal performance is shown.

14. SUBJECT TERMS

Quantitative Feedback Theory, Flight Control Systems, Remotely Piloted Vehicles, Aircraft, Research Aircraft, Aerospace Systems

15. NUMBER OF PAGES

274

16. PRICE CODE

17. SECURITY CLASSIFICATION OF REPORT	18. SECURITY CLASSIFICATION OF THIS PAGE	19. SECURITY CLASSIFICATION OF ABSTRACT	20. LIMITATION OF ABSTRACT
Unclassified	Unclassified	Unclassified	UL

GENERAL INSTRUCTIONS FOR COMPLETING SF 298

The Report Documentation Page (RDP) is used in announcing and cataloging reports. It is important that this information be consistent with the rest of the report, particularly the cover and title page. Instructions for filling in each block of the form follow. It is important to ***stay within the lines*** to meet ***optical scanning requirements.***

Block 1 Agency Use Only *(Leave blank)*

Block 2. Report Date. Full publication date including day, month, and year, if available (e g 1 Jan 88). Must cite at least the year.

Block 3. Type of Report and Dates Covered State whether report is interim, final, etc. If applicable, enter inclusive report dates (e.g. 10 Jun 87 - 30 Jun 88).

Block 4. Title and Subtitle. A title is taken from the part of the report that provides the most meaningful and complete information. When a report is prepared in more than one volume, repeat the primary title, add volume number, and include subtitle for the specific volume On classified documents enter the title classification in parentheses.

Block 5. Funding Numbers. To include contract and grant numbers; may include program element number(s), project number(s), task number(s), and work unit number(s). Use the following labels:

C	- Contract	PR	- Project
G	- Grant	TA	- Task
PE	- Program Element	WU	- Work Unit Accession No.

Block 6. Author(s) Name(s) of person(s) responsible for writing the report, performing the research, or credited with the content of the report. If editor or compiler, this should follow the name(s).

Block 7. Performing Organization Name(s) and Address(es). Self-explanatory

Block 8. Performing Organization Report Number. Enter the unique alphanumeric report number(s) assigned by the organization performing the report.

Block 9. Sponsoring/Monitoring Agency Name(s) and Address(es). Self-explanatory.

Block 10. Sponsoring/Monitoring Agency Report Number. *(If known)*

Block 11. Supplementary Notes. Enter information not included elsewhere such as. Prepared in cooperation with..., Trans. of..., To be published in.... When a report is revised, include a statement whether the new report supersedes or supplements the older report.

Block 12a. Distribution/Availability Statement. Denotes public availability or limitations. Cite any availability to the public. Enter additional limitations or special markings in all capitals (e.g. NOFORN, REL, ITAR).

- DOD - See DoDD 5230.24, "Distribution Statements on Technical Documents."
- DOE - See authorities.
- NASA - See Handbook NHB 2200.2.
- NTIS - Leave blank.

Block 12b. Distribution Code.

- DOD - Leave blank.
- DOE - Enter DOE distribution categories from the Standard Distribution for Unclassified Scientific and Technical Reports.
- NASA - Leave blank.
- NTIS - Leave blank.

Block 13. Abstract. Include a brief *(Maximum 200 words)* factual summary of the most significant information contained in the report.

Block 14. Subject Terms. Keywords or phrases identifying major subjects in the report.

Block 15. Number of Pages. Enter the total number of pages.

Block 16. Price Code. Enter appropriate price code *(NTIS only)*.

Blocks 17. - 19. Security Classifications. Self-explanatory. Enter U.S. Security Classification in accordance with U.S. Security Regulations (i.e., UNCLASSIFIED). If form contains classified information, stamp classification on the top and bottom of the page.

Block 20. Limitation of Abstract. This block must be completed to assign a limitation to the abstract. Enter either UL (unlimited) or SAR (same as report). An entry in this block is necessary if the abstract is to be limited. If blank, the abstract is assumed to be unlimited.